

# **Design of optical semiconductors optimized for photocatalytic organic synthesis**

*Thesis submitted in partial fulfillment of the requirements for the degree of Doctor of Philosophy in Chemical and Biological Engineering, at the Faculty of Engineering, University of Porto*

***Ana Raquel Almeida Fernandes***

**Supervisors:**

Professor Cláudia Sofia Castro Gomes da Silva

Professor Joaquim Luís Bernardes Martins de Faria

Doctor Maria José Fernandes Sampaio



ASSOCIATE LABORATORY  
LABORATORY OF SEPARATION AND REACTION ENGINEERING  
LABORATORY OF CATALYSIS AND MATERIALS







*A mais uma etapa concluída  
A mais uma batalha vencida*



## **Agradecimentos**

Desejo expressar os meus sinceros agradecimentos ao Programa Regional Operacional do Norte de Portugal (NORTE2020) suportado pelo Fundo Social Europeu (FSE), pelo financiamento da bolsa de doutoramento com referência NORTE-08-5369-FSE-000028.

Ao Laboratório de Catálise e Materiais (LCM), integrado no Laboratório Associado LSRE-LCM, agradeço pelos recursos disponíveis para a realização desta tese.

À minha orientadora, Professora Cláudia Sofia Gomes Castro da Silva, e aos meus coorientadores Professor Doutor Joaquim Luís Bernardes Martins de Faria e Doutora Maria José Fernandes Sampaio, pelo acompanhamento e confiança em mim depositada ao longo destes 4 anos. Gostaria de deixar um agradecimento especial à Doutora Maria José Fernandes Sampaio por ter percorrido comigo todo este caminho, sem nunca me deixar desistir e mostrando-me sempre que todos os obstáculos eram ultrapassáveis. Acima de tudo, agradeço pela companhia, compreensão e amizade que sempre demonstrou e que ficarão sempre na minha memória.

Agradeço também aos diretores, professores e investigadores do Laboratório Associado LSRE-LCM, pela disponibilidade e auxílio, sempre que necessário, permitindo assim o meu enriquecimento científico.

Ao Doutor Carlos Pinto Moreira de Sá, diretor do CEMUP, e ao Doutor Pedro Bandeira Tavares (UTAD), por permitirem a realização e auxiliarem na correta interpretação dos dados obtidos por técnicas específicas de caracterização de materiais.

Ao Doutor João Nunes, à Engenheira Rita Pontes, à Mestre Carolina Nunes e restantes equipa de investigação pela oportunidade de realizar um estágio na BLC3 – Campus de Tecnologia e Inovação, proporcionando-me um crescimento tanto pessoal como profissional.

Aos meus amigos, em especial ao André, à Joana e à Amélia, pela amizade, apoio, e acima de tudo, por todas as risadas que demos juntos, pois foram fundamentais para ultrapassar os momentos mais difíceis deste trajeto.

A todos os restantes colegas do LSRE-LCM, pela partilha de conhecimento, de aventuras e de boa disposição.

Por fim, quero agradecer à minha família e ao meu namorado Tiago, pelo amor e pelo apoio incondicional que sempre demonstraram. Em especial, agradeço ao Tiago por ter sido o meu suporte nesta jornada e, por continuar a sê-lo também na vida. Não há palavras para expressar o tamanho da minha gratidão.





## Abstract

Partial oxidation of alcohols into aldehydes, ketones and acids is an essential reaction in organic chemistry, adopted in the manufacturing of an incredible amount of products. The tremendous environmental impact of conventional processes industrially adopted has been a significant concern of modern society.

By combining heterogeneous photocatalysis' operational advantages with the vast range of materials engineering possibilities, highly selective and efficient systems can be designed to achieve a valid industrial application.

The present work relies on the photocatalytic production of aromatic aldehydes (vanillin, *p*-anisaldehyde, benzaldehyde and piperonal) and vitamin B3, using their respective alcohols as starting molecules.

The research was initiated with the synthesis of vanillin (VAD) from vanillyl alcohol (VA) under UV-LED irradiation and argon atmosphere, using a carbon nanofiber-zinc oxide (CNF/ZnO) composite as photocatalyst.

The incorporation of the carbon phase in ZnO increased the specific surface area ( $S_{BET}$ ) and the materials' photocatalytic performance. The latter was attributed to the efficient separation of charge carriers generated on the optical semiconductor due to the electron scavenger character of CNF. The presence of reactive oxygen species (ROS) in the reaction medium promoted faster oxidation of the starting alcohol but negatively affected the selectivity. With the best performing material (10%CNF/ZnO), the maximum of selectivity towards the synthesis of VAD was 67%, representing a significant increase when compared to previous studies (<27%). The same photocatalyst was successfully applied in the selective synthesis of other aromatic aldehydes, namely *p*-anisaldehyde (AAD), piperonal (PAD), and benzaldehyde (BAD). There is a direct relationship between the efficiency of the photocatalytic oxidation of the alcohols and the activating nature of their aromatic ring substituents. AAD proved to be a highly reactive substrate, with 66% conversion after 8 h of irradiation.

Considering the negative impact of the use of metal oxide photocatalysts in the environmental sustainability of the photocatalytic approach, the research was focused on the preparation and evaluation of graphite-like carbon nitride (GCN)-based catalysts in the photocatalytic synthesis of AAD.

Morphologically modified GCN-based materials (GCN-UL, GCN-OM and GCN-MP) exhibited physical defects on their surface, which increased their  $S_{BET}$ . A high amount of nitrogen vacancies was identified in these catalysts, indicating many reactive sites to catalyze redox reactions. The textural and morphological modifications induced in

GCN an enhanced light absorption capacity and reduced electron ( $e^-$ )/hole ( $h^+$ ) recombination rate, contributing to its improved photocatalytic performance. GCN-UL was the best photocatalyst reaching 60% yield at 64% conversion for AAD production after 4 h of UV-LED radiation under deoxygenated conditions. Under oxygenated conditions (air), the process efficiency was increased to 79% yield at 92% conversion only after 1.5 h reaction. All photocatalysts kept their performance when using visible-LED radiation under air atmosphere. Trapping of photogenerated  $h^+$  and radicals by selective scavengers showed that reactive holes ( $h_r^+$ ) played the primary role in the AAD synthesis under deoxygenated conditions. Under oxygenated conditions, the process is governed by the effect of ROS, namely superoxide radicals ( $O_2^{\cdot-}$ ), with a significant contribution of  $h_r^+$ .

Citric acid-modified graphite-like carbon nitride materials (GCN-zCA) presented surface porosity, defective polymeric structure, and enhanced visible light absorption in the 450-700 nm range, attributed to the existence of mid-gap states and  $n-\pi^*$  electronic transitions. All the modified catalysts presented high selectivity (>99%) towards the conversion of AA into AAD under visible-LED irradiation. The best performing photocatalyst (GCN-20CA) reached 63% yield (contrasting with 22% obtained with bulk GCN) after 4 h reaction. Moreover, GCN-20CA practically duplicated the hydrogen ( $H_2$ ) production compared to bulk GCN (75 and 44  $\mu\text{mol } H_2$  evolved in 3 h, respectively) by using platinum nanoparticles as co-catalyst and EDTA as the sacrificial electron donor. Moreover, AA was successfully used as a sacrificial agent for water splitting, with simultaneous production of AAD and  $H_2$ . Reusability tests showed that GCN-20CA remained stable in consecutive runs for AAD synthesis and  $H_2$  production.

Copolymerized GCN-based materials (GCN-BAr, GCN-ABN and GCN-ATCN) presented a highly defective surface than bulk GCN due to the presence of nitrogen vacancies. With the thermal exfoliation at 500°C under air flow, the defects were kept on the surface of the catalysts and the graphitic layers of tris-s-triazine rings split, which resulted in an increased  $S_{BET}$ . Barbituric acid (BAr) was the only copolymerization agent that revealed an improvement of the photocatalytic performance of the modified catalysts both before (GCN-BAr) and after (GCN-BAr-500) the thermal exfoliation when compared to the non-copolymerized materials (GCN and GCN-500, respectively). In fact, after 1.5 h of UV-LED radiation under oxygenated conditions, GCN-BAr reached 93% of conversion and 89% of yield, while GCN-BAr-500 presented a faster production, with 98% of conversion and 96% of yield only after

0.5 h of reaction. The reusability tests performed with both catalysts proved their operational stability after three consecutive runs, keeping high production efficiency. Thermally post-treated GCN-based catalysts (GCN-A-500, GCN-A-550, GCN-A-600 and GCN-A-620) revealed a less crystalline structure, with high degree of destruction of the graphite-like layers. In GCN-A-600 and GCN-A-620, a significant increase occurred in light absorption in the visible range of the electromagnetic spectrum, with a high contribution of the  $n-\pi^*$  electronic transitions excitation process. GCN-A-620 was the best performing catalyst, with 91% of selectivity and 98% conversion after 1 h of visible-LED radiation under oxygenated conditions. Using UV-LED and simulated solar light as irradiation sources, GCN-A-620 exhibited a reduction in conversion (67% and 43%, respectively) compared to visible-LED radiation. However, selectivity was positively affected, with a significant increase to 98% and 100% in both cases, indicating a good use of solar light to promote photocatalytic reactions.

By comparing the best performing material developed with the published results on the photoconversion of AA into AAD, it was observed a clear improvement in the energy efficiency of the designed processes, with less energy spent to achieve improved performances.

In the last stage of the study, GCN-based catalysts (GCN, GCN-500 and GCN-A-620) were applied to the synthesis of vitamin B3 (VB3) through the oxidation of 3-pyridinemethanol (3PM). The oxidation of the starting alcohol (3PM) resulted in the formation of the respective aldehyde (3-pyridinecarboxaldehyde; 3PC) and the acid (VB3). GCN-A-620 revealed a highly efficient performance, with 100% of 3PM conversion and selectivity towards VB3 production after 7 h of irradiation, achieving the best result among all the catalysts already reported in the literature.

The immobilized GCN-A-620 in sodium alginate (SA) membrane (GCN-A-620\_SA) also revealed great potential as photocatalyst in this particular synthesis process, allowing foreseeing the designed system as a valuable alternative for an industrial application context.



## Resumo

A oxidação parcial de álcoois a aldeídos, cetonas e ácidos é uma reação essencial na química orgânica, adotada no fabrico de uma grande quantidade de produtos. O tremendo impacto ambiental dos processos convencionais adotados industrialmente tem sido uma grande preocupação da sociedade moderna.

Combinando as vantagens operacionais da fotocatalise heterogénea com a enorme variedade de possibilidades de engenharia de materiais, sistemas altamente seletivos e eficientes podem ser projetados para alcançar uma aplicação industrial válida.

O presente trabalho baseia-se na produção fotocatalítica de aldeídos aromáticos (vanilina, *p*-anisaldeído, benzaldeído e piperonal) e vitamina B3, utilizando os seus respetivos álcoois como moléculas iniciais.

A investigação foi iniciada com a síntese de vanilina (VAD) a partir de álcool vanílico (VA) sob irradiação UV-LED e na ausência de oxigénio, usando um compósito de nanofibras de carbono e óxido de zinco (CNF/ZnO) como fotocatalisador.

A incorporação da fase de carbono permitiu aumentar a área de superfície específica ( $S_{BET}$ ) e o desempenho fotocatalítico dos materiais. Este último foi atribuído à eficiente separação dos transportadores de carga gerados no semiconductor ótico devido ao caráter de sequestrador de eletrões das CNF. A presença de espécies reativas de oxigénio (ROS) no meio reacional promoveu uma oxidação mais rápida, mas afetou negativamente a seletividade.

Com o material que demonstrou melhor desempenho (10% CNF/ZnO), o máximo de seletividade para a síntese de VAD foi de 67%, representando um aumento significativo quando comparado a estudos anteriores (<27%). O mesmo fotocatalisador foi aplicado com sucesso na síntese seletiva de outros aldeídos aromáticos, nomeadamente o *p*-anisaldeído (AAD), o piperonal (PAD) e o benzaldeído (BAD). A eficiência da oxidação fotocatalítica dos álcoois foi diretamente afetada pela natureza ativadora ou desativadora dos substituintes do anel aromático. O AA provou ser o álcool mais reativo, com 66% de conversão após 8 h de irradiação. Considerando o impacto negativo do uso de catalisadores de óxido metálicos na sustentabilidade ambiental da tecnologia fotocatalítica, o estudo foi focado na preparação de materiais de nitreto de carbono semelhantes à grafite (GCN) e sua avaliação na síntese fotocatalítica de AAD.

Materiais baseados em GCN modificados morfologicamente (GCN-UL, GCN-OM e GCN-MP) exibiram defeitos físicos na superfície, o que aumentou a sua  $S_{BET}$ . Uma grande perda de átomos de azoto foi identificada nestes catalisadores, indicando um

aumento dos locais reativos disponíveis para catalisar reações redox. As modificações texturais e morfológicas induziram uma maior capacidade de absorção de luz e a redução da taxa de recombinação elétron ( $e^-$ )/buraco ( $h^+$ ), contribuindo para o seu melhor desempenho fotocatalítico. O GCN-UL foi o fotocatalisador que apresentou melhor desempenho, atingindo 60% de rendimento em 64% de conversão para produção de AAD após 4 h de radiação UV-LED na ausência de oxigénio. Na presença de oxigénio (sob atmosfera de ar), a eficiência do processo foi aumentada para 79% de rendimento em 92% de conversão após 1,5 h de reação.

Todos os fotocatalisadores mantiveram seu desempenho ao usar radiação LED visível sob atmosfera de ar. O aprisionamento de  $h^+$  foto gerados e radicais por catadores seletivos mostrou que, na ausência de oxigénio, os buracos reativos ( $h_r^+$ ) desempenharam o papel principal na síntese de AAD. Na presença de oxigénio, o processo é regido pelo efeito dos radicais superóxidos ( $O_2^{\cdot-}$ ), com uma contribuição significativa dos  $h_r^+$ .

Os materiais de nitreto de carbono modificados por ácido cítrico (GCN-zCA) apresentaram porosidade superficial, estrutura polimérica defeituosa e maior absorção de luz visível na faixa de 450-700 nm, atribuída à existência de estados intermediários e transições eletrónicas  $n-\pi^*$ .

Todos os catalisadores modificados apresentaram alta seletividade (>99%) para a conversão de AA em AAD sob radiação LED visível, com o fotocatalisador com melhor desempenho (GCN-20CA) atingindo 63% de rendimento (contrastando com 22% obtido com GCN) após 4 h de reação. Além disso, o GCN-20CA praticamente duplicou a produção de hidrogénio ( $H_2$ ) quando comparado ao GCN (75 e 44  $\mu\text{mol } H_2$  após 3 h, respetivamente), usando nanopartículas de platina como co-catalisador e EDTA como dador de elétrões. Além disso, o AA foi usado com sucesso como agente de sacrifício para oxidação da água, com produção simultânea de AAD e  $H_2$ . Os testes de estabilidade operacional mostraram que o GCN-20CA permaneceu estável durante três reações consecutivas, tanto para síntese de AAD quanto para produção de  $H_2$ .

Os materiais derivados de GCN obtidos por copolimerização (GCN-BAr, GCN-ABN e GCN-ATCN) apresentaram uma superfície altamente alterada quando comparados com o GCN, devido à perda de átomos de azoto. Com a exfoliação térmica a 500°C sob fluxo de ar, os defeitos foram mantidos na superfície dos catalisadores e as camadas de grafite com anéis de tris-s-triazina foram afastadas, o que resultou no aumento da  $S_{BET}$ . O ácido barbitúrico (BAr) foi o único agente de copolimerização que revelou um impacto positivo do desempenho fotocatalítico dos catalisadores

modificados tanto antes (GCN-BAr) quanto após (GCN-BAr-500) a exfoliação térmica, quando comparado aos materiais não copolimerizados (GCN e GCN-500, respetivamente).

De facto, após 1,5 h de irradiação UV-LED sob condições oxigenadas, o GCN-BAr atingiu 93% de conversão e 89% de rendimento, enquanto que o GCN-BAr-500 apresentou uma produção mais rápida, com 98% de conversão e 96% de rendimento após 0,5 h de reação. Os testes de reutilização realizados com ambos os catalisadores provaram sua estabilidade operacional após três ciclos oxidativos consecutivos, mantendo alta eficiência de produção.

Os catalisadores baseados em GCN tratados termicamente (GCN-A-500, GCN-A-550, GCN-A-600 e GCN-A-620) revelaram uma estrutura menos cristalina, com um alto grau de destruição das camadas grafíticas.

No caso do GCN-A-600 e GCN-A-620, ocorreu um aumento significativo na absorção de luz na faixa visível do espectro eletromagnético, com uma alta contribuição das transições eletrónicas  $n-\pi^*$  no processo de excitação. O GCN-A-620 foi o catalisador com melhor desempenho, com 91% de seletividade e 98% de conversão após 1 h de radiação LED visível sob condições oxigenadas. Usando radiação UV-LED e luz solar simulada como fontes de irradiação, o GCN-A-620 exibiu uma redução na conversão (67% e 43%, respetivamente) quando comparado à radiação LED visível. No entanto, a seletividade foi positivamente afetada, com aumento significativo em ambos os casos (de 91% para 98% e 100%), o que pode indicar um uso válido da luz solar para promover reações fotocatalíticas.

Ao comparar os materiais desenvolvidos com os melhores desempenhos fotocatalíticos com os resultados publicados sobre a fotoconversão de AA em AAD, observou-se uma clara melhoria no que diz respeito à eficiência energética, com uma redução na energia gasta para alcançar desempenhos fotocatalíticos melhorados.

Na última etapa do estudo, catalisadores baseados em GCN (GCN, GCN-500 e GCN-A-620) foram aplicados na síntese de vitamina B3 (VB3), através da oxidação de 3-piridinametanol (3PM). A oxidação do álcool (3PM) resultou na formação do respetivo aldeído (3-piridinocarboxaldeído; 3PC) e do ácido (VB3).

O GCN-A-620 revelou desempenho altamente eficiente, com 100% de conversão de 3PM e seletividade para a produção de VB3 após 7 h de irradiação, alcançando o melhor resultado entre todos os catalisadores já relatados na literatura.

O GCN-A-620 imobilizado em membranas de alginato de sódio (GCN-A-620\_SA) revelou também grande potencial como fotocatalisador neste processo particular de

síntese, permitindo considerar o sistema desenvolvido como uma alternativa valiosa para a aplicação num contexto industrial.



---

**Table of contents**

ABSTRACT	I
RESUMO	V
TABLE OF CONTENTS	IX
LIST OF FIGURES	XIII
LIST OF TABLES	XIX
LIST OF SCHEMES	XXI
LIST OF ABBREVIATIONS AND SYMBOLS	XXIII
MATERIALS NOMENCLATURE	XXVII

**PART I – CHAPTER 1** **1**

GENERAL INTRODUCTION	1
1.1 IMPORTANCE OF PARTIAL OXIDATION OF ALCOHOLS	3
1.2 MOVING THE PARADIGM FROM MOLECULAR PHOTOCHEMISTRY TO PHOTOCATALYTIC SYNTHESIS	5
1.3 SEMICONDUCTOR PHOTOCATALYSIS – MECHANISMS AND APPLICATIONS	7
1.4 PREPARATION AND PROPERTIES OF PHOTOCATALYTIC MATERIALS	10
1.5 AIMS AND OBJECTIVES	13
1.6 DESCRIPTION OF THE PERFORMED WORK	13
1.7 MAIN FINDINGS	14
1.8 THESIS OUTLINE	15

**PART I – CHAPTER 2** **17**

STATE-OF-THE-ART	17
2.1 SEMICONDUCTOR PHOTOCATALYTIC SYNTHESIS OF ALDEHYDES, KETONES AND ACIDS THROUGH PARTIAL OXIDATION OF ALCOHOLS	19
2.1.1 BENZALDEHYDE	19
2.1.2 <i>P</i> -ANISALDEHYDE	21
2.1.3 VANILLIN	23
2.1.4 PIPERONAL	25
2.1.5 VITAMIN B3	26

2.2 FUTURE PERSPECTIVES 27

**PART II – CHAPTER 3 31**

---

SYNTHESIS OF VANILLIN USING CNF/ZNO PHOTOCATALYSTS 31

3.1 INTRODUCTION 33

3.2 EXPERIMENTAL 33

3.2.1 MATERIALS 33

3.2.2 SYNTHESIS OF CNF/ZNO COMPOSITES 34

3.2.3 CHARACTERIZATION OF THE PHOTOCATALYSTS 34

3.2.4 PHOTOCATALYTIC EXPERIMENTS 35

3.2.5 ANALYTICAL TECHNIQUES 36

3.3 RESULTS AND DISCUSSION 36

3.3.1 CHARACTERIZATION OF CNF/ZNO COMPOSITES 36

3.3.2 PHOTOCATALYTIC SELECTIVE SYNTHESIS OF VANILLIN 42

3.3.3 PHOTOCATALYTIC SELECTIVE SYNTHESIS OF OTHER AROMATIC  
ALDEHYDES 47

3.4 CONCLUSIONS 51

**PART II – CHAPTER 4 53**

---

PHOTOCATALYTIC SYNTHESIS OF *p*-ANISALDEHYDE BY GRAPHITE-LIKE CARBON  
NITRIDE-BASED MATERIALS 53

4.1 INTRODUCTION 55

4.2 EXPERIMENTAL 56

4.2.1 MATERIALS 56

4.2.2 BULK GCN 56

4.2.3 MORPHOLOGICALLY MODIFIED GCN 56

4.2.4 CITRIC ACID-MODIFIED GCN 58

4.2.5 COPOLYMERIZED GCN 58

4.2.6 THERMALLY POST-TREATED GCN 58

4.3 CHARACTERIZATION OF THE CATALYSTS 59

4.4 PHOTOCATALYTIC SETUP 60

4.5 ANALYTICAL PROCEDURES 61

---

4.6 MORPHOLOGICALLY-MODIFIED GCN-BASED PHOTOCATALYSTS	62
4.6.1 CHARACTERIZATION	62
4.6.2 PHOTOCATALYTIC RESULTS	67
4.6.3 REACTION PATHWAY	70
4.7 CITRIC ACID-MODIFIED GCN-BASED CATALYSTS	73
4.7.1 CHARACTERIZATION	73
4.7.2 PHOTOCATALYTIC RESULTS	80
4.8 COPOLYMERIZED GCN-BASED CATALYSTS	86
4.8.1 CHARACTERIZATION	86
4.8.2 PHOTOCATALYTIC RESULTS	93
4.9 THERMALLY POST-TREATED GCN-BASED MATERIALS	96
4.9.1 CHARACTERIZATION	96
4.9.2 PHOTOCATALYTIC RESULTS	102
4.9.3 EVALUATION OF PHOTOCATALYTIC MATERIALS FOR THE SYNTHESIS OF <i>P</i> -ANISALDEHYDE	103
4.10 CONCLUSIONS	108
<b>PART II – CHAPTER 5</b>	<b>109</b>
SYNTHESIS OF VITAMIN B3 USING GCN-BASED PHOTOCATALYSTS	109
5.1 INTRODUCTION	111
5.2 EXPERIMENTAL	111
5.2.1 MATERIALS	111
5.2.2 SYNTHESIS AND CHARACTERIZATION OF GCN-BASED CATALYSTS	111
5.2.3 PHOTOCATALYTIC EXPERIMENTS	112
5.2.4 ANALYTICAL PROCEDURE	112
5.3 RESULTS AND DISCUSSION	113
5.3.1 CHARACTERIZATION OF GCN-BASED CATALYSTS	113
5.3.2 PHOTOCATALYTIC RESULTS	116
5.4 CONCLUSIONS	122
<b>PART III – CHAPTER 6</b>	<b>125</b>
FINAL REMARKS AND FUTURE WORK	125

---

*TABLE OF CONTENTS*

---

6.1 FINAL REMARKS	127
6.2 FUTURE WORK	129
REFERENCES	131

## List of figures

### PART I – CHAPTER 1

- Fig. 1.1 Selective oxidation of (A) primary and (B) secondary alcohols ( $R_1, R_2 \neq H$ ;  $[O]$  represents the oxidizing agent).----- 3
- Fig. 1.2 Diagram of photocatalytic phenomena at a semiconductor/liquid interface. Straight and waved lines correspond to radiative and nonradiative processes, respectively. The dark vertical bar indicates the interface between the semiconductor and liquid phase. (For number meaning refer to the body text). ----- 8
- Fig. 1.3 Reaction pathway for the synthesis of carbon nitride using dicyandiamide as precursor.-----12

### PART II – CHAPTER 3

- Fig. 3.1 SEM micrographs of a) ZnO, b) 5%CNF/ZnO, c) 10%CNF/ZnO, d) 15%CNF/ZnO and e) 20%CNF/ZnO. TEM image of f) CNF. Highlighted zones: I) ZnO tetrapods, II) long tubular CNF and III) ZnO agglomerates. -----37
- Fig. 3.2 TG analysis of i) ZnO, ii) 5%CNF/ZnO, iii) 10%CNF/ZnO, iv) 15%CNF/ZnO, v) 20%CNF/ZnO and vi) CNF.-----38
- Fig. 3.3 Isotherms of  $N_2$  adsorption-desorption at  $-196^\circ C$  for i) ZnO, ii) 5%CNF/ZnO, iii) 10%CNF/ZnO, iv) 15%CNF/ZnO, v) 20%CNF/ZnO and vi) CNF.-----40
- Fig. 3.4 a) Photograph, b) DR UV-Vis spectra expressed in Kubelka-Munk (KM) equivalent absorption units and c) the respective Tauc plots of i) ZnO, ii) 5%CNF/ZnO, iii) 10%CNF/ZnO, iv) 15%CNF/ZnO, v) 20%CNF/ZnO and vi) CNF. -----40
- Fig. 3.5 a) Solid-state PL spectra of i) ZnO, ii) 5%CNF/ZnO, iii) 10%CNF/ZnO, iv) 15%CNF/ZnO and v) 20%CNF/ZnO obtained upon excitation at 340 nm. Inset shows a zoom of the emission bands in the visible region. b) ZnO fluorescence emission intensity (measured at the maximum of emission) in function of CNF percentage.--41
- Fig. 3.6 Normalized concentration of VA during the photolysis experiment ( $\square$ ) and using only CNF as catalyst ( $\blacksquare$ ), under UV-LED irradiation ( $\lambda_{max} = 370$  nm) over 4 h reaction.-----42
- Fig. 3.7 a) Effect of ZnO load on X, S and Y at 1 h of reaction. b) Effect of CNF content on X, S and Y in long-term (8 h) reactions (0% CNF content corresponds to bare ZnO).-----43

Fig. 3.8 Concentration profile of VAD over 2 h of reaction, using ZnO (▲, ■) and 10%CNF/ZnO (△, □) as catalysts, under air (□, ■) and argon (△, ▲) atmospheres. 45

Fig. 3.9 Normalized concentration of VA over 4 h of reaction under argon atmosphere, using ZnO (▲) and 10%CNF/ZnO (△) as catalysts, in the presence of a hole scavenger (0.1 M EDTA). -----47

Fig. 3.10 Concentration profile of *p*-anisaldehyde (AAD), benzaldehyde (BAD), piperonal (PAD) and vanillin (VAD) over 480 min of reaction, using (a) ZnO and (b) 10%CNF/ZnO as catalysts. -----48

**PART II – CHAPTER 4**

Fig. 4.1 SEM micrographs of a) bulk GCN, b) GCN-MP, c) GCN-OM and d) GCN-UL. -----62

Fig. 4.2 FTIR-ATR spectra of i) GCN, ii) GCN-MP, iii) GCN-OM and iv) GCN-UL. Highlighted zones A, B and C denote characteristic IR bands of carbon nitride materials. -----63

Fig. 4.3 a) C1s and b) N1s XPS spectra of GCN, GCN-MP, GCN-OM and GCN-UL. -----65

Fig. 4.4 a) DRUV-vis spectra (inset shows the respective Tauc plot) and b) solid state PL spectra of i) bulk GCN, ii) GCN-MP, iii) GCN-OM and iv) GCN-UL. Dashed line indicates the wavelength of maximum PL intensity for bulk GCN. -----66

Fig. 4.5 a) Normalized concentration of AA and b) AAD using GCN (◇, ◆), GCN-MP (○, ●), GCN-OM (△, ▲), GCN-UL (□, ■) and TiO<sub>2</sub> P25 (▷, ►) along 240 min reaction under deoxygenated conditions. c) X, S and Y using the photocatalysts under deoxygenated conditions after 240 min of irradiation. d) Effect of  $S_{BET}$  in the photocatalytic performance of all catalysts. Solid line represents the linear fitting ( $r^2 > 0.98$ ). Reaction time of maximum AAD concentration (■) and the respective values of X and Y, using the GCN-based photocatalysts under oxygenated conditions, using UV-LED (e) and visible-LED (f) irradiation. -----68

Fig. 4.6 Effect of scavengers in the photocatalytic performance of GCN-UL under air (black columns) and argon (red columns) atmospheres, using a UV-LED irradiation source. The X and S values are determined to the maximum of AAD production, with the indication of the respective reaction time (■). -----71

- Fig. 4.7 Possible reaction mechanism for the equilibrated photocatalytic cycle of AA selective oxidation to AAD over the GCN-UL photocatalyst, starting at the reductive channel (A) or, in alternative, at the oxidative channel (B).-----72
- Fig. 4.8 SEM micrographs of a) GCN, b) GCN-5CA, c) GCN-10CA, d) GCN-15CA, e) GCN-20CA and f) GCN-25CA. Black arrows indicate surface defects. -----74
- Fig. 4.9 a) Photograph, b) DR UV-Vis spectra, c) bandgap energy ( $E_g$ ) and d) transition energy ( $E_T$ ) determined from the respective Tauc plots for i) GCN, ii) GCN-5CA, iii) GCN-10CA, iv) GCN-15CA, v) GCN-20CA and vi) GCN-25CA. -----75
- Fig. 4.10 a) PL emission spectra and b) normalized PL emission spectra under excitation at 370 nm of i) GCN, ii) GCN-5CA, iii) GCN-10CA, iv) GCN-15CA, v) GCN-20CA and vi) GCN-25CA. Excitation spectra of all catalysts under emission at c) 463 nm and d) 528 nm. Highlighted zones Z1, Z2 and Z3 indicate the most relevant differences between the spectra. -----77
- Fig. 4.11 (a) C1s and (b) N1s XPS spectra of GCN and GCN-zCA materials (z = 5, 10, 15, 20, 25). Dashed lines indicate the shifted peaks. -----79
- Fig. 4.12 FTIR-ATR spectra of i) GCN, ii) GCN-5CA, iii) GCN-10CA, iv) GCN-15CA, v) GCN-20CA and vi)GCN-25CA. Highlighted zones A, B and C denote characteristic IR bands of carbon nitride materials. -----80
- Fig. 4.13 a) Normalized concentration of AA and b) profile of AAD production along 240 min reaction, using TiO<sub>2</sub> P25, GCN and GCN-zCA (z = 5, 10, 15, 20, 25) as catalysts.-----81
- Fig. 4.14 a) Photocatalytic H<sub>2</sub> production, using GCN and GCN-20CA as catalysts, upon 180 min of visible-LED irradiation ( $\lambda_{max} = 412$  nm) in the presence of Pt (3 wt. %) and EDTA (0.02M). b) Reusability of GCN-20CA as photocatalyst for H<sub>2</sub> production in four consecutive cycles, using EDTA and AA aqueous solutions (0.02 M) as sacrificial agents. -----82
- Fig. 4.15 Transient photocurrent response of GCN (black) and GCN-20CA (orange) at a constant applied potential of 0.2 V vs Ag/AgCl, with 30 s simulated solar light (100 mW·cm<sup>-2</sup>) on/off cycles during 1000 s. -----83
- Fig. 4.16 Valence band (VB) XPS spectra of GCN and GCN-20CA. Linear fitting was used to determine the VB potential.-----84
- Fig. 4.17 Band structure of GCN and GCN-20CA. -----85

Fig. 4.18 SEM micrographs of GCN-Z and GCN-Z-500 materials (Z = BAr, ABN and ATCN). Highlighted zones (X1, X2 and X3) indicates important textural characteristics of each catalyst. -----87

Fig. 4.19 FTIR-ATR spectra of a) GCN-Z and b) GCN-Z-500 materials (Z = BAr, ABN and ATCN). Highlighted regions (A, B, C) correspond to characteristic IR bands of GCN-based materials. -----89

Fig. 4.20 C1s and N1s XPS spectra of GCN-500, GCN-BAr-500, GCN-ABN-500 and GCN-ATCN-500. -----90

Fig. 4.21 (a, c) DRUV-vis spectra and (b, d) Tauc plot analysis of GCN-Z and GCN-Z-500 materials (Z = BAr, ABN and ATCN). Highlighted zone indicates the Urbach tails. -----91

Fig. 4.22 (a, b) PL and (c, d) normalized PL spectra of GCN-Z and GCN-Z-500 materials -----92

Fig. 4.23 a, b) Normalized AA and c, d) AAD concentrations using TiO<sub>2</sub> P25 (×), GCN-Z (○, △, ◇, □) and GCN-Z-500 (●, ▲, ◆, ■) catalysts. X and S obtained using e) GCN-Z and f) GCN-Z-500 catalysts (over 90 and 30 min, respectively). Reuse experiment using g) GCN-BAr and h) GCN-BrA-500 as photocatalyst in three consecutive cycles. \*The values of X and S of TiO<sub>2</sub> P25 were determined at the maximum of AAD production (20 min). -----94

Fig. 4.24 SEM micrographs of GCN and the thermally post-treated GCN. -----97

Fig. 4.25 a) FTIR-ATR spectra and b) XRD pattern of i) GCN, ii) CN-A-500, iii) CN-A-550, iv) CN-A-600 and v) CN-A-620. Highlighted zones A, B and C indicate the characteristic bands of GCN-based catalysts. -----99

Fig. 4.26 a) Photograph, b) DR UV-vis spectra, c) Tauc plot, d) PL spectra and e) normalized PL intensity of i) GCN, ii) GCN-A-500, iii) GCN-A-550, iv) GCN-A-600 and v) GCN-A-620. Dashed zones indicate the b) Urbach tails and d) the wavelength of the maximum of PL intensity of GCN. Highlighted zone Z1 indicate the second band of PL emission.----- 100

Fig. 4.27 a) Normalized AA and b) AAD concentrations using TiO<sub>2</sub> P25 (×), GCN (○) and GCN-A-Z (△, ◇, □, ◇) as catalysts. c) X and S obtained using GCN-A-Z catalysts, over 60 min of reaction under visible-LED radiation. d) Comparison of the photocatalytic performance of GCN-A-620 under different radiation sources, over 60



---

min of reaction. \*The values of X and S of TiO<sub>2</sub> P25 were determined at the maximum of AAD production (45 min).----- 102

## PART II – CHAPTER 5

Fig. 5.1 SEM micrographs of a) GCN, b) GCN-500 and c) GCN-A-620. d) Barret-Joyner-Halenda pore volume distribution derived from the N<sub>2</sub> adsorption isotherms at -196°C of ----- 113

Fig. 5.2 XRD pattern of i) GCN, ii) GCN-500 and iii) GCN-A-620 catalysts. ----- 115

Fig. 5.3 a) DR UV-vis spectra (inset shows the respective Tauc plot) and b) PL spectra (inset shows the normalized PL intensity) of i) GCN, ii) GCN-500 and iii) GCN-A-620. Highlighted zones Z1 and Z2 indicate the two bands of PL emission.----- 115

Fig. 5.4 Absorption spectra of i) 3-pyridinemethanol (3PM), ii) 3-pyridinecarboxaldehyde (3PC) and iii) vitamin B3 (VB3); iv) intensity of irradiation of visible LEDs ( $\lambda_{max} = 412\text{nm}$ ).----- 117

Fig. 5.5 a) Normalized 3PM, b) 3PC and c) VB3 concentrations over 7 h of irradiation ( $\lambda_{max} = 412\text{ nm}$ ) using GCN ( $\blacktriangleright$ ), GCN-500 ( $\circ$ ) and GCN-A-620 ( $\square$ ) as catalysts. d, e) X, S and Y achieved for the photooxidation of 3PM into 3PC and VB3 at the maximum of their concentration. f) Photograph of the immobilized GCN-A-620\_SA used in the photocatalytic reaction. g) Normalized 3PM ( $\blacklozenge$ ), 3PC ( $\blacklozenge$ ) and VB3 ( $\blacklozenge$ ) concentrations over 7 h reaction using GCN-A-620\_SA. ----- 119



## List of tables

### PART I – CHAPTER 2

Table 2.1 Studies published on the heterogeneous photocatalytic synthesis of benzaldehyde through the conversion of benzyl alcohol in the last three years. -----	20
Table 2.2 Publications on the heterogeneous photocatalytic synthesis of <i>p</i> -anisaldehyde through the conversion of <i>p</i> -anisyl alcohol. -----	22
Table 2.3 Publications on the heterogeneous photocatalytic synthesis of vanillin through the conversion of vanillyl alcohol.-----	24
Table 2.4 Publications on the heterogeneous photocatalytic synthesis of piperonal through the conversion of piperonyl alcohol. -----	25
Table 2.5 Publications on the heterogeneous photocatalytic synthesis of vitamin B3 through the conversion of 3-pyridinemethanol. -----	27

### PART II – CHAPTER 3

Table 3.1 Carbon content (%) and specific surface area ( $S_{BET}$ ) of ZnO and of the composite catalysts.-----	39
Table 3.2 Published works about the photocatalytic synthesis of vanillin using vanillyl alcohol as starting molecule.-----	46
Table 3.3 Conversion (X) and selectivity (S) of AAD, BAD, PAD and VAD production after 8 h of reaction with ZnO and 10%CNF/ZnO. -----	49
Table 3.4 Chemical structure and substituent groups of vanillyl alcohol (VA), benzyl alcohol (BA), piperonyl alcohol (PA) and <i>p</i> -anisyl alcohol (AA), and the respective Hammett constants ( $\sigma_p$ and $\sigma_m$ ).-----	50

### PART II – CHAPTER 4

Table 4.1 Bandgap energy ( $E_g$ ), transition energy ( $E_T$ ) and atomic percentage of carbon and nitrogen of GCN and GCN-zCA catalysts ( $z = 5, 10, 15, 20, 25$ ). -----	76
Table 4.2 C/N molar ratio obtained from elemental analysis and specific surface area ( $S_{BET}$ ) of GCN-Z and GCN-Z-500 catalysts ( $Z = \text{BAr, ABN and ATCN}$ ). -----	88
Table 4.3 Specific surface area ( $S_{BET}$ ), pore volume ( $V_{\text{pore}}$ ), C/N molar ratio obtained through elemental analysis, full width at half maximum (FWHM) of the (002) diffraction line, and crystallite size ( $d$ ) of the synthesized catalysts-----	98

Table 4.4 Published works on the photoconversion of *p*-anisyl alcohol (AA) into *p*-anisaldehyde (AAD). ----- 106

**PART II – CHAPTER 5**

Table 5.1 Atomic ratio between carbon and nitrogen obtained through elemental analysis, specific surface area ( $S_{BET}$ ), full width at half maximum (FWHM) of the (002) peak, and crystallite size ( $d$ ) of the synthesized catalysts.----- 114

Table 5.2 Comparison between the published results on the heterogeneous photocatalytic synthesis of vitamin B3 (VB3) through the conversion of 3-pyridinemethanol (3PM) and the present study. ----- 121

**PART III – CHAPTER 6**

Table 6.1 Compilation of the best photocatalytic results obtained for the target molecules synthesized during this PhD study. ----- 128

## List of schemes

### PART II – CHAPTER 3

Scheme 3.1 a) Photograph and b) schematic representation of the photocatalytic experimental setup operating under batch mode. -----35

### PART II – CHAPTER 4

Scheme 4.1 a, b) Photographs of the photocatalytic setup, using a solar simulator as irradiation source. Dashed line and arrow indicate the position of the lamp. -----60

Scheme 4.2 Diagram of photocatalytic conversion of AA into AAD under deoxygenated and oxygenated conditions, using GCN-UL as photocatalyst and UV-LED as light source. -----73









**List of abbreviations and symbols**

3PC	3-Pyridinecarboxaldehyde
3PM	3-Pyridinemethanol
AA	<i>p</i> -Anisyl alcohol
AAD	<i>p</i> -Anisaldehyde
ABN	2-Aminobenzonitrile
ACN	Acetonitrile
AOPs	Advanced oxidation processes
ATCN	2-Aminothiophene-3-carbonitrile
ATR	Attenuated total reflectance
BA	Benzyl alcohol
BAr	Barbituric acid
BAD	Benzaldehyde
BQ	Benzoquinone
BTF	Benzotrifluoride
CA	Citric acid
CB	Conduction band
CNF	Carbon nanofiber
CNT	Carbon nanotube
CTAB	Hexadecyltrimethylammonium bromide
CVD	Chemical vapor deposition
<i>d</i>	Crystallite size
DAD	Diode Array Detector
DCN	Dicyandiamide
DR UV-Vis	Diffuse-reflectance UV–Visible
<i>E</i>	Energy efficiency parameter
<i>e</i> <sup>-</sup>	Electrons
EDTA	Ethylenediaminetetraacetic acid
<i>E<sub>g</sub></i>	Bandgap energy

$e_r^-$	Reactive electrons
FHWM	Full width at half maximum
FTIR	Fourier transform infrared
GC	Gas chromatography
$g-C_3N_4$ , GCN	Graphite-like carbon nitride
$h^+$	Hole
$H_2$	Hydrogen
$HO^\cdot$	Hydroxyl radicals
HPLC	High-performance liquid chromatography
$h_r^+$	Reactive holes
$h\nu$	Energy of the photon
LED	Light-emitting diode
NAD	Nicotinamide-adenine-dinucleotide
$Nuc^-$	Nucleophile
$O_2^{\cdot-}$	Superoxide radicals
$P$	Power
PA	Piperonyl alcohol
PAD	Piperonal
PCME	<i>p</i> -Cresyl-methyl ether
PL	Photoluminescence
PVP K30	Polyvinylpyrrolidone K30
ROS	Reactive oxygen species
$S$	Selectivity
SA	Sodium alginate
SBA-15	Mesoporous silica sieve
$S_{BET}$	Brunauer-Emmett-Teller specific surface area
SC	Semiconductor
SEM	Scanning electron microscopy
$S_N1$	Unimolecular nucleophilic substitution

S <sub>N</sub> 2	Bimolecular nucleophilic substitution
<i>t</i>	Time
<i>t</i> -BuOH	<i>t</i> -Butyl alcohol
TEM	Transmission electronic microscopy
TEMPO	2,2',6,6'-Tetramethylpiperidine-N-oxyl
TEOS	Tetraethyl orthosilicate
TG	Thermogravimetry
TiO <sub>2</sub>	Titanium dioxide
TS-1	Titanium silicalite
UV	Ultraviolet
V	Reaction volume
VA	Vanillyl alcohol
VAD	Vanillin
VB	Valence band
VB3	Vitamin B3
V <sub>pore</sub>	Pore volume
X	Conversion
XPS	X-ray photoelectron spectroscopy
XRD	X-ray diffraction
Y	Yield
Zn	Zinc
ZnO	Zinc oxide



---

## Materials nomenclature

### PART II – CHAPTER 3

XCNF/ZnO Composites with X% (X = 5, 10, 15 and 20) of CNF and ZnO

### PART II – CHAPTER 4

GCN	Bulk graphite-like carbon nitride
GCN-UL	Urchin-like GCN
GCM-OM	3D Ordered macroporous GCN
GCN-MP	Mesoporous GCN
GCN-zCA	GCN modified with z mg (z = 5, 10, 15, 20 and 25) of citric acid
GCN-BAr	GCN obtained by copolymerization of DCN with Barbituric acid (BAr)
GCN-ABN	GCN obtained by copolymerization of DCN with ABN
GCN-ATCN	GCN obtained by copolymerization of DCN with ATCN
GCN-500	GCN subjected to a thermal post-treatment (under air) at 500°C
GCN-BAr-500	GCN-BAr subjected to a thermal post-treatment (under air) at 500°C
GCN-ABN-500	GCN-ABN subjected to a thermal post-treatment (under air) at 500°C
GCN-ATCN-500	GCN-ATCN subjected to a thermal post-treatment (under air) at 500°C
GCN-A-Z	GCN subjected to a thermal post-treatment (under nitrogen) at Z°C (Z = 500, 550, 600 and 620)









# Part I



# Chapter 1

## ***General introduction***

This chapter provides the contextualization of the research topic, focusing on the emergent need to develop sustainable processes of organic synthesis. It begins with the importance of partial oxidation of alcohols at industry level and a brief review of the organic synthesis evolution, from molecular photochemistry to the photocatalytic approach.

A theoretical explanation about the mechanisms and the main applications of semiconductor photocatalysis fundamentals is performed, with the presentation of the photocatalytic materials used in the PhD study.

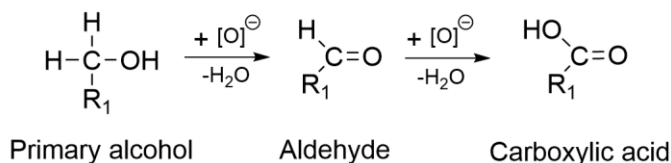
The research aims and objectives are included at the end of this chapter, with a brief description of the performed work and the main findings. The thesis outline is also presented.



## 1.1 Importance of partial oxidation of alcohols

Selective alcohol oxidation to their carbonyl and carboxyl respectively is a pivotal reaction in the organic chemistry field. Aldehydes, ketones and acids have a wide application in pharmaceutical, and cosmetic industries, as precursors and intermediates for synthesizing several flavoring agents, drugs, vitamins, and fragrances [1–6]. Mechanistically, primary and secondary alcohols undergo a nucleophilic substitution of the hydroxyl group to obtain aldehydes and carboxylic acids, and ketones, respectively [2,7,8]. According to the organic chemistry principles, the oxidation of primary alcohols to aldehydes follows a bimolecular nucleophilic substitution ( $S_N2$ ) mechanism in one single step (concerted reaction), with the attack of the oxidizing agent occurring at the same time that the leaving group leaves, without the formation of an intermediate species (Fig. 1.1A) [8]. This type of reaction usually occurs in the alcohol's less-substituted carbons once that the alkyl group creates steric hindrance, inhibiting the oxidant from accessing the electrophilic carbons [8]. If a stoichiometric amount of oxidant is present, the reaction can be considered as a second-order overall. In the case that oxidizing agent is in excess, the oxidative reaction is regarded as a pseudo-first-order. The overoxidation of the aldehyde leads to the respective carboxylic acid (Fig. 1.1A) [8].

A)



B)

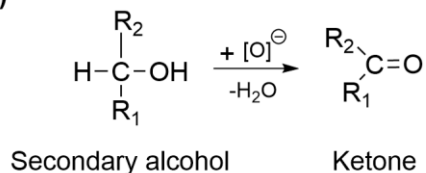


Fig. 1.1 Selective oxidation of (A) primary and (B) secondary alcohols ( $R_1, R_2 \neq \text{H}$ ;  $[\text{O}]^\ominus$  represents the oxidizing agent).

Regarding the oxidation of secondary alcohols, the nucleophilic substitution is unimolecular ( $S_N1$ ; Fig. 1.1B), with the attack of oxidizing agent to the secondary alcohol to generate the ketone, with no further oxidation. Considering the  $S_N1$  mechanism, the kinetics of oxidation of the secondary alcohols can be described as a

first-order reaction, where the rate depends only on the concentration of the substrate [8]. The S<sub>N</sub>1 mechanism preferably occurs at more substituted carbons once that alkyl groups may act as electron donors and stabilize the positive charge of the carbocation [8].

In industrial processes, the synthesis of carbonyl and carboxylic compounds are mostly performed by partial oxidation of alcohols. Nevertheless, these processes require harsh operating conditions (temperature and pressure), the use of hazardous chemicals as oxidizing agents, which lead to tremendous energetic demand and to the generation of large volumes of hazardous effluents [1,2,6,7]. Therefore, with the growing concern about the sustainability and the green character of organic chemistry, chemical yield started to share its determining role in the efficiency of the process with its ecological impact. Anastas and Warner [9] proposed 12 guidelines that define the concept of green chemical process or product: i) prevent waste; ii) atom economy; iii) less hazardous synthesis; iv) design benign chemicals; v) use benign solvents and auxiliaries; vi) design for energy efficiency; vii) use of renewable feedstocks; viii) reduce derivatives; ix) catalysis; x) design for degradation; xi) real-time analysis preventing pollution; xii) prevent accidents through benign chemistry. In this way, catalytic technologies greatly contributed to the establish this concept in the industrial processes of organic synthesis [4,7,9,10].

Particularly in fine chemical production, partial oxidation of alcohols still favors the use of stoichiometric oxidants, as permanganate, and chromium reagents, rather than clean oxidants, namely oxygen (O<sub>2</sub>), and hydrogen peroxide (H<sub>2</sub>O<sub>2</sub>) [7]. Nevertheless, some examples were successfully applied at the industrial level to replace classical routes of synthesis. BASF produces more than 10<sup>3</sup> tons per year [6] of isoprenal (3-methyl-3-butenal), an intermediate in the synthesis of citral (3,7-dimethyl-octa-2,6-dien-al), by oxidizing its respective alcohol (isoprenol; 3-methyl-3-butenol) with O<sub>2</sub> on a solid catalyst (silver) in the gas phase [11,12]. This catalytic system is also adopted by the same company in the synthesis of formaldehyde through oxidative dehydrogenation of methanol, achieving 90% of overall yield and reducing the O<sub>2</sub> demand to 40% of the stoichiometric value [7,13,14]. In the synthesis of methoxyacetic acid, an essential intermediate in the production of fungicides, O<sub>2</sub> acts as the oxidizing agent to convert 2-methoxyethanol in the presence of a Pt catalyst [15].

Some catalytic methods have gained relevance in the fine chemical industry by focusing on converting alcohol to their respective carbonyl compounds. TEMPO (2,2',6,6'-tetramethylpiperidine-*N*-oxyl), a stable free radical, is the primary choice of catalyst in the industry for the oxidation of primary alcohols [4,5,7,16]. Besides

presenting high performance under mild conditions and allowing the use of inexpensive compounds as co-oxidants (e.g. sodium hypochlorite), TEMPO has high selectivity for the production of aldehydes, acting as radical scavenger preventing further oxidation caused by the presence of O<sub>2</sub> [2–5,17]. Progesterone production from stigmasterol is an example of its application as a catalyst in organic synthesis by Pharmacia and Upjohn company [18]. Pfizer also developed a process to obtain the proline derivative [19,20], an intermediate of the HIV protease inhibitor, which involves the partial aerobic oxidation of one alcohol to its respective ketone, using TEMPO as the catalyst. By combining TEMPO with metal catalysts and biocatalysts and choosing an appropriate solvent, a new range of opportunities was created in the aerobic catalytic oxidation of alcohols [3,4,7,16,17,21,22]. Moreover, metallic and organometallic catalysts accessed higher selectivity in this oxidative system [23,24]. For H<sub>2</sub>O<sub>2</sub>, its industrial application as an oxidant is more complicated than molecular oxygen once it must be used in a 30% v/v aqueous solution to be safe to handle. In this way, the development of heterogeneous titanium silicalite (TS-1) and other recyclable catalysts was the key to promote the industrial use of H<sub>2</sub>O<sub>2</sub> in oxidative processes [7,25].

Despite the evolution observed in oxidation reactions at the industrial level, by adopting innovative catalytic technologies with lower environmental impact than the classical oxidative methods, some issues remain to overcome to reach greener processes of partial oxidation of alcohols into aldehydes, ketones and acids.

## **1.2 Moving the paradigm from molecular photochemistry to photocatalytic synthesis**

The great effort made by academic and industrial communities produced greener alternative processes for the synthesis of several carbonyl and carboxylic compounds. The application of catalytic technologies in partial oxidation of alcohols effectively increased their green character, but do not satisfy all the principles defined for the green chemistry concept. Biocatalytic-based processes are considered environmentally friendly routes in the organic synthesis, due to the mild conditions of operation and the relatively low amount and non-toxicity of the waste produced [10,26,27]. However, biocatalysts require strict control of reaction parameters, as temperature, pH, ionic strength, to ensure their maximum performance [26,27], which can be extremely difficult and costly at the industrial level. Therefore, photo-activated processes are considered a valuable alternative due to the use of light to promote chemical reactions [28–31].

Photochemistry is the branch of chemistry that deals with light-driven chemical transformations. From an environmental perspective, photochemical systems are widely advantageous because activation is carried out under mild conditions of temperature and pressure, and is promoted by photon absorption, leaving no residue at the end of the process [28]. Inspired by the process of natural photosynthesis, Giacomo Ciamician, a pioneer in photochemistry applied to organic synthesis, proposed the use of solar energy, an inexhaustible and clean source of energy, as the key to reach the energetic sustainability of industrial chemical processes [31,32]. Additionally, several photochemical reactions using sunlight as an energy source were reported, as the cycloaddition of ketones to alkenes (Paternò-Büchi reaction) [33], the reaction of diketones in the presence of olefins to synthesize 1,4-dioxins [34] and the isomerization of cinnamic and other unsaturated acids [35]. However, solar energy is a challenge to industrial organic synthesis since most organic compounds cannot absorb in the visible range of the solar spectrum [31,36]. Since UV only accounts for 5% of the total solar irradiation reaching Earth's surface [37,38], the use of this type of radiation to promote chemical reactions requires the utilization of sophisticated photoreactors, equipped with expensive and highly energy-consuming artificial radiation sources [31,36]. One strategy for harnessing solar energy for organic synthesis processes is applying organic and inorganic compounds that strongly absorb in the visible range and, consequently, can act as mediators in photon absorption. The synthesis of ascaridole (an anthelmintic compound) using air as oxidant and natural chlorophylls as photosensitizer constitute an essential milestone in organic synthesis driven by sunlight [39].

With the energetic crisis of fossil fuels and the concern about the environmental impact of large-scale processes, the research on photocatalysis started to gain higher interest in the 1970s [40], especially after the work of Fujishima and Honda on the hydrogen (H<sub>2</sub>) production through photocatalytic water-splitting on titanium dioxide electrodes [41].

Most of the photocatalytic reactions are mediated by homogeneous catalysts, as polyoxometalates [42], metal complexes [43,44], and metal-free organic dyes [45,46]. However, the high solubility of homogeneous photocatalysts makes it difficult to recover them from the reaction medium, inhibiting their reuse [40,47]. This has been the great motivation for the desirable development of heterogeneous systems in the past few decades, with semiconductor materials playing a fundamental role due to their high reactivity, excellent stability, chemical inertness, low cost, and reusability [48]. Considering their suitable physicochemical, optical, and electronic properties,



several metal oxide semiconductor materials, as titanium dioxide, zinc oxide, and magnetite, have been extensively applied in photocatalytic systems mainly focusing on the degradation of pollutants and hydrogen production [49,50].

With the growing research into more sustainable organic synthesis processes, particularly in the partial oxidation of alcohols into carbonyl and carboxylic compounds, semiconductor photocatalysis may be considered one of the most promising alternatives to some of the conventional methods industrially applied.

### 1.3 Semiconductor photocatalysis – mechanisms and applications

Conventional processes for the synthesis of organic compounds typically require severe operating conditions to achieve profitable yields. Light as an energy source to activate a semiconductor material capable of catalyzing chemical reactions under mild operation conditions may drive to more sustainable processes, without compromising the yield of reactions [51]. Contrariwise to the conventional industrial processes, photocatalytic synthesis may reduce the energetic requirement by using efficient light sources, like light-emitting diodes (LEDs), and working under room temperature and atmospheric pressure. Moreover, water as a solvent avoids toxic waste production, reducing or eliminating the post-treatment costs [51].

Analogously to the overall process of heterogeneous catalysis, semiconductor photocatalysis can be divided into five distinct steps: i) diffusion of the substrates from the reaction medium to the surface of the semiconductor; ii) adsorption of substrate molecules on the surface of the catalyst; iii) conversion of the reactant into the desired product; iv) desorption of the product molecules; v) diffusion of the product from the surface of the catalyst to the reaction medium [52]. The conversion of the reactant molecules (step iii) is initiated with the irradiation of semiconductor material by specific energy ( $h\nu$ ,  $h$  is Planck constant, and  $\nu$  is photon's frequency). When  $h\nu$  is higher than the bandgap energy ( $E_g$ ) of the catalyst, electrons ( $e^-$ ) are excited from the lower energy state (valence band, VB) to a higher energy state (conduction band, CB) (Fig. 1.2, [53–55]). In this excitation process, holes ( $h^+$ ) are created in the VB. If  $e^-$  and  $h^+$  reach active sites in the surface of the semiconductor material (Fig. 1.2, step 2), they become reactive charge carriers ( $e^-$ ,  $h^+$ ), available for catalyzing redox reactions (Fig. 1.2, steps 3 and 4). In photocatalytic processes,  $h^+$  are the primary responsible for the oxidation of substrates (X) (Fig. 1.2, step 4) while  $e^-$  promote the reduction of chemical species (Y) (Fig. 1.2, step 3), like oxygen, ions and other molecules [51,53–56]. However, due to the high instability of excited  $e^-$ , they can easily lose energy under

radiative and non-radiative recombination processes, returning to the VB (Fig. 1.2, step 1).

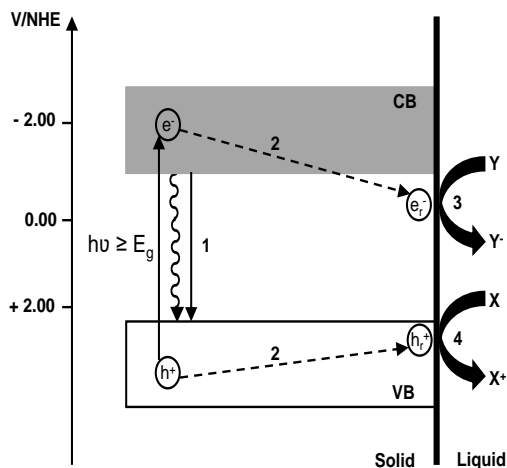


Fig. 1.2 Diagram of photocatalytic phenomena at a semiconductor/liquid interface. Straight and wavy lines correspond to radiative and nonradiative processes, respectively. The dark vertical bar indicates the interface between the semiconductor and liquid phase. (For number meaning refer to the body text).

According to Gerisher and Heller [57], in an effective semiconductor photocatalytic process, the consumption rate of  $e^-$  and  $h^+$  should be equal in the overall reaction. When a deviation occurs in the catalytic equilibrium, the charge balance includes the fraction of  $e^-$  and  $h^+$  that are trapped in bulk defects, which decreases the efficiency of the semiconductor [57,58].

Two critical parameters should be evaluated to determine if a semiconductor material can catalyze a specific redox reaction. Firstly, both reduction and oxidation potentials of starting molecules must be located within the bandgap of the catalyst [55]. On the other hand, the semiconductor material must absorb light in the wavelength of emission of the radiation source. Light absorption by the starting reactant should be avoided to eliminate the possibility of photolysis, i.e., conversion promoted by light exposure [55].

The factors that can interfere in the photocatalytic reaction are mainly related with the catalyst (load, surface properties, chemical composition), the conditions of the reaction medium (pH, solvent), the substrate (concentration, chemical properties), light source (wavelength, intensity), and oxygen concentration [59].

In terms of the reaction mechanism, the oxygen concentration is probably the most determining factor, with a crucial effect on the oxidative and reductive routes.

After the irradiation of the semiconductor (SC; eq. 1.1), if oxygen is present in the reaction medium, it can act as an electron acceptor, being reduced by  $e_r^-$  on the CB to generate superoxide ( $O_2^{\cdot-}$ ) radicals (eq. 1.2) [52,54,60]. In optical semiconductor-based systems, the reaction between the adsorbed water molecules and  $h_r^+$  in the VB (eq. 1.3) leads to the generation of hydroxyl ( $HO^{\cdot}$ ) radicals [61]. However, in carbon nitride materials,  $HO^{\cdot}$  radicals are generated through the reduction of hydrogen peroxide (eq. 1.4 and 1.5) [62].



In photodegradation processes, the oxidative pathway promoted by  $HO^{\cdot}$  radicals (eq. 1.6) is hardly explored, due to the highly reactive ability of this specific radical, allowing the mineralization of several organic compounds [63]. Contrariwise, in synthesis systems, the oxidation through  $HO^{\cdot}$  radicals is avoided due to its low selectivity, which reduces the overall efficiency of the process.

The less reactive  $O_2^{\cdot-}$  radicals and photogenerated  $h_r^+$  can also convert substrate molecules (eqs. 1.7 and 1.8, respectively) [52,54,60].



In the absence of oxygen, reactive oxygen species (ROS) are not generated, and the oxidation reaction is exclusively driven by photogenerated  $h_r^+$  (eq. 1.8). Moreover,  $e_r^-$  on the CB are available to promote the reduction of  $H^+$  into hydrogen ( $H_2$ ) under specific reaction conditions (eq. 1.9) [57,58].



Semiconductor photocatalysis has been extensively applied in advanced oxidation processes (AOPs) to treat domestic wastewater and industrial effluents to eliminate contaminants [64,65]. Several types of contaminants, such as pharmaceuticals [66,67], parabens [68,69], phenolics [62,70,71] and dyes [72,73] were successfully removed from aqueous effluents through semiconductor photocatalysis. Microbial

contaminants can also be inactivated by using semiconductor photocatalysis [74,75], which has been explored to develop self-cleaning fabrics and surfaces [76–78].

Another important application of semiconductor photocatalysis is the production of H<sub>2</sub> through water-splitting [79], which started with the research of Fujishima and Honda [41] in the initial years of the development of photocatalysis. Hydrogen has been considered a valuable alternative as energy carrier once it can be extracted from sustainable sources, as water and biomass; it has a high energy yield per mass; and its end-use does not produce toxic waste or has any harmful effect in the environment [80]. Compared to photobiological and thermochemical water-splitting, photocatalysis promoted by semiconductor materials is considered a cleaner technology to obtain hydrogen once it achieves satisfying solar to hydrogen efficiency; it has low process cost; and it allows to recover both hydrogen and oxygen [80]. The photocatalytic production of hydrogen was also reported by using organic compounds as substrates, as biomass [81], saccharides [82] and single-chain alcohols as sacrificial electron donors (photocatalytic reforming processes) [82,83].

In the last decade, the research about the selective synthesis started to gain relevance in the photocatalytic field, with an exponential increase in the number of published papers. Reductive and oxidative reactions are the main responsible for the production of a wide variety of fine chemicals. The photocatalytic reduction of carbon dioxide (CO<sub>2</sub>) is a perfect example of the positive aspects of the application of semiconductor photocatalysis in synthesis processes [84]. This process enables the capture of CO<sub>2</sub> from the atmosphere and also, allows the synthesis of a wide range of valuable chemicals, as ethanol [85], hydrogen [85], methane [86], carbon monoxide [87], and methanol [88]. On the other hand, oxidative processes also contribute to the wide range of semiconductor photocatalysis applications. Hydrocarbons, aromatic compounds, and alcohols are examples of molecules already studied as substrates in selective photocatalytic oxidations [89–93].

#### **1.4 Preparation and properties of photocatalytic materials**

Several semiconductor materials have been applied as photocatalysts in oxidative systems. An ideal photocatalyst should present several characteristics, namely i) photo-stability, ii) chemical and biological inertness, iii) high availability and low cost, and iv) high ability to adsorb molecules under irradiation [94].

TiO<sub>2</sub> was the first semiconductor applied in a photocatalytic context by Fujishima and Honda [41] for the water-splitting process.

The most common crystalline structure of TiO<sub>2</sub> applied in photocatalysis is anatase or a mixture of anatase and rutile phases [38,94,95]. The anatase phase is reported to achieve the best compromise between photoactivity and photostability [94], which explains its higher contribution (between 70% and 80%) to the total composition of commercial TiO<sub>2</sub> P25, the most used photocatalyst [96]. However, the presence of rutile crystallites allows a faster electron transition from rutile to lower energy anatase, which results in more efficient charge separation and, consequently, in an enhanced photoactivity [97,98]. The bandgap energy of TiO<sub>2</sub> varies between 3.0 eV (100% rutile phase) and 3.2 eV (100% anatase phase), requiring UV light irradiation to photogenerate e<sup>-</sup>/h<sup>+</sup> pairs [99]. Moreover, TiO<sub>2</sub> is a typical *n*-type semiconductor, with the acceptor energy level near its conduction band [99]. Despite all the successful applications of TiO<sub>2</sub> in different photocatalytic systems, its low absorption in the visible spectral range ( $\lambda > 400$  nm) and the capacity of absorbing a small fraction (<5%) of the incident solar radiation reaching the Earth's surface are considered drawbacks for its industrial application [37,38]. Moreover, TiO<sub>2</sub> has been incorporated in several massively used specialty materials, like paints, sunscreens, and food coloring, leading to high consumption of this material [100]. Therefore, a great effort has been put towards developing materials with similar or better photocatalytic performances.

ZnO is an *n*-type semiconductor material with bandgap energy similar to TiO<sub>2</sub> (3.4 eV) [99]. Regarding crystallinity, this material can present three different structures, namely hexagonal wurtzite, cubic zinc-blende, and cubic rock-salt [101,102]. ZnO has been applied in the degradation of organic contaminants [71,103], disinfection systems [104], water-splitting processes [105], and, more recently, in the synthesis of fine chemicals [106,107]. ZnO exhibits important properties, namely a strong oxidation ability, low cost, biocompatibility, non-toxicity, and high photosensitivity, that widely contribute to its application in photocatalytic processes [99,108]. Besides, the significant influence of the preparation methods in its morphology results in forming an extensive range of nanostructures, such as nanorods, nanofibers, nanowires, nanotubes, nanoneedles, nanosheets, and nanoflowers [109,110]. As occurs with TiO<sub>2</sub>, ZnO has a limited absorption capacity in the visible region of the solar spectrum [111,112], which constitutes a drawback, considering solar-driven applications. To overcome this limitation, carbon materials such as activated carbon, carbon dots, carbon nanotubes and nanofibers, graphene, fullerene, and three-dimensional carbon, have been successfully applied in the preparation of heterojunctions with metal oxides, like TiO<sub>2</sub> and ZnO [104,113]. In this type of catalyst, the carbon phase acts as a

photoelectron sink to drive away the photogenerated  $e^-$ , inhibiting the recombination with  $h^+$  and, consequently, enhancing irradiation efficiency [104,113].

In the last years, a specific carbon-based material, graphitic carbon nitride (g-C<sub>3</sub>N<sub>4</sub>), has attracted great attention in the scientific community considering its suitable bandgap energy (2.7 eV), its easy surface modification and its easy fabrication through thermal polymerization of abundant nitrogen-rich precursors, like melamine, cyanamide, dicyandiamide and urea [114,115]. The tris-s-triazine-based structure is the most common and stable repeating unit of carbon nitride (Fig. 1.3) at ambient conditions.

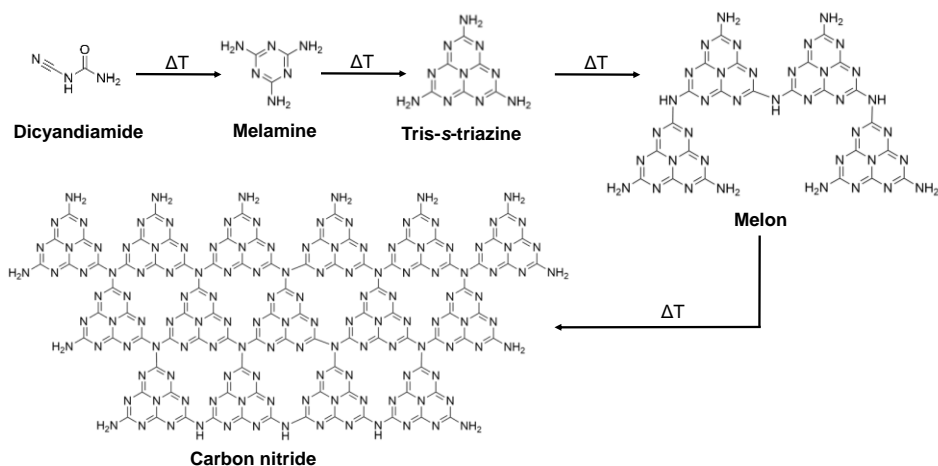


Fig. 1.3 Reaction pathway for the synthesis of carbon nitride using dicyandiamide as precursor.

This melon structure is obtained through the polycondensation of nitrogen-rich precursors that will originate the melem (tris-s-triazine) units (Fig. 1.3) [116].

The first report about g-C<sub>3</sub>N<sub>4</sub> as photocatalyst dates from 2009 by Wang and coworkers, with hydrogen production through the water-splitting process under visible irradiation [116]. Since then, researchers have adopted g-C<sub>3</sub>N<sub>4</sub>-based materials as one of the most promising catalysts for visible-light-driven applications. Thousands of works on applying this semiconductor material in all photocatalysis fields have already shown its greater efficiency. However, due to the high degree of condensation, bulk g-C<sub>3</sub>N<sub>4</sub> usually has a low surface area and high  $e^-/h^+$  recombination rate, negatively affecting its photocatalytic performance. Therefore, different approaches have been effectively applied to tune g-C<sub>3</sub>N<sub>4</sub> properties, as templating routes [117–119], thermal and mechanical post-treatment [70,120], doping with heteroatoms [121–123], grafting chemical structures through copolymerization [124–126], and producing

heterojunctions with other materials [105,127,128]. Such physical and chemical modifications are applied for inducing the efficiency of this material.

So far, the application of g-C<sub>3</sub>N<sub>4</sub> materials in the photocatalytic conversion of alcohols into carbonyl and carboxylic compounds has achieved promising results. However, there is still a lot to explore to maximize the benefits of applying these processes industrially. The development of new and improved photocatalysts allows the design of highly efficient and sustainable systems, which served as a basis for the present work.

### **1.5 Aims and objectives**

Conventional processes developed for organic synthesis require a rather high temperature and pressure and the use of organic solvents to reach satisfactory yields, which leads to increased production costs and environmental damage. The photocatalytic synthesis of organic compounds, particularly in the case of selective oxidation of alcohols into carbonyl and carboxylic compounds, constitutes a more sustainable route since it can be driven at mild operation conditions, using water as the solvent, metal-free catalysts and light (instead of temperature) for reaction activation. Therefore, the choice and design of photocatalytic materials is an undeniable challenge to reach a desirable efficiency in the synthesis process, as the chemical and electronic properties of semiconductor materials directly affect their photocatalytic performance.

The objectives of the present study rely upon i) on the development of new and sustainable photocatalysts, with improved performance; ii) on the decrease of the environmental footprint of photocatalytic reactions by using LED technology and aqueous solutions; and iii) on the synthesis of aldehydes, ketones and acids used as intermediates or final products in the industry through semiconductor photocatalysis.

### **1.6 Description of the performed work**

The work here presented is divided into three main lines: i) photocatalytic materials, ii) photocatalytic conversions, and iii) process development.

The synthesized materials consisted of ZnO/carbon nanofibers (CNF) hybrids and carbon nitride derivatives. All the catalysts were applied in the selective oxidation of alcohols into carbonyl and carboxyl compounds. Ultrapure water was used as a solvent in all reactions to avoid the generation of hazardous effluents, and LED systems (UV and visible) were adopted as irradiation source, aiming at reducing the

energy expenditure of the process. All reactions were carried out at room temperature and atmospheric pressure.

Firstly, the photocatalytic oxidation of vanillyl alcohol into vanillin, an aromatic aldehyde widely used in food, cosmetic and pharmaceutical industries, was studied under an inert atmosphere, using a composite catalyst composed by ZnO and CNF. The work was extended to the synthesis of a series of aromatic aldehydes, namely benzaldehyde, *p*-anisaldehyde and piperonal due to their industrial interest.

In a second study, the focus was on the synthesis of *p*-anisaldehyde through the selective oxidation of *p*-anisyl alcohol. Metal oxide-based photocatalysts were replaced by metal-free semiconductor materials based on graphite-like carbon nitride (referred as GCN).

Lastly, the synthesis of vitamin B3 (nicotinic acid) and 3-pyridinecarboxaldehyde through the oxidation of 3-pyridinemethanol was studied using a GCN-based catalyst with extended absorption capacity in the visible spectrum region. The immobilization of GCN-based materials was also evaluated, seeking to develop continuous operation photocatalytic synthesis processes.

## 1.7 Main findings

The present work provides a useful application of heterogeneous photocatalysis to synthesize value-added chemicals with potential use in the pharmaceutical industry. It was proved that i) vanillin can be selectively synthesized through semiconductor photocatalysis under an inert atmosphere using composite catalysts of ZnO and CNF, that presented an improved performance when compared to neat ZnO; ii) different approaches can be adopted to tune morphological optical and electronic properties of GCN; iii) the photocatalytic performance of GCN-based catalysts towards the production of *p*-anisaldehyde can be influenced by the modifications induced in the catalysts and also by the operational conditions adopted; iv) the selective photocatalytic production of vitamin B3 can be an effective alternative to the conventional industrial processes, revealing high potential in terms of efficiency.

The developed systems are proposed as more sustainable alternatives to the conventional industrial processes, by working under mild conditions of temperature and pressure, avoiding the use of organic solvents and by using an efficient radiation source, without compromising yield and selectivity.



## 1.8 Thesis outline

The present dissertation is divided into three parts (I, II and III), with six chapters. The part I encompasses an introductory discussion to contextualize the theme under research, as well as its aims and objectives, and main findings (Chapter 1). A broad state-of-the-art on the heterogeneous photocatalytic synthesis of carbonyl and carboxyl compounds through the oxidation of alcohols (Chapter 2) is also included in this part.

Part II addresses the experimental work developed during the PhD studies, and includes Chapter 3 to 5. The third chapter reports vanillin production through the photoconversion of vanillyl alcohol, using heterojunction photocatalysts composed of ZnO and CNF. Moreover, other aromatic alcohols were studied to infer the effect of the electronic nature of the functional group linked to the aromatic ring in the efficiency (in terms of conversion and selectivity) of the photocatalytic process. The fourth chapter focuses on the photocatalytic transformation of *p*-anisyl alcohol into *p*-anisaldehyde using GCN, a metal-free semiconductor material, as a catalyst. Due to its low surface area and high electron/hole recombination rate, three methodologies (hard-templating, co-polymerization, and a thermal post-treatment) were investigated to improve the photocatalytic performance of GCN under LED irradiation. Chapter 5 reports the application of GCN-based catalyst in the photocatalytic conversion of 3-pyridinemethanol into 3-pyridinecarboxaldehyde and vitamin B3.

Lastly, Chapter 6 is dedicated to the final remarks and suggestions for future work, which is included in part III.







## Chapter 2

### ***State-of-the-art***

This chapter provides a review of semiconductor photocatalysis application to the partial oxidation of alcohols to synthesize aldehydes, ketones, and acids. The particular cases of some aromatic aldehydes, namely benzaldehyde, *p*-anisaldehyde, vanillin, piperonal, and vitamin B3 were explored, identifying research opportunities. A critical reflection about the future of semiconductor photocatalysis in the organic synthesis field was also presented at the end of this chapter.



## **2.1 Semiconductor photocatalytic synthesis of aldehydes, ketones, and acids through partial oxidation of alcohols**

Carbonyl and carboxyl compounds are essential intermediates in industrial organic synthesis processes. Partial oxidation of alcohols into aldehydes, ketones, and acids through semiconductor photocatalysis has been investigated as a valuable alternative to avoid the hazardous conditions of conventional oxidative methods.

The first reports on the selective oxidation of alcohols into carbonyl compounds were published in 1981, using alkyl alcohols (2-propanol and 2-butanol) to produce the corresponding ketones [129,130]. However, the study on the selective conversion of aromatic alcohols has been the central focus of the scientific community due to the great range of industrial applications of their respective carbonyl and carboxyl compounds [3,7]. The present thesis focuses on the selective synthesis of aromatic aldehydes (benzaldehyde, *p*-anisaldehyde, vanillin and piperonal) and acids (vitamin B3) through the partial oxidation of the respective alcohols.

The state-of-the-art on the photocatalytic production of these specific compounds is presented below.

### **2.1.1 Benzaldehyde**

With an annual production of more than 7000 tons, obtained mostly through synthetic chemistry, benzaldehyde is the second most important aromatic aldehyde at the industrial level, after vanillin [131,132]. Due to its characteristic odor similar to almond, benzaldehyde is widely applied as a flavoring agent in cosmetic, food and beverage industries [133]. Regarding pharmaceutical applications, benzaldehyde is used as an intermediate in the synthesis of several drugs, such as antibiotics (phenylglycine [134]), antihistamines (pseudoephedrine [135] and L-phenylacetylcarbinol [136]) and antihypertensives (3,4-dihydro-pyrimidin-2(1*H*)-one [137]).

Industrially, benzaldehyde is mainly obtained through the hydrolysis of benzylidene chloride [138] and by the partial oxidation of toluene [139,140]. However, these processes require hazardous operating conditions, namely high temperature, the use of acids and metal catalysts [138–140], increasing their environmental impact.

Table 2.1 Studies published on the heterogeneous photocatalytic synthesis of benzaldehyde through the conversion of benzyl alcohol in the last three years.

Entry	Catalyst	Solvent	Atmosphere	Irradiation system	Reaction time (h)	X (%)	S (%)	Ref.
1	Pd/TiO <sub>2</sub> nanowires	No solvent	Air	Halogen lamp	4	81.9	69.7	[141]
2	Cu@NALC/TiO <sub>2</sub> /AC	ACN	Air	Solar simulator	6	100	< 99	[142]
3	AgBr@TiO <sub>2</sub> /GO	ACN	Air	Xenon lamp	4	78	n.i.	[143]
4	Fe-doped SrTiO <sub>3</sub>	Water	Argon	Xenon lamp	6	30	< 99	[144]
5	Pd/H <sub>2</sub> Ti <sub>3</sub> O <sub>7</sub> nanowires	No solvent	Oxygen	Halogen lamp	4	72	73.2	[145]
6	Zn <sub>3</sub> In <sub>2</sub> S <sub>6</sub> @ZnO	BTF	Oxygen	Xenon lamp	2	91.3	97	[146]
7	Ni/ZnCdS nanoparticles	ACN	Nitrogen	Xenon lamp	3	40.4	57.7	[147]
8	CoFe <sub>2</sub> O <sub>4</sub> /Ag <sub>2</sub> MoO <sub>4</sub>	ACN	Air	Halogen lamp	0.5	82	100	[148]
9	C <sub>3</sub> N <sub>4</sub>	Water	Air	Fluorescent lamp	4	50	82	[149]
10	g-CN-T	Water	Air	UV-LED	2	58	80	[150]
11	Pt-g-C <sub>3</sub> N <sub>4</sub>	Water	Argon	Xenon lamp	20	40	90	[151]
12	Au-g-C <sub>3</sub> N <sub>4</sub>	Water	Argon	UV-LED	4	60	64	[92]
13	P-doped g-C <sub>3</sub> N <sub>4</sub>	Water	Air	Fluorescent lamp	4	8	100	[121]
14	Fe <sub>3</sub> O <sub>4</sub> /g-C <sub>3</sub> N <sub>4</sub>	Water	Argon	UV-LED	2	46	100	[152]
15	Nitric acid-modified g-C <sub>3</sub> N <sub>4</sub>	ACN	Oxygen	Xenon lamp	9	68.3	< 99	[153]
16	Boron carbon nitride	BTF	Oxygen	Visible LED	4	70	80	[154]

n.i. not indicated; BTF: Benzotrifluoride; ACN: Acetonitrile; X: Conversion; S: Selectivity



With the ever-increasing concern about implementing sustainable practices in the industry, benzaldehyde synthesis using photocatalytic semiconductor materials must be considered a valuable alternative. The works on the photocatalytic production of benzaldehyde started using toluene as the oxidation substrate [155,156]. However, the harmful effects of toluene in human health promoted the search for alternative molecules, namely benzyl alcohol. In 2007, Gassim et al. [157] reported the photocatalytic conversion of benzyl alcohol into benzaldehyde, under an oxygen atmosphere and UV irradiation, using a modified-TiO<sub>2</sub> anatase photocatalyst.

Up to date, almost two hundred papers were published using benzyl alcohol as starting molecule for benzaldehyde synthesis, with 70% of the studies being published in the last five years (data obtained from a search in Scopus database, using the keywords “photocatalysis”, “benzyl alcohol” and “oxidation”). In Table 2.1 is presented a brief compilation of recent works published on this topic.

Metal-based catalysts are the most applied materials in the photocatalytic production of benzaldehyde, achieving high values of conversion (*X*) and selectivity (*S*) (Table 2.1, entries 1-8). However, with the safety issues related to the leaching of metals, and the cost and environmental impact of utilizing this type of materials, metal-free catalysts, as the case of g-C<sub>3</sub>N<sub>4</sub>, started to gain relevance (Table 2.1, entries 9-16). The performance of these materials is quite similar to the metal-based ones, indicating that metals can be successfully replaced without compromising efficiency. Several methodologies have been applied to improve the photocatalytic performance of g-C<sub>3</sub>N<sub>4</sub>, as thermal post-treatment (Table 2.1, entry 10), metal (Table 2.1, entries 11 and 12) and heteroatom doping (Table 2.1, entry 13), heterojunction with other materials (Table 2.1, entry 14), copolymerization with organic molecules (Table 2.1, entry 15 and 16), among others. The use of water as solvent (Table 2.1, entries 9-14) avoids the use of organic compounds, as acetonitrile (ACN) and benzotrifluoride (BTF) (Table 2.1, entries 15 and 16), and consequently, eliminates the production of hazardous effluents. The combination of metal-free catalysts with the emergent irradiation systems, namely LEDs (Table 2.1, entries 10, 12, 14, and 16), has also been explored seeking for more energy-efficient synthesis processes.

### 2.1.2 *p*-Anisaldehyde

*p*-Anisaldehyde (or 4-methoxybenzaldehyde) is an aromatic aldehyde applied as a flavoring agent in food and beverage industries [158]. Also pharmaceutical and cosmetic industries are great consumers of *p*-anisaldehyde, namely in the synthesis of octyl methoxy cinnamate (sunscreen agent) [159] and diltiazem (calcium blocker

hypertension drug) [160,161]. The conventional synthesis of *p*-anisaldehyde is a two-step process, involving first the methylation of *p*-cresol into *p*-cresyl-methyl ether (PCME), using dimethyl sulfate or chloromethane, followed by the oxidation of PCME to *p*-anisaldehyde, using manganese dioxide and sulfuric acid as oxidants [162]. BASF, one of the major producers of *p*-anisaldehyde, developed a cleaner alternative to the oxidation step through the electrochemical conversion of PCME into *p*-anisaldehyde dimethyl acetal [163]. However, the hazardous conditions adopted in the methylation step are common to all industrial processes already implemented.

Table 2.2 compiles all the results published on this topic.

Table 2.2 Publications on the heterogeneous photocatalytic synthesis of *p*-anisaldehyde through the conversion of *p*-anisyl alcohol.

Entry	Catalyst	Solvent	Atmosphere	Irradiation system	Reaction time (h)	X (%)	S (%)	Ref.
1	Anatase TiO <sub>2</sub>	Water	Oxygen	Mercury lamp	7.7	65	65	[164]
2	Rutile TiO <sub>2</sub>	Water	Oxygen	Mercury lamp	2.36	50	60	[165]
3	Rutile TiO <sub>2</sub>	Water	Oxygen	Mercury lamp	8.8	50	62	[166]
4	Brookite TiO <sub>2</sub>	Water	Oxygen	Mercury lamp	2.1	50	24	[167]
5	Brookite TiO <sub>2</sub>	Water	Air	Fluorescent lamp	4	44	32	[168]
6	TiO <sub>2</sub>	Water	Air	Fluorescent lamp	2.3	18	90	[169]
7	Pt/TiO <sub>2</sub>	Water	Nitrogen	Xenon lamp	3	56	100	[170]
8	F-doped TiO <sub>2</sub>	Water	Air	Fluorescent lamp	4	13	56	[171]
9	N-doped TiO <sub>2</sub>	Water	Oxygen	Mercury lamp	1	10	90	[172]
10	TiO <sub>2</sub> -graphene	BTF	Oxygen	Xenon lamp	20	70	>99	[173]
11	WO <sub>3</sub> /TiO <sub>2</sub>	Water	Air	Mercury lamp	6	50	54	[174]

12	TiO <sub>2</sub> /Ag/DIOL	Water	Air	Fluorescent lamp	4	54	85	[175]
13	Ag <sub>3</sub> PO <sub>4</sub>	Water	Air	Solar simulator	2	>85	>99	[176]
14	Pt/ nanoporous Bi <sub>2</sub> WO <sub>6</sub>	Water	Air	Halogen lamp	4	>95	>99	[177]
15	CdS	Water	Oxygen	Xenon lamp	3	25	60	[178]
16	N-doped g-C <sub>3</sub> N <sub>4</sub>	ACN	Oxygen	Xenon lamp	9	86	>99	[153]
17	P-doped g-C <sub>3</sub> N <sub>4</sub>	Water	Oxygen	Halogen lamp	4	35	100	[121]
18	mpg-CN	Water	Oxygen	Xenon lamp	3	56	89	[178]
19	g-CN-T	Water	Air	UV-LED	0.75	>99	>99	[150]

BTF: Benzotrifluoride; ACN: Acetonitrile; X: Conversion; S: Selectivity

As previously observed for benzaldehyde production, metal-based materials are the most applied catalysts in the photocatalytic oxidation of *p*-anisyl alcohol into *p*-anisaldehyde, achieving high values of conversion and selectivity (Table 2.2, entries 1-15). Carbon nitride-based materials have also been explored (Table 2.2, entries 16-19) to synthesize this aldehyde, and satisfactory performances were also reached. Contrariwise to benzaldehyde, the photocatalytic production of *p*-anisaldehyde was mainly performed in aqueous solutions, avoiding the use of organic solvents (Table 2.2, entries, 1-9, 11-15, 17-19). However, traditional mercury, xenon and fluorescent lamps remain the most adopted radiation sources. In this way, the use of LEDs may be an important factor for increasing the energy efficiency of the photocatalytic conversion process, by reducing the reaction time and improving the light emission (Table 2.2, entry 19).

### 2.1.3 Vanillin

Among all the aromatic aldehydes, vanillin (or 4-hydroxy-3-methoxybenzaldehyde) is the most important at the industrial level, with a wide application as a flavoring agent in food, beverage, and cosmetic industries [179] and, also, as a building block in chemical synthesis of some pharmaceutical drugs, such as L-Dopa [180] and Trimethoprim [181]. The natural sources of vanillin (bean and pod of Vanilla orchid) are scarce and the extraction is not economically viable [182], which led to the

development of alternative synthetic routes. More than 20000 tons of vanillin is currently produced synthetically every year, mainly obtained from guaiacol, a petrochemical-derived compound, and lignin [107,182–185]. Although the guaiacol route is highly selective to the vanillin synthesis, its petroleum-based character limits its use [185]. On the other hand, the oxidation of lignin originates from a complex mixture of compounds, reducing the yield of the process [182]. Therefore, novel and improved synthesis routes with low ecological impact are highly desired.

The first studies on the photocatalytic synthesis of vanillin used *trans*-ferulic acid as a precursor molecule and TiO<sub>2</sub>-based materials as photocatalysts [179,186]. However, low selectivity was observed due to the high number of intermediate species formed during the *trans*-ferulic acid oxidation [179,186]. The use of pervaporation membranes coupled to the photocatalytic system allowed to increase the selectivity of the process, but the yield remained unsatisfactory (< 5%) [187,188]. In this way, vanillyl alcohol has been studied as an alternative precursor. Table 2.3 compiles all the results published on the photocatalytic conversion of vanillyl alcohol into vanillin, using semiconductor materials.

Table 2.3 Publications on the heterogeneous photocatalytic synthesis of vanillin through the conversion of vanillyl alcohol.

Entry	Catalyst	Solvent	Atmosphere	Irradiation system	Reaction time (h)	X (%)	S (%)	Ref.
1	Au-Pd nanoparticles	Dioxane	Air	Xenon lamp	24	53	50	[189]
2	Home-prepared TiO <sub>2</sub>	Water	Air	Fluorescent lamp	1.5	15	21	[179]
3	5%N-CNT/ZnO	Water	Argon	UV-LED	0.25	15	27	[107]
4	g-CN-T	Water	Air	UV-LED	1	75	3	[150]

X: Conversion; S: Selectivity

The use of metal nanoparticles as photocatalysts in vanillin synthesis achieved both X and S higher than 50% (Table 2.3, entry 1). However, this result was only obtained after 24 h of irradiation, using an organic compound (dioxane) as solvent (Table 2.3, entry 1). By using metal oxides or heterojunctions between metal oxide catalysts and carbon phases, like carbon nanotubes (CNT), the reaction time required to reach a significant selectivity can be reduced (Table 2.3, entries 2 and 3). Moreover, it can

also be observed that the inert atmosphere favors the selectivity towards vanillin production. Up to now, only one work reported the photocatalytic production of vanillin through vanillyl alcohol oxidation, using carbon nitride as catalyst (Table 2.3, entry 4). However, the selectivity obtained with this metal-free material is still very low, which denotes the need for searching for new catalysts, with improved efficiency.

#### 2.1.4 Piperonal

Piperonal (3,4-(methylenedioxy)benzaldehyde) is a floral fragrance, with a cherry-like aroma, applied in food, perfumery, and cosmetic industries [190]. Additionally, piperonal exhibits also great pharmaceutical potential, namely in the treatment of obesity [191,192], sleep deprivation [193] and inflammatory conditions [194].

In the nineteenth century, piperonal was produced from alkaline pyrolysis of piperin to piperonic acid, with a further oxidation step by potassium permanganate, which led to its designation as piperonal [195]. Due to the prohibitive cost of this process of synthesis, the industrial production of this aldehyde started to be performed through the isomerization of safrole, with the propenyl group being oxidized by ozone or potassium dichromate [190,195]. Considering the environmental problems associated with this route, alternative methodologies were developed and are now industrially implemented, using 1,2-methylenedioxybenzene [196] and 3,4-dihydroxybenzaldehyde [197] as starting reagents. Also, piperonyl alcohol was explored as a precursor in catalytic processes to obtain its respective aldehyde [198–200]. However, the reactions occurred under high temperatures and required organic solvents, as toluene [198–200].

Table 2.4 Publications on the heterogeneous photocatalytic synthesis of piperonal through the conversion of piperonyl alcohol.

Entry	Catalyst	Solvent	Atmosphere	Irradiation system	Reaction time (h)	X (%)	S (%)	Ref.
1	TiO <sub>2</sub>	Water	Air	Fluorescent lamp	0.5	30	18	[190]
2	g-CN-T	Water	Air	UV-LED	4	50	16	[150]

X: Conversion; S: Selectivity

There are few works about the photocatalytic conversion of piperonyl alcohol into piperonal and they are compiled in Table 2.4.

Nevertheless, the process lacks selectivity either using metal oxide catalysts such as  $\text{TiO}_2$  (Table 2.4, entry 1) or metal-free materials as carbon nitride (Table 2.4, entry 2). Therefore, the plenty of room is left for the design of novel and improved catalysts, optimization of the operating conditions, and the development of effective photoreactors for the selective photocatalytic conversion of piperonyl alcohol into piperonal.

### 2.1.5 Vitamin B3

Vitamin B3 (or nicotinic acid) is a water-soluble vitamin that acts as a building block in the synthesis of nicotinamide-adenine-dinucleotide (NAD), which plays a major role in the redox reactions occurred in living cells [201]. The primary application of vitamin B3 relies on medicine, namely in the treatment of pellagra disease and alcoholism [202,203]. Moreover, clinical studies proved the positive impact of vitamin B3 administration in high cholesterol and coronary heart disease patients [204,205]. Due to the great importance of vitamin B3 for human life, more than 22000 tons are produced in all world per year, being Lonza, Degussa, and BASF the leading producers [206]. Since the human body does not produce this vitamin, it has to be obtained through food, such as wheat, tuna, salmon and pork and beef liver, or by the ingestion of supplements [201]. Currently, most of the vitamin B3 is chemically produced by the ammoxidation and oxidation of pyridines, under alkali conditions and high pressure [201,207,208]. Vitamin B3 can also be produced through the photocatalytic oxidation of 3-pyridinemethanol. Table 2.5 compiles the published works on this topic.

The research performed in the photocatalytic oxidation of 3-pyridinemethanol into vitamin B3 has been focused on using  $\text{TiO}_2$ -based materials as photocatalysts and traditional radiation sources (Table 2.5, entries 1-5). Using neat  $\text{TiO}_2$  under a continuous nitrogen flow, high selectivity was achieved (87%) in reduced reaction time (0.75 h; Table 2.5, entry 1). The composite between  $\text{TiO}_2$  and graphene (Table 2.5, entry 2) revealed a lower production efficiency, with modest values of  $X$  and  $S$  after an extended reaction time (5 h). Under oxygenated conditions, no significant difference was observed in the photocatalytic performance of  $\text{TiO}_2$  nanotubes and  $\text{Pt/TiO}_2$  (Table 2.5, entries 3 and 4). The construction of a heterojunction between Ag doped  $\text{TiO}_2$  and  $g\text{-C}_3\text{N}_4$  allowed to drastically increase conversion and selectivity (Table 2.5, entry 5) compared to the previous catalysts. However, extensive reaction time was required to achieve this result (9 h).

Table 2.5 Publications on the heterogeneous photocatalytic synthesis of vitamin B3 through the conversion of 3-pyridinemethanol.

Entry	Catalyst	Solvent	Atmosphere	Irradiation system	Reaction time (h)	X (%)	S (%)	Ref.
1	TiO <sub>2</sub>	Water	Nitrogen	High-pressure UV lamp	0.75	30	87	[209]
2	TiO <sub>2</sub> /graphene	Water	Nitrogen	Mercury lamp	5	63	35	[210]
3	TiO <sub>2</sub> nanotubes	Water	Air	Fluorescent lamp	n.i.	15	35	[211]
4	Pt/TiO <sub>2</sub>	Water	Air	Fluorescent lamp	3	15	45	[212]
5	Ag@TiO <sub>2</sub> /g-C <sub>3</sub> N <sub>4</sub>	Water	Air	Halogen lamp	9	100	100	[213]

n.i. – Not indicated; X: Conversion; S: Selectivity

Although the comparison of photocatalytic performance of a semiconductor material is usually performed through the conversion, selectivity, and yield achieved in the synthesis process, several operational parameters should be considered. In all works presented in this chapter, important parameters are identified, namely the catalyst chosen, the solvent, the atmosphere, the irradiation source and the time of irradiation. However, other aspects, such as the catalyst load, the initial concentration of the alcohol, the reaction volume and the power of the irradiation source, directly interfere with the results obtained in a photocatalytic process.

## 2.2 Future perspectives

Semiconductor photocatalysis has shown great potential as a sustainable technology for the partial oxidation of alcohols. The milder conditions adopted in photocatalytic processes, as well as the use of light as an energy source to drive chemical reactions constitute environmental and economic advantages compared to conventional methods [214].

The synergy between materials engineering and semiconductor photocatalysis can open an enormous range of possibilities to improve the efficiency of photocatalytic

processes. The development of highly selective photocatalysts constitutes one of the main goals in this field. Moreover, the preparation of visible-light activated materials is of major importance, considering using sunlight as a radiation source [37]. In this view, carbon-based semiconductors are an appealing class of materials, due to their unique properties, namely their good electron conductivity, large surface area, excellent physicochemical stability, and facile synthesis [114,215].

From a practical perspective, the immobilization of catalysts combined with continuous-flow reaction systems can provide a powerful tool to improve the applicability of photocatalytic processes, allowing the reuse of catalyst and avoiding time-consuming and highly-cost catalyst separation [216,217].

Another aspect that contributes to increasing the efficiency of the photocatalytic process is the design of the photoreactor. The activity in the reaction systems is directly affected by the illuminated area and light intensity, which makes efficient irradiation of the catalyst a great challenge [218]. LEDs present lower power consumption, more life span, more physical resistance, smaller size and faster switching than traditional light sources [219].

In conclusion, there are many gaps and technological drawbacks related to the application of semiconductor photocatalysis in the organic synthesis that justify the development and research of novel and improved reactive systems.



## Part II



## Chapter 3

### ***Synthesis of vanillin using CNF/ZnO photocatalysts***

In the present chapter, the photocatalytic synthesis of vanillin (VAD) was explored through the oxidation of vanillyl alcohol (VA). Hybrid photocatalysts of zinc oxide (ZnO) and carbon nanofibers (CNF) were prepared and thoroughly characterized.

The incorporation of the carbon phase in ZnO was found to increase the surface area and the photocatalytic performance of the materials. The latter was attributed to the efficient separation of charge carriers generated on the optical semiconductor. With the best performing material, the selectivity of the synthesis towards vanillin generation was increased by a factor of 2.5 compared to previous studies, with the additional advantage of carrying the reaction in aqueous medium. The same photocatalyst was successfully applied to the selective synthesis of other aromatic aldehydes, namely *p*-anisaldehyde, piperonal, and benzaldehyde. A relationship between the efficiency of the photocatalytic oxidation of the alcohols and the activating nature of their aromatic ring substituents was proposed.

**This chapter is based on the following article:**

R. A. Fernandes, M. J. Sampaio, E. S. da Silva, P. Serp, J. L. Faria, C. G. Silva, Synthesis of selected aromatic aldehydes under UV-LED irradiation over a hybrid photocatalyst of carbon nanofibers and zinc oxide. *Catal. Today*. 328 (2019) 286-292, reproduced by permission of Elsevier.



### 3.1 Introduction

Vanillin is the major component of natural vanilla, which is one of the most important flavoring agents used in food, cosmetic and pharmaceutical industries [187]. Vanillin production is mainly carried out through a synthetic route, once the natural sources (bean and pod of Vanilla orchid) are scarce and the extraction from these sources is not economically profitable [179]. There are a few reports about the synthesis of vanillin by heterogeneous photocatalysis [107,179,186]. Yet, all these reports showed that selectivity of the referred processes is still limited in terms of industrial application. In the field of neat optical semiconductors, ZnO presents electronic properties similar to the benchmark TiO<sub>2</sub>. Moreover, its lower cost and morphological versatility may be envisaged as promising aspects to promote its use as an alternative to TiO<sub>2</sub> [100,220]. Several modifications have been performed in neat ZnO for increasing its photoefficiency, including doping with metals (Ni, Cu, Mg, Ag) and non-metals (N, S), formation of heterojunctions by combination with other semiconductors and coupling with carbon materials [104]. Composites of ZnO and carbon materials proved to be promising catalysts in the decomposition of several organic pollutants [11,23,24] and already in organic synthesis [107]. In these examples, carbon nanofibers (CNF) can act as photoexcited electron scavenger, storing the excited electrons generated during the irradiation of ZnO, or alternatively as photosensitizers, improving light absorption [22].

### 3.2 Experimental

#### 3.2.1 Materials

Zinc flake (325 mesh size, >99%), vanillyl alcohol (VA, 4-hydroxy-3-methoxybenzyl alcohol, C<sub>8</sub>H<sub>10</sub>O<sub>3</sub>, >98%), *p*-anisyl alcohol (AA, 4-methoxybenzyl alcohol, C<sub>8</sub>H<sub>10</sub>O<sub>2</sub>, 98%), vanillin (VAD, C<sub>8</sub>H<sub>8</sub>O<sub>3</sub>, 99%) and zinc (Zn) metal powder were purchased from Alfa Aesar. Tetrahydrofuran (C<sub>4</sub>H<sub>8</sub>O, >99%), benzyl alcohol (BA, C<sub>7</sub>H<sub>8</sub>O, >99%), piperonyl alcohol (PA, C<sub>8</sub>H<sub>8</sub>O<sub>3</sub>, 98%), *p*-anisaldehyde (AAD, C<sub>8</sub>H<sub>8</sub>O<sub>2</sub>, 98%), benzaldehyde (BAD, C<sub>7</sub>H<sub>6</sub>O, >99%), piperonal (PAD, C<sub>8</sub>H<sub>6</sub>O<sub>3</sub>, 99%), ethylenediaminetetraacetic acid (EDTA, ≥ 98%) and hydrochloric acid (HCl, 37 wt.%) were purchased from Sigma-Aldrich. Formic acid (CO<sub>2</sub>H<sub>2</sub>, 98%) was purchased from Fluka. Methanol (CH<sub>4</sub>O, 99.6%) was purchased from VWR™. All the reagents were used without further purification. Ultra-pure water was obtained from a Direct-Q Millipore system

### 3.2.2 Synthesis of CNF/ZnO composites

CNF and ZnO tetrapods were synthesized at Laboratoire de Chimie de Coordination, INP-ENSIACET, Université de Toulouse (France). CNF were prepared by catalytic chemical vapor deposition (CVD) and the purification was performed using hydrochloric acid over 12 h [221].

To synthesize ZnO tetrapods, Zn metal powder was melted under argon flow atmosphere at 900°C and oxidized maintaining a flow of air in the opposite direction. The particles of ZnO were collected using cold traps and no further purification was performed [222].

The CNF/ZnO composites were prepared by adding 0.200 g of ZnO to a suspension of a given amount of CNF in tetrahydrofuran under vigorous stirring, followed by sonication for 30 min. The obtained solution was stirred for 1 h and the so obtained solid was then filtered, washed and dried at 60°C for 12 h.

The catalysts were denoted as xCNF/ZnO, where  $x$  is the weight percentage of CNF in relation to the mass of ZnO in the composite. For example, 10%CNF/ZnO means that the composite catalyst was prepared using a suspension with 10 mg of CNF and 100 mg of ZnO.

### 3.2.3 Characterization of the photocatalysts

The morphology of ZnO and composite catalysts was analyzed by scanning electron microscopy (SEM), using a FEI Quanta 400 FEG ESEM/EDAX Genesis X4M (15 keV) instrument. CNF was characterized by transmission electron microscopy (TEM), using a TEM-FEI Tecnai-G2-20-FEI 2006 microscope at 200 kV.

The effective content of carbon material in each catalyst was determined by the thermogravimetric (TG) analysis, through the heating of samples from 50°C to 900°C at 10°C min<sup>-1</sup> rate under air flow using a STA 490 PC/4/H Luxx Netzsch thermal instrument.

The diffuse-reflectance UV–Vis spectra (DR UV-Vis) of the materials were obtained in a JASCO V-560 UV-Vis spectrophotometer equipped with an integrating sphere attachment (JASCO ISV-469). The bandgap of the catalysts was determined from the respective Tauc plot.

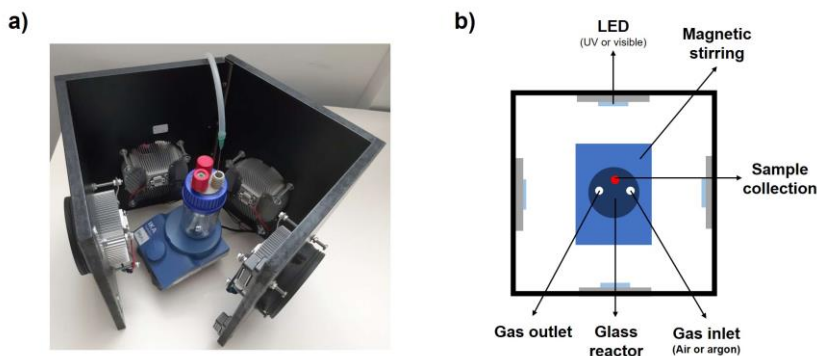
The Brunauer-Emmett-Teller (BET) specific surface area ( $S_{BET}$ ) was determined through the N<sub>2</sub> adsorption isotherm at -196°C in the relative pressure range 0.05–0.20, using a Quantachrome NOVA 4200e apparatus.

Solid state photoluminescence (PL) spectra were obtained at room temperature on a JASCO (FP 82000) fluorescence spectrometer with a 150W Xenon lamp as light

source, under 340 nm excitation, using bandwidths of 2.5 nm for emission and excitation.

### 3.2.4 Photocatalytic experiments

The photocatalytic synthesis of vanillin (VAD) by ZnO was investigated through the oxidation of vanillyl alcohol (VA) in a cylindrical glass reactor (Scheme 3.1) filled with 50 mL of 0.50 mM alcohol aqueous solution. The experiments were carried out at room temperature ( $\sim 20^{\circ}\text{C}$ ), without pH adjustment (*ca.* 5.7). The effect of catalyst load in the catalyst performance was studied by varying the ZnO load between 0.10 and 1.2  $\text{g L}^{-1}$ . The effect of CNF content (from 0 to 20 *wt%*) and the presence of oxygen in the reaction medium were also evaluated. A study without the presence of any catalyst was also performed to evaluate the possibility of photolysis. The application of the photocatalytic system to the synthesis of other aromatic aldehydes, namely *p*-anisaldehyde (AAD), benzaldehyde (BAD) and piperonal (PAD) was also studied starting from the respective alcohols (*p*-anisyl (AA), benzyl (BA) and piperonyl (PA) alcohols).



Scheme 3.1 a) Photograph and b) schematic representation of the photocatalytic experimental setup operating under batch mode.

The reaction medium was continuously saturated with argon ( $20 \text{ mL min}^{-1}$ ;  $T \sim 20^{\circ}\text{C}$  and  $P = 1 \text{ atm}$ ) and kept in dark conditions for 15 min. The irradiation was performed using a four UV-LED system (Scheme 3.1) emitting at 370 nm located symmetrically from the outside at 4 cm from the reactor wall. The average nominal irradiance of each UV-LED was  $450 \text{ W m}^{-2}$ , determined using a UV-vis spectroradiometer (OceanOptics USB2000 +). The suspension was irradiated for 8 h and samples (0.30 mL) were periodically withdrawn to monitor alcohol and aldehyde concentration by High-Performance Liquid Chromatography (HPLC).

### 3.2.5 Analytical techniques

The concentration of alcohols and aldehydes was monitored through HPLC, using a Shimadzu Corporation apparatus equipped with a Diode Array Detector (DAD; SPD M20A). A Kinetex™ F5 1.7  $\mu\text{m}$  100 Å column (100 mm x 2.1 mm) was used with a solvent delivery pump (LC-30AD) using a flow rate fixed at 0.15 mL min<sup>-1</sup>. The temperature of the column oven and autosampler were set at 35°C and 4.0°C, respectively. An equilibrated mixture of 0.1% v/v of formic acid (A) and methanol (B) with volume ratio of 30:70 (A:B) was isocratically eluted for 15 min. The concentrations of VA, VAD, PA and PAD were determined at 230 nm. The BA concentration was determined at 207 nm, while BAD concentration was determined at 250 nm. The AA and AAD concentrations were determined at 226 nm and 282 nm, respectively.

According to the chemical stoichiometry, one molecule of alcohol can be oxidized to one molecule of aldehyde (1:1). The synthesis of aldehydes only starts when the irradiation source is turned on, which means that the initial concentration of aldehyde is zero. The alcohol conversion (*X*), selectivity (*S*) and yield (*Y*) towards the aldehyde production are then defined as:

$$X (\%) = \frac{[ALC]_0 - [ALC]_t}{[ALC]_0} \times 100 \quad 3.1$$

$$S (\%) = \frac{[ALD]_t - [ALD]_0}{[ALC]_0 - [ALC]_t} \times 100 = \frac{[ALD]_t}{[ALC]_0 - [ALC]_t} \times 100 \quad 3.2$$

$$Y (\%) = \frac{[ALD]_t - [ALD]_0}{[ALC]_0} \times 100 = \frac{[ALD]_t}{[ALC]_0} \times 100 \quad 3.3$$

in which,  $[ALC]_0$  is the initial concentration of alcohol (mM),  $[ALC]_t$  is the concentration of alcohol (mM) at a given time *t*, and  $[ALD]_t$  is the concentration of aldehyde (mM) at a given time *t*. It is worth mentioning that following the adopted definitions, it results that  $Y = \frac{X \times S}{100}$ .

## 3.3 Results and discussion

### 3.3.1 Characterization of CNF/ZnO composites

The morphology of the catalysts was observed by scanning and transmission electron microscopy (SEM and TEM, respectively, Fig. 3.1). The SEM micrograph of ZnO (Fig. 3.1a) reveal the presence of tetrapod-like structures (zone I) with needles growing from a central particle, as previously documented [71,222]. The incorporation of CNF in ZnO phase does not induce any morphological modification on ZnO tetrapods, but induced their aggregation on the side-walls of CNF and the generation of interstices



in the ZnO phase (Figs. 3.1b-e), as reported in the literature for studies using composite catalysts constituted by metal oxides and carbon materials [72,223]. The presence of the carbon phase in 5%CNF/ZnO (Fig. 3.1b) was difficult to detect due to the low content of CNF in composite material, with few small fibers being observed. By increasing the CNF content to 10%, a higher amount of fibers can be observed (Fig. 3.1c).

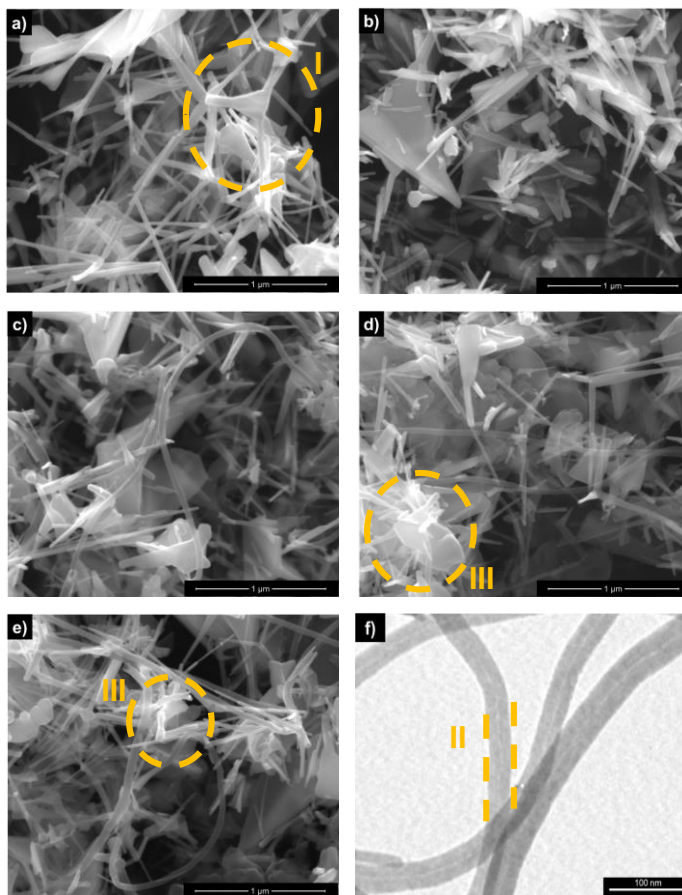


Fig. 3.1 SEM micrographs of a) ZnO, b) 5%CNF/ZnO, c) 10%CNF/ZnO, d) 15%CNF/ZnO and e) 20%CNF/ZnO. TEM image of f) CNF. Highlighted zones: I) ZnO tetrapods, II) long tubular CNF and III) ZnO agglomerates.

The SEM image of 10%CNF/ZnO (Fig. 3.1c) shows a good distribution of CNF on the ZnO phase, providing a better contact between the two phases, which is known to favor the photocatalytic activity. Additionally, it is evident that the increase of the CNF content to 15% and 20% (Figs. 3.1d and e, respectively) leads to the formation of ZnO agglomerates (Fig. 3.1d, zone III) surrounding CNF. These features may indicate the existence of physical segregation between both phases, reducing their interactions.

This behavior has already been reported in previous studies using carbon/metal oxide photocatalysts [107,224]. In the present work, the phase segregation may be attributed to the use of pristine CNF to prepare the hybrid material (without any surface treatment for increasing their dispersibility in the solvent), and their tendency to aggregate during the synthesis procedure, thus impeding the dispersion of ZnO. TEM analysis of CNF (Fig. 3.1f) shows a long tubular structure (zone II), with a diameter of ca. 30 nm.

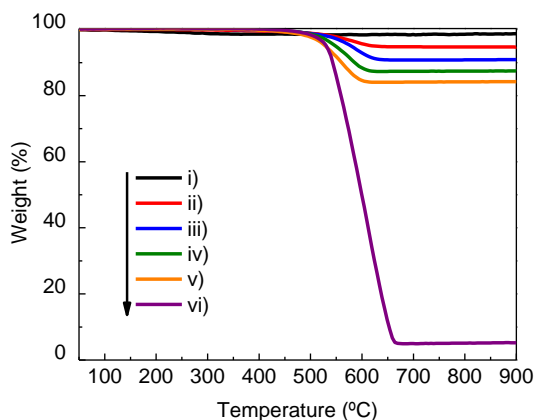


Fig. 3.2 TG analysis of i) ZnO, ii) 5%CNF/ZnO, iii) 10%CNF/ZnO, iv) 15%CNF/ZnO, v) 20%CNF/ZnO and vi) CNF.

The composition and surface thermodynamics of the composite materials was assessed by TG analysis (Fig. 3.2 and Table 3.1). Bare ZnO, CNF and composites were submitted to a thermal process until 900°C under air flow and the content of CNF was determined (Fig. 3.2). As expected, no significant mass loss was verified in ZnO, since the material is quite stable in this range of temperature [107]. The TG profile of CNF shows about 5% of residue, which may be indicative of the presence of catalyst metal used to grown the CNF [221]. The composite materials show a weight loss at around 550°C, which also occurs in the case of CNF, due to the carbon gasification [225]. The theoretical carbon content (%) in composite materials was determined (Table 3.1) considering the weight of CNF used in the preparation of the composite material in relation to its total weight. The values indicate a weight loss between 4-15% for the different composite materials, which agrees with their nominal carbon content.

The surface area ( $S_{BET}$ ) of bare ZnO, CNF and composite materials are listed in Table 3.1. The experimental  $S_{BET}$  of bare ZnO was found to be very low ( $11 \text{ m}^2 \text{ g}^{-1}$ ) comparing with that of CNF ( $81 \text{ m}^2 \text{ g}^{-1}$ ).

Table 3.1 Carbon content (%) and specific surface area ( $S_{BET}$ ) of ZnO and of the composite catalysts.

Catalyst	Carbon content (%)		$S_{BET}$ (m <sup>2</sup> g <sup>-1</sup> )	
	Experimental	Theoretical	Experimental	Theoretical <sup>a</sup>
ZnO <sup>b</sup>	n. a.	n. a.	11	n. d.
5%CNF/ZnO	4.04	4.76	12	14
10%CNF/ZnO	7.75	9.09	15	18
15%CNF/ZnO	11.3	13.0	15	21
20%CNF/ZnO	14.5	16.7	18	25
CNF <sup>b</sup>	94.7	100	81	n.d.

<sup>a</sup> The theoretical surface area was determined considering the experimental weight content of ZnO and CNF in the catalyst. <sup>b</sup> n.a. – not applied, n.d. – not determined.

As expected, an enhancement in the  $S_{BET}$  of the composites was verified with the incorporation of CNF in the metal oxide phase, which is related with the increase of CNF content from 5% to 20%. Additionally, the experimental  $S_{BET}$  of composite materials is slightly lower than the theoretical one, obtained from the relative weight fraction of the CNF and ZnO phases in each composite (Table 3.1). This deviation may be attributed to the surface contact between CNF and ZnO tetrapods and the agglomeration of ZnO over CNF, as observed in SEM micrographs [71]. Bare ZnO, CNF and the composite materials produce isotherms type II, according to the IUPAC classification (Fig. 3.3), which are characteristics of non-porous materials. However, it is visible a type H3 hysteresis loop, which could be explained in terms of the interstices formed between the aggregates of ZnO and CNF [226,227]. The incorporation of CNF led to a change in the color of the composite materials, from white (ZnO) to black (CNF) (Fig. 3.4a), which is related with their higher absorption in the visible region ( $\lambda > 400$  nm; Fig. 3.4b). This variation is associated with the inherent ability of CNF to absorb light (Fig. 3.4b) and with the creation of an electronic interphase interaction between the CNF and ZnO phases [82,107]. The bandgap energy ( $E_g$ ) for neat ZnO, taken from the Tauc plot, accounts for a value of 3.28 eV (Fig. 3.4c). In a qualitative way the Tauc analysis of the composite suggests that, in small amounts (*i.e.* for 5%CNF/ZnO), the carbon phase does not affect the  $E_g$  of ZnO. Increasing the amount of CNF to 15 and 20% results in a small decrease in the  $E_g$  of the ZnO. This is possibly due to the presence of ZnO aggregates (SEM analysis), as previously reported [228].

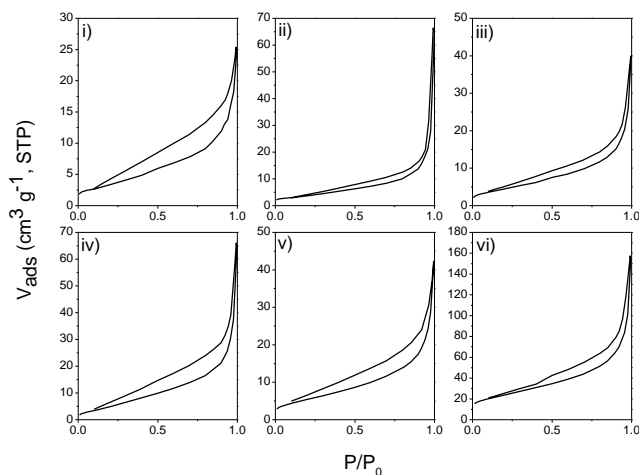


Fig. 3.3 Isotherms of  $N_2$  adsorption-desorption at  $-196^\circ\text{C}$  for i) ZnO, ii) 5%CNF/ZnO, iii) 10%CNF/ZnO, iv) 15%CNF/ZnO, v) 20%CNF/ZnO and vi) CNF.

The determination of  $E_g$  of CNF through a similar Tauc plot, was not possible due to their high absorption in whole UV-Vis range [229].

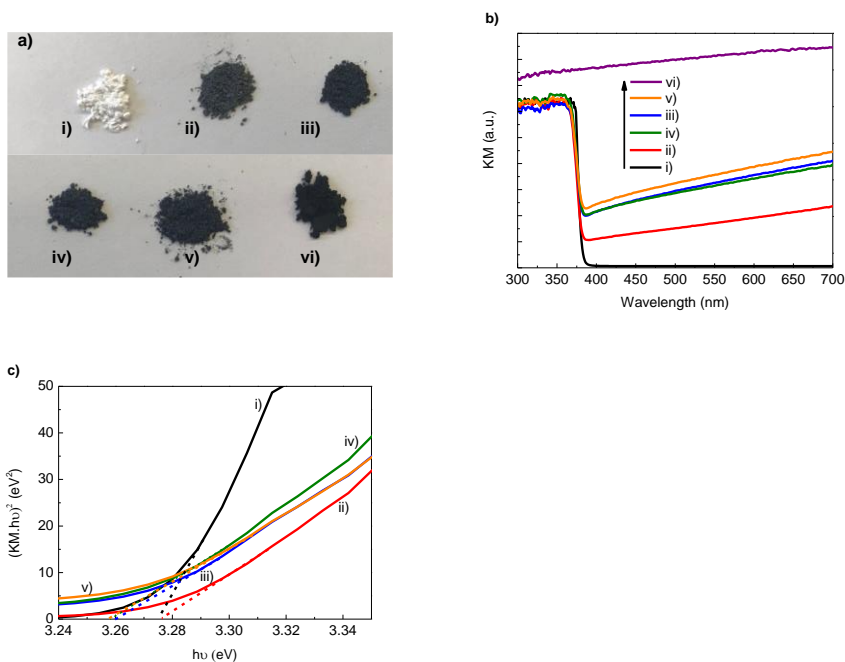


Fig. 3.4 a) Photograph, b) DR UV-Vis spectra expressed in Kubelka-Munk (KM) equivalent absorption units and c) the respective Tauc plots of i) ZnO, ii) 5%CNF/ZnO, iii) 10%CNF/ZnO, iv) 15%CNF/ZnO, v) 20%CNF/ZnO and vi) CNF.

To evaluate the degree of charge separation and transportation in the prepared materials, photoluminescence (PL) measurements were performed (Fig. 3.5). The PL emission spectra of ZnO reveals an intense UV peak ( $\lambda_{max} = 379.6$  nm, Fig. 3.5a) due to the exciton recombination on the surface of ZnO tetrapods [71,110]. Additionally, several peaks are observed in the visible range, including a broad peak at 540 nm (inset Fig. 3.5a), usually associated to the presence of defects on the catalyst surface [71,110]. With the incorporation of CNF on the metal oxide phase, the PL intensity of ZnO is significantly quenched in both emission regions (Fig. 3.5a), indicating that the recombination of the photogenerated charge carriers was greatly inhibited in the CNF/ZnO nanostructures. It follows that the CNF serves as an efficient electron sink, and scavenges away the electrons, hindering recombination [71,107], therefore improving the separation of charge carriers, resulting in higher photocatalytic activity [230].

As clearly observed in Fig. 3.5b, the composite containing 10% of CNF leads to the highest quenching of the fluorescence emission. Among all the composites, 10%CNF/ZnO presents the most efficient separation of charge carriers, which is beneficial to enhance the interfacial charge transfer to adsorbed substrates, thereby improving the photocatalytic performance [230].

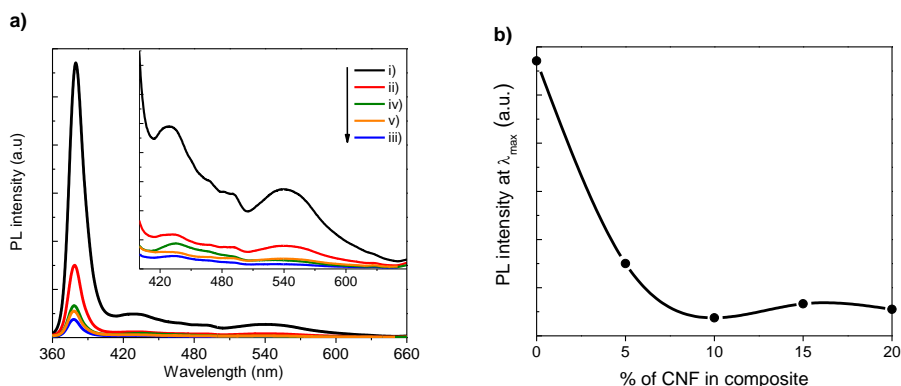


Fig. 3.5 a) Solid-state PL spectra of i) ZnO, ii) 5%CNF/ZnO, iii) 10%CNF/ZnO, iv) 15%CNF/ZnO and v) 20%CNF/ZnO obtained upon excitation at 340 nm. Inset shows a zoom of the emission bands in the visible region. b) ZnO fluorescence emission intensity (measured at the maximum of emission) in function of CNF percentage.

Furthermore, the inhibition of fluorescence is accompanied by a small blue shift of the maximum emission of ZnO, resultant of the interaction between the metal oxide and the carbon phase (Fig. 3.5a). On the other hand, a further increase in the

content of CNF to 15 and 20% causes a small increase in the fluorescence emission intensity in both emission regions (Fig. 3.5b), in relation to the composite with 10% of CNF. This increase might be related with ZnO agglomeration evident in SEM micrographs (Figs. 3.1d and e), which hinders the efficient interfacial charge transfer between ZnO and CNF, enhancing the recombination of electron-hole.

### 3.3.2 Photocatalytic selective synthesis of vanillin

The effect of CNF incorporation in the photocatalytic performance of the ZnO-based materials was evaluated in the synthesis of VAD through oxidation of VA under UV-LED irradiation ( $\lambda_{max} = 370$  nm) and argon atmosphere, using water as solvent. In the absence of catalyst (Fig. 3.6), a negligible decrease in VA concentration was observed at the end of 4 h reaction, proving the photo-inertness of the parent alcohol molecule under the present irradiation conditions. Moreover, the adsorption experiment shown less than 2% of decrease in VA over 4 h.

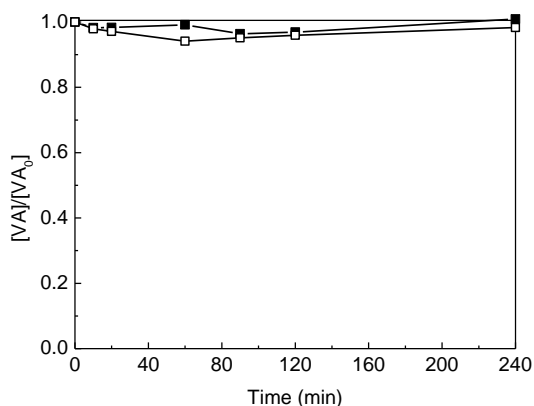


Fig. 3.6 Normalized concentration of VA during the photolysis experiment (□) and using only CNF as catalyst (■), under UV-LED irradiation ( $\lambda_{max} = 370$  nm) over 4 h reaction.

The amount of catalyst used is an important parameter that needs to be optimized for avoiding the useless excess of it, as well as to ensure an efficient absorption of the irradiating photons. An excess of catalyst concentration may produce screening effects, which can lead to a decrease of the photocatalytic efficiency of the process. Therefore, the optimization of the ZnO load was performed by varying the amount suspended between 0.10 and 1.2 g L<sup>-1</sup>. The activity and selectivity of the catalysts was evaluated in terms of *X*, *S* and *Y*, determined after 1 h of reaction (Fig. 3.7a).

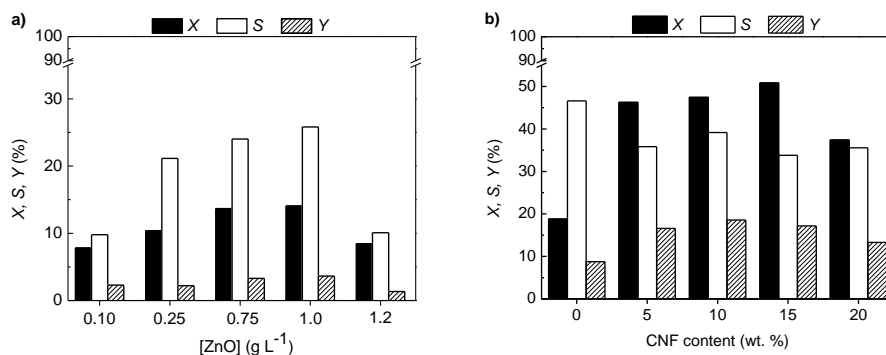


Fig. 3.7 a) Effect of ZnO load on X, S and Y at 1 h of reaction. b) Effect of CNF content on X, S and Y in long-term (8 h) reactions (0% CNF content corresponds to bare ZnO).

From the conversion values was found a direct dependency with the amount of catalyst up to 0.75 g L<sup>-1</sup>, confirming the heterogeneous nature of the catalytic regime. However, above this catalyst charge the reaction becomes independent of the catalyst load. This behavior corresponds to the maximum amount of catalyst at which all the particles are totally irradiated, as well to the reaction conditions such as reactor geometry and radiation configuration [37]. For catalyst loads between 0.75 g L<sup>-1</sup> and 1.0 g L<sup>-1</sup>, a maximum of 14% for VA conversion, 25% of selectivity and 3% of yield towards VAD production was found. The efficiency decreased for higher ZnO load (1.2 g L<sup>-1</sup>), with a decrease in X, S and Y (Fig. 3.7a). As already mentioned above, these results may be explained by the increase in opacity of the reaction medium, triggering a significant amount of light scattering [103]. Additionally, agglomeration (particle-particle interaction) is favored for higher catalyst load, which may lead to the reduction of active sites on the surface of the catalyst for light irradiation and substrate adsorption, decreasing the efficiency of the photocatalytic system [231]. Considering the obtained results, 0.75 g L<sup>-1</sup> of catalyst was chosen as the optimal catalyst load for the subsequent studies using both ZnO and CNF/ZnO hybrids.

The effect of carbon phase on ZnO performance was therefore studied in the photocatalytic synthesis of VAD over 8 h reaction, using different contents of CNF (5, 10, 15 and 20 wt.%). The photocatalytic results presented in Fig. 3.7b reveal that the incorporation of CNF promotes an increase of the efficiency in terms of yield towards VAD production when compared with bare ZnO, after 8 h of reaction. The higher photocatalytic performance of CNF/ZnO nanostructures was already reported in literature [104,107,230]. With the introduction of CNF into the matrix, excited electrons in the conduction band of ZnO are prone to be transferred to the surface of CNF,

promoting an efficient separation of electron-hole compared to bare ZnO. The holes left the valence band of ZnO may act as active sites for oxidation of the adsorbed molecules, as in the case of VA, adding to the catalytic activity [230,232].

An experiment using bare CNF was performed (Fig. 3.6), and the results showed that it lacks photoactivity for VA oxidation. Thus, the photo-efficiency of the hybrid CNF/ZnO materials cannot be rationalized in terms of an additive catalytic action of CNF and ZnO, but attributed to an electronic synergetic effect between the carbon and metal oxide phases, as revealed by PL spectroscopy (Fig. 3.5).

When the CNF content was raised up to 10 wt.%, a continuous increase in selectivity and yield is observed (Fig. 3.7b). However, for higher CNF content (15 and 20 wt.%), the suspensions are darkened, which might promote light absorption and scattering, decreasing the catalytic performance, leading to lower values of *S* and *Y* (Fig. 3.7b). Although these two materials present the highest surface areas (Table 3.1) and the formation of aggregates (Fig. 3.1), the higher recombination of charge carriers demonstrated by PL studies might be accountable for the lower activity of the composites.

Among all the composites tested, the 10%CNF/ZnO showed the best photocatalytic performance with *ca.* *X* = 50%, *S* = 40% and *Y* = 20% at the end of 8 h of reaction (Fig. 3.7b). The higher photocatalytic performance of this material might be ascribed to a more efficient separation of the photogenerated electron-hole and increased surface area. SEM image also reveals an efficient interface contact between ZnO and CNF phases, which contributes to the efficient charge carrier separation, as observed by PL results. Furthermore, the increase in the surface area contributes to create more active sites for adsorption of VA, which are beneficial to promote the photocatalytic activity.

Generally, heterogeneous photocatalytic oxidation processes are carried out under an aerobic atmosphere. Therefore, in order to assess the role of oxygen in the photocatalytic synthesis of VAD, reactions were performed using ZnO and the best performing composite (10%CNF/ZnO) in the presence of oxygen (by saturating the suspensions with air, Fig. 3.8).



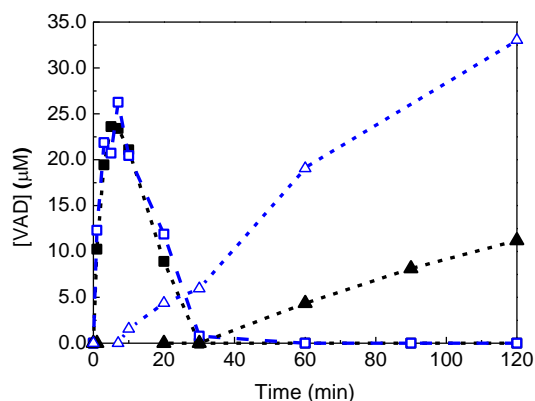


Fig. 3.8 Concentration profile of VAD over 2 h of reaction, using ZnO ( $\blacktriangle$ ,  $\blacksquare$ ) and 10%CNF/ZnO ( $\triangle$ ,  $\square$ ) as catalysts, under air ( $\square$ ,  $\blacksquare$ ) and argon ( $\triangle$ ,  $\blacktriangle$ ) atmospheres.

The saturation of the reaction medium with argon promotes a continuous synthesis of VAD using both materials over 2 h of reaction. On the other hand, in the presence of oxygen, it is possible to observe a maximum in the VAD production at 5 min of reaction and its total disappearance after 30 min using both ZnO and 10%CNF/ZnO. Although VA oxidation was enhanced in presence of air, *S* was negatively affected, reaching merely 7% contrasting with 40% for the reactions using argon (determined for the maximum of VAD concentration, Fig. 3.8). The presence of oxygen acts as electron acceptor, generating ROS [231,233–235], contributing to the increase in VA conversion, but negatively affecting selectivity for VAD production, due to the highly unselective nature of these chemical species. Under these conditions, the overoxidation of the aldehydes is expected with its conversion to short chain carboxylic acids, CO<sub>2</sub> and H<sub>2</sub>O [179]. When air is replaced by an inert gas such as argon, the formation of ROS is inhibited, resulting in an increase in the selectivity of the reaction towards the formation of the aromatic aldehyde. In this case, the main reactive species present in the photocatalytic reactions are expected to be mostly photogenerated  $h\nu^+$  and  $e^-$  [236].

A summary of the results reported in the literature for the photocatalytic synthesis of vanillin from vanillyl alcohol both in the presence and absence of oxygen is depicted in Table 3.2.

Augugliaro et al. [179] achieved 21% of *S* in the VAD synthesis after 90 min of reaction, using a home prepared TiO<sub>2</sub> (HPC3), under air. In a recent work of Sampaio et al. [107], selectivity was increased up to 27% in only 20 min of irradiation using a ZnO/N-doped carbon nanotube composite catalyst. In the present work, although increasing

the reaction time from 20 to 60 min, selectivity for VAD production was increased by 2.5 times, reaching 67% using the best performing composite catalyst, 10%CNF/ZnO (Table 3.2).

Table 3.2 Published works about the photocatalytic synthesis of vanillin using vanillyl alcohol as starting molecule.

Catalyst	Gas bubbled	Irradiation time (min)	X (%)	S (%)	Ref.	
<b>P25-TiO<sub>2</sub></b>	O <sub>2</sub>	30	40	9	[179]	
	Air	30	17	16		
<b>Merck</b>	O <sub>2</sub>	30	14	15		
	Air	60	19	14		
<b>HPC3</b>	O <sub>2</sub>	60	16	13		
	Air	90	15	21		
<b>HP0.5</b>	O <sub>2</sub>	60	11	20		
	Air	120	13	16		
<b>ZnO</b>	Argon	20	12	24		[107]
<b>5%N-CNT/ZnO</b>	Argon	20	15	27		
<b>ZnO</b>	<b>Argon</b>	<b>90</b>	<b>3</b>	<b>50</b>	<b>Present work</b>	
<b>10%CNF/ZnO</b>	<b>Argon</b>	<b>60</b>	<b>6</b>	<b>67</b>		

X: conversion; Y: yield

To investigate the reaction pathway of photocatalytic synthesis of VAD, aqueous solutions in the presence of EDTA (hole scavenger) and the catalysts ZnO and 10%CNF/ZnO were irradiated under UV-LED light (Fig. 3.9).

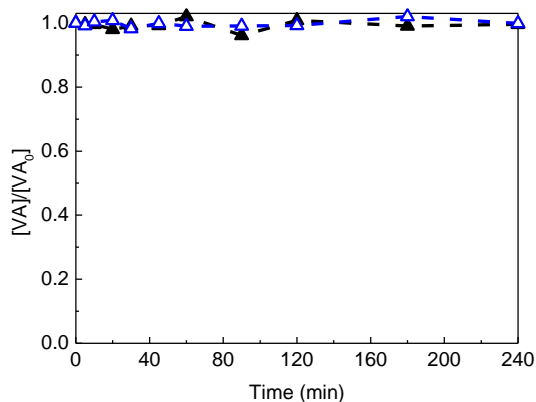


Fig. 3.9 Normalized concentration of VA over 4 h of reaction under argon atmosphere, using ZnO ( $\blacktriangle$ ) and 10%CNF/ZnO ( $\triangle$ ) as catalysts, in the presence of a hole scavenger (0.1 M EDTA).

Under these conditions, EDTA inhibited the photocatalytic synthesis of VAD for both catalysts (Fig. 3.9), implying that the photocatalytic production of VAD occurs mainly through oxidation of VA by photogenerated  $h\nu^+$  with  $H^+$  abstraction [107]. On the other hand,  $e^-$  at the conduction band of the photocatalyst may drive the reduction of  $H^+$  to  $H_2$ , considered a valuable by-product of the process.

### 3.3.3 Photocatalytic selective synthesis of other aromatic aldehydes

Considering the photocatalytic performance of ZnO and 10%CNF/ZnO in the synthesis of VAD, the synthesis of other aromatic aldehydes was evaluated under similar reaction conditions. *p*-Anisyl alcohol (AA), piperonyl alcohol (PA) and benzyl alcohol (BA) were used as substrate molecules for the production of their respective aldehydes. The reactions were performed using the best operational conditions found for VAD production, *i.e.*, a catalyst load of  $0.75 \text{ g L}^{-1}$  and under anaerobic conditions. As observed in Fig. 3.10, the photoproduction of VAD, *p*-anisaldehyde (AAD) and piperonal (PAD) continuously increase over the time using both catalysts. On the other hand, the profile of benzaldehyde (BAD) production does not follow the same tendency, reaching a maximum of concentration at 90 min, after which the concentration starts to decrease, due to its overoxidation to benzoic acid, as confirmed by HPLC analysis. This behavior has already been reported in previous studies being attributed to the attack of hydroxyl radicals, formed from the reaction of  $HO^-$  with positive holes, to BAD molecules [92,133].

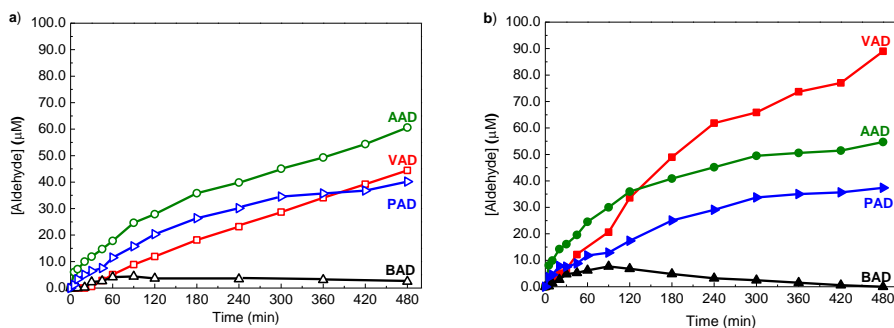


Fig. 3.10 Concentration profile of *p*-anisaldehyde (AAD), benzaldehyde (BAD), piperonal (PAD) and vanillin (VAD) over 480 min of reaction, using (a) ZnO and (b) 10%CNF/ZnO as catalysts.

The conversion and selectivity obtained for the different aldehydes after 8 h of reaction is summarized in Table 3.3. In terms of selectivity for aldehyde production using both ZnO and 10%CNF/ZnO materials, a higher efficiency for the photocatalytic synthesis of VAD through the oxidation of VA was found, reaching 47% and 39% of S, respectively. However, in relation to the alcohol conversion, the results revealed different behavior, being AA and PA the substrates that present higher X for both catalysts. According to Yurdakal et al. [237], electronic properties of substituent groups affect the rate of oxidation of aromatic alcohols and this phenomena can be interpreted through the Hammett relationship [238].

The substituent groups can act as electron-donor or electron-withdrawing groups, depending on their Hammett constant in *para*- and *meta*- positions ( $\sigma_p$  and  $\sigma_m$ , respectively, Table 3.4) [237,238]. VA, AA and PA are benzyl alcohol derivatives, with different substituent groups in *para*- and *meta*- positions (Table 3.4). The alcohols studied in this work present mostly negative Hammett constants ( $\sigma < 0$ ), *i.e.* electron-donor groups, resulting in an activating tendency of these groups for alcohol oxidation. At variance, for positive Hammett constants ( $\sigma > 0$ ), *i.e.*, electron-withdrawing groups, substituent groups have a deactivating effect over the reactivity of aromatic ring [239]. Generally, heterogeneous photocatalytic reactions are known as electrophilic processes, thus the presence of electron-donating groups in aromatic rings accelerate the chemical reactions, while the presence of electron-withdrawing substituents retards the reaction [239]. AA and PA molecules exhibits a methoxy ( $-\text{OCH}_3$ ) and a methylenedioxy ( $-\text{O}_2\text{CH}_2$ ) group, respectively, which are electron-donors, thus the highest conversions observed for these alcohols may be attributed to the activating nature of their substituent groups. In the case of BA, the presence of *p*-hydrogen, which may act also as electron-withdrawing (low activating) showed negligible

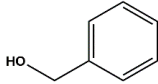
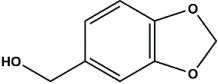
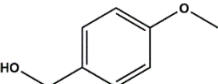
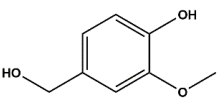
efficiency for BAD production when compared with attached substituents groups of the previous alcohols.

Table 3.3 Conversion (X) and selectivity (S) of AAD, BAD, PAD and VAD production after 8 h of reaction with ZnO and 10%CNF/ZnO.

Catalyst	Substrate	Product	X (%)	S (%)
ZnO	VA	VAD	19	47
	PA	PAD	52	17
	BA	BAD	36	2
	AA	AAD	44	30
10%CNF/ZnO	VA	VAD	47	39
	PA	PAD	57	14
	BA	BAD	22	9
	AA	AAD	66	19

In the case of VA, the aromatic ring has attached two substituent groups ( $-OH$  and  $-OCH_3$  on *para*- and *meta*-position, respectively). Considering the Hammett constants for both substituents and their respective positions (Table 3.4), one can infer that the combination of a very strong ( $-OH$ ) and a less strong ( $-OCH_3$ ) activating group may decrease the positive impact of  $-OH$  (in *para*-position over the reactivity of aromatic ring), leading to a decrease of the expected conversion of VA when compared with other studied aromatic alcohols.

Table 3.4 Chemical structure and substituent groups of vanillyl alcohol (VA), benzyl alcohol (BA), piperonyl alcohol (PA) and *p*-anisyl alcohol (AA), and the respective Hammett constants ( $\sigma_p$  and  $\sigma_m$ ).

Compound	Chemical structure	Substituent		Hammett constant ( $\sigma$ )	
		<i>para</i> -	<i>meta</i> -	$\sigma_p$	$\sigma_m$
BA		-H	-H	0.000	0.000
PA		-O <sub>2</sub> CH <sub>2</sub>	-O <sub>2</sub> CH <sub>2</sub>	-0.159	-0.159
AA		-OCH <sub>3</sub>	-H	-0.268	0.000
VA		-OH	-OCH <sub>3</sub>	-0.370	0.115

Overall, the results here presented indicate that the photocatalytic oxidation of aromatic alcohols under anaerobic conditions follows a characteristic and unique pathway depending on the nature and position of the substituents groups on the aromatic ring. On the other hand, the properties of the photocatalysts used on this type of reaction assume an important role for achieving high selectivity for aldehydes production.

### 3.4 Conclusions

Neat ZnO and composites made of ZnO and CNF prepared with different amounts of carbon phase (5 to 20 wt%) possess a significant photocatalytic activity and selectivity towards the synthesis of vanillin under 370 nm UV-LED irradiation.

The best performing catalyst was 10%CNF/ZnO, in which the presence of this amount of carbon phase was reflected in an effective increase of the surface area and efficient charge separation and transportation. The optimal load for this particular catalyst was found to be 0.75 g L<sup>-1</sup>, reflecting the optimal balance between photon absorption, suspension light scattering and substrate adsorption.

In the absence of oxygen, selectivity towards vanillin, either for ZnO or 10%CNF/ZnO is increased.

The role of CNF is to act as electron acceptor, decreasing the recombination rate of the photogenerated  $e^-/h^+$  pairs. Mechanistically, photogenerated holes at the surface of ZnO are responsible for the oxidation of vanillyl alcohol, while electrons at the CNF phase are available for reducing H<sup>+</sup> (from water and/or from alcohol dehydrogenation) to H<sub>2</sub>.

The photocatalytic system used proved to be about 2.5 times more selective than those reported in literature for the photocatalytic synthesis of vanillin.

The photocatalysts ZnO and 10%CNF/ZnO were also equally successful in the synthesis of other selected aromatic aldehydes.









# Chapter 4

## ***Photocatalytic synthesis of *p*-anisaldehyde by graphite-like carbon nitride-based materials***

The work presented in this chapter relies on the modification of graphite-like carbon nitride (GCN) through different techniques namely hard-templating, copolymerization and thermal post-treatment routes.

The GCN-based catalysts exhibited different morphological, electronic, and optical properties, depending on the modification procedure adopted.

The photocatalytic performance of all materials was tested on the conversion of *p*-anisyl alcohol (AA) into *p*-anisaldehyde (AAD), using UV and/or Vis radiation sources.

The mechanism of the reaction was also investigated by assessing the role of oxygen in the reaction.

The designed photocatalytic systems proved to be valuable alternatives to the conventional processes of the synthesis of AAD, achieving high values of conversion and yield, with a low energy demand.

### **This chapter is based on the following articles:**

R. A. Fernandes, M. J. Sampaio, J. L. Faria, C. G. Silva, Aqueous solution photocatalytic synthesis of *p*-anisaldehyde by using graphite-like carbon nitride photocatalysts obtained via the hard-templating route. *RSC Adv.*, 10 (2020), 19431-19442, reproduced by permission of Royal Society of Chemistry.

R. A. Fernandes, M. J. Sampaio, E. S. da Silva, H. Boumeriame, T. Lopes, L. Andrade, A. Mendes, J. L. Faria, C. G. Silva, Sustainable production of *p*-anisaldehyde and hydrogen by using a citric acid-modified carbon nitride optical semiconductor, *Appl. Catal. A: Gen.*, 609 (2021), 117912, reproduced by permission of Elsevier.



#### 4.1 Introduction

Graphite-like carbon nitride (here labelled as GCN) is a metal-free polymeric semiconductor constituted by tris-*s*-triazine units [70,240], which possesses a bandgap (2.7 eV) narrower than that of the reference photocatalyst: the titanium dioxide (3.0-3.2 eV) [241]. Thus, making it facile activation in a visible part of the electromagnetic spectrum, which represents a significant advantage concerning solar-driven processes [70,240]. In addition to its chemical and thermal stability, GCN also possesses suitable VB and CB for several redox reactions [242]. Bulk GCN presents a stacked 2D layered structure formed through  $sp^2$  hybridization of carbon and nitrogen atoms bounded by van der Waals forces [242]. This specific arrangement of carbon and nitrogen atoms promotes a  $\pi$ -conjugated structure, responsible for the photocatalytic activity of GCN [115]. However, the catalytic performance of this photocatalyst is negatively affected by its low surface area, high  $e^-/h^+$  recombination rate and lack of activity above 460 nm, being necessary to adopt strategies to overcome these limitations [92,115,242,243].

Templating routes have the ability to introduce morphological modifications in GCN [117–119,244–248], by using soft or hard templates, as consequence the physical properties as porosity, structure, morphology, surface area and size, can be tuned in order to improve the photocatalytic performance of the catalysts to a specific application [115].

Copolymerization approaches can also be adopted to enhance optical properties of GCN-based catalysts [124,125,249–255] through the extending of its  $\pi$ -conjugated system [115,256]. Therefore, the delocalization of the  $\pi$  electrons can be achieved by modifying and anchoring with aromatic groups or organic additives, as citric acid, barbituric acid,  $\beta$ -cyclodextrine, during the thermal treatment with GCN precursors to obtain catalysts with modulated intrinsic properties [124,125,126,249–255,257,258]. Also thermal exfoliation has been explored as an efficient route to tune the optical, morphological, and electronic properties of GCN [259–261]. During the heating process, the breakage of hydrogen bonds responsible for the aggregation between the layers of GCN lead to the splitting of the graphite-like layers [70,120,150,260] and also, to the introduction of defects on the surface of the catalyst [259,262,263], resulting in an enhancement of the photocatalytic activity.

## 4.2 Experimental

The main objective of this chapter is the development of GCN-based materials for the photocatalytic production of *p*-anisaldehyde, using highly efficient radiation sources. Therefore, the following subsections describe the main approaches used in the preparation of GCN photocatalysts.

### 4.2.1 Materials

Dicyandiamide (DCN, 99%), hexadecyltrimethylammonium bromide (CTAB, 99%), polyvinylpyrrolidone K30 (PVP K30), hydrochloric acid (HCl, 37%), silicon dioxide (SBA-15, 99.6%), *p*-anisaldehyde (AAD, 98%), benzoquinone (BQ, 98%), citric acid (CA,  $\geq 99.5\%$ ), chloroplatinic acid hydrate ( $\text{H}_2\text{PtCl}_6 \cdot x\text{H}_2\text{O}$ , 99.9%), barbituric acid (BA, 99%), 2-aminothiophene-3-carbonitrile (ATCN, 97%), 2-aminobenzonitrile (ABN, 98%) and ethylenediaminetetraacetic acid (EDTA,  $\geq 98\%$ ) were purchased from Sigma-Aldrich. Acetaldehyde ( $\text{C}_2\text{H}_4\text{O}$ ,  $\geq 99\%$ ), tetraethyl orthosilicate (TEOS, 99%) and formic acid ( $\text{HCO}_2\text{H}$ , 98%) were acquired from Fluka. Ammonium hydroxide ( $\text{NH}_4\text{OH}$ , 28%), *t*-Butyl alcohol (*t*-BuOH, 99%) and *p*-anisyl alcohol (AA, 98%) were obtained from Alfa Aesar. Sulfuric acid ( $\text{H}_2\text{SO}_4$ , 95-98%) was purchased from Labor and ethanol ( $\text{CH}_3\text{CH}_2\text{OH}$ , p. a.) was supplied from Panreac. Hydrofluoric acid (HF, 48%) and methanol ( $\text{CH}_3\text{OH}$ , 99.6%) were purchased from VWR<sup>TM</sup>. Titanium dioxide ( $\text{TiO}_2$ ) Aeroxide<sup>®</sup> P25 powder was supplied by Evonik and used as received. All the reagents were used without further purification. Ultra-pure water was obtained from a Direct-Q Millipore system.

### 4.2.2 Bulk GCN

The synthesis of bulk GCN was performed by thermal decomposition of DCN precursor as reported elsewhere [120]. Briefly, DCN was heated at  $2^\circ\text{C min}^{-1}$  up to  $550^\circ\text{C}$  in a muffle apparatus. The obtained yellow solid was washed with deionized water to remove unreacted precursor or impurities and then, dried overnight at  $100^\circ\text{C}$ .

### 4.2.3 Morphologically modified GCN

Morphologically modified GCN was obtained via the hard-templating route using three different methodologies as described below, leading to materials with distinct properties. The resulting GCN-based materials were labelled as urchin-like GCN (GCN-UL), 3D ordered macroporous GCN (GCN-OM) and mesoporous GCN (GCN-MP).

The GCN-UL was synthesized according to a previously reported methodology [118]. Firstly, silica (SiO<sub>2</sub>) template was prepared through the modified Stöber method [264]. For the typical synthesis of this template, 0.64 g of CTAB, 15 ml of acetaldehyde solution (40 wt%), and 12 ml of water were added and stirred at 27°C for 5 min. Then 2.8 ml of NH<sub>4</sub>OH (28 wt%) was quickly added and the mixture was stirred for 30 min. After this, 2.8 ml of TEOS was added into the solution and stirred for 24 h. The resulting brown mixture was filtered, washed with deionized water and dried at 60°C overnight. The SiO<sub>2</sub> template was then mixed with dicyandiamide in a mass ratio of 1:1. The mixture was placed in a crucible and the same thermal treatment used for producing bulk GCN was performed as described in section 4.2.2. The GCN-UL was washed several times with deionized water and dried at 100°C overnight.

The GCN-OM was prepared as previously reported [117]. For the synthesis of the silica nanospheres, two solutions were necessary: i) a solution containing 10 mL of TEOS in 50 mL of ethanol (solution A); and ii) a water-ethanol solution (1:2) prepared from an aqueous solution of NH<sub>4</sub>OH in which were added 50 mL of ethanol with vigorous stirring (solution B). Then, both solutions (A and B) were mixed and stirred at 40°C for 2.5 h. After the treatment, a solution containing 10 mL of TEOS, 2 g of PVP K30 and 40 mL of ethanol was added dropwise with vigorous stirring and left at 40°C for 2 h. Then, the mixture was left at room temperature overnight. Afterwards, the solution was centrifuged to align the structure and the solid dried at 100°C. Lastly, the aligned SiO<sub>2</sub> solid was calcined at 700°C for 6 h to remove residual reagents. Finally, 0.8 g of SiO<sub>2</sub> nanospheres were pre-treated with 10 mL of 1M HCl solution, then dried at 100°C. Afterwards, 2 g of dicyandiamide was mixed with the pre-treated SiO<sub>2</sub> nanospheres and the mixture subjected to the heating program of applied to produce GCN.

The synthesis of GCN-MP was performed by adding 2 g of dicyandiamide, 75 µL of concentrated sulfuric acid and 1 g of SBA-15 to a 50 mL of deionized water [248]. The suspension was sonicated for 30 min and stirred at 70°C for 6 h. After this, the mixture was filtered and dried at 100°C to obtain a white solid. The white solid was placed in a crucible into the furnace and underwent the heating program used to produce GCN. Finally, the material was washed with deionized water and dried at 100°C for 12 h.

All the GCN-based materials (GCN-UL, GCN-OM and GCN-MP) were post-treated with 4M HF for 72 h to remove their specific template and dried at 100°C.

#### 4.2.4 Citric acid-modified GCN

The citric acid-modified GCN was obtained through a thermal copolymerization route [251]. Briefly, 2 g of dicyandiamide was mixed with different amounts of citric acid (CA; 5, 10, 15, 20 and 25 mg). The mixture was placed into a crucible and subjected to the same thermal treatment used to produce bulk GCN. The obtained brownish solids were washed with ultra-pure water and dried at 100°C for 12 h. The catalysts were denoted as GCN-zCA, where z corresponds to the amount of CA (mg) used in the synthesis of each material.

#### 4.2.5 Copolymerized GCN

The copolymerized GCN was also obtained through thermal approach, using barbituric acid (BAr), 2-amino-3-carbonitrile (ATCN) and 2-aminobenzonitrile (ABN) as copolymerization agents [125,258,265]. Briefly, 2 g of dicyandiamide was added to 10 mL of ultra-pure water, followed by the addition of 0.05 g of one of the selected compounds (BAr, ATCN or ABN). Firstly, the suspension was mixed under magnetic stirring for 1 h at room temperature. Then, it was kept at 60°C until water evaporation. The solid residue was put into a crucible and submitted to the same thermal treatment as bulk GCN. The obtained materials were washed with ultra-pure water and dried at 100°C for 12 h. Depending on the copolymerization agent used, the catalysts were denoted as GCN-Z, where Z refers to the copolymerization agent (BAr, ABN and ATCN).

Both GCN and GCN-Z were subject to a second thermal treatment as described elsewhere [120]. Briefly, 0.95 g of each catalyst was put in a crucible and heated in a muffle furnace at 2°C min<sup>-1</sup> up to 500°C and the temperature was kept for 2 h. The post-treated catalysts were designed as GCN-Z-500, where Z refers to the copolymerization agent (BAr, ABN and ATCN).

#### 4.2.6 Thermally post-treated GCN

The thermally post-treated GCN was synthesized through a thermal procedure applied to bulk GCN. Briefly, 1 g of bulk GCN was put into a quartz tubular reactor and it was heated in a vertical furnace at 5°C min<sup>-1</sup> up to a certain final temperature (500 - 700°C) under a continuous nitrogen flow (80 mL min<sup>-1</sup>,  $T \sim 20^\circ\text{C}$ ,  $P = 1 \text{ atm}$ ). The desired temperature was kept for 2 h. The obtained solid was washed with deionized water and dried at 60°C overnight. The thermally post-treated catalysts were denoted GCN-



A-Z, where Z refers to the final temperature of heating treatment (500, 550, 600 and 620°C).

### 4.3 Characterization of the catalysts

The morphology of the materials was assessed by SEM, as described in Chapter 3, section 3.2.3.

The chemical composition of the materials was determined by elemental analysis. Carbon, nitrogen, and hydrogen (C, N and H) contents were determined in a Vario micro cube analyzer (Elementar GmbH), by combustion of the samples at 1050°C. Each sample was analyzed in triplicate.

Fourier transform infrared (FTIR) measurements (4000–600  $\text{cm}^{-1}$ ) were performed in a JASCO FT/IR-6800 spectrometer (JASCO Analytical Instruments, USA) equipped with a MIRacle™ Single Reflection ATR (attenuated total reflectance ZnSe crystal plate) accessory (PIKE Technologies, USA). The analyses were performed using 256 scans with a resolution of 4  $\text{cm}^{-1}$ .

The DR UV-Vis analyses and the determination of the bandgap energy of the materials were carried out as mentioned in Chapter 3, section 3.2.3.

The  $S_{\text{BET}}$  was determined as described in Chapter 3, section 3.2.3.

PL spectra were obtained at room temperature on a JASCO (FP 82000) fluorescence spectrometer with a 150W Xenon lamp as a light source using both excitation and emission bandwidth fixed at 2.5 nm. The excitation wavelength was set at 370 nm, and the emission was measured in the 380–650 nm range.

X-ray photoelectron spectroscopy analysis (XPS) was performed in a Kratos AXIS Ultra HAS equipment and Al monochromator operating at 15 kV (90 W) in hybrid mode. Binding energy values were referred to the C1s peak at 284.4 eV. The obtained spectra were analyzed and deconvoluted using the CasaXPS software.

X-ray diffraction (XRD) analysis of the powdered catalysts was carried out in a PANalytical X'Pert MPD instrument equipped with a X'Celerator detector and secondary monochromator (Cu Ka k = 0.154 nm, 50 kV, 40 mA; data recorded at a 0.017° step size, 100 s/step).

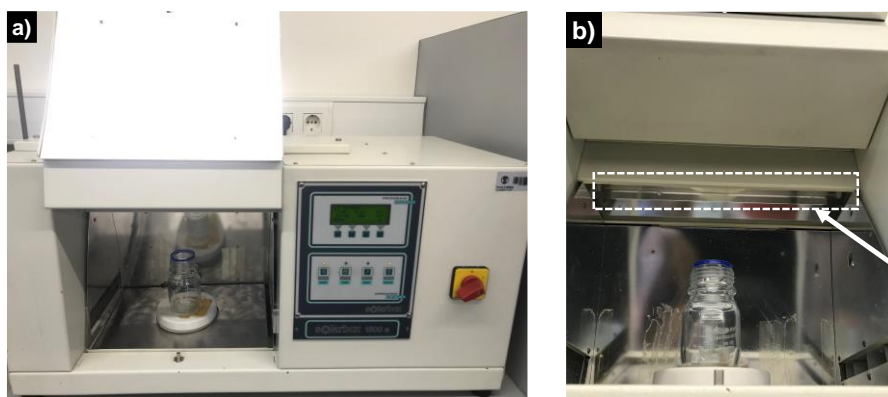
Photoelectrochemical characterization was performed using an electrochemical workstation ZENNIUM (Zahner Elektrik, Germany) controlled by Thales software package (Thales Z 2.0) in a conventional three electrode cell, using a 99.9% pure platinum wire (Alfa Aesar, Germany) as counter electrode and an Ag/AgCl/sat. KCl electrode (Metrohm, Switzerland) as reference. The cell was filled with 1.0 M  $\text{Na}_2\text{SO}_4$  aqueous electrolyte solution without additives in which the working electrode was

immersed. The working electrode was prepared on F-doped SnO<sub>2</sub>-coated glass (FTO glass). A mixture containing 5 mg of powder selected samples, 50  $\mu$ L of Nafion solution 5 wt%, 250  $\mu$ L isopropanol and 1 mL of deionized water was prepared and left under continuous stirring. The slurry was then spread onto FTO glass with a fixed area using Kapton tape. After air-drying, the electrode was annealed at 150°C for 30 min in air to improve adhesion.

The on/off photocurrent response plots were measured in ambient conditions and illuminated by sunlight provided by a class B solar simulator equipped with a 150 W Xenon lamp (Oriel, Newport, USA) and an AM 1.5 G filter (1 kW m<sup>-2</sup>, 25°C; Newport, USA) calibrated with a c-Si photodiode (Newport, USA). The transient photocurrent measurements were carried at an applied potential of 0.2 V vs. Ag/AgCl during 1000 s with pulses of 30 s light on followed by 30 s light off.

#### 4.4 Photocatalytic setup

The photocatalytic efficiency of the GCN-based materials was investigated in the synthesis of AAD through the oxidation of AA. The experiments were carried out in the same photocatalytic experimental setup presented in Chapter 3, section 3.2.4 (Scheme 3.1). Additional experiments were carried out under simulated solar light for 120 min, using a Solarbox 1500e system (CO.FO.MEGRA) with a nominal average light intensity of 50.0 mW cm<sup>-2</sup> (Scheme 4.1).



Scheme 4.1 a, b) Photographs of the photocatalytic setup, using a solar simulator as irradiation source. Dashed line and arrow indicate the position of the lamp.

In that case, the reactor was placed in the bottom center of the solar simulator and the suspensions were irradiated from the top. The catalyst charge was set as 0.75 g L<sup>-1</sup> and the reactions were performed under oxygenated (air) and deoxygenated (argon) atmospheres. A dark period of 30 min was performed to establish the adsorption-

desorption equilibrium (<2% of adsorption in all cases). In a typical experiment, the suspension was irradiated for 4 h and samples (0.30 mL) were periodically withdrawn to evaluate the AA and AAD concentrations. The nominal average irradiance of UV ( $\lambda_{max} = 370$  nm) and visible ( $\lambda_{max} = 412$  nm) LEDs was  $49.8 \text{ mW cm}^{-2}$  and  $45.0 \text{ mW cm}^{-2}$ , respectively and it was determined as described in Chapter 3, section 3.2.4. The reactor was filled with 50.0 mL of 0.50 mM AA aqueous solution and the reactions were carried out at room temperature (20°C) and without pH adjustment (ca. 5.4).

The determination of AA conversion ( $X$ ) and selectivity ( $S$ ) and yield ( $Y$ ) towards the AAD production was determined through the equations 3.1, 3.2 and 3.3, indicated in Chapter 3, section 3.2.5. For the reuse tests, the catalyst was recovered after each reaction by filtration, washed with ultra-pure water and dried at 60°C for 12 h.

Photocatalytic experiments in the presence of scavengers (1.0 mM) for the hydroxyl radical (*t*-BuOH), superoxide radical (BQ) and photogenerated holes (EDTA) were also performed with selected samples to assess the photocatalytic reaction pathway. As mentioned before, H<sub>2</sub> can be generated as by-product during the photocatalytic synthesis of organic compounds under specific reactional conditions. Therefore, selected catalysts were used for the H<sub>2</sub> evolution reactions. In that cases, 100 mL of an aqueous solution of EDTA or AA (0.02 M) were used as sacrificial electron donors. In addition, platinum (Pt) nanoparticles (3.0 wt%) were added to the suspension as co-catalyst. The synthesis of Pt nanoparticles followed a reported procedure [250]: an aqueous solution of dihydrogen hexachloroplatinate (IV) hexahydrate (60 mg in 20 mL of water) was added dropwise to a methanol solution containing L-ascorbic acid (600 mg in 180 mL of methanol). After this, the mixture was stirred at 90°C for 3 h under reflux. After cooling, the suspension was centrifuged and the solid washed twice with fresh methanol. The solid was then dried at room temperature and was resuspended in a certain volume of water. The reactor was saturated with nitrogen for 30 min prior to irradiation, to ensure the total removal of oxygen. Then, the suspensions were irradiated for 3 h and the H<sub>2</sub> evolution was monitored through gas chromatography (GC). For the reuse tests, the system was evacuated before each new cycle of 3 h and a certain amount of fresh sacrificial agent was added to the reactor.

#### 4.5 Analytical procedures

The determination of AA and AAD concentrations was carried out according to the procedure previously described in Chapter 3, section 3.2.5.

The evolved  $H_2$  was measured using an on-line gas chromatograph (Inficon Micro GC 3000, Agilent) equipped with a  $5\text{\AA}$  molsieve column and a micro-TCD detector, using argon as carrier gas.

## 4.6 Morphologically-modified GCN-based photocatalysts

### 4.6.1 Characterization

The morphology of GCN and GCN-structured materials was analyzed by SEM (Fig. 4.1).

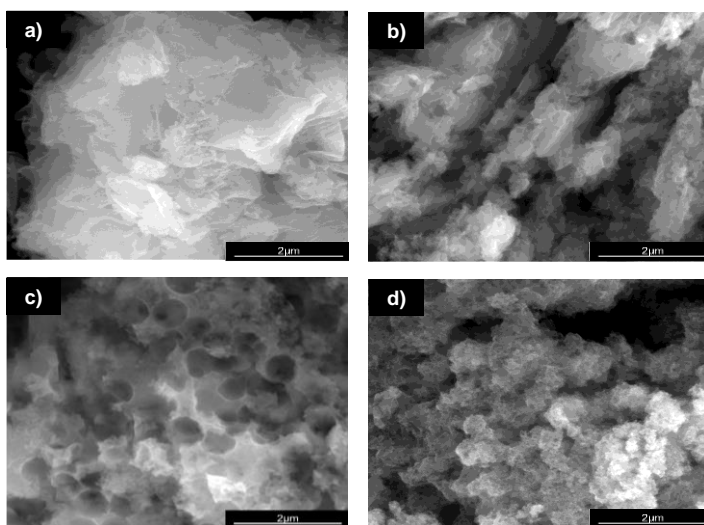


Fig. 4.1 SEM micrographs of a) bulk GCN, b) GCN-MP, c) GCN-OM and d) GCN-UL.

As already documented, bulk GCN materials are commonly characterized by compact structures, which contributes to the low  $S_{BET}$  [120,266]. In this work, the same morphology was observed (Fig. 4.1a), as well as low  $S_{BET}$  was found ( $7\text{ m}^2\text{ g}^{-1}$ ), which may indicate a limited number of active sites in the bulk GCN surface. The preparation of GCN-based catalysts through hard-templating has been reported as a route to change the morphology by increasing the surface area of the resulting materials [247]. The GCN-MP, GCN-OM and GCN-UL materials were synthesized using three different templates of  $\text{SiO}_2$ , the commercial mesostructured silica (SBA-15), core-shell  $\text{SiO}_2$  nanospheres and flower-like  $\text{SiO}_2$  nanoparticles, respectively. As displayed in Figs. 4.1b, c and d, the introduction of these templates in the process of synthesis of GCN induced a change on its morphology. In the case of GCN-MP, it is possible to observe a multilayer stacking structure (Fig. 4.1b), similar to the morphology of bulk GCN, some induced defects are also detected, which may indicate a mesoporous structure.

In terms of  $S_{BET}$ , the results revealed an increase of 57% ( $11 \text{ m}^2 \text{ g}^{-1}$ ) when compared to bulk GCN.

Regarding GCN-OM, the introduction of  $\text{SiO}_2$  nanospheres led to the detection of well-defined macropores on its surface, which are distinguishable in Fig. 4.1c. The preparation of GCN-based catalysts through hard-templating has been reported as a route to change the morphology by increasing the surface area of the resulting materials [117–119,264,267] as occurred in the case of the GCN-OM ( $20 \text{ m}^2 \text{ g}^{-1}$ ). In the case of GCN-UL, the particles are smaller (Fig. 4.1d), which is in line with an increase in the  $S_{BET}$  ( $28 \text{ m}^2 \text{ g}^{-1}$ ).

Besides, from SEM micrographs is also possible to infer that the morphological modifications occurred mainly on the surface of the catalysts, reinforcing the impact of hard-templating in the surface area of GCN, which was enhanced by the following order  $\text{GCN} (7 \text{ m}^2 \text{ g}^{-1}) < \text{GCN-MP} (11 \text{ m}^2 \text{ g}^{-1}) < \text{GCN-OM} (20 \text{ m}^2 \text{ g}^{-1}) < \text{GCN-UL} (28 \text{ m}^2 \text{ g}^{-1})$ .

The similarity of the FTIR-ATR spectra (Fig. 4.2) confirms that the base structure of the GCN materials is kept. The presence of an IR band at  $3000\text{--}3250 \text{ cm}^{-1}$  is due to the N—H stretching vibrations of primary and secondary amines (zone A, Fig. 4.2) [117,118,120,248]. The band at  $1500\text{--}1700 \text{ cm}^{-1}$ , is characteristic of the C—N stretching vibrations, while the  $1200\text{--}1400 \text{ cm}^{-1}$  band represents the aromatic C—N stretching (zone B, Fig. 4.2).

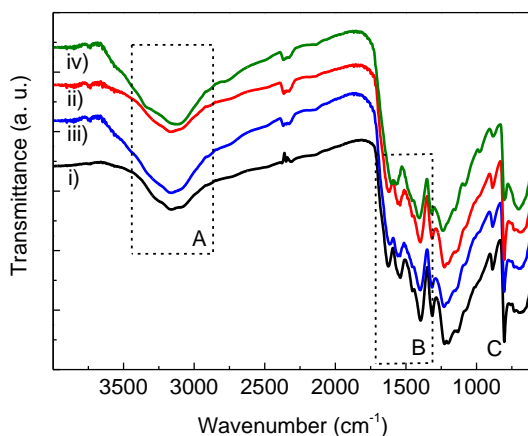


Fig. 4.2 FTIR-ATR spectra of i) GCN, ii) GCN-MP, iii) GCN-OM and iv) GCN-UL. Highlighted zones A, B and C denote characteristic IR bands of carbon nitride materials.

The sharp peak identifies the CN heterocycles of the triazine ring at around  $800 \text{ cm}^{-1}$  (zone C, Fig. 4.2) [117,118,120,248].

Analysis of the XPS spectra provided information on the elemental composition of the prepared materials (Fig. 4.3).

The C1s XPS spectra of bulk GCN and GCN-based catalysts (Fig. 4.3a) show how the binding energy of the carbon depends on the type of hybridization and nature of the main peaks detected for carbon (C1, C2, C3 and C4) in the deconvolution of the individual spectrum. The C1s binding energy at 284.4 eV (C1) is generally attributed to the impurity carbon, as in graphitic domains [268–271]. The binding energy at 286.0 eV (C2) is ascribed to  $sp^3$ -bonded defects on the GCN surface due to the amino functional groups (C—NH<sub>2</sub>) [119,120]. The dominant C3 peak located at 288.0 eV is assigned to the presence of  $sp^2$ -hybridized C atoms in N-containing aromatic rings (N—C=N) [118–120]. Between 293.0 and 294.0 eV is located the C4 peak, which is related to the  $\pi$  electron delocalization in melon heterocycles [118,246,272].

Concerning the N1s XPS spectra (Fig. 4.3b), it is possible to isolate four different binding energies (N1, N2, N3 and N4). The N1s energy of 398.6 eV (N1) is commonly ascribed to the  $sp^2$ -bonded nitrogen involved in triazine rings (C—N=C) [118,247].

The binding energy of 399.4 eV (N2) is attributed to the presence of tertiary N in N—(C)<sub>3</sub> structures, which corroborates the effective polymerization of dicyandiamide into GCN [118,247]. The N3 peak located at 400.4 eV is related to the presence of —NH and —NH<sub>2</sub> groups [120,247]. The relocation of positive charges in melon heterocycles and cyano groups is confirmed through the N4 peak at 404.4 eV [119,120].

The XPS analysis reinforces the previous FTIR-ATR results, showing that the incorporation of SiO<sub>2</sub> templates in the process of synthesis did not induce any chemical modification on GCN, with no additional element identified in the survey.

However, there are significant differences in the amounts of each of the extracted binding energies of the N1s XPS spectra concerning the GCN-UL and GCN samples. The ratio between N1 and N2 binding energies expresses the presence structural defects applied to the C—N plane, due to the presence of nitrogen vacancies that promote the conversion of C—N=C into N—(C)<sub>3</sub> [124,126,249,273,274]. The N1/N2 peak ratio follows the order GCN > GCN-MP > GCN-OM > GCN-UL (1.74, 1.42, 1.40 and 0.75, respectively). The observed decrease indicates the presence of nitrogen vacancies at  $sp^2$ -bonded nitrogen (N1) in the modified catalysts. It is the GCN-UL that presents the lowest ratio, which indicates the highest nitrogen loss at the N1 site. Additionally, the modified catalysts also present the highest contribution of N2 peak

and lower of N1 peak, being GCN-UL the catalyst with the highest and lowest value, respectively (Fig. 4.3). These observations indicate that GCN-UL presents a higher density of nitrogen-vacancy defects than the other modified catalysts [124,126,273,274].

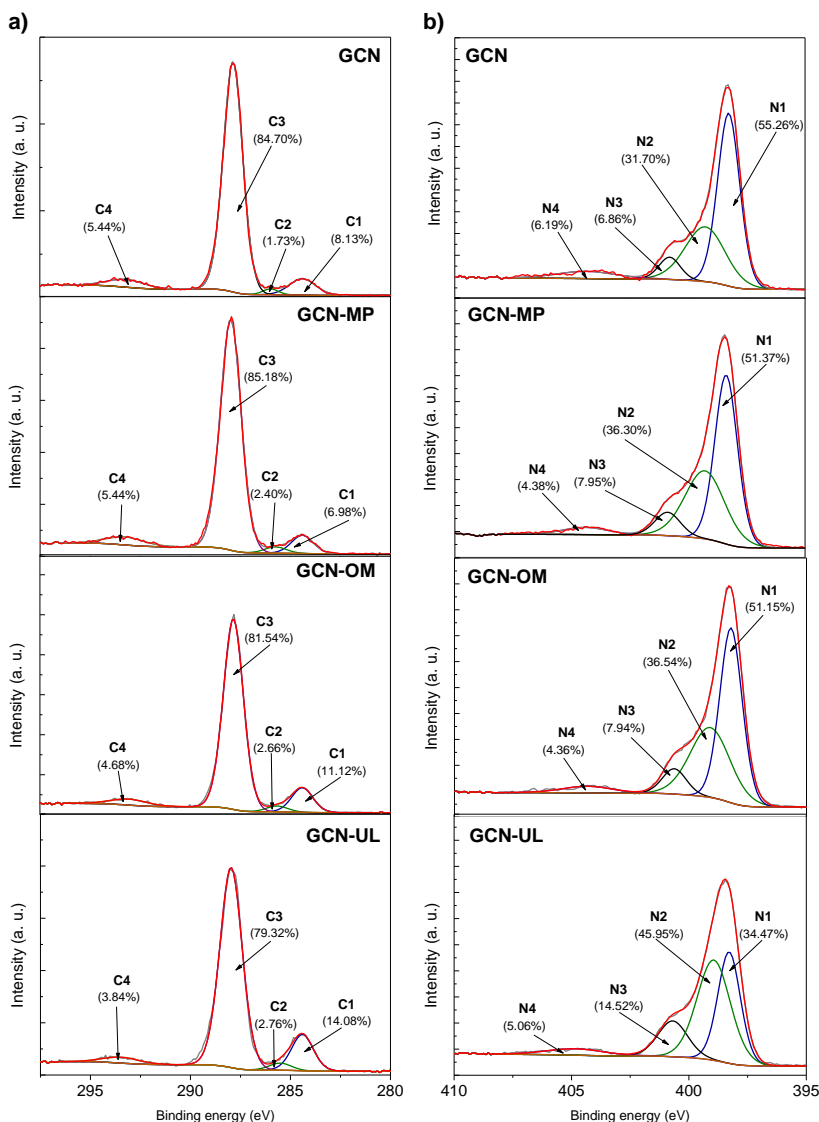


Fig. 4.3 a) C1s and b) N1s XPS spectra of GCN, GCN-MP, GCN-OM and GCN-UL.

By DRUV-vis and PL spectroscopies was accessed the electronic properties of GCN-based materials. The bulk GCN presents an absorption maximum at 370 nm resulting from the characteristic  $\pi$ - $\pi^*$  transitions owing to the heterocyclic aromatic system (Fig. 4.4a) [120,249]. Moreover, it presents also a characteristic high absorption band in the

visible spectral region ( $\lambda < 450$  nm, Fig. 4.4a) corresponding to the bandgap transition [120]. The spectrum of GCN-MP is very similar to that of bulk GCN. In the case of GCN-OM and GCN-UP, the low wavelength resolution is lost. However, new important features are visible in their spectra. For GCN-OM there is a significant blue shift of the spectrum, that will influence the bandgap of this photocatalyst. On the other hand, for GCN-UL there is a tail absorption that extends to the visible part of the spectrum.

The  $E_g$  for each of the photocatalysts was determined by the corresponding Tauc plot (inset Fig. 4.4a). The bulk GCN holds a bandgap energy of 2.86 eV, which is in agreement with the literature [115,120,275]. A similar bandgap was observed for GCN-MP (2.88 eV), while a shift towards higher values of  $E_g$  was observed for GCN-OM and GCN-UL (2.99 and 3.00 eV, respectively). This variation may be caused by the quantum size effects, which are due to the change in the electronic structure of the elements constituting GCN with decreasing of their size [276,277].

The PL spectra of bulk GCN and the GCN-based materials (Fig. 4.4b) were obtained at room temperature with excitation at 370 nm.

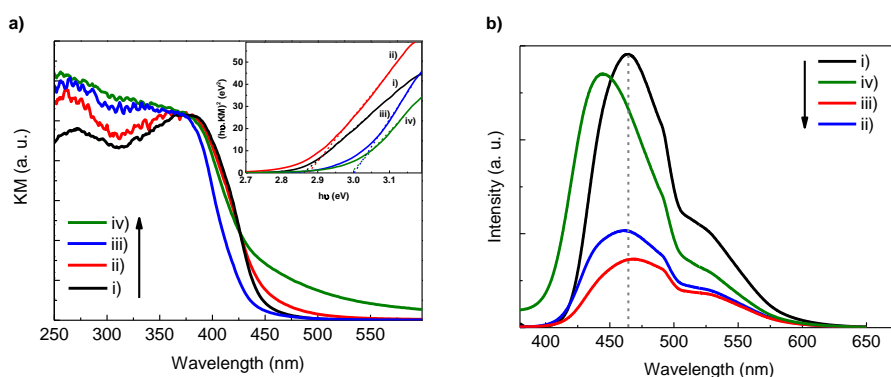


Fig. 4.4 a) DRUV-vis spectra (inset shows the respective Tauc plot) and b) solid state PL spectra of i) bulk GCN, ii) GCN-MP, iii) GCN-OM and iv) GCN-UL. Dashed line indicates the wavelength of maximum PL intensity for bulk GCN.

As shown in Fig. 4.4b, the incorporation of  $\text{SiO}_2$  templates decreases the intensity of the photoluminescence of the photocatalysts. The high luminescence intensity of GCN materials is usually related to the high recombination rate between the photogenerated  $e^-/h^+$  pairs, which can be due to the inefficient separation between these charge carriers, leading to low activities in photocatalytic applications [278]. The quenching detected in the emission of light in the form of luminescence of GCN-UL, GCN-MP and GCN-OM may indicate an improved  $e^-/h^+$  separation efficiency and an extended charge carrier lifetime [279]. Another important aspect concerning the PL spectra of



the synthesized materials is the wavelength of maximum intensity peak. In the case of GCN, the maximum of luminescence occurs at 468 nm (Fig. 4.4b). A shift to lower wavelengths occurred to GCN-UL and GCN-OM (444 and 461 nm, respectively), and a slight shift to higher wavelengths (489 nm) was verified in the case of GCN-MP (Fig. 4.4b). The blue shift observed in the wavelength of the maximum of PL intensity of GCN-UL and GCN-OM is in line with the variation also observed in  $E_g$ .

#### 4.6.2 Photocatalytic results

The designed photocatalysts were used in the controlled oxidation of AA to AAD in aqueous solution using LED light sources.

Generally, the photocatalytic synthesis of aldehydes from the corresponding alcohols is performed under air saturation, once the presence of dissolved oxygen in the reaction medium allows the generation of ROS, which have a substantial contribution to the oxidative pathway [280]. However, the oxidation of alcohols by ROS is a highly unselective route, leading to the production of side-products and reducing the selectivity of the photocatalytic process. Working under an inert atmosphere, using argon or nitrogen, limits the oxidation to the photogenerated holes, forcing it to the valence band of the semiconductor as already reported in literature [92].

Using the GCN-based photocatalysts, the synthesis of AAD in the absence of oxygen, performed with very high conversions and yields (Fig. 4.5).

The morphological modifications produced in the GCN surface promote not only an increase in the AA conversion rate (Fig. 4.5a) but also an enhancement in the yield of AAD (Fig. 4.5b), compared to the bulk GCN material.

The bulk GCN reached 20% of AA conversion, while the modified materials (GCN-MP, GCN-OM and GCN-UL) achieved 36%, 44% and 64%, respectively (Fig. 4.5c) after 240 min of reaction. In terms of AAD synthesis, it was found a maximum concentration of 0.08 mM after 240 min of reaction with the bulk GCN material (Fig. 4.5b). Concerning the GCN-based materials, the concentration of AAD duplicated to GCN-MP (0.15 mM) and triplicated to GCN-OM and GCN-UL (0.27 mM) in the same reaction time (Fig. 4.5b).

According to the results obtained both in AA oxidation and in AAD production, the photocatalytic performance of GCN-based catalysts increases by the following order: GCN < GCN-MP < GCN-OM < GCN-UL. This relation was also observed in the surface area value (Chapter 4, section 4.6.1). It is well established in the literature that in heterogeneous photocatalytic processes the specific surface area can significantly affect the efficiency of the catalysts, with a highly defective surface area resulting in a

higher surface area and, consequently, in more active sites available for reactivity between the molecules and the catalyst surface [117–119,247,248,281].

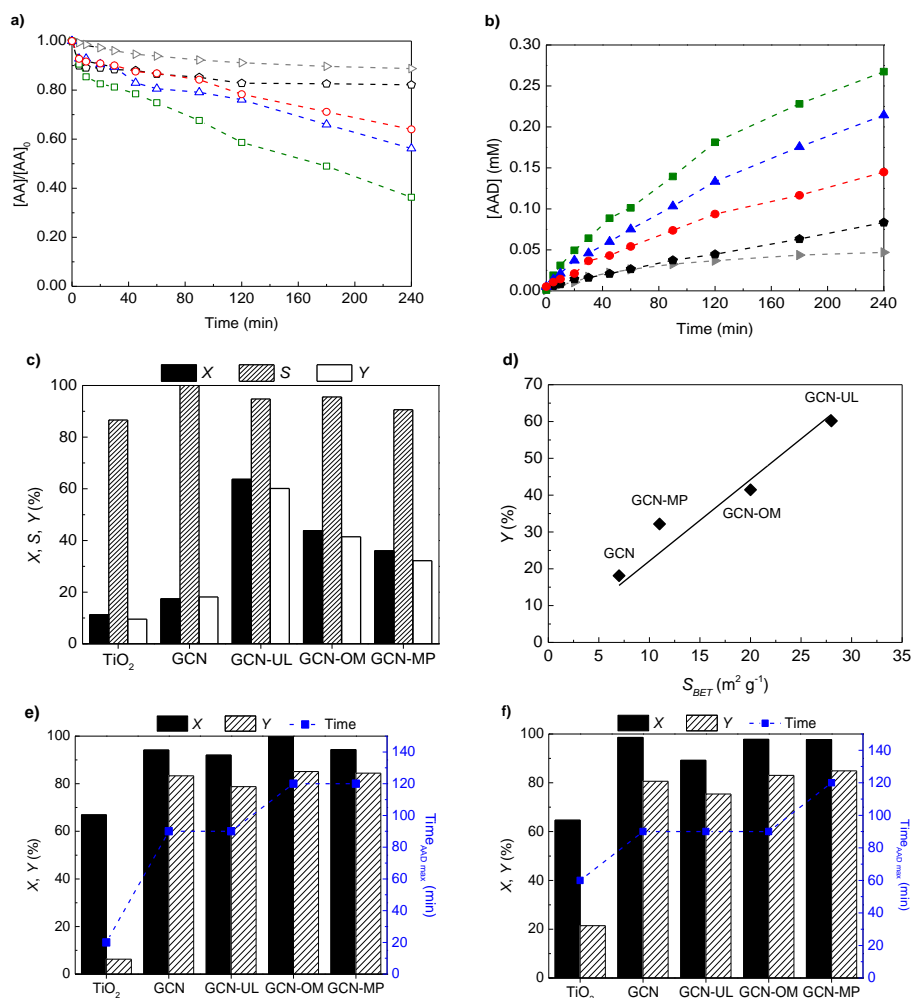


Fig. 4.5 a) Normalized concentration of AA and b) AAD using GCN ( $\diamond$ ,  $\blacklozenge$ ), GCN-MP ( $\circ$ ,  $\bullet$ ), GCN-OM ( $\Delta$ ,  $\blacktriangle$ ), GCN-UL ( $\square$ ,  $\blacksquare$ ) and TiO<sub>2</sub> P25 ( $\triangleright$ ,  $\blacktriangleright$ ) along 240 min reaction under deoxygenated conditions. c) X, S and Y using the photocatalysts under deoxygenated conditions after 240 min of irradiation. d) Effect of  $S_{BET}$  in the photocatalytic performance of all catalysts. Solid line represents the linear fitting ( $r^2 > 0.98$ ). Reaction time of maximum AAD concentration ( $\blacksquare$ ) and the respective values of X and Y, using the GCN-based photocatalysts under oxygenated conditions, using UV-LED (e) and visible-LED (f) irradiation.

As previously discussed, the morphological modifications induced on the surface of GCN-based catalysts led to an increase in their  $S_{BET}$ . The defects introduced on the

surface of the catalysts (as confirmed by SEM analyses, Fig. 4.1) can act as active sites, enhancing the oxidation of organics, while the reduced particle size maximizes the surface contact ratio, which usually leads to more efficient systems [118]. Correspondingly, the presence of these defects enhances the performance of the photocatalysts, by acting as active sites for the photogeneration of  $e_r^-$  and  $h_r^+$  in the conduction and valence bands, respectively [124,126,249,273].

By introducing surface modifications, the yield ( $Y$ ) increases from 18% (GCN) to 32% (GCN-MP), 42% (GCN-OM) and 60% (GCN-UL) over 4 h reaction (Fig. 4.5c).

The higher efficiency of GCN-based materials seems to indicate that the morphological and textural properties are responsible for the enhancement of the GCN-based materials for AAD production. In fact, the relation between the  $S_{BET}$  of GCN-based materials and their photocatalytic performance on the production of AAD seems to be linear, with the increase of  $Y$  with the increase in  $S_{BET}$  (Fig. 4.5d). Moreover, the higher amount of nitrogen vacancies detected by XPS analysis can also contribute to the activity enhancement of these photocatalysts, due to electron relocation [153].

Since for field applications working under air is preferable, the catalysts were tested under those conditions (Fig. 4.5e). Not surprisingly, the conversion of AA increased in the presence of oxygen, achieving more than 95% of  $X$  after 120 min of reaction for all GCN-based catalysts (Fig. 4.5e). The increase in the conversion of AA combined with the high selectivity (above 80%) for the GCN-based catalysts significantly increases the yield of the photocatalytic production of AAD under air saturation (Fig. 4.5e). Owing to the presence of oxygen the peak for AAD yield was reached at significantly reduced reaction times (between 90 and 120 min, Fig. 4.5e), compared with that under an argon atmosphere, in which the production of AAD was continuously increasing over 240 min of reaction (Fig. 4.5b).

The results under oxygenated conditions can be ascribed to the highly oxidative species, such as hydroxyl and superoxide radicals, when compared to the photogenerated  $h_r^+$ . Depending on the photocatalysts properties and reaction conditions, when ROS are present in the medium, the oxidation of organic compounds seem to be widely enhanced [153], and thus  $h_r^+$  acting as a secondary oxidative route. Thus, the presence of oxygenated species on the reaction medium for AAD production seems to hide the positive impact of the morphological and textural modifications in the photocatalytic performance of GCN-based materials.

One of the most attractive characteristics of GCN-based materials is their ability to absorb light in the visible range, unlike  $TiO_2$  P25 [214]. Following the results obtained

under air atmosphere and UV-LED irradiation ( $\lambda_{max} = 370$  nm), the efficiency of GCN-based catalysts was evaluated under air atmosphere but using visible LEDs emitting at 412 nm (Fig. 4.5f).

The photocatalytic synthesis of AAD through the oxidation of AA under visible light irradiation kept the higher values of  $X$  and  $Y$ , reaching more than 90% and 75%, respectively for all GCN-based materials (Fig. 4.5f), without compromising selectivity (> 80%). The SiO<sub>2</sub> templates incorporated during the synthesis procedure of structured GCN catalysts may promote multiple scattering and slow photon effects, responsible for improving inner light reflection [118,248,282,283]. As displayed in Figs. 4.5a-c and e, the commercial TiO<sub>2</sub> P25 exhibits slight efficiency compared with the GCN-based catalysts, presenting lower AA conversion and selectivity to AAD. Besides, under visible light irradiation (Fig. 4.5f), the TiO<sub>2</sub> P25 also showed much lower efficiency for AA conversion, which was already expected since TiO<sub>2</sub> P25 presents residual visible-light absorption capacity.

### 4.6.3 Reaction pathway

Based on the described results, the photocatalytic oxidative synthesis of AAD from AA depends on the reduction/oxidation properties of the templated GCN materials. The reaction can either proceed by the oxidative channel of the photocatalyst, using the photogenerated holes as oxidation agent or through the reductive channel, using ROS generated in the conduction band as the oxidation agent.

To investigate both possibilities, GCN-UL was used as probe photocatalyst under UV-LED illumination (Fig. 4.6).

Because of the nature of the photocatalyst, the participation of HO• radicals as oxidative ROS species is expected to be irrelevant [284]. The addition of *t*-BuOH did not change the conversion and selectivity of the reaction significantly (Fig. 4.6). A slight decrease was observed in the rate as the time for conversion increased somewhat.

Adding EDTA (an  $h^+$  scavenger) the effect on the final conversion and selectivity was similar to that of *t*-BuOH, however, the rate was decreased by more than two times as the time for final conversion went from 90 to 180 min. It follows that there is an apparent dependency on the heterogeneous conversion of AA by the photogenerated holes of the GCN-UL photocatalyst.

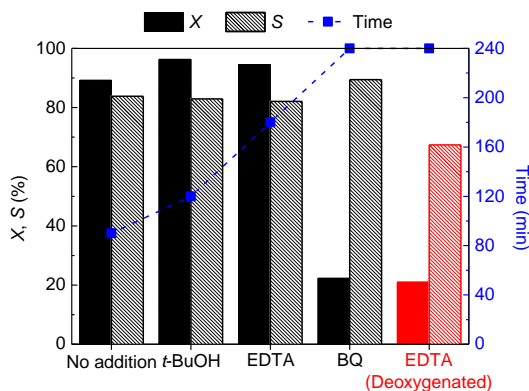


Fig. 4.6 Effect of scavengers in the photocatalytic performance of GCN-UL under air (black columns) and argon (red columns) atmospheres, using a UV-LED irradiation source. The X and S values are determined to the maximum of AAD production, with the indication of the respective reaction time (■).

Finally, in the presence of benzoquinone (BQ, a  $O_2^{\bullet-}$  scavenger) the reaction was significantly slowed down: it took 240 min to reach a little over 20% conversion.

Despite the oxidative channel of the GCN being important, there is no doubt that the  $O_2^{\bullet-}$  radicals are determinant to the reaction mechanism. Scavenging the holes (with EDTA) in the absence of oxygen (therefore no  $O_2^{\bullet-}$ , thus a double scavenging experiment) led to a result similar to the one obtained in the presence of BQ (Fig. 4.6). The photocatalytic synthesis of aromatic aldehydes both in the presence and absence of oxygenated species is already mentioned in the literature [106,107,153,240,285]. The presented observations confirm those reports and can be outlined by the proposed mechanism (Fig. 4.7).

The photocatalytic synthesis of alcohols described in literature is mainly concerned with  $TiO_2$ -assisted photocatalysis, following basically two mechanisms: direct oxidation by photogenerated holes or bulk oxidation through  $HO^{\bullet}$  radical [286]. Due to the nature of GCN-UL and the reported scavenging experiments, the involvement of the  $HO^{\bullet}$  radical is ruled out. In this case, the main mechanism is based in the direct oxidation on the photogenerated holes on the GCN-UL (Fig. 4.7B), and to the indirect oxidative  $H_2O_2$  elimination by the superoxide radical anion  $O_2^{\bullet-}$  (Fig. 4.7A).

The photogenerated excited electron  $e^-$  occurring at the conduction band reacts with the adsorbed molecular oxygen  $O_2$ , to generate the  $O_2^{\bullet-}$  which in the presence of the AA produces a charge separated dehydrogenated radical anion of the AA and hydrogen peroxide  $H_2O_2$ . Oxidative electron transfer to the photogenerated hole of the valence band of GCN-UL results in the corresponding AAD formation (Fig. 4.7A).

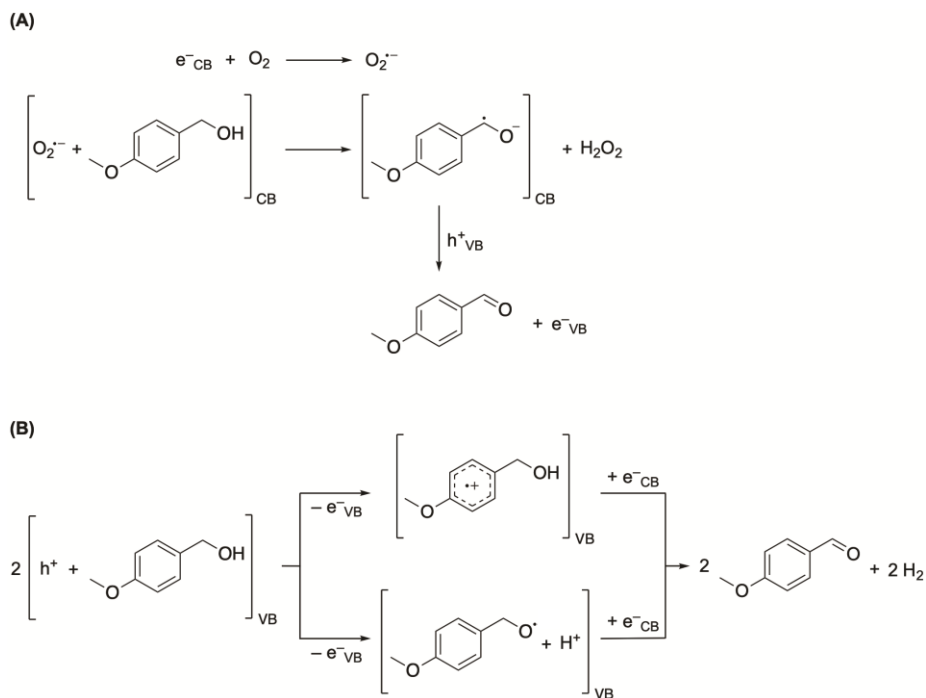


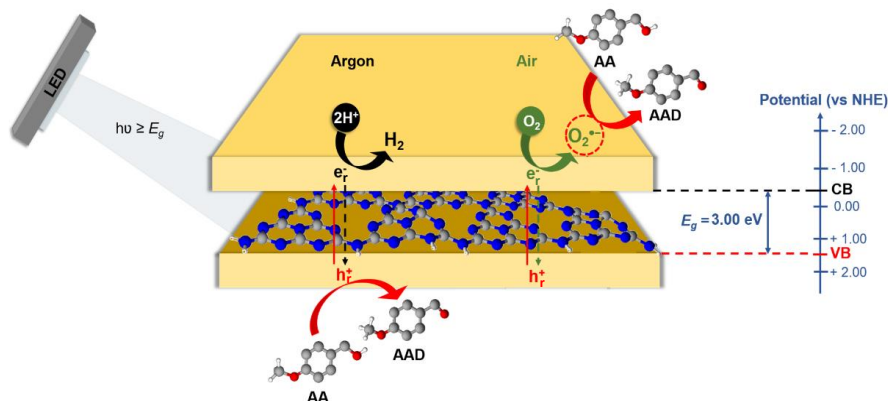
Fig. 4.7 Possible reaction mechanism for the equilibrated photocatalytic cycle of AA selective oxidation to AAD over the GCN-UL photocatalyst, starting at the reductive channel (A) or, in alternative, at the oxidative channel (B).

Oxidation of the adsorbed AA molecule directly on the photogenerated holes at the valence band of the GCN-UL leads to any of two, the formation of the AA radical cation, or the deprotonated AA radical (Fig. 4.7B). Either oxidized species adsorbed over the photoexcited GCN-UL will accept back an electron to produce the AAD and molecular hydrogen (Fig. 4.7B).

Each of the pathways is a very beautiful example of a closed path oxidation/reduction mechanism, or vice-versa, occurring on the surface of the photoexcited GCN-UL photocatalyst. The driving force for such an efficient process is the natural recombination of the photogenerated electrons and holes. That steep kinetic control also provides the means to the controlled reaction, preventing further oxidation the corresponding carboxylic acid.

In general, for these GCN materials, it can be disguise two operative pathways: one prevalent in deoxygenated conditions, which runs effectively through the oxidative channel were AAD is mostly produced directly through the photogenerated holes; the other is running on the reductive channel, in the presence of molecular oxygen (air conditions), using the effectively generated  $O_2^{\cdot-}$  by indirect oxidation in the conduction

band (Scheme 4.2). Briefly, upon UV-LED illumination ( $\lambda_{\text{max}}=370$  nm), photogenerated  $e^-/h^+$  pairs occur in the surface of the GCN-UL, providing the redox channels for the reactions. In the absence of oxygen,  $h^+$  in the VB is the only responsible for the conversion of AA. Under these conditions, the photogenerated  $e^-$  in the CB leads to the reduction of  $H^+$  to  $H_2$ .



Scheme 4.2 Diagram of photocatalytic conversion of AA into AAD under deoxygenated and oxygenated conditions, using GCN-UL as photocatalyst and UV-LED as light source.

On the other hand, in the presence of oxygen, the photogenerated  $e^-$  in the CB leads to the formation of  $O_2^{\cdot-}$  radicals. These radical species, together with the photogenerated  $h^+$  on the VB, seems to play the leading role on the high efficiency for AAD production under oxygenated conditions.

## 4.7 Citric-acid modified GCN-based catalysts

### 4.7.1 Characterization

The morphology of GCN-zCA catalysts was evaluated by SEM analyses (Fig. 4.8). For comparison purposes, a SEM image of bulk GCN is also shown (Fig. 4.8a). As previously mentioned, bulk GCN presents a highly stacked structure, with solid aggregates of graphite-like layers (Fig. 4.8a) [150,249,250,287]. SEM micrographs of CA-modified catalysts (Figs. 4.8b-f) reveal the presence of surface porosity (indicated by the arrows in Fig. 4.8), suggesting the occurrence of defects in the GCN polymeric network [117,118,249]. This holey texture can be attributed to the pyrolysis of citric acid during the thermal polymerization process, which occurs at temperature between 150 and 250 °C, causing the rupture of the GCN interlayer bonds [288,289].

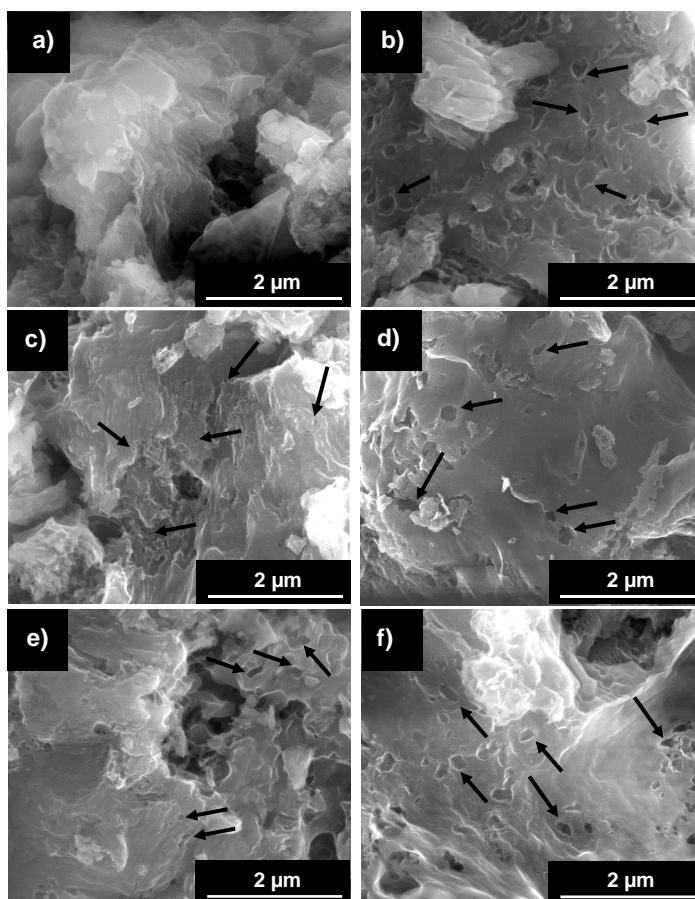


Fig. 4.8 SEM micrographs of a) GCN, b) GCN-5CA, c) GCN-10CA, d) GCN-15CA, e) GCN-20CA and f) GCN-25CA. Black arrows indicate surface defects.

The optical properties of citric acid-modified catalysts were assessed by DR UV-vis (Fig. 4.9) and PL spectroscopies (Fig. 4.10).

The citric acid incorporation promoted a change in the catalysts color, from yellow (bulk GCN) to brown (GCN-zCA) (Fig. 4.9a), in line with the expanded absorption mostly in the 450 to 700 nm range (Fig. 4.9b) [249,251]. The higher the amount of citric acid used in the synthesis, the darker the final material is, with a progressive increase in the absorption tail (Urbach tail, highlighted zone in Fig. 4.9b) in the visible spectral region [153,249,251,290].



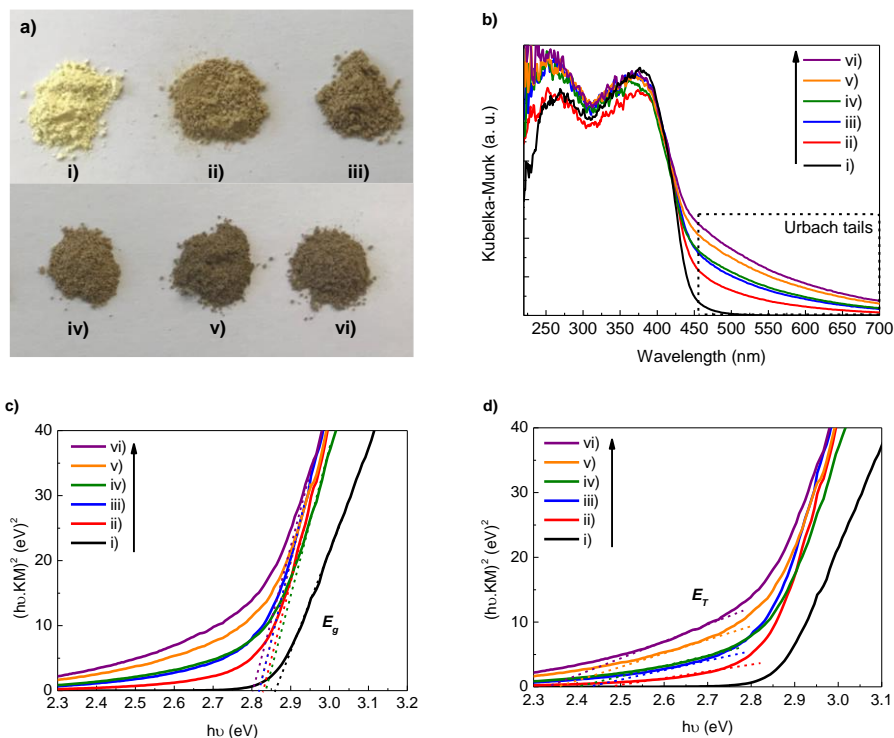


Fig. 4.9 a) Photograph, b) DR UV-Vis spectra, c) bandgap energy ( $E_g$ ) and d) transition energy ( $E_\tau$ ) determined from the respective Tauc plots for i) GCN, ii) GCN-5CA, iii) GCN-10CA, iv) GCN-15CA, v) GCN-20CA and vi) GCN-25CA.

The Urbach tail is usually associated to the presence of mid-gap states located within the bandgap [249,290–293], being ascribed to  $n-\pi^*$  electronic transitions involving the nitrogen lone pairs of electrons in heptazine and s-triazine rings, that are promoted by the defective structure of GCN-zCA catalysts [258,293,294]. These mid-gap states may favor the separation of photogenerated  $e^-/h^+$ , increase the lifetime of the charge carriers and prevent their recombination [273,292,293]. The existence of the Urbach tail in the absorption spectra indicate that the materials may absorb photons with lower energy than the  $E_g$  [249,273,295]. The transition energy ( $E_\tau$ ), that is associated to the presence of the Urbach tails (Fig. 4.9b), was determined through Tauc plot analysis (Fig. 4.9d). The values of  $E_\tau$  decreased from 2.49 eV to 2.35 eV with an increase in the amount of CA (Table 4.1). The values of  $E_g$  were also determined through Tauc plot analysis (Fig. 4.9c). A slightly decrease was noticed from 2.86 eV (bulk GCN) to 2.80 eV (GCN-25CA) (Table 4.1).

Table 4.1 Bandgap energy ( $E_g$ ), transition energy ( $E_T$ ) and atomic percentage of carbon and nitrogen of GCN and GCN-zCA catalysts ( $z = 5, 10, 15, 20, 25$ ).

Catalyst	$E_g$ (eV)	$E_T$ (eV)	C (%) <sup>*</sup>	N (%) <sup>*</sup>	C/N
<b>GCN</b>	2.86	n.a.	44.3	53.6	0.826
<b>GCN-5CA</b>	2.83	2.49	45.3	51.8	0.875
<b>GCN-10CA</b>	2.82	2.43	45.2	52.7	0.858
<b>GCN-15CA</b>	2.84	2.41	44.8	52.7	0.850
<b>GCN-20CA</b>	2.82	2.37	46.0	52.2	0.881
<b>GCN-25CA</b>	2.80	2.35	45.4	52.2	0.870

n.a.: not applicable; <sup>\*</sup> obtained from XPS analysis

PL measurements were performed to further evaluate the electronic modifications induced by including CA in the synthesis of GCN materials. PL emission spectra of all materials were obtained upon excitation at 370 nm at room temperature (Figs. 4.10a and b), while excitation spectra were recorded with emission wavelength set at 463 and 528 nm (Figs. 4.10c and d, respectively).

The PL emission spectrum of GCN reveals a strong emission peak at 463 nm (Fig. 4.10a) resulting from direct electron-hole recombination [249,296]. By adding citric acid, the fluorescence intensity is drastically quenched (Fig. 4.10a), indicating inhibition of the recombination of the photogenerated charge carriers. Therefore, the defect sites formed through the addition of citric acid may act as trapping centers, allowing the relocalization of the charge carriers into the carbon nitride skeleton, thus promoting their efficient separation, efficient surface transfer, and improving the photoefficiency of the materials [242].

Upon normalization of the PL emission spectra (Fig. 4.10b), the modified materials show an increase in the intensity of the emission band with a maximum centered at 528 nm (Z1). This more protruding band of the modified materials may be ascribed to the activation of  $n-\pi^*$  transitions involving the nitrogen lone pair electrons in the carbon nitride structure, resultant from a distorted structure owing to the presence of defects, as reported in literature [249,296]. These results are consistent with the Urbach tails observed in the DR UV-vis spectra (Fig. 4.9b) and with the excitation spectra of GCN and GCN-modified catalysts at 463 and 528 nm (Figs. 4.10c and d). The excitation

spectra of all materials recorded at 463 nm (Fig. 4.10c) reveal three maxima with wavelengths at 276, 371 and 425 nm. The first two are related with its maximum absorption, while the last is related with the band edge (Fig. 4.9b).

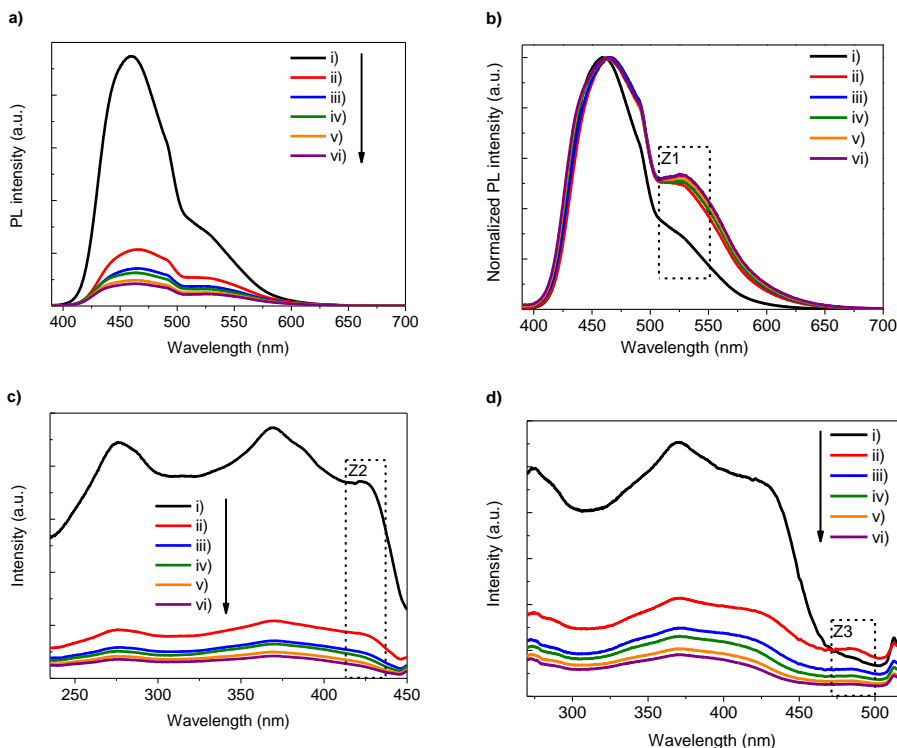


Fig. 4.10 a) PL emission spectra and b) normalized PL emission spectra under excitation at 370 nm of i) GCN, ii) GCN-5CA, iii) GCN-10CA, iv) GCN-15CA, v) GCN-20CA and vi) GCN-25CA. Excitation spectra of all catalysts under emission at c) 463 nm and d) 528 nm. Highlighted zones Z1, Z2 and Z3 indicate the most relevant differences between the spectra.

As for the excitation spectra recorded at 528 nm (Fig. 4.10d), the CA-modified materials present a new excitation band at 488 nm (Z3), in addition to the three bands observed in the excitation spectra recorded at 463 nm (Fig. 4.10c). The new band may be related with the presence of mid-gap states (Fig. 4.9b) due to the existence of stronger  $n-\pi^*$  transitions in modified catalysts that are promoted by nitrogen vacancies and by the porosity induced at the materials surface. As so, the PL results support the assumption of a new electron transfer pathway involving lower-energy photon excitation, in which the migration and separation of the charge carriers to the surface of the catalyst is enhanced.

The surface chemistry of CA-modified GCN catalysts was assessed by XPS analysis (Fig. 4.11 and Table 4.1). The XPS analysis of bulk GCN was also presented for comparison purposes. The XPS survey of all catalysts confirmed that they are mostly composed of nitrogen and carbon. A minor peak was also identified at 530.9 eV due to the presence of residual oxygen from adsorbed water [249,297]. The atomic analysis of the catalysts denoted a slight decrease in the nitrogen content on the surface of all modified catalysts (Table 4.1). Moreover, all GCN-zCA materials present a higher C/N atomic ratio than bulk GCN (Table 4.1). The increase in the C/N atomic ratio may be ascribed to the presence of nitrogen vacancies in GCN framework rather than C-doping, as determined by comparing the N1/N2 peak ratio in the XPS spectra of bulk and modified GCN materials [124,153,249,274,290].

The deconvolution of C1s and N1s spectra (Figs. 4.11a and b) was quite similar to the previous results presented in Fig. 4.3, section 4.6.1, with C1, C2, C3 and C4 peaks in the case of C1s spectra and N1, N2, N3 and N4 in the N1s spectra. Although no additional peak was identified, a shift of C3, N1 and N3 peaks to lower binding energies was observed for GCN-zCA materials when compared to GCN, probably due to electron redistribution on the graphitic ring [153,249,251,290].

The N1/N2 peak ratio is of 1.74 (GCN), 1.74 (GCN-5CA), 1.61 (GCN-10CA), 1.44 (GCN-15CA), 1.26 (GCN-20CA) and 1.40 (GCN-25CA). The lower the N1/N2 ratio, the highest is the prevalence of nitrogen vacancies at  $sp^2$ -bonded nitrogen (N1) [124]. Thus, it can be inferred that among all the materials GCN-20CA presents the highest amount of nitrogen vacancies. Moreover, it is also possible to verify that the modified catalysts present higher contribution of the N2 peak and lower contribution of the N1 peak than bulk GCN, being also GCN-20CA the catalyst with the highest and lowest value, respectively (Fig. 4.11b). These observations suggest that GCN-20CA presents higher density of nitrogen-vacancy defects than the other modified catalysts [124,126,273,274].

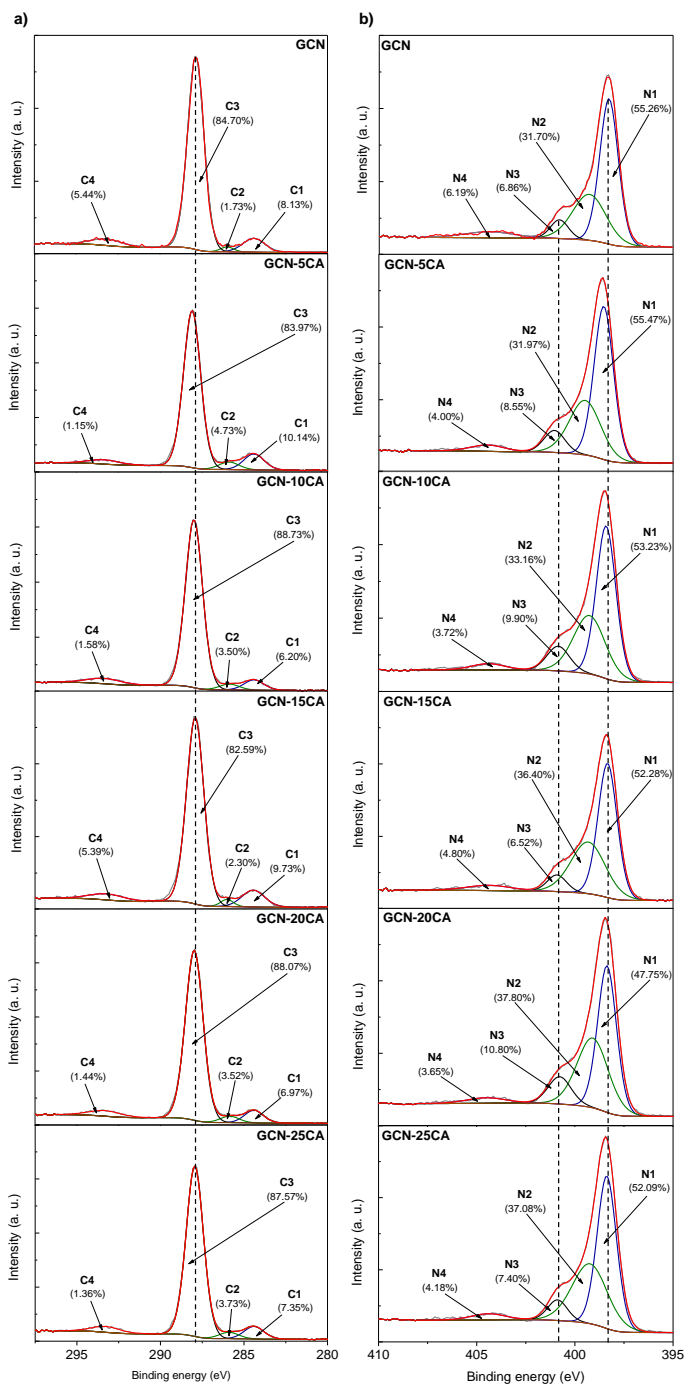


Fig. 4.11 (a) C1s and (b) N1s XPS spectra of GCN and GCN-zCA materials (z = 5, 10, 15, 20, 25). Dashed lines indicate the shifted peaks.

FTIR analysis of GCN-zCA (Fig. 4.12), revealed that the introduction of CA did not produce any significant change in the base structure of GCN.

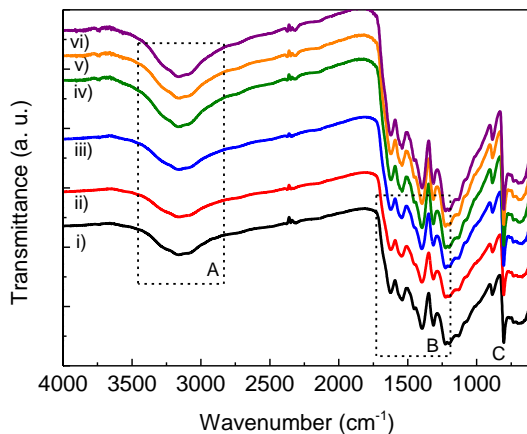


Fig. 4.12 FTIR-ATR spectra of i) GCN, ii) GCN-5CA, iii) GCN-10CA, iv) GCN-15CA, V) GCN-20CA and vi)GCN-25CA. Highlighted zones A, B and C denote characteristic IR bands of carbon nitride materials.

All catalysts present similar spectra, presenting the same characteristic IR bands of GCN-based materials, as previously observed in Fig. 4.2, section 4.6.1.

#### 4.7.2 Photocatalytic results

The photocatalytic efficiency of GCN and GCN-zCA materials was assessed through the photocatalytic oxidation of AA to AAD. Selected materials were also used as photocatalysts for H<sub>2</sub> evolution from water splitting.

The reactions were performed under deoxygenated conditions and using visible LED radiation ( $\lambda_{max} = 412$  nm). In the absence of catalyst, no production of AAD or hydrogen was verified.

The concentration profiles of AA conversion and AAD production over 240 min of reaction using bulk GCN and GCN-zCA materials are depicted in Figs. 4.13a and b, respectively. The reactions were also performed using the most applied photocatalyst (TiO<sub>2</sub> P25) for comparison purposes.

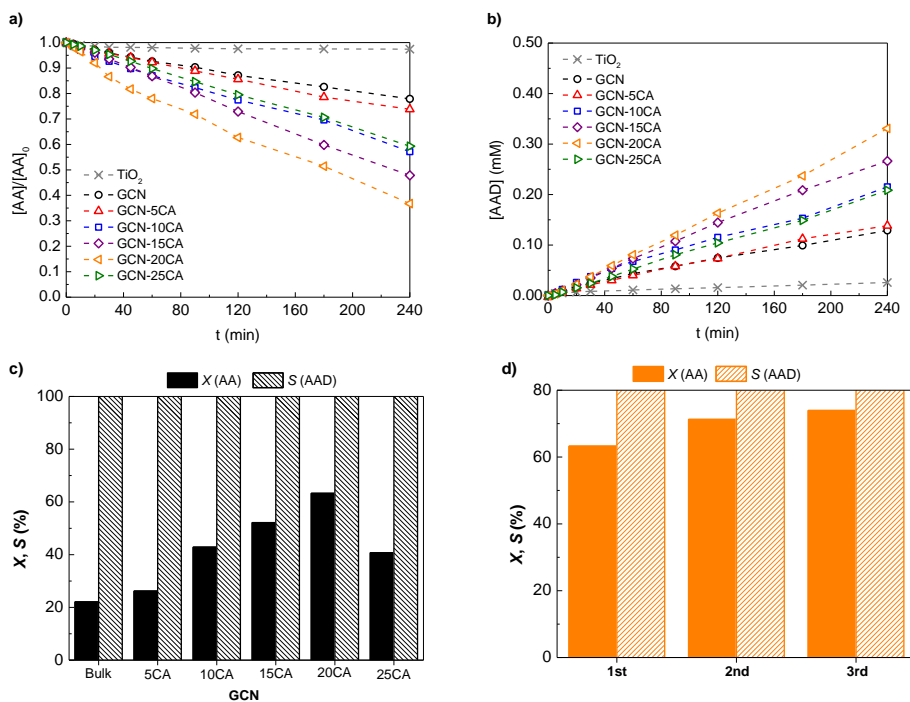


Fig. 4.13 a) Normalized concentration of AA and b) profile of AAD production along 240 min reaction, using TiO<sub>2</sub> P25, GCN and GCN-zCA (z = 5, 10, 15, 20, 25) as catalysts. c) Conversion (X) and selectivity (S) of bulk GCN and GCN-zCA materials after 240 min of irradiation. d) Reuse assessment of GCN-20CA.

As expected, the photocatalytic efficiency of the commercial TiO<sub>2</sub> P25 is very low compared with the GCN-zCA materials (Figs. 4.13a and b). As mentioned previously, the low adsorption of TiO<sub>2</sub> P25 in the visible range contribute for its low efficiency under the experimental conditions. Overall, the incorporation of CA during the synthesis of GCN resulted in materials with enhanced efficiency for AA conversion, while keeping the selectivity towards AAD production at >99% for all catalysts (Fig. 4.13c).

An AA conversion of 22% after 4 h of reaction was obtained using GCN, while this value increased to 26, 43 and 63 % with the amount of CA increases from 5 to 10 and 20 mg, respectively (Fig. 4.13c). A further increase in CA to 25 mg leads to a decrease in AA conversion to 41%. The same tendency was observed in terms of AAD yield, being a maximum of 64% obtained for GCN-20CA after 4 h of irradiation. The reusability of this material towards the synthesis of AAD from AA was evaluated over three consecutive reactions (Fig. 4.13d). It is possible to observe that GCN-20CA

holds high stability in the consecutive runs, maintaining the values of AA conversion and selectivity towards AAD production above 63% and 90%, respectively.

The best performing material for the synthesis of AAD, GCN-20CA, was also tested towards hydrogen production from water using the same light source ( $\lambda_{max} = 412$  nm). In addition to the catalyst and light, the photocatalytic water splitting process usually requires a co-catalyst and a sacrificial electron donor to proceed. Platinum nanoparticles were used as standard co-catalyst while EDTA (0.02 M) was initially chosen as sacrificial electron donor. The photocatalytic performance of GCN-20CA was then compared with bulk GCN (Fig. 4.14a).

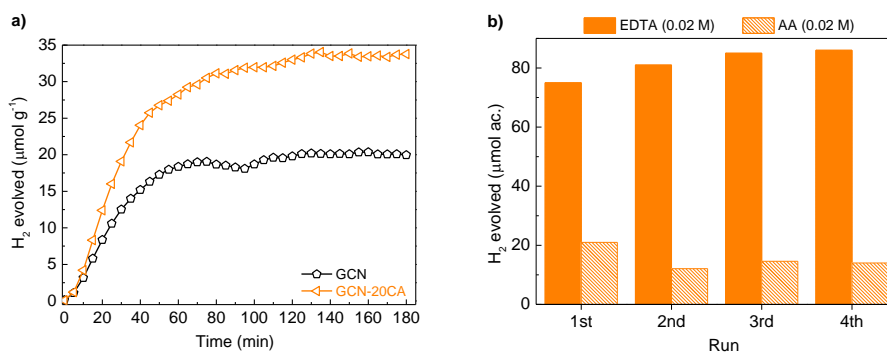


Fig. 4.14 a) Photocatalytic H<sub>2</sub> production, using GCN and GCN-20CA as catalysts, upon 180 min of visible-LED irradiation ( $\lambda_{max} = 412$  nm) in the presence of Pt (3 wt. %) and EDTA (0.02M). b) Reusability of GCN-20CA as photocatalyst for H<sub>2</sub> production in four consecutive cycles, using EDTA and AA aqueous solutions (0.02 M) as sacrificial agents.

As depicted in Fig. 4.14a, GCN-20CA presents higher rate of H<sub>2</sub> production when compared to GCN, duplicating the amount of gas evolved, which indicates that the addition of CA improves the efficiency of the catalyst, both in the production of H<sub>2</sub> from water splitting (Fig. 4.14) and in the synthesis of AAD (Fig. 4.13b).

As already mentioned, the conversion of aromatic alcohols into the corresponding aldehydes in the absence of oxygen results from the oxidative dehydrogenation of the alcohol driven by the photogenerated holes, whereas, the H<sup>+</sup> is simultaneously converted into H<sub>2</sub> by the electrons at the conduction band of the photocatalyst [92,152,158].

In this view, photocatalytic reactions using GCN-20CA as catalyst, Pt nanoparticles as co-catalyst and AA as sacrificial agent for H<sub>2</sub> production were performed (Fig. 4.14b). As expected, the amount of H<sub>2</sub> produced from aqueous solutions of AA was much



lower than that formed using EDTA (23  $\mu\text{mol}$  and 75  $\mu\text{mol}$  evolved after 180 min, respectively) due to the higher propensity of EDTA to be oxidized [298,299].

Since the reusability and stability of the materials are crucial in heterogeneous processes, a study was performed using GCN-20CA as catalysts in consecutive reactions using either EDTA or AA as sacrificial agents (Fig. 4.14b). In the reaction using EDTA,  $\text{H}_2$  production was maintained in values between 75 and 86  $\mu\text{mol}$  after 180 min of irradiation. For the reactions with AA, the  $\text{H}_2$  evolution decreased *ca.* 40% from the first to the second run and then maintained the photocatalytic activity with a production of 14  $\mu\text{mol}$  of  $\text{H}_2$  after four consecutive runs. As the material is recovered, washed, and finally added to a fresh solution of AA, it is possible that some by-products accumulate on the surface of the catalyst, blocking the access to the active sites and thus decreasing its photocatalytic activity.

In order to ascertain the photoactivity of the best performing catalyst, GCN-20CA, the transient photocurrent responses of this material and of bulk GCN applied over FTO coated glass substrates were determined at 0.2 V vs. Ag/AgCl during 1000 s with on/off cycles (30 s each) of simulated solar light ( $100 \text{ mW cm}^{-2}$ ). As shown in Fig. 4.15, it is notorious that GCN-20CA produces a higher photocurrent density than the bulk GCN, given by the larger difference (higher gap) between the recorded current response under dark and in light conditions. In fact, when the light was turned on, an improvement on the photocurrent response of *ca.* 42 % was registered for GCN-20CA compared to GCN. The latter observation suggested that less recombination and longer lifetimes of the photoinduced electron–hole pairs are achieved for the GCN-20CA.

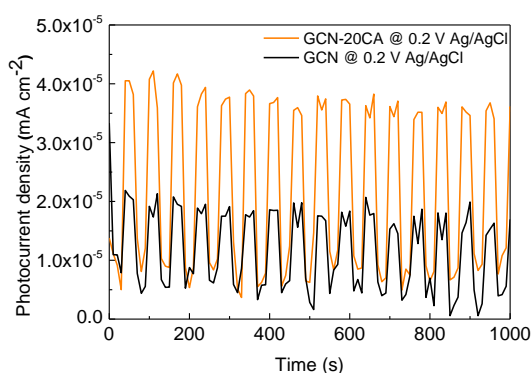


Fig. 4.15 Transient photocurrent response of GCN (black) and GCN-20CA (orange) at a constant applied potential of 0.2 V vs Ag/AgCl, with 30 s simulated solar light ( $100 \text{ mW}\cdot\text{cm}^{-2}$ ) on/off cycles during 1000 s.

All the above results on the photocatalytic efficiency of GCN-zCA materials may be rationalized in terms of their intrinsic optical, electronic, and structural properties. As previously discussed, the defective surface of GCN-zCA catalysts led to an enhancement in light absorption in the whole spectral range (Fig. 4.9a) [125,249,251,258,265,293,294,300]. Moreover, GCN-zCA present a slightly lower  $E_g$  than GCN, indicating that modified materials may require less energy to undergo photoexcitation. In addition, these materials also presented a notorious decrease in the recombination of  $e^-/h^+$  pairs, as inferred from the photoluminescence results (Fig. 4.10a), which can be attributed to their improved properties of charge trapping and transferring, which allows the improvement of their photocatalytic performance [115,242]. It was also observed that the addition of CA during the thermal condensation procedure promoted a reduction in the amount of heptazine units (XPS analysis, Fig. 4.11), which are usually associated to the planar structure of GCN [301]. By reducing their contribution in the GCN matrix, defects are induced on the surface of the catalyst (as observed by SEM, Fig. 4.8) contributing to the enhanced photocatalytic efficiency of the CA-modified materials [153,251,290–292,302,303]. As previously discussed, GCN-20CA presents the lowest contribution of heptazine units (lowest N1 peak, Fig. 4.11), conferring its higher oxidative ability when compared with the other modified catalysts. Moreover, the occurrence of nitrogen vacancies in a higher extent in this particular catalyst (higher C/N atomic ratio and lower XPS N1/N2 peak ratio) may also rationalize its improved photocatalytic performance.

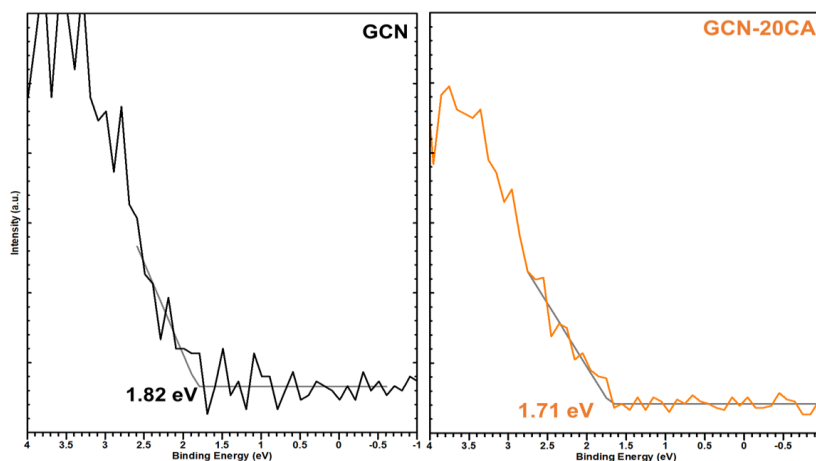


Fig. 4.16 Valence band (VB) XPS spectra of GCN and GCN-20CA. Linear fitting was used to determine the VB potential.

Analysis of the XPS valence band of GCN and GCN-20CA (Fig. 4.16) shows that the addition of CA induced an up-shift of a ca. 0.11 eV in the valence band potential of GCN-20CA when compared with bulk GCN (1.82 eV).

Considering the VB position and the  $E_g$  previously determined through Tauc plot analysis (Table 4.2), the CB of GCN is situated at -1.04 eV, while that of GCN-20CA shifts to -1.11 eV (Fig. 4.17). Moreover, the mid-gap states position can be estimated considering the transition energy of GCN-20CA ( $E_T = 2.37$  eV, Table 4.2), and the valence band potential obtained from XPS analysis. Due to the *n*-type semiconductor behavior of GCN-20CA, the mid-gap states are located below the edge of CB [249,293,298] with a position estimated at -0.66 eV. Moreover, both CB and mid-gap states of GCN-20CA are more negative than the water reduction potential (0.00 V vs NHE) [304], which indicates that electrons trapped both in CB and mid-gap states contribute for the  $H_2$  production (Fig. 4.17).

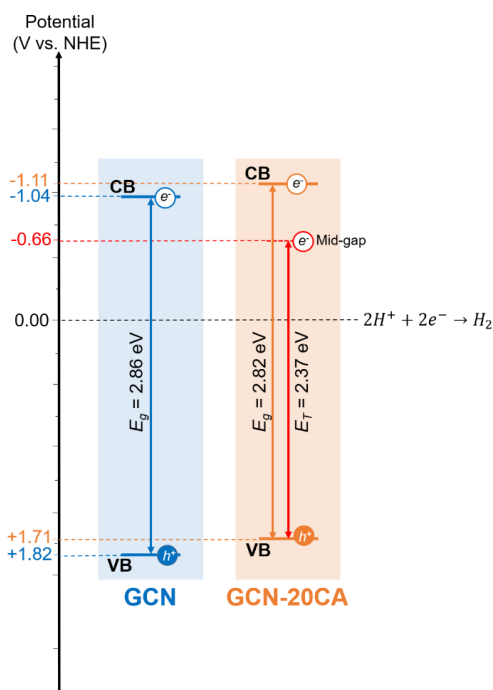


Fig. 4.17 Band structure of GCN and GCN-20CA.

Overall, the high efficiency of GCN-20CA photocatalyst towards both AAD and  $H_2$  production may be ascribed to the combination of unique features, namely: i) the existence of structural defects induced by the inclusion of CA during the synthesis procedure; ii) increased light absorption in the visible region of the electromagnetic

spectrum (450 - 700 nm), and iii) improved charge separation efficiency due to the presence of mid-gap states. These features open-up the possibility of using CA-modified GCN catalysts, in particularly GCN-20CA, in solar-driven applications. Moreover, the conversion of AA into AAD with simultaneous evolution of H<sub>2</sub> is of particular interest from the point of view of process integration and energy conversion.

## 4.8 Copolymerized GCN-based catalysts

### 4.8.1 Characterization

The morphological properties of copolymerized GCN were assessed through SEM and compared with bulk GCN, as displayed in Fig. 4.18.

By applying a copolymerization agent during the synthesis of GCN, the highly stacked lamellar structure (Fig. 4.18, highlighted zone X1) remained stable for GCN-BAr, GCN-ABN and GCN-ATCN (Fig. 4.18). However, some defects were detected on the lamellar surface of all copolymerized catalysts (Fig. 4.18, highlighted zone X3), resulting in a highly irregular surface. This fact may occur due to the chemical reaction promoted between the copolymerization agents (BAr, ABN and ATCN) and dicyandiamide (GCN precursor) [305]. No significant variation was noticed in the  $S_{BET}$  value of GCN-BAr, GCN-ABN and GCN-ATCN when compared to bulk GCN (Table 4.2).

All synthesized photocatalysts (GCN, GCN-BAr, GCN-ABN and GCN-ATCN) were further subjected to a thermal post-treatment at 500°C (GCN-500, GCN-BAr-500, GCN-ABN-500 and GCN-ATCN-500). According to previous studies [70,120], subjecting GCN bulk materials to high temperatures leads to the breaking of van der Waals forces and hydrogen bonds, which results in catalysts with thinner and split layers. The SEM analysis of GCN-500 corroborates this statement, with the observation of thin lamellar structures (Fig. 4.18, highlighted zone X2). GCN-BAr-500, GCN-ABN-500 and GCN-ATCN-500 also present this specific alteration in their morphology, yet with a much lower prevalence than GCN-500 (Fig. 4.18, highlighted zone X2). In addition, a clear increase occurred in the  $S_{BET}$  with the thermal exfoliation procedure (Table 4.2), promoted by the splitting of the GCN layers. In fact, GCN-500 and GCN-BAr-500 increased their surface area in ca. 10 times after the thermal post-treatment (60 and 70 m<sup>2</sup> g<sup>-1</sup>, respectively, Table 4.2), while GCN-ABN-500 and GCN-ATCN-500 reached a  $S_{BET}$  ca. 30 times higher (214 and 226 m<sup>2</sup> g<sup>-1</sup>, respectively, Table 4.2).

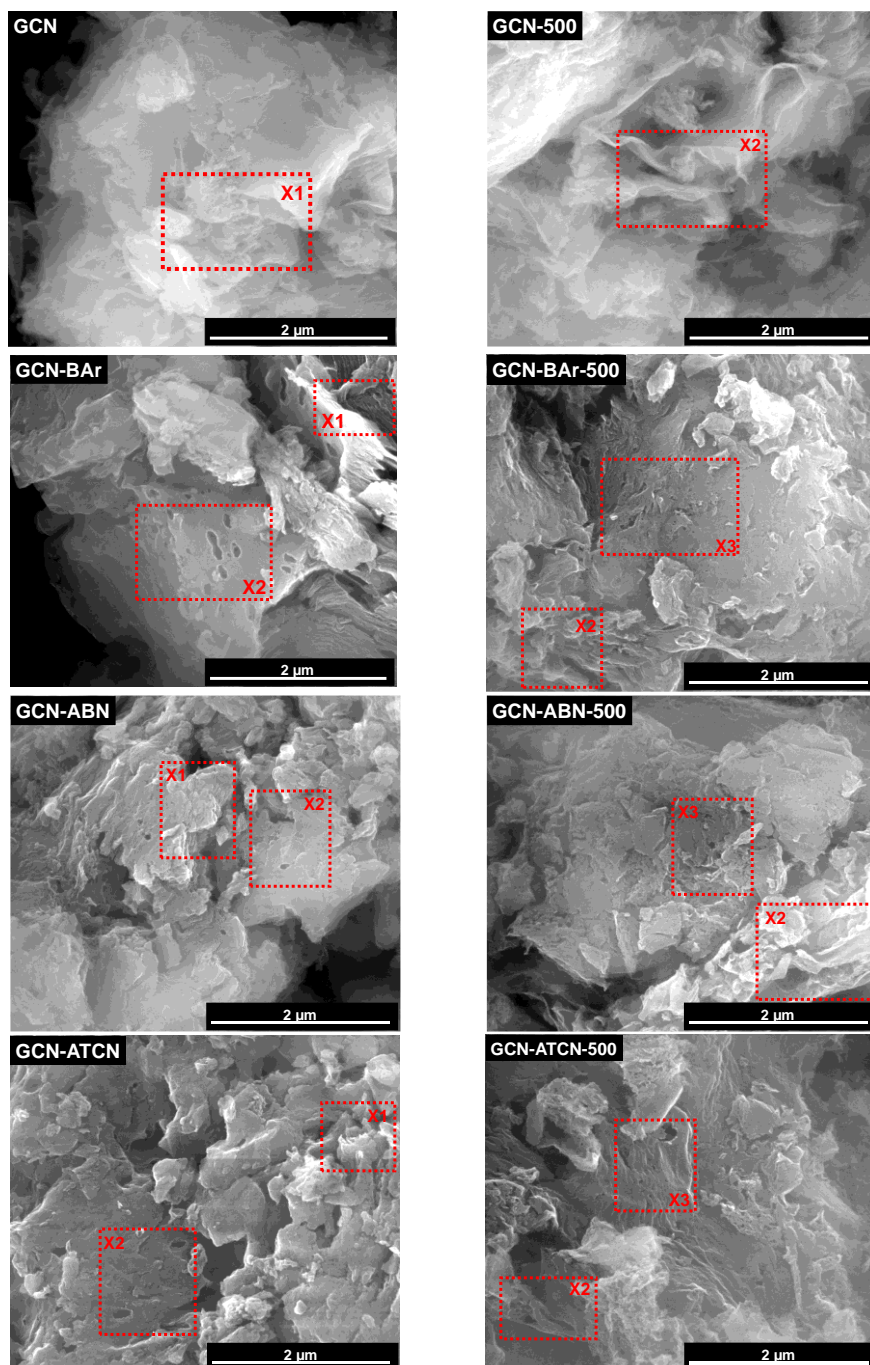


Fig. 4.18 SEM micrographs of GCN-Z and GCN-Z-500 materials (Z = BAR, ABN and ATCN). Highlighted zones (X1, X2 and X3) indicates important textural characteristics of each catalyst.

Table 4.2 C/N molar ratio obtained from elemental analysis and specific surface area ( $S_{BET}$ ) of GCN-Z and GCN-Z-500 catalysts (Z = BAr, ABN and ATCN).

Catalyst	C/N ratio	$S_{BET}$ ( $m^2 g^{-1}$ )
<b>GCN</b>	0.561	7
<b>GCN-BAr</b>	0.571	7
<b>GCN-ABN</b>	0.563	7
<b>GCN-ATCN</b>	0.568	8
<b>GCN-500</b>	0.561	60
<b>GCN-BAr-500</b>	0.582	70
<b>GCN-ABN-500</b>	0.563	214
<b>GCN-ATCN-500</b>	0.585	226

Regarding to elemental analysis, bulk GCN has a C/N ratio of 0.561 (Table 4.2), due to the incomplete polymerization of dicyandiamide [249]. By applying copolymerization agents, the C/N ratio had no significant variation in the case of GCN-ABN (0.563, Table 4.2) when compared to bulk GCN. In the case of GCN-ATCN and GCN-BAr, a more pronounced increase was observed (0.568 and 0.571, respectively; Table 4.2), being GCN-BAr the copolymerized catalyst that reached the highest value. The increase in C/N ratio of GCN through copolymerization approach may indicate a replacement of nitrogen atoms of heptazine rings by carbon or loss of nitrogen atoms in the form of ammonia, originating nitrogen vacancies in the copolymerized materials [124,274]. In fact, according to Zhang et al. [125], BAr groups can be directly incorporated in the heptazine units of carbon nitride through thermal polymerization with dicyandiamide, promoting the substitution of nitrogen by carbon atoms into the tris-s-triazine heterocycles. In another study carried out by the same group [265] is proposed a mechanism for the reaction between ABN and dicyandiamide, by nucleophilic addition, to form 2,4-diaminoquiazoline, which has a similar structure to melamine. The polymerization of this monomer leads to the grafting of benzene rings to the GCN matrix, increasing the carbon content. Regarding to the modification with ATCN, it was hypothesized by Zhang et al. [306] that sulfur atoms can be incorporated in the copolymerized catalysts due to the grafting of thiophene motifs into the carbon

nitride matrix. However, elemental analysis and XPS survey of GCN-ATCN and GCN-ATCN-500 did not identify such element. The low amount of ATCN added (0.05 g) to dicyandiamide (2 g) may be an explanation to this finding.

After the thermal exfoliation process, the C/N ratio of GCN-500 and GCN-ABN-500 did not suffer significant variation when compared to the starting materials, while an increase was observed for GCN-BAr-500 and GCN-ATCN-500 (0.582 and 0.585, respectively; Table 4.2).

Although elemental analysis showed a quantitative variation in C/N ratio, no change was observed in FTIR spectra of GCN-Z (Fig. 4.19a) and GCN-Z-500 (Fig 4.19b) materials, presenting the same IR bands previously identified in Fig. 4.2, section 4.6.1.

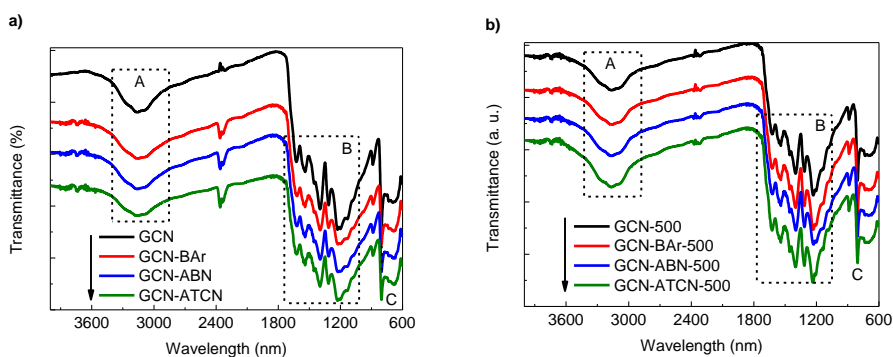


Fig. 4.19 FTIR-ATR spectra of a) GCN-Z and b) GCN-Z-500 materials (Z = BAr, ABN and ATCN). Highlighted regions (A, B, C) correspond to characteristic IR bands of GCN-based materials.

The surface chemistry of all catalysts was studied through XPS analysis. Similar results were obtained for C1s and N1s spectra of GCN-Z and GCN-Z-500 materials, considering the results of other GCN-based catalysts (Figs. 4.3 and 4.11, sections 4.6.1 and 4.7.1, respectively). To avoid replication of results, only the spectra of GCN-Z-500 materials are presented in Fig. 4.20.

Although no significant difference was observed in the deconvolution of C1s and N1s spectra of all samples (Fig. 4.20), relevant variations were identified in the contribution of N1 and N2 binding energies. As previously referred, the ration between N1 and N2 peaks allow to establish a relation with the presence of nitrogen vacancies in the heptazine rings [124,126,274]. In this way, N1/N2 ratio was determined for all samples and follows the order GCN-BAr-500 < GCN-500 < GCN-ABN-500 < GCN-ATCN-500 (1.17, 1.35, 1.46 and 2.11, respectively). As can be observed, only GCN-BAr-500 present lower N1/N2 ratio than GCN-500, which means that GCN-BAr-500 has the

highest loss of nitrogen at the N1 site and, consequently, a higher density of nitrogen vacancy defects than the other copolymerized catalysts [124,126,274]. The same tendency was also observed in GCN-Z catalysts, with GCN-BAR being the material with the lowest N1/N2 ratio.

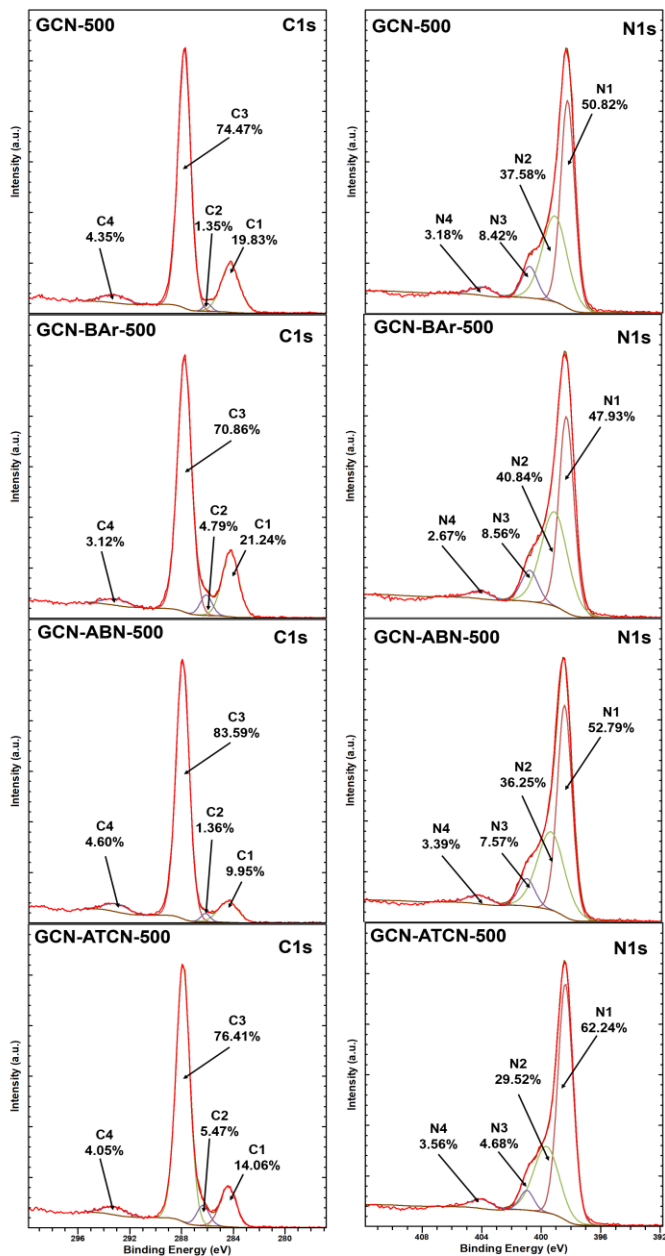


Fig. 4.20 C1s and N1s XPS spectra of GCN-500, GCN-BAR-500, GCN-ABN-500 and GCN-ATCN-500.



The absorption ability of the GCN-based catalysts was assessed through DRUV-vis spectroscopy.

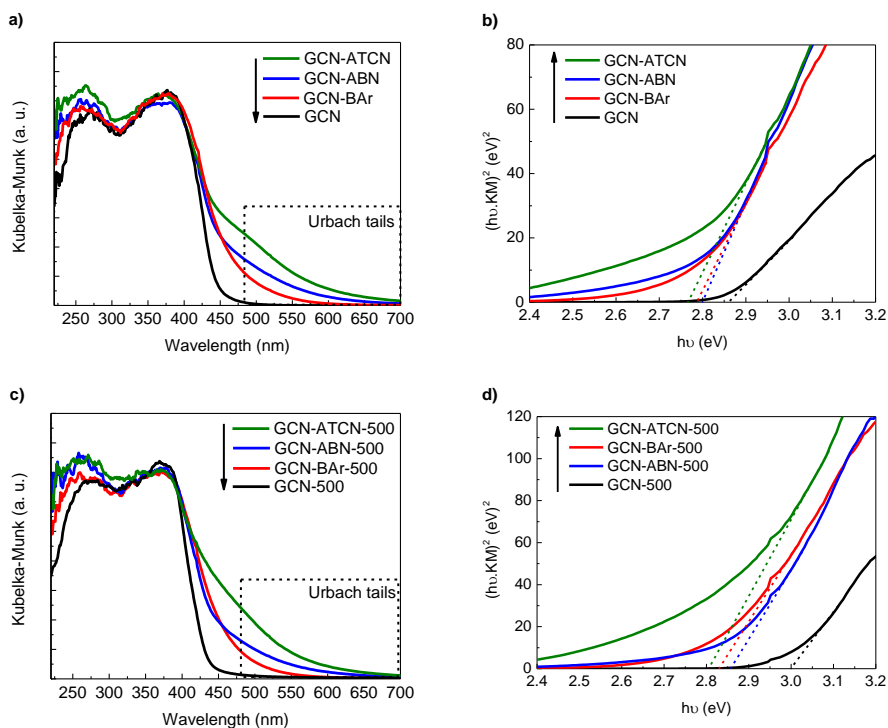


Fig. 4.21 (a, c) DRUV-vis spectra and (b, d) Tauc plot analysis of GCN-Z and GCN-Z-500 materials (Z = BAr, ABN and ATCN). Highlighted zone indicates the Urbach tails.

By using BAr, ATCN and ABN as copolymerization agents, the absorption edge shifts to longer wavelengths when compared to bulk GCN (Fig. 4.21a), indicating an improved light harvesting mainly due to the narrowing of the bandgap. Moreover, the copolymerization approach allowed extending the absorption capacity of the modified catalysts (Fig. 4.21a) in the visible-light region (Urbach tail, highlighted zone), which may favor the photocatalytic activity concerning solar-driven processes.

The extended absorption ability of copolymerized catalysts resulted in a decrease in the value of  $E_g$  (Fig. 4.21b) from 2.86 eV (GCN) to 2.80, 2.79 and 2.77 eV (GCN-ABN, GCN-BAr and GCN-ATCN, respectively). The thermal post-treatment induced a shift in the band edge of GCN-Z-500 materials (Fig. 4.21c) when compared to the starting materials. Consequently, an increase of the  $E_g$  of the GCN-Z-500 materials (Fig. 4.21d) occurred, varying from 3.00 eV (GCN-500) to 2.86, 2.83 and 2.78 eV (GCN-ABN-500, GCN-BAr-500 and GCN-ATCN-500, respectively). The existence of thinner

plates of carbon nitride in GCN-Z-500 catalysts may contribute to the quantum confinement effect, leading to the shift of conduction and valence band (CB and VB, respectively) in opposite directions, which may explain the variation observed in their  $E_g$  [260,307,308].

The electronic properties of GCN-Z and GCN-Z-500 materials were evaluated through PL analysis by excitation light at 370 nm and the results are depicted in Fig. 4.22.

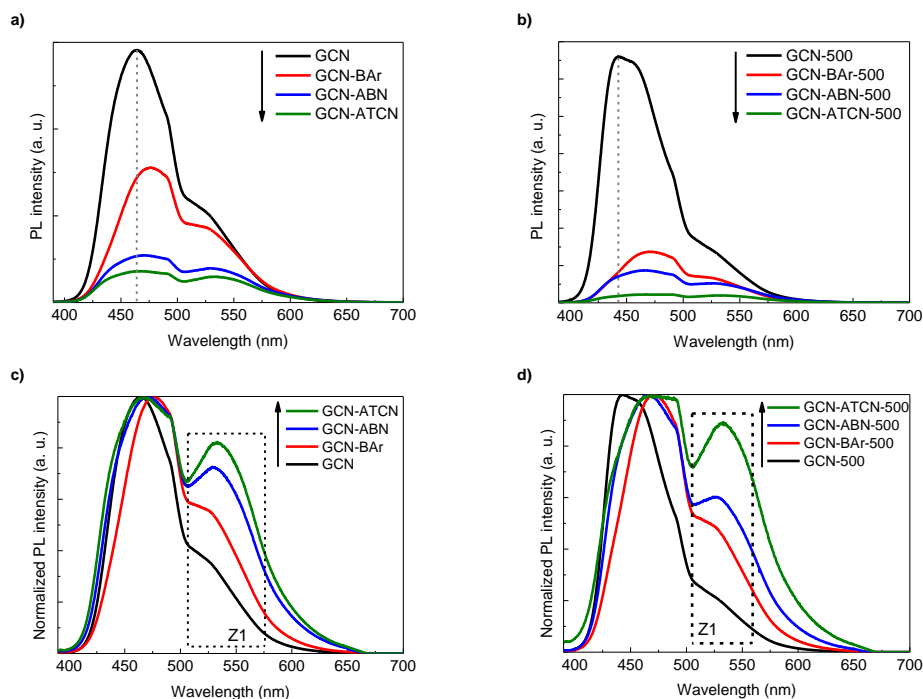


Fig. 4.22 (a, b) PL and (c, d) normalized PL spectra of GCN-Z and GCN-Z-500 materials (Z = BAr, ABN and ATCN). Dashed line indicates the wavelength of maximum PL intensity of GCN and GCN-500. Highlighted zone (Z1) indicates the enhanced emission band.

The addition of copolymerization agents resulted in a decreased PL intensity of modified catalysts when compared to GCN and GCN-500 (Figs. 4.22a and b, respectively). The textural modifications induced on the surface of the catalysts allowed the extension of the  $\pi$ -conjugation system to visible light range due to the delocalization of  $e_r^-$  and  $h_r^+$  into the graphite-like matrix of carbon nitride, which is in line with DRUV-vis results (Fig. 4.21). In this way, the defects on copolymerized catalysts may act as trapping sites to photogenerated charge carriers, reducing their recombination [249].

Additionally, the first peak of luminescence of GCN at *ca.* 464 nm was shifted to higher wavelengths in modified catalysts both before and after the thermal post-treatment (Figs. 4. 22a and 22b, respectively), which is in line with the variation also denoted in  $E_g$  (Figs. 4.21b and d).

The normalization of all PL spectra (Figs. 4.22c and d) revealed an enhancement of the second emission band (highlighted zone Z1) in modified materials comparing to the GCN and GCN-500, which agrees with the existence of the Urbach tails in the DRUV-vis spectra of the copolymerized catalysts (Fig. 4.21).

#### 4.8.2 Photocatalytic results

The photocatalytic performance of both GCN-Z and GCN-Z-500 catalysts was evaluated through the selective oxidation of AA into AAD under oxygenated conditions, using UV-LED irradiation system ( $\lambda_{\max} = 370$  nm). The results obtained using GCN-Z and GCN-Z-500 materials are shown in Fig. 4.23.

GCN and GCN-Z materials exhibit a slower oxidation of AA than TiO<sub>2</sub> P25 under oxygenated conditions using UV-light radiation (Fig. 4.23a). In fact, TiO<sub>2</sub> P25 reached almost total AA conversion after 60 min of reaction (Fig. 4.23a), while the GCN-Z catalysts only achieved the same result for the reaction times above 120 min (Fig. 4.23a). The high conversion of AA using TiO<sub>2</sub> P25 may be attributed, not only to the increased surface area ( $57 \text{ m}^2 \text{ g}^{-1}$ ) when compared to GCN-Z materials (between 7 and  $8 \text{ m}^2 \text{ g}^{-1}$ , Table 4.2), but also the high photonic efficiency presented by TiO<sub>2</sub> P25 under UV radiation [309]. Among all GCN-Z materials, GCN-BAr proved to be the best performing catalyst, achieving complete conversion of AA at 120 min (Fig. 4.23a), representing a reduction of 33% in the reaction time when compared to the bulk material. Both GCN-ABN and GCN-ATCN presented a slower rate of AA conversion than bulk GCN (Fig. 4.23a), which indicates a negative impact of the copolymerization procedure on the photocatalytic activity of these materials. By subjecting GCN and GCN-Z materials to the thermal post-treatment at 500°C, AA conversion was highly improved, with >60% achieved in all cases after 40 min of reaction (Fig. 4.23b), following the order GCN-BAr-500 > GCN-500 > GCN-ATCN-500 > GCN-ABN-500, which coincides with that observed for the original catalysts (Fig. 4.23a).

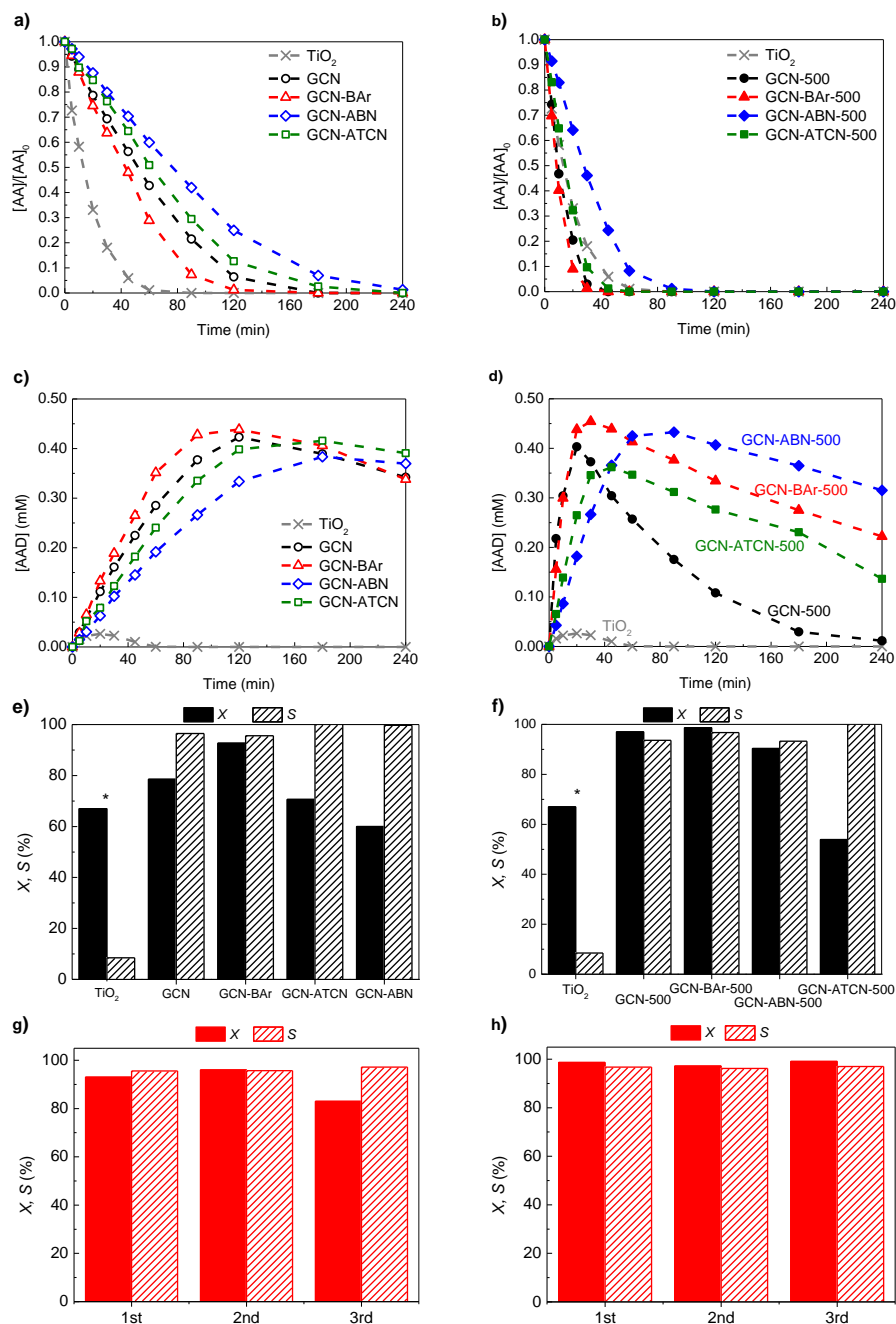


Fig. 4.23 a, b) Normalized AA and c, d) AAD concentrations using  $TiO_2$  P25 ( $\times$ ), GCN-Z ( $\circ$ ,  $\triangle$ ,  $\diamond$ ,  $\square$ ) and GCN-Z-500 ( $\bullet$ ,  $\blacktriangle$ ,  $\blacklozenge$ ,  $\blacksquare$ ) catalysts. X and S obtained using e) GCN-Z and f) GCN-Z-500 catalysts (over 90 and 30 min, respectively). Reuse experiment using g) GCN-BAR and h) GCN-BAR-500 as photocatalyst in three consecutive cycles. \*The values of X and S of  $TiO_2$  P25 were determined at the maximum of AAD production (20 min).

Although TiO<sub>2</sub> P25 had reached faster AA oxidation (Fig. 4.23a), the production of AAD was significantly lower when compared to GCN-Z materials (Fig. 4.23c). The maximum of AAD concentration reached by TiO<sub>2</sub> P25 was nearly 0.03 mM after 20 min of reaction (Fig. 4.23c). After this period, the AAD concentration started to decrease due to the over oxidation of the aldehyde. In the case of bulk GCN, the production of AAD reached 0.42 mM after 120 min of reaction (Fig. 4.23c).

The performance of the materials obtained by copolymerization followed the same tendency already observed in AA oxidation, with GCN-BAr showing higher rate of AAD synthesis than bulk GCN (Fig. 4.23c), while GCN-ABN and GCN-ATCN show a slower capacity of AAD production (Fig. 4.23c). After the thermal post-treatment at 500°C (Fig. 4.23d), the photocatalytic synthesis of AAD was improved for GCN-500 and copolymerized catalysts (GCN-BAr-500, GCN-ABN-500 and GCN-ATCN-500) by reducing the time required to reach the maximum of production of the aldehyde.

The determination of X, S and Y for all the photocatalytic reactions allowed to compare the performance of GCN-Z (Fig. 4.23e) and GCN-Z-500 (Fig. 4.23f) materials for the photocatalytic synthesis of AAD from AA. In the case of GCN-Z catalysts (Fig. 4.23e), all values were determined at 90 min of reaction. Due to the increase in the rate of AAD production, the values calculated for the GCN-Z-500 materials refers to 30 min of reaction (Fig. 4.23f). TiO<sub>2</sub> P25 was used for comparison in both cases, with X, S and Y being calculated after 20 min of reaction.

Although TiO<sub>2</sub> P25 presented a high conversion of AA (67%, Fig. 4.23e), the prevalence of hydroxyl radicals in the oxidative mechanism negatively affected the selectivity of the process (8.5%, Fig. 4.23e) [121,310]. By using bulk GCN as photocatalyst, the value of both X and S were increased to 79% and 97%, respectively (Fig. 4.23e). All GCN-Z catalysts achieved selectivity higher than 95% after 90 min of irradiation.

The above results suggest that depending on the copolymerization agent, different effects are observed in the performance of the GCN-Z catalysts when compared to bulk GCN (Fig. 4.23e). In fact, the material obtained through the copolymerization of dicyandiamide with BAr (GCN-BAr) was the best performing catalyst, achieving 93% of X and 96% of S after 90 min of reaction (Fig. 4.23e). Both ATCN and ABN compounds induced modifications on GCN that decreased the photocatalytic performance of the resulting catalysts when compared to bulk GCN (Fig. 4.23e). With the thermal post-treatment, selectivity of the catalysts was not affected, being higher than 94% in all cases (Fig. 4.23f). On the other hand, a significant increase in the conversion (> 90%, Fig. 4.23f) was achieved by using GCN-500, GCN-BA-500 and

GCN-ATCN-500 in a lower reaction time (30 min, Fig. 4.23f). The great increase observed in the  $S_{BET}$  of the GCN-Z-500 materials when compared to the pristine ones (Table 4.2) may rationalize the improvement verified in their photocatalytic performance.

As previously discussed, the addition of copolymerization agents (BAr, ATCN and ABN) promoted a defective surface of copolymerized materials (SEM micrographs, Fig. 4.18) due to the loss of nitrogen atoms, as confirmed both through the increase in the C/N ratio (Table 4.2) and through the existence of mid-gap states (Fig. 4.21). The decrease observed in the  $E_g$  of GCN-Z and GCN-Z-500 materials when compared to GCN and GCN-500, respectively, indicate that a lower amount of energy is required to photoexcite those materials. Moreover, their reduced recombination rate between the charge carriers contribute to a higher photo efficiency, which may result in an improved photocatalytic performance towards AAD synthesis.

However, only BAr proved to have a positive impact over the catalytic performance of bulk GCN (Figs. 4.23e and f). The formation of nitrogen vacancies can effectively reduce the charge-transfer barrier and improve the photocatalytic performance by trapping charge carriers, avoiding their recombination and promoting overall efficiency [311–313]. According to the XPS analyses (Fig. 4.20), BAr was the copolymerization agent that induced a higher decrease in N atoms at N1 site and, consequently, the highest amount of nitrogen vacancies in the heptazine rings at this site in both GCN-Z and GCN-Z-500 catalysts. This finding may explain the enhanced activity of GCN-BA and GCN-BA-500 when compared to the other copolymerized catalysts. On the other hand, due to the *n*-type behavior of carbon nitride [301], the mid-gap states are located within its CB, which means that additional electrons are trapped and available to promote reduction reactions.

## 4.9 Thermally post-treated GCN-based materials

### 4.9.1 Characterization

Bulk GCN was subjected to a thermal post-treatment at different temperatures (500, 550, 600 and 620°C) under inert atmosphere.

The morphological analysis of thermally post-treated GCN-based materials was assessed through SEM.

The modified catalysts (GCN-A-Z) presented a highly defective structure, with well-defined pores on their surface (Fig. 4.24). Regarding the literature, the heating of carbon nitride leads to the loss of amino groups originated by the incomplete

polymerization of GCN precursor (DCN) [263,312,314,315]. With the increase in the final temperature of the thermal post-treatment, the pore volume of the catalysts increases from 0.056 cm<sup>3</sup> g<sup>-1</sup> of GCN-A-500 to 0.263 cm<sup>3</sup> g<sup>-1</sup> of GCN-A-620 (Table 4.3). In terms of  $S_{BET}$ , no significant variation was observed in the case of GCN-A-500, GCN-A-550 and GCN-A-600 when compared to bulk GCN (Table 4.3). However, in the case of GCN-A-620,  $S_{BET}$  increases to 22 m<sup>2</sup> g<sup>-1</sup> (Table 4.3). The combination between the morphology, pore volume and the  $S_{BET}$  may indicate that a highly irregular material with an enhanced amount of active sites is created by subjecting bulk GCN to high temperatures under inert atmosphere [260,263,316,317].

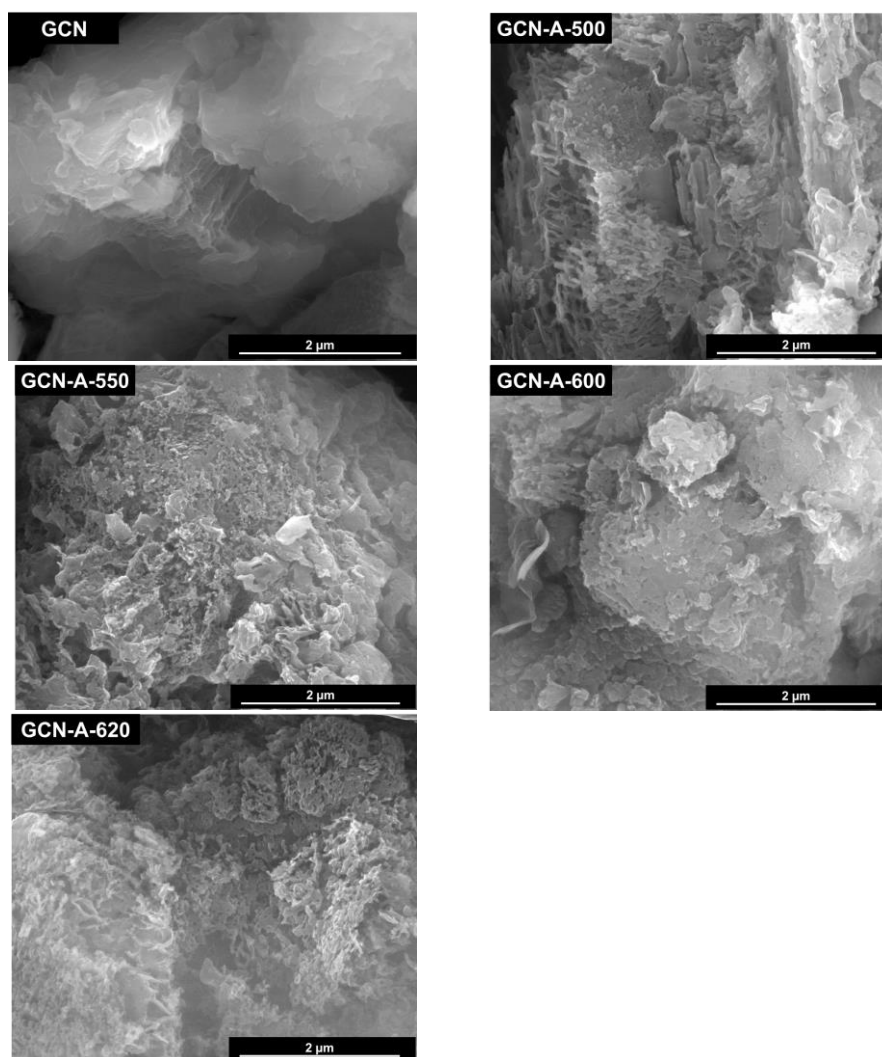


Fig. 4.24 SEM micrographs of GCN and the thermally post-treated GCN.

Through elemental analysis, it was possible to observe an increase in the C/N ratio from 0.56 (bulk GCN) to 0.58 (GCN-A-620, Table 4.3) with the increase in the temperature of the thermal treatment, which may indicate a gradual decrease in the atomic content of nitrogen in the carbon nitride matrix. According to literature, the loss of amino groups during the heating procedure may alter the structure of the material, leading to the appearance of N vacancies in heptazine rings [312,314,315,318].

Table 4.3 Specific surface area ( $S_{BET}$ ), pore volume ( $V_{pore}$ ), C/N molar ratio obtained through elemental analysis, full width at half maximum (FWHM) of the (002) diffraction line, and crystallite size ( $d$ ) of the synthesized catalysts

Catalyst	$S_{BET}$ ( $m^2 g^{-1}$ )	$V_{pore}$ ( $cm^3 g^{-1}$ )	C/N ratio	FWHM ( $^\circ$ )	$d$ (nm)
<b>GCN</b>	7	0.054	0.561	2.09	4.2
<b>GCN-A-500</b>	9	0.056	0.568	2.27	4.1
<b>GCN-A-550</b>	9	0.073	0.571	2.35	3.8
<b>GCN-A-600</b>	10	0.108	0.579	2.94	3.1
<b>GCN-A-620</b>	22	0.263	0.580	3.65	2.8

No significant difference was noticed in the FTIR spectra of GCN-A-Z materials when compared to bulk GCN (Fig. 4.25a), with the presence of the three characteristic bands (highlighted zones A, B and C), as previously discussed in Chapter 4, section 4.6.1. The crystal structure of GCN-A-Z materials was also evaluated through XRD analysis (Fig. 4.25b).

All GCN-based catalysts exhibit two main characteristic peaks: a main diffraction peak at  $27.4^\circ$  (Fig. 4.25b) corresponding to the (002) plane, ascribed to the distance between the graphitic layers [319,320] and a less intense peak at  $13.0^\circ$  (Fig. 4.25b), attributed to the (100) plane, ascribed to the intralayer spacing [319,320]. It can be observed that GCN-A-500, GCN-A-550 and GCN-A-600 presented a more intense (002) peak when compared to bulk GCN (Fig. 4.25b), possibly caused by the splitting of the graphitic layers during the thermal treatment. In bulk GCN, strands of melon units with amino groups are linked through hydrogen bonds, forming layers [315]. With the thermal post-treatment, hydrogen bonds can be broken, resulting in the split of the graphitic layers and, consequently in the increase in the intraplanar distance [260,314,315,318]. Contrariwise, GCN-A-620 exhibits a sharply decreased (002)



peak, which may indicate that the post-treatment at higher temperature (620°C) may lead to a significant destruction of the polymeric structure of GCN [315].

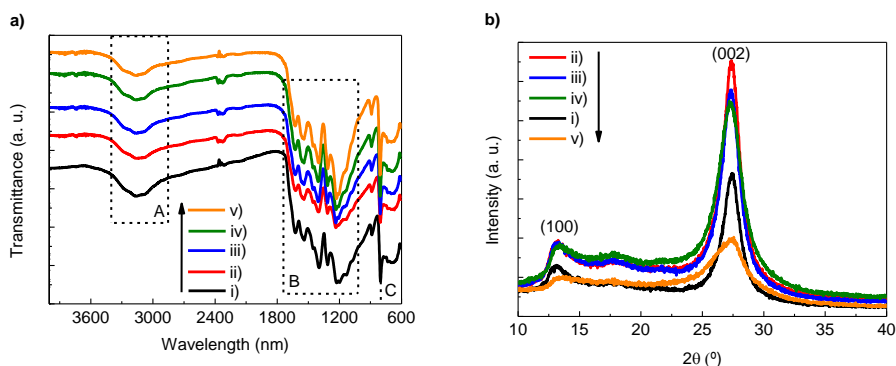


Fig. 4.25 a) FTIR-ATR spectra and b) XRD pattern of i) GCN, ii) CN-A-500, iii) CN-A-550, iv) CN-A-600 and v) CN-A-620. Highlighted zones A, B and C indicate the characteristic bands of GCN-based catalysts.

The full width at half maximum (FWHM) of the XRD peak (002) was determined for all catalysts (Table 4.3). A gradual increase was observed in the FWHM, from 2.09° of bulk GCN to 2.27°, 2.35°, 2.94° and 3.65° for GCN-A-500, GCN-A-550, GCN-A-600 and GCN-A-620, respectively (Table 4.3). This variation may suggest that modified catalysts possessed a less crystalline structure than bulk GCN with no long-range atomic order due to their highly distorted morphology [300]. The average crystallite size ( $d$ , Table 4.3) was calculated through Debye-Scherrer equation (eq. 4.4) [70,321]:

$$d = \frac{k\lambda}{\beta \cos\theta} \quad 4.4$$

where  $\lambda$  is the wavelength of the light used in the XRD analysis (Cu-K $\alpha$  radiation),  $k$  is the Scherrer constant (0.9),  $\theta$  is the diffraction angle, and  $\beta$  is the full width at half maximum (FWHM) of the sharp peaks.

As can be observed, the value of  $d$  decreased from 4.2 nm of bulk GCN to 2.8 nm in the case of GCN-A-620 (Table 4.3), with the gradual decrease occurring with the increase in the temperature of the thermal post-treatment. This result also indicates the loss of crystallinity in modified catalysts due to the heating procedure.

The optical and electronic properties of GCN-A-Z materials were also evaluated through DRUV-vis and PL spectroscopies (Fig. 4.26).

As referred in literature, the thermal post-treatment applied to bulk GCN may induce an enhancement in light absorption in the visible range spectrum ( $\lambda > 400$  nm) due to

the change in the color of the catalysts, from yellow to orange (Fig. 4.26a) [312,315,317,318], which is an advantage concerning solar-driven processes.

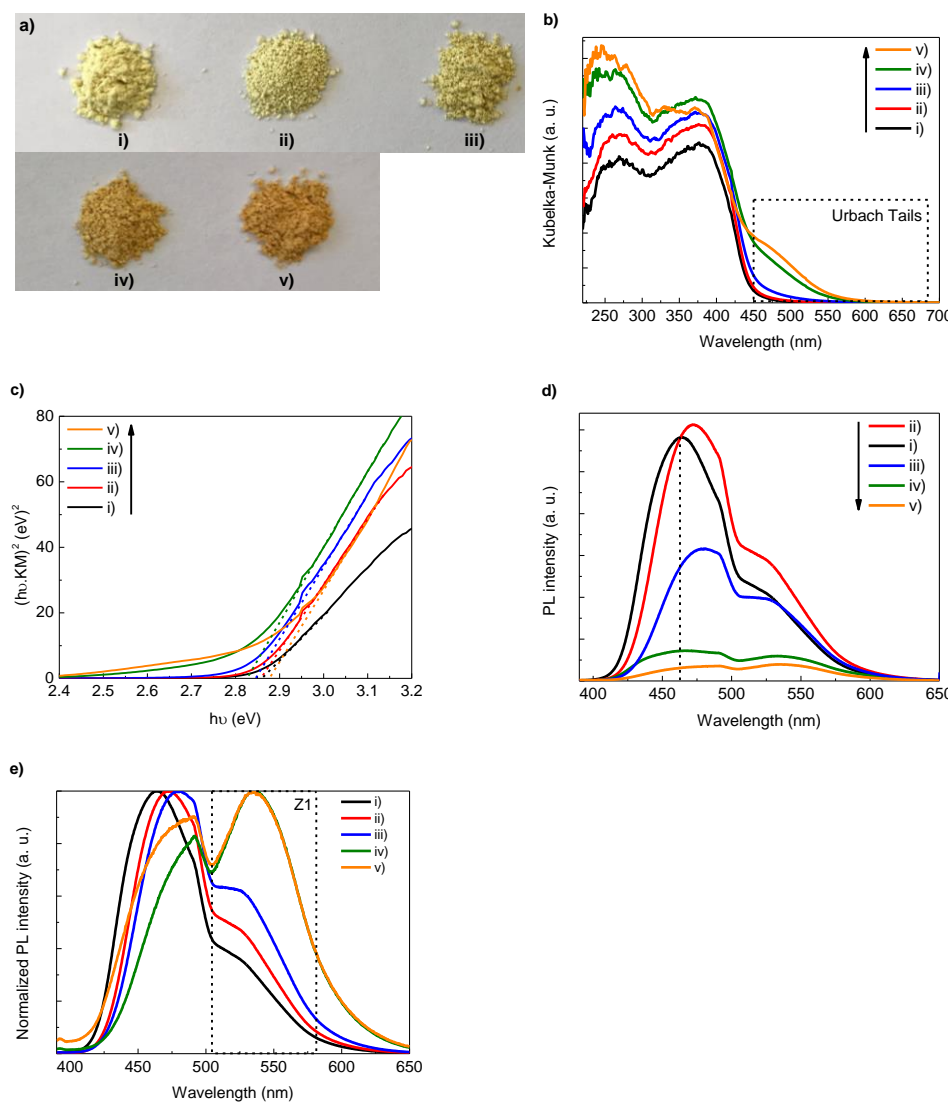


Fig. 4.26 a) Photograph, b) DR UV-vis spectra, c) Tauc plot, d) PL spectra and e) normalized PL intensity of i) GCN, ii) GCN-A-500, iii) GCN-A-550, iv) GCN-A-600 and v) GCN-A-620. Dashed zones indicate the b) Urbach tails and d) the wavelength of the maximum of PL intensity of GCN. Highlighted zone Z1 indicate the second band of PL emission.

In the case of GCN-A-500 and GCN-A-550, no significant variation was observed in their absorption ability when compared to bulk GCN (Fig. 4.26b). However, GCN-A-

600 and GCN-A-620 registered a sharp enhancement in light absorption, particularly from 450 nm to 600 nm (Urbach tails, Fig. 4.26b).

As concluded in previous studies, the presence of the Urbach tails in DRUV-vis spectra of GCN-A-600 and GCN-A-620 may be related with the existence of midgap states within their bandgap, resulting from the  $n \rightarrow \pi^*$  electronic transitions favored by the distorted structure of GCN-A-Z catalysts [312,314,318]. Regarding to photocatalytic purposes, the midgap states may have a positive impact acting as electron scavengers, reducing the recombination rate between  $e^-$  and the photogenerated  $h^+$  and contributing to the generation of  $O_2^{\cdot -}$  [312,314,318].

The determination of the  $E_g$  of the modified catalysts (Fig. 4.26c) revealed a gradual decrease from 2.86 eV (bulk GCN) to 2.86, 2.83 and 2.82 eV as the temperature of the thermal post-treatment increases up to 500°C, 550°C and 600°C, respectively. The red-shift observed in the  $E_g$  of GCN-A-500, GCN-A-550 and GCN-A-600 may be caused by the changes induced in the microstructure of carbon nitride due to the breakdown of the hydrogen bonds and loss of amino groups [314,318]. In the case of GCN-A-620, a blue shift occurred in the  $E_g$  to 2.88 eV (Fig. 4.26c), possibly promoted by the extensive destruction of the 2D layers of carbon nitride.

The PL intensity was drastically quenched in the first emission band (dashed line, Fig. 4.26d) by subjecting bulk GCN to the thermal post-treatment (Fig. 4.26d), due to the highly efficient charge carrier separation promoted by the presence of midgap states [263,312,314,315,318]. GCN-A-620 presented the lowest PL intensity among all catalysts, which may reveal a highly efficient charge separation with lower energy lost in recombination processes. Moreover, a red-shift was also observed in the wavelength of the maximum of PL intensity of all GCN-A-Z catalysts when compared to bulk GCN (Fig. 4.26e), which is in agreement with the DRUV-vis results. A second PL emission band near to 550 nm (highlighted zone Z1, Fig. 4.26e) is also identified in the PL spectra of GCN-A-Z catalysts, with a clear enhancement comparing with bulk GCN. Previous works established a relation between the favoring of forbidden  $n \rightarrow \pi^*$  electronic transitions in semiconductor materials due to the creation of nitrogen vacancies with the enhancement of this second PL emission band [263,312,314,315,318]. Considering that GCN-A-600 and GCN-A-620 exhibited the highest increase in this band (Fig. 4.26e), it can be inferred that  $n \rightarrow \pi^*$  electronic transitions represented the main route for the excitation of  $e^-$  in these catalysts.

## 4.9.2 Photocatalytic results

Thermally post-treated GCN-based catalysts were tested in the photocatalytic conversion of AA into AAD, under oxygenated conditions, using the visible-LED irradiation system ( $\lambda_{max} = 412$  nm) previously described in Chapter 4, section 4.4.

Bulk GCN achieved total conversion of AA after 180 min of radiation (Fig. 4.27a). The post-treated materials promoted a faster oxidation, with 100% of AA conversion after 90 min (GCN-A-500 and GCN-A-620, Fig. 4.27a) and 120 min (GCN-A-550 and GCN-A-600, Fig. 4.27a) of reaction. As expected, all GCN-A-Z materials proved to have higher oxidative ability than  $\text{TiO}_2$  P25 (Fig. 4.27a), due to the reduced capacity of light absorption of  $\text{TiO}_2$  P25 in the visible range.

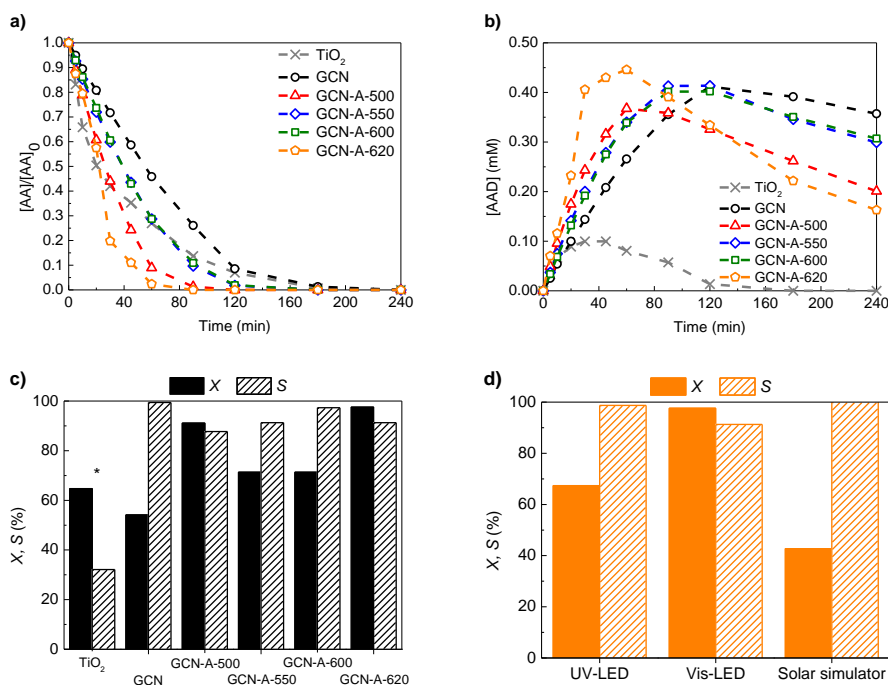


Fig. 4.27 a) Normalized AA and b) AAD concentrations using  $\text{TiO}_2$  P25 (x), GCN (o) and GCN-A-Z (Δ, ◇, □, ◊) as catalysts. c) X and S obtained using GCN-A-Z catalysts, over 60 min of reaction under visible-LED radiation. d) Comparison of the photocatalytic performance of GCN-A-620 under different radiation sources, over 60 min of reaction. \*The values of X and S of  $\text{TiO}_2$  P25 were determined at the maximum of AAD production (45 min).

Regarding to the production of AAD, bulk GCN reached 0.40 mM after 120 min of reaction (Fig. 4.27b). The maximum of AAD production using GCN-A-500 (0.37 mM; Fig. 4.27b) was achieved after 60 min of radiation, representing a reduction of 50% in

the time of reaction when compared with the bulk catalyst. In the case of GCN-A-550 and GCN-A-600, similar productions were obtained, with 0.40 mM of AAD being synthesized after 90 min (Fig. 4.27b). Using GCN-A-620 as photocatalyst, 0.45 mM of AAD were produced only after 60 min of reaction (Fig. 4.27b).

All GCN-based catalysts presented selectivity higher than 90% (Fig. 4.27c). The best performing catalyst was GCN-A-620, with  $S = 91\%$  and  $X = 98\%$  after 60 min of radiation (Fig. 4.27c).

Among all modified catalysts, GCN-A-620 exhibited the highest values of  $S_{BET}$  and  $V_{pore}$  (Table 4.3). Moreover, the higher C/N ratio in the case of GCN-A-620 (Table 4.3) allowed to infer that a high amount of N vacancies was generated on its surface and, consequently, an enhanced catalytic activity when compared to the other photocatalysts [153,263,290]. Regarding to crystallinity properties, GCN-A-620 presented also the lowest crystalline structure (Fig. 4.25b and Table 4.3). According to literature, crystalline semiconductor materials are the most applied in the photocatalytic field due to the presence of a long-range atomic order maintained by the hydrogen bonds between the amino groups of each polymeric unit, which enables the efficient charge carriers separation [300,322,323]. In the less crystalline materials, the hydrogen bonds are broken, leading to the creation of many structural defects usually associated with an extended visible light absorption and also to a reduced recombination rate between  $e_r^-$  and photogenerated  $h_r^+$  [124,153,153,300,324].

Lastly, GCN-A-620 presented the lowest PL intensity and  $E_g$  (Figs. 4.26b and c), which contributed to an efficient activation of this semiconductor by visible-LED system and to an improved photocatalytic performance [124,153,263].

The photocatalytic performance of GCN-A-620 under visible-LED radiation was compared with its photocatalytic activity under UV-LED radiation and simulated solar light (Fig. 4.27d). A decrease was observed in the AA conversion in both cases, (67% and 43% using UV-LED and simulated solar light radiation, respectively). However, selectivity was widely improved to 98% and 100%, respectively (Fig. 4.27d), suggesting that solar light may be successfully used as light source for the synthesis of AAD using GCN-A-620 as photocatalyst.

### 4.9.3 Evaluation of photocatalytic materials for the synthesis of *p*-anisaldehyde

Table 4.4 compiles the published works on the photocatalytic conversion of AA to AAD together with selected results obtained during the present study.

TiO<sub>2</sub>-based catalysts are the most applied materials (Table 4.4, entries 1-12). Several methodologies were adopted to improve TiO<sub>2</sub>-based catalysts performance, such as metal- and elemental-doping approach (Table 4.4, entries 7-9) and the formation of heterojunctions with other catalysts (Table 4.4, entries 10-12). By using metal-containing catalysts, namely Ag<sub>3</sub>PO<sub>4</sub> (Table 4.4, entry 13) and Pt/nanoporous Bi<sub>2</sub>WO<sub>6</sub> (Table 4.4, entry 14), high yields were achieved (>80%). However, this type of catalysts has a profoundly negative impact over environmental sustainability in opposition to metal-free catalysts, as carbon nitride (Table 4.4, entries 16-18). Opposing the modest yields (9%) obtained for *N*-doped g-C<sub>3</sub>N<sub>4</sub> (Table 4.4, entry 16) are the more effective *P*-doped g-C<sub>3</sub>N<sub>4</sub> (Table 4.4, entry 17) and mpg-CN (Table 4.4, entry 18) photocatalysts.

Overall, the best performing catalysts of each type found in this study were i) the morphologically-modified GCN-UL catalyst, with *Y* >75% and *X* >89% after 1.5 h reaction under vis-LED radiation in the presence of oxygen (Table 4.4, entry 19); ii) the citric acid-modified GCN-20CA, resulting in *X* = 71% and *Y* = 65% after 4 h of vis-LED radiation under argon atmosphere (Table 4.4, entry 20); iii) the copolymerized catalyst GCN-BAR-500, which produced a significant enhancement in the production of AAD, with a maximum of *X* = 99% and *Y* = 96% after 0.5 h under oxygenated conditions and UV-LED irradiation (Table 4.4, entry 21); and iv) the thermally post-treated GCN-A-620, reaching *X* = 98% and *Y* = 90% after 1 h of reaction, under vis-LED irradiation in the presence of oxygen (Table 4.4, entry 22). Comparatively to the previously reported photocatalysts, these materials surpass the performance of most of them.

A critical aspect in the photocatalytic processes is the type of radiation source adopted. Analyzing Table 4.4, it can be stated that the photocatalytic conversion of AA to AAD has been mainly driven by conventional light sources, like xenon, fluorescent and halogen lamps. Contrariwise to the conventional lamps, LEDs offer high energy efficiency, with longer lifetime and higher flexibility to the reactor design [325–327]. An energy efficiency parameter (*E*) was defined in terms of the moles of AAD produced per initial AA concentration, per watt, per hour, to compare the results compiled in Table 4.4 as follows:

$$E = \frac{Y \times V}{P \times t} = \frac{[\text{AAD}] \times V}{[\text{AA}]_0 \times P \times t} \quad 4.1$$

in which *Y* is the yield towards AAD synthesis, [AAD] and [AA]<sub>0</sub> are the molar concentration of *p*-anisaldehyde at a given time and the initial molar concentration of

*p*-anisyl alcohol (mM), respectively,  $V$  is the reaction volume (mL),  $P$  is the power of the radiation source (W), and  $t$  is the irradiation time (h).

The results obtained with the developed catalysts (GCN-UL, GCN-20CA, GCN-BAr-500 and GCN-A-620) provide efficiency in excess of 0.625, 0.203, 2.40 and 1.12 mL  $W^{-1} h^{-1}$ , respectively, in terms of mol of AAD per initial molar concentration of AA. These results directly bound with the improved photocatalytic performance of the photocatalysts and the low energetic demand of the light sources. In this sense, the present work represents a technological breakthrough in the ecological impact of the photoconversion as means of converting AA into AAD.

Table 4.4 Published works on the photoconversion of *p*-anisyl alcohol (AA) into *p*-anisaldehyde (AAD).

Entry	Catalyst	Irradiation source	Power (W)	V (mL)	Gas	$\tau$ (h)	X (%)	Y (%)	Energy efficiency <sup>b</sup> (E)	Ref.
1	Anatase TiO <sub>2</sub>	Hg lamp	125	500	O <sub>2</sub>	7.7	65	42	0.218	[164]
2	Rutile TiO <sub>2</sub>	Hg lamp	125	500	O <sub>2</sub>	2.36	50	30	0.508	[165]
3	Rutile TiO <sub>2</sub>	Hg lamp	450	500	O <sub>2</sub>	8.8	50	31	3.91×10 <sup>-2</sup>	[166]
4	Brookite TiO <sub>2</sub>	Hg lamp	125	500	O <sub>2</sub>	2.1	50	12	0.229	[167]
5	Brookite TiO <sub>2</sub>	UV fluorescent lamp	45	150	Air	4	44	12	0.117	[168]
6	TiO <sub>2</sub>	UV fluorescent lamp	45	150	Air	2.3	20	18	0.261	[169]
7	Pt/TiO <sub>2</sub> <sup>a</sup>	Xenon lamp	n. i.	n. i.	N <sub>2</sub>	3	56	56	n. d.	[170]
8	F-doped TiO <sub>2</sub>	UV fluorescent lamp	45	150	Air	4	23	13	0.108	[171]
9	N-doped TiO <sub>2</sub>	Solar light simulator	1500	150	O <sub>2</sub>	1	10	9	9.00×10 <sup>-3</sup>	[172]
10	TiO <sub>2</sub> -graphene	Xenon lamp	300	1.5	O <sub>2</sub>	20	70	70	1.75×10 <sup>-4</sup>	[173]
11	WO <sub>3</sub> /TiO <sub>2</sub>	Hg lamp	450	5	O <sub>2</sub>	6	50	27	5.00×10 <sup>-4</sup>	[174]

<sup>a</sup> n.i. – not indicated; n. d. – not determined. <sup>b</sup> Units of E: mol<sub>AAD</sub> mL<sup>-1</sup> mol<sup>-1</sup> AA<sub>0</sub> W<sup>-1</sup> h<sup>-1</sup>. X: conversion. Y: yield



Table 4.4 Published works on the photoconversion of *p*-anisyl alcohol (AA) into *p*-anisaldehyde (AAD) (cont.).

Entry	Catalyst	Irradiation source	Power (W)	V (mL)	Gas	$\tau$ (h)	X (%)	Y (%)	Energy efficiency <sup>b</sup> (E)	Ref.
12	TiO <sub>2</sub> /Ag/DIOL	UV fluorescent lamp	45	150	Air	4	54	46	0.383	[175]
13	Ag <sub>3</sub> PO <sub>4</sub>	Solar light simulator	230	130	Air	2	>85	84	0.237	[176]
14	Pt/ nanoporous Bi <sub>2</sub> WO <sub>6</sub>	Tungsten-halogen lamp	230	130	Air	4	>95	>94	0.133	[177]
15	CdS	Xenon lamp	300	20	O <sub>2</sub>	3	25	15	3.33×10 <sup>-3</sup>	[178]
16	N-doped g-C <sub>3</sub> N <sub>4</sub>	Xenon lamp	300	10	O <sub>2</sub>	9	86	85	3.33×10 <sup>-4</sup>	[153]
17	P-doped g-C <sub>3</sub> N <sub>4</sub>	Halogen lamp	100	150	O <sub>2</sub>	4	35	100	0.375	[121]
18	mpg-CN	Xenon lamp	300	20	O <sub>2</sub>	3	56	50	1.11×10 <sup>2</sup>	[178]
19	GCN-UL	Vis-LED	40	50	Air	1.5	89	75	0.625	Present study
20	GCN-20CA	Vis-LED	40	50	Argon	4	71	65	0.203	
21	GCN-BAR-500	UV-LED	40	50	Air	0.5	99	96	2.40	
22	GCN-A-620	Vis-LED	40	50	Air	1	98	90	1.12	

<sup>a</sup> n.i. – not indicated; n. d. – not determined. <sup>b</sup> Units of E: mol<sub>AAD</sub> mL<sup>-1</sup> mol<sup>-1</sup> AA<sub>0</sub> W<sup>-1</sup> h<sup>-1</sup>. X: conversion. Y: yield

## 4.10 Conclusions

Graphite like carbon nitride (GCN)-based photocatalysts were obtained through hard-templating, copolymerization and thermal post-treatment routes.

The photocatalysts were thoroughly characterized and tested in the selective synthesis of *p*-anisaldehyde through the oxidation of *p*-anisyl alcohol.

All the techniques adopted for the modification of GCN allowed to obtain materials with distinct morphological, electrical and optical properties, which were reflected in their photocatalytic performance.

The results obtained at different activation wavelengths in the electromagnetic spectrum, confirm the enormous ability of GCN-based materials to operate under open-air solar conditions. Moreover, the presence/absence of oxygen directly interferes with the rate of oxidation and also with the by-products obtained in the photocatalytic process. In this way, all operation reaction parameters involved in the process should be studied, including atmosphere medium conditions, light sources, pH, initial concentration, temperature, among others if aiming at commercial application.

The present studies present heterogeneous photocatalysis using GCN-based catalysts as a viable alternative to the conventional processes used for *p*-anisaldehyde synthesis. Moreover, the metal-free character of the catalysts, the use of aqueous solutions, the low-cost and efficient irradiation sources (UV- or visible-LED) constitute positive aspects compared to the conventional organic synthesis processes.

## Chapter 5

### ***Synthesis of vitamin B3 using GCN-based photocatalysts***

In the previous chapter, GCN-based catalysts were successfully applied in the synthesis of *p*-anisaldehyde through the oxidation of *p*-anisyl alcohol. Due to the encouraging results obtained using thermally post-treated materials, GCN-A-620 was chosen as photocatalyst for the conversion of 3-pyridinemethanol into vitamin B3. For comparison purposes, the photocatalytic performance of both bulk GCN and thermally post-treated GCN-500 was also evaluated.

The operational conditions adopted (visible-LED radiation source and oxygenated atmosphere) were defined to reduce the environmental impact of the photocatalytic process.

Aiming at a more technological approach, GCN-A-620 was immobilized into a sodium alginate membrane (GCN-A-620\_SA), showing promising results for the synthesis of vitamin B3.



## 5.1 Introduction

In order to reduce the environmental impact of the industrial production of vitamin B3, heterogeneous photocatalysis has been explored as a valuable alternative to the well-established processes, using an alcohol (3-pyridinemethanol) as starting molecule, and TiO<sub>2</sub>-based materials as photocatalysts [209–213]. Although these processes achieved promising results of selectivity and yield, their sustainability is limited due to the leaching and scarcity of metallic elements. Therefore, the development of metal-free catalysts represents an interesting route to overcome these limitations in order to design sustainable synthesis processes.

As mentioned in Chapter 1, section 1.3, GCN-based materials present a wide range of optical, electronical and chemical properties that have promoted their application in a wide variety of photocatalytic systems, achieving promising results [214,328]. In fact, the present dissertation is also a prove on the successful application of GCN-based catalysts in synthesis processes, namely in the case of AAD (Chapter 4). However, the use of powdered catalysts usually requires the additional separation steps to recover the desired product, increasing the cost of the global process. Therefore, the immobilization of photocatalysts may constitute a powerful strategy to overcome these technological limitations, putting closer the possibility of photocatalytic systems to be implemented at industrial level.

## 5.2 Experimental

### 5.2.1 Materials

Dicyandiamide (DCN, 99%), calcium chloride (CaCl<sub>2</sub>, > 99%) 3-Pyridinemethanol (3PM, 98%), 3-Pyridinecarboxaldehyde (3PC, 98%) and Vitamin B3 (VB3, ≥ 98%) were purchased from Sigma-Aldrich. Formic acid (HCO<sub>2</sub>H, 98%) was purchased from Fluka. Methanol (CH<sub>3</sub>OH, 99.6%) and sodium alginate were supplied by VWR™. All the reagents were used without further purification. Ultra-pure water (≥ 18 MΩ cm<sup>-1</sup>) was used in the preparation of the aqueous solutions.

### 5.2.2 Synthesis and characterization of GCN-based catalysts

The synthesis of bulk GCN, GCN-500 and GCN-A-620 were performed as described in Chapter 4, sections 4.2.2, 4.2.5 and 4.2.6, respectively.

The characterization of the photocatalysts GCN, GCN-500 and GCN-A-620 was thoroughly discussed in Chapter 4, sections 4.6.1, 4.8.1 and 4.9.1, respectively.

GCN-A-620 was immobilized on a sodium alginate (SA) membrane by adapting the procedure described elsewhere [329]. For this, 1 g of SA was added to 40 mL of ultrapure water. The mixture was magnetically stirred and heated in a paraffin bath at 50°C until the complete dissolution of sodium alginate. Then, 50 mg of GCN-A-620 was added, and the stirring and temperature were kept until it reaches a homogeneous dispersion. The immobilization was finished by immersing the homogeneous dispersion into a solution of 3% (w/v) of calcium chloride for 8 h, promoting SA cross-linking. Lastly, the GCN-A-620 membrane (GCN-A-620\_SA) was left into 150 mL of ultrapure water for 24 h to remove any impurities.

### 5.2.3 Photocatalytic experiments

The photocatalytic efficiency of GCN, GCN-500 and GCN-A-620 catalysts were evaluated in the oxidation of aqueous 3PM (0.10 mM) to 3PC and VB3. All experiments were carried out in the same experimental setup that was presented in Chapter 3, section 3.2.4, Scheme 3.1.

The experiments were performed under oxygenated conditions (continuous air flow), using a four visible LED system ( $\lambda_{max} = 412$  nm) as radiation source. A dark period of 30 min was initially established to reach the adsorption-desorption equilibrium (<2% of adsorption). The suspension was irradiated for 7 h and the 3PM, 3PC and VB3 concentrations were monitored by HPLC (0.30 mL of volume for each sample).

Regarding to the immobilized GCN-A-620 (GCN-A-620\_SA), the membrane (40 mm x 50 mm, with 5 mm of thickness) was placed in the photoreactor, covering its walls. The solution of 3PM was added and the photocatalytic reaction was carried out under the same conditions than the powdered catalysts.

The 3PM conversion ( $X$ ), selectivity ( $S$ ) and yield ( $Y$ ) towards the VB3 and 3PC production were determined as indicated in Chapter 3, section 3.2.4.

### 5.2.4 Analytical procedure

The HPLC analyses were performed in a Shimadzu Corporation apparatus equipped with a Diode Array Detector (SPD M20A). A Surf C18 AQ 100A 3 $\mu$ m (100 x 2.1mm) column was used with a solvent delivery pump (LC-30AD) at a flow rate fixed at 0.25 mL min<sup>-1</sup>. The temperature of the column oven and autosampler were set at 40°C and 4.0°C, respectively. An equilibrated mixture of acetonitrile (A) and ammonium acetate 40 mM (B) with a ratio of 2:98 (A:B) was isocratically eluted for 15 min. The 3PM and VB3 concentrations were determined at 260 nm, while 3PC concentration was calculated at 230 nm.

## 5.3 Results and discussion

### 5.3.1 Characterization of GCN-based catalysts

Although GCN, GCN-500 and GCN-A-620 were extensively characterized in the Chapter 4, selected characterization results were presented in this Chapter in order to better correlate their properties with the photocatalytic efficiency towards the production of VB3. Representative SEM micrographs of GCN, GCN-500 and GCN-A-620 are depicted in Fig. 5.1.

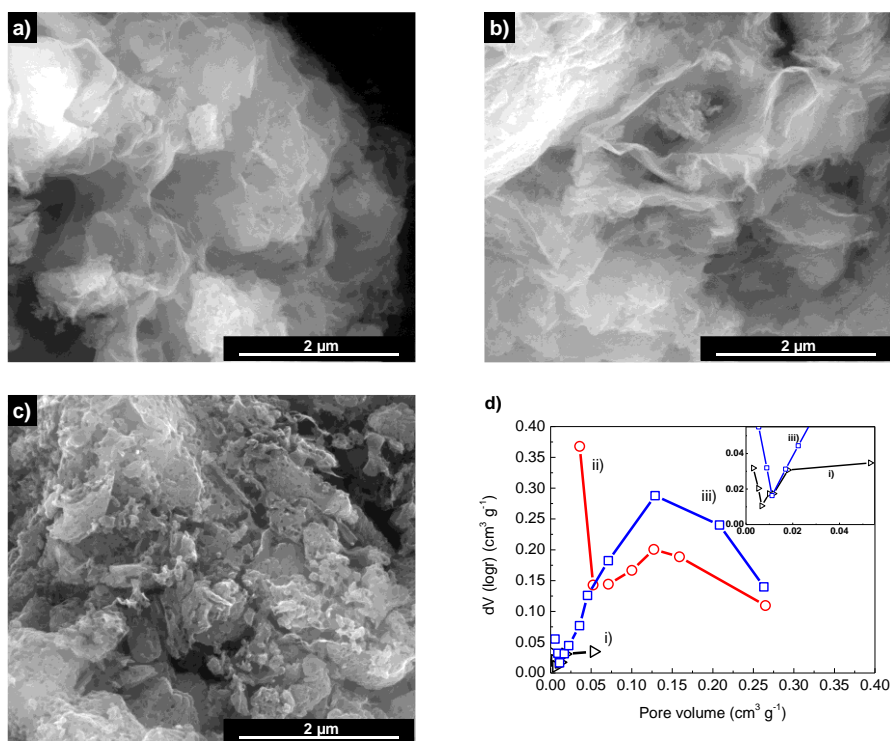


Fig. 5.1 SEM micrographs of a) GCN, b) GCN-500 and c) GCN-A-620. d) Barret-Joyner-Halenda pore volume distribution derived from the  $N_2$  adsorption isotherms at  $-196^\circ\text{C}$  of i) GCN, ii) GCN-500 and iii) GCN-A-620. Inset shows a magnification of the BJH pore volume distribution.

As previously discussed in Chapter 4, section 4.8.1, the thermal post-treatment at  $500^\circ\text{C}$  under air flow (GCN-500, Fig. 5.1b) applied to bulk GCN promoted the split of the layers of carbon and nitrogen due to the breaking of Van der Waals forces and hydrogen bonds [120,150], leading to a less compact structure, and consequently, to a sharply increase in its  $S_{BET}$  ( $60\text{ m}^2\text{ g}^{-1}$ , Table 5.1). GCN-A-620 (Fig. 5.1c) presented

a defective surface, with a highly porous structure, which is also reflected in its  $S_{BET}$  ( $22 \text{ m}^2 \text{ g}^{-1}$ , Table 5.1). This fact is in line with the pore volume distribution of GCN-based materials (Fig. 5.1d). In the case of GCN and GCN-500, pore volume may be related with the interstices/distance between the layers of carbon nitride once that these materials did not exhibit pores on their surface.

GCN has an almost negligible pore volume (Fig. 5.1d), which agrees with the aggregation between its layers (Fig. 5.1a). In the case of GCN-500, the pore volume distribution varies from  $0.036 \text{ cm}^3 \text{ g}^{-1}$  and  $0.265 \text{ cm}^3 \text{ g}^{-1}$  (Fig. 5.1d), which may be related with the distance between the graphitic layers. GCN-A-620 also presents a broad distribution of pore volume (from  $0.005 \text{ cm}^3 \text{ g}^{-1}$  to  $0.263 \text{ cm}^3 \text{ g}^{-1}$ ), being the material that exhibits a high amount of pores with larger volume (Fig. 5.1d).

The determination of C/N ratio through the atomic composition obtained through elemental analysis indicate an increase from 0.56 in bulk GCN and GCN-500 (Table 5.1) to 0.58 in the case of GCN-A-620 (Table 5.1), which may confirm the loss of nitrogen atoms in the aromatic units [259,262].

Table 5.1 Atomic ratio between carbon and nitrogen obtained through elemental analysis, specific surface area ( $S_{BET}$ ), full width at half maximum (FWHM) of the (002) peak, and crystallite size ( $d$ ) of the synthesized catalysts.

Catalyst	$S_{BET}$ ( $\text{m}^2 \text{ g}^{-1}$ )	C/N ratio	FWHM ( $^\circ$ )	$d$ (nm)
<b>GCN</b>	7	0.56	2.09	4.2
<b>GCN-500</b>	60	0.56	2.23	3.9
<b>GCN-A-620</b>	22	0.58	2.54	3.8

The crystallinity of GCN-based catalysts was evaluated through XRD analyses and their patterns are depicted in Fig. 5.2.

All GCN-based catalysts exhibit the two main peaks previously identified in Chapter 4, section 4.9.1. GCN-500 presented the highest intensity of the (002) peak, which is in accordance with the previous finding about the splitting of layers. However, the FWHM of (002) peak (Table 5.1) decreased in GCN-500 when compared to bulk GCN, which may indicate a decrease in the crystallinity of the material promoted by the thermal treatment.



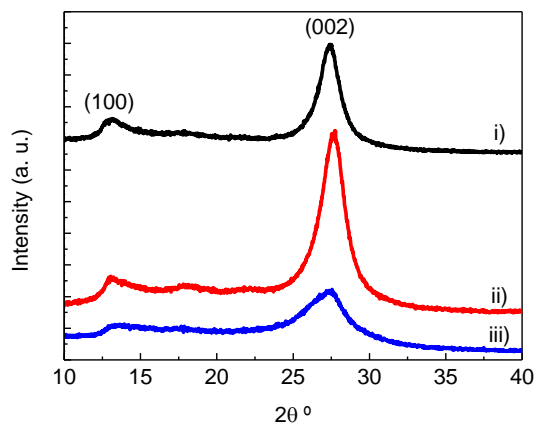


Fig. 5.2 XRD pattern of i) GCN, ii) GCN-500 and iii) GCN-A-620 catalysts.

In the case of GCN-A-620, a sharp decrease was observed in the intensity of both XRD peaks (Fig. 5.2), suggesting a less crystalline structure with no long-range atomic order when compared to bulk GCN and GCN-500, possibly due to its holey-surface that created a highly distorted structure [300]. The size of the crystallite ( $d$ , table 5.1) was determined through the Scherrer (eq. 4.1), following the order GCN > GCN-500 > GCN-A-620.

The optical and electronic properties of GCN-based catalysts were evaluated through DRUV-vis and PL spectroscopies (Fig. 5.3).

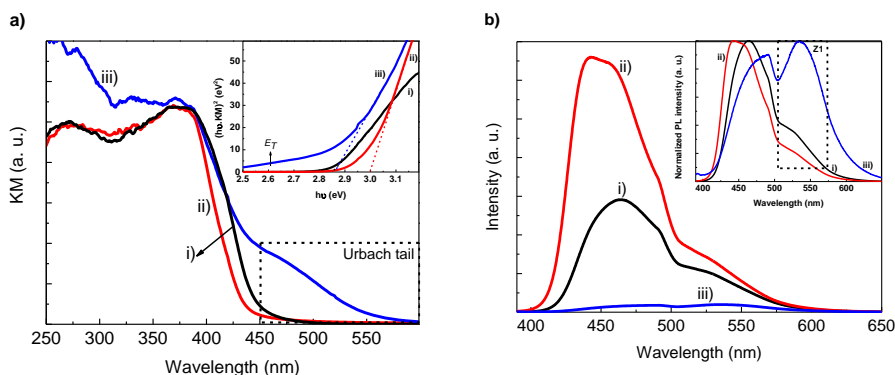


Fig. 5.3 a) DR UV-vis spectra (inset shows the respective Tauc plot) and b) PL spectra (inset shows the normalized PL intensity) of i) GCN, ii) GCN-500 and iii) GCN-A-620. Highlighted zones Z1 and Z2 indicate the two bands of PL emission.

Although the DRUV-vis spectrum profile of GCN-500 was very similar to that of GCN, a blue shift was observed in its bandgap transition (Fig. 5.3a), resulting in an increase

of 0.14 eV in its  $E_g$  (3.00 eV, inset Fig. 5.3a). The shift in the  $E_g$  of GCN-500 when compared to bulk GCN can be attributed to the quantum size effect promoted by its thinner layers (as confirmed through SEM micrographs) [68,120].

Regarding to GCN-A-620, an extension up to 550 nm occurred in the absorption band in the visible range of spectrum (Urbach tail, Fig. 5.3a), which is related with the existence of additional electronic transitions within the bandgap of the catalyst, as also shown from Tauc plot analysis (inset Fig. 5.3a).

In terms of PL intensity, GCN-500 presented a higher value in the whole spectral range than bulk GCN (Fig. 5.3b), attributed to the loss of amino groups during the thermal treatment, promoting defects on the GCN matrix acting as active sites for  $e^-/h^+$  recombination [68,249,296,330]. As previously observed, GCN-A-620 presented a drastic decrease in PL intensity (Fig. 5.3b) when compared to bulk GCN due to the modified arrangement of C and N atoms in carbon nitride matrix [300]. It can be also observed a blue shift in the maximum of PL intensity of GCN-500 when compared to bulk GCN (from 463 nm to 444 nm, inset Fig. 5.3b, highlighted zone Z1), which can be explained by the thickness of the layers of GCN-500 [68]. Contrariwise, GCN-A-620 presents a red-shift in its PL peak from 463 nm to 489 nm (inset Fig. 5.3b, highlighted zone Z1) due to the extension of carbon nitride network [331]. The second PL peak presented a sharp increase in intensity in the case of GCN-A-620, due to its highly distorted structure when compared to bulk GCN and GCN-500 [158,249,296]. Therefore, the electronic excitation in GCN-A-620 is expected to be more effective due to the contributions of the two types of transitions.

### 5.3.2 Photocatalytic results

Primary alcohols can be used as starting molecules to obtain both aldehydes and acids through oxidative routes [8]. Considering the industrial relevance of 3PC and VB3, it was evaluated the photocatalytic performance of GCN, GCN-500 and GCN-A-620 in the selective aerobic oxidation of 3PM, under visible-LED radiation ( $\lambda_{max} = 412$  nm).

The starting alcohol proved to have high photochemical stability in the absence of catalyst, once no conversion of 3PM was observed after 7 h of reaction, due to the lack of light absorption in the wavelength of irradiation of visible-LED system (Fig. 5.4).

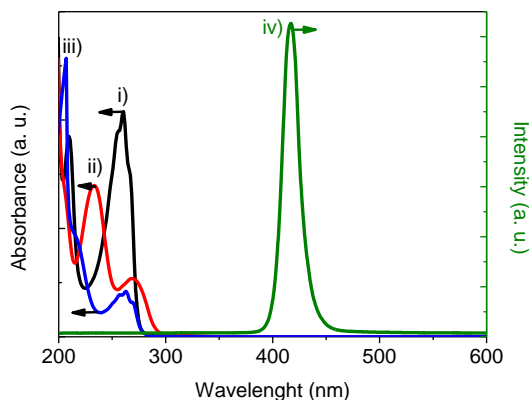


Fig. 5.4 Absorption spectra of i) 3-pyridinemethanol (3PM), ii) 3-pyridinecarboxaldehyde (3PC) and iii) vitamin B3 (VB3); iv) intensity of irradiation of visible LEDs ( $\lambda_{max} = 412\text{nm}$ ).

The concentration profiles of 3PM, 3PC and VB3 during the photocatalytic reactions are shown in Figs. 5.5a, b and c, respectively.

It is possible to observe the complete oxidation of 3PM in the presence of bulk GCN only after 7 h of reaction (Fig. 5.5a). In the case of GCN-500, the rate of alcohol oxidation was increased, with more than 95% of 3PM being converted after 5 h (Fig. 5.5a). GCN-A-620 was the photocatalyst that presented a faster conversion of 3PM, with total oxidation after 2 h of reaction (Fig. 5.5a). Regarding to the 3PC and VB3 production (Figs. 5.5b and c, respectively), similar behavior was observed, with GCN-A-620 reaching the highest production rate of both compounds. In fact, GCN-A-620 achieved near 0.09 mM of 3PC after 1 h of reaction (Fig. 5.5b) and 0.1 mM of VB3 after 6 h (Fig. 5.5c), representing a significant improvement when compared to bulk GCN (Fig. 5.5b and c). As previously mentioned, in the absence of a strong oxidizing agent, the partial oxidation of primary alcohols usually contemplates two stages, with a first oxidation to the aldehyde, followed by the over oxidation to the acid [8]. Through the analysis of the profiles of concentration of 3PC (Fig. 5.5b) and VB3 (Fig. 5.5c) it is possible to infer that the photocatalytic conversion of 3PM into VB3 occurs through an indirect pathway, being 3PC an intermediary compound. By determining the photocatalytic parameters  $X$ , and  $S$  and  $Y$  towards the production of both 3PC and VB3, it was possible to clearly compare the three materials. **All the catalysts proved to be highly selective for aldehyde production, with  $S > 99\%$  (Fig. 5.5d).** Bulk GCN achieved higher conversion and yield ( $> 95\%$ ) than GCN-500 and GCN-A-620 (Fig. 5.5d).

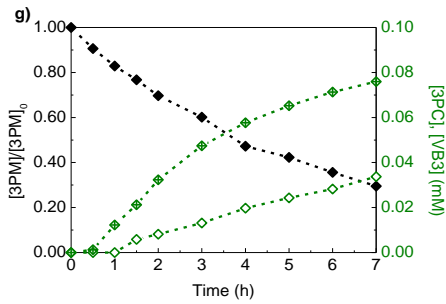
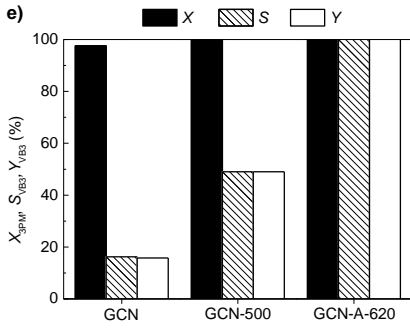
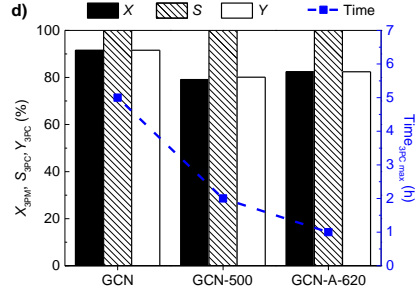
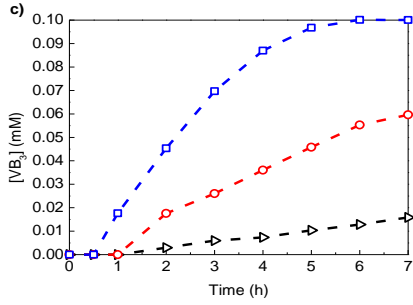
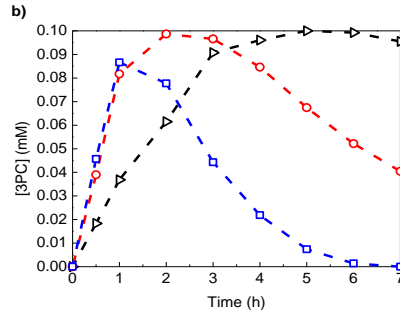
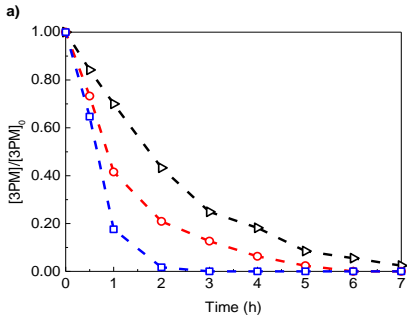


Fig. 5.5 a) Normalized 3PM, b) 3PC and c) VB3 concentrations over 7 h of irradiation ( $\lambda_{\max} = 412$  nm) using GCN ( $\triangleright$ ), GCN-500 ( $\circ$ ) and GCN-A-620 ( $\square$ ) as catalysts. d, e) X, S and Y achieved for the photooxidation of 3PM into 3PC and VB3 at the maximum of their concentration. f) Photograph of the immobilized GCN-A-620\_SA used in the photocatalytic reaction. g) Normalized 3PM ( $\blacklozenge$ ), 3PC ( $\blacklozenge$ ) and VB3 ( $\blacklozenge$ ) concentrations over 7 h reaction using GCN-A-620\_SA.

However, due to the slower conversion of 3PM, the maximum production of 3PC was only obtained after 5 h of reaction (Fig. 5.5d). Contrariwise, GCN-500 and GCN-A-620 showed an improved performance, by reaching ca. 80% of X and Y in shorter reaction times (2 h and 1 h, respectively; Fig. 5.5d). This relation was also observed in VB3 production (Fig. 5.5e), with GCN-500 and GCN-A-620 being more efficient than bulk GCN. In fact, after 7 h of reaction, GCN presented a very low selectivity (16%) and yield (15.8%) towards VB3 production (Fig. 5.5e). In the case of GCN-500, selectivity and yield increased to 49% (Fig. 5.5e). GCN-A-620 proved to be the best performing catalyst, achieving 100% of S and Y after 7 h of reaction (Fig. 5.5e).

As demonstrated in chapter, GCN-A-620 presents a highly irregular surface (Fig. 5.1c), with decreased crystallinity (Fig. 5.2), caused by the loss of nitrogen atoms (Table 5.2) during the post-treatment at high temperature (620°C) under nitrogen flow. This morphological alteration resulted in increased light absorption in visible range, and consequently, in the creation of mid-gap states located within the bandgap (Fig. 5.3a, Table 5.2). Moreover, the reduced recombination between  $e^-$  and the photogenerated  $h^+$  (Fig. 5.3b) contributes to a highly efficient oxidative process, favoring the conversion of 3PM into 3PC and VB3 when GCN-A-620 is used as photocatalyst.

In order to avoid the post-separation, the best performing catalyst (GCN-A-620) was immobilized in a sodium alginate membrane (GCN-A-620\_SA, Fig. 5.5f) and its performance was evaluated under the same operational conditions adopted for the powdered materials.

The immobilized catalyst proved to be able to produce both 3PC and VB3, achieving 0.075 mM and 0.034 mM after 7 h of irradiation, respectively (Fig. 5.5g). It is known that immobilized catalysts have a decreased interaction with target molecules, due to mass transfer limitations promoted by the support [68,332]. However, the elimination of a post-treatment step to remove powdered catalyst from the reaction medium can be a great advantage both from technological and economic points of view.

In Table 5.2 is presented a comparison between the studies found in literature (entries 1-5) on the photocatalytic conversion of 3PM into VB3 and the results obtained in the present study (entries 6-9).

As previously referred, TiO<sub>2</sub>-based materials are the most used photocatalysts in the synthesis of VB3 (Table 5.2, entries 1-5). However, due its metal-based character, novel and improved catalysts were synthesized in order to reduce (Table 5.2, entries 4 and 5) or even eliminate metallic compounds (Table 5.2, entries 6-9). The incorporation of carbon materials in composite catalysts with TiO<sub>2</sub> allowed to achieve a better relation between the values of *X* and *S* (Table 5.2, entries 4 and 5), contributing to the design of more efficient processes of synthesis. In fact, by using Ag@TiO<sub>2</sub>/g-C<sub>3</sub>N<sub>4</sub> as photocatalyst, a total conversion of 3PM with 100% selectivity towards VB3 production were achieved after 9 h of irradiation under air atmosphere, using a conventional light source (Table 5.2, entry 5). In the present work, all powdered GCN-based catalysts presented higher conversion of 3PM (> 98%; Table 5.2, entries 6-8) than the majority of the previously reported catalysts (Table 5.2, entries 1-4). By using the thermal post-treated catalysts (GCN-500 and GCN-A-620; Table 5.2, entries 7 and 8), the selectivity was three and six times higher, respectively, when compared to bulk GCN (Table 5.2, entry 6). The best performing catalyst, GCN-A-620 (Table 5.2, entry 8), achieved similar results those reported using Ag@TiO<sub>2</sub>/g-C<sub>3</sub>N<sub>4</sub> (Table 5.2, entry 5) in less time (7 h instead of 9 h). Moreover, the irradiation source adopted in the present study (visible-LED system) exhibits important environmental advantages when compared to the conventional halogen lamps, which accounts for the sustainability of the photocatalytic process here proposed. The promising results of conversion and selectivity (71% and 34%, respectively) obtained using the immobilized catalyst (GCN-A-620\_SA; Table 5.2, entry 9) opens up the possibility of using this process for the production of VB3 in continuous-flow reactors.

Analogous to the analysis performed in Table 4.4, section 4.9.3, Chapter 4, the energy efficiency (*E*) was determined for each photocatalytic system, according to the eq. 4.1.

Table 5.2 Comparison between the published results on the heterogeneous photocatalytic synthesis of vitamin B3 (VB3) through the conversion of 3-pyridinemethanol (3PM) and the present study.

Entry	Catalyst	Gas	Irradiation system	Power (W)	V (mL)	Reaction time (h)	X (%)	S (%)	Energy efficiency <sup>a</sup> (E)	Ref.
1	TiO <sub>2</sub>	Nitrogen	High-pressure UV	125	n.i.	0.75	30	87	n.d.	[209]
2	TiO <sub>2</sub> nanotubes	Air	Fluorescent lamp	24	150	n.i.	15	35	n.d.	[211]
3	Pt/TiO <sub>2</sub>	Air	Fluorescent lamp	100	150	3	15	45	2.63x10 <sup>2</sup>	[212]
4	TiO <sub>2</sub> /graphene	Nitrogen	Mercury lamp	125	n.i.	5	63	35	n.d.	[210]
5	Ag@TiO <sub>2</sub> /g-C <sub>3</sub> N <sub>4</sub>	Air	Halogen lamp	n.i.	150	9	100	100	n.d.	[213]
6	GCN	Air	Vis-LED	40	50	7	98	16	2.82x10 <sup>2</sup>	Present study
7	GCN-500						100	49	8.93x10 <sup>2</sup>	
8	GCN-A-620						100	100	0.179	
9	GCN-A-620_SA						71	34	4.29x10 <sup>2</sup>	

n.i. – not indicated; n.d. – not determined; <sup>a</sup> Units of E: mol<sub>VB3</sub> mL<sup>-1</sup> 3PM W<sup>-1</sup> h<sup>-1</sup>; X: Conversion; S: Selectivity

Due to the lack of information provided for the authors, this parameter was only determined for the work developed by Yurdakal et al. [212] (Table 5.2, entry 3) and for the reactions carried out during the present study (Table 5.2, entries 6-9).

As previously observed in the case of the production of *p*-anisaldehyde (Table 4.4, section 4.9.3, Chapter 4), the photocatalytic systems developed in the present study proved to have higher *E* than the published works (Table 5.2), revealing a significative reduction in the ecological impact of this synthesis process.

## 5.4 Conclusions

GCN-based photocatalysts (bulk GCN, GCN-500 and GCN-A-620) were successfully applied in the synthesis of vitamin B3 (VB3), through the oxidation of 3-pyridimethanol (3PM) under visible-LED radiation ( $\lambda_{max} = 412$  nm) in the presence of oxygen.

The oxidation of the starting alcohol (3PM) resulted in the formation of the respective aldehyde (3-pyridinecarboxaldehyde; 3PC) and the acid (VB3).

GCN-A-620 revealed to be highly efficient, with 100% of 3PM conversion and selectivity towards VB3 production after 7 h of irradiation, achieving the best result among all the catalysts already reported in literature.

GCN-A-620 presented a highly defective surface, with a significant reduction in its crystallinity and improved photoabsorption, when compared to the other tested materials. This irregular morphology caused by the presence of nitrogen vacancies in the heptazine rings, led to the creation of midgap states within the bandgap of the catalyst, which improved its oxidative activity.

The study involving the use of immobilized GCN-A-620 (GCN-A-620\_SA) revealed the great potential of this photocatalytic system to be used in real case applications.



## Part III



## Chapter 6

### ***Final remarks and future work***

The final chapter highlights the conclusions about the previous chapters. Suggestions for the future work are also proposed.



## 6.1 Final remarks

In the present dissertation, heterogeneous photocatalysis was studied as an alternative route to synthesize several organic compounds with wide application in chemical and pharmaceutical industry, namely aromatic aldehydes, and vitamin B3. In Table 6.1 is shown a compilation of the best photocatalytic results obtained in terms of conversion and selectivity for the target molecules synthesized during the present dissertation. The operational conditions adopted in each study are also presented.

Some important findings can be highlighted through the analysis of Table 6.1:

- i) the association between a metal-based catalyst (ZnO) with a carbon material (CNF) can effectively produce a hybrid photocatalyst with improved performance (10%CNF/ZnO), due to the electron scavenger character of the carbon phase (Table 6.1, entry 1);
- ii) the functional groups linked to the aromatic ring of the starting alcohol conditions the efficiency of the photocatalytic oxidation through their electron-donating or withdrawing character (Table 6.1, entries 1-4);
- iii) the hard-templating route proved to be effective in improving the photocatalytic performance of GCN-based materials (Table 6.1, entry 5) by tuning  $S_{BET}$ , through the induction of physical defects on their surface;
- iv) the addition of citric acid results in highly defective materials due to the presence of midgap states. These intermediary states act as electron scavengers, promoting an enhancement of visible light absorption and a significant reduction in the  $e^-/h^+$  recombination rate. Moreover, the increase in photocurrent proved to have a positive impact in the photocatalytic activity of GCN-based catalysts (Table 6.1, entry 6);
- v) the nitrogen vacancies present in the heptazine rings of the copolymerized GCN-based catalysts play a major role in the improvement of their photocatalytic activity (Table 6.1, entry 7). However, the choose of the copolymerization agent determines the extension of this impact. By exposing the copolymerized material to a thermal exfoliation process, the  $S_{BET}$  is sharply enhanced due to the splitting of layers, with a clear impact in its photocatalytic performance (Table 6.1, entry 8);
- vi) under nitrogen flow, the thermal post-treatment induces significant changes in crystal structure of GCN-based catalysts, with a high destruction of the graphite-like layers related with the loss of amino groups from the heptazine units. This alteration resulted in an improved photocatalytic performance (Table 6.1, entries 9 and 10), due

to the increase observed in light absorption in the visible range, with a great contribution of  $n-\pi^*$  electronic transitions in the excitation process;

Table 6.1 Compilation of the best photocatalytic results obtained for the target molecules synthesized during this PhD study.

Target molecule	Catalyst	Atmosphere	Irradiation system	Reaction time (h)	X (%)	S (%)
Vanillin	10%CNF/ZnO	Argon	UV-LED	1	6	67
Benzaldehyde				1.5	36	2
Piperonal				8	57	14
<i>p</i> -Anisaldehyde	GCN-UJ	Air	Vis-LED	1.5	89	84
<i>p</i> -Anisaldehyde	GCN-20CA-	Argon	Vis-LED	4	71	92
	GCN-BAR	Air	UV-LED	1.5	93	96
	GCN-BAR-500	Air	UV-LED	0.5	99	97
Vitamin B3	GCN-A-620	Air	Vis-LED	1	98	92
	GCN-A-620- GCN-A-620_SA	Air	Vis-LED	7	100 71	100 34

X: conversion; S: selectivity

Entry	1	2	3	4	5	6	7	8	9	10	11
-------	---	---	---	---	---	---	---	---	---	----	----

- vii) the promising performance of the immobilized GCN-based catalysts (Table 6.1, entry 11) in the oxidation process, allowed to foresee a successful application of this type of materials in a continuous-flow mode, avoiding the post-separation costs;
- viii) under deoxygenated conditions, the photocatalytic oxidation of alcohols by GCN-based catalysts is governed by the photogenerated  $h\nu^+$ , leaving  $e^-$  available to promote the reduction of  $H^+$  into  $H_2$ ; on the other hand, the presence of oxygen in the reaction medium leads to the generation of highly reactive  $O_2^{\cdot-}$ , which have also a significant contribution to the oxidative route;
- ix) the use of LEDs as radiation source allows to reduce the energetic input required to promote the activation of the photocatalysts, and, consequently, to reduce the ecological impact of the synthesis process.

## 6.2 Future work

Considering the conclusions of this research project, some suggestions are given to possibly develop in the future.

An interesting study relies on the application of GCN-based catalysts in other chemical reactions. In the present dissertation only oxidation/dehydrogenation processes were studied using alcohols as starting molecules. Due to their importance at industrial level, the study of the application of photocatalysis to other chemical transformations, such as the reduction of carbonyl compounds and nitrogen-containing molecules, carboxylations and cycloadditions, is of great interest.

Concerning the industrial application of the photocatalytic systems, the use of immobilized materials represents a major advantage, not only to avoid the post-separation costs but also to allow the continuous-flow operation. Therefore, new and improved techniques of immobilization may be developed in order to extend the potential applicability of GCN-based catalysts. Another important aspect relies in the development of reactor configurations providing both improved mass transfer and catalyst illumination and permitting operation under continuous-flow mode.









---

**References**

- [1] Xu, C.; Zhang, C.; Li, H.; Zhao, X.; Song, L.; Li, X. An Overview of Selective Oxidation of Alcohols: Catalysts, Oxidants and Reaction Mechanisms. *Catal. Surv. from Asia* **2016**, *20* (1), 13–22.
- [2] Sheldon, R. A. Recent Advances in Green Catalytic Oxidations of Alcohols in Aqueous Media. *Catal. Today* **2015**, *247*, 4–13.
- [3] Kopylovich, M.; Ribeiro, A.; Alegria, E.; Martins, N.; Martins, L.; Pombeiro, A. Catalytic Oxidation of Alcohols: Recent Advances. In *Advances in Organometallic Chemistry*; Pérez, P. J., Ed.; Elsevier Inc., 2015; Vol. 63, pp 91–174.
- [4] Sheldon, R. A.; Arends, I. W. C. E. Catalytic Oxidations of Alcohols. In *Advances in Catalytic Activation of Dioxygen by Metal Complexes*; Simándi, L. I., Ed.; Springer US: Boston, MA, 2002; pp 123–155.
- [5] Caron, S.; Dugger, R. W.; Ruggeri, S. G.; Ragan, J. A.; Ripin, D. H. B. Large-Scale Oxidations in the Pharmaceutical Industry. *Chem. Rev.* **2006**, *106* (7), 2943–2989.
- [6] Teles, J. H.; Hermans, I.; Franz, G.; Sheldon, R. A. Oxidation. In *Ullmann's Encyclopedia of Industrial Chemistry*; Wiley-VCH Verlag GmbH & Co. KGaA, 2015; pp 1–103.
- [7] Sheldon, R.; Arends, I.; Hanefeld, U. Catalytic Oxidations. In *Green Chemistry and Catalysis*; Wiley Online Books; Wiley-VCH Verlag GmbH & Co. KGaA, 2007; pp 133–221.
- [8] Smith, M. B.; March, J. *March's Advanced Organic Chemistry*, Sixth.; John Wiley & Sons, Inc.: Hoboken, New Jersey Published, 2007.
- [9] Anastas, P. T.; Warner, J. C. *Green Chemistry: Theory and Practice*; Oxford University Press: Oxford, 1998.
- [10] Albini, A.; Protti, S. *Paradigms in Green Chemistry and Technology*; Sharma, S. K., Ed.; Springer, 2016.
- [11] Dudeck, C.; Diehm, H.; Brunnmueller, F.; Meissner, B.; Fliege, W. Preparation of 3-Alkyl-Buten-1-Als. US4165342A, 1978.

- [12] Wegner, G.; Kaibel, G.; Therre, J.; Aquila, W.; Fuchs, H. Continuous Method for Producing Citral. WO2008/037693, 2008.
- [13] Lefferts, L.; van Ommen, J. G.; Ross, J. R. H. The Silver-Oxygen Interaction in Relation to Oxidative Dehydrogenation of Methanol. *Appl. Catal.* **1987**, *31* (2), 291–308.
- [14] Sun, Q.; Shen, B.; Fan, K.; Deng, J. Roles of Surface and Subsurface Oxygen in the Dehydrogenation of Methanol on Silver Surface. *Chem. Phys. Lett.* **2000**, *322* (1), 1–8.
- [15] Leupold, E.; Blau, W.; Baltes, H. Verfahren Zur Herstellung von Alkoxyessigsaeuren. DE2936123, 1981.
- [16] Ciriminna, R.; Pagliaro, M. Industrial Oxidations with Organocatalyst TEMPO and Its Derivatives. *Org. Process Res. Dev.* **2010**, *14* (1), 245–251.
- [17] Tojo, G.; Fernández, M. Selective Oxidations of Allylic and Benzylic Alcohols in the Presence of Saturated Alcohols. In *Oxidation of Alcohols to Aldehydes and Ketones: A Guide to Current Common Practice*; Springer: Boston, MA, 2006; pp 289–330.
- [18] Hewitt, B. D. Conversion of Bisnoralcohol to Bisnoraldehyde. WO/1995/016698, 1995.
- [19] Rossi, F.; Corcella, F.; Caldarelli, F. S.; Heidempergher, F.; Marchionni, C.; Augadro, M.; Cattaneo, M.; Ceriani, L.; Visentin, G.; Ventrella, G.; Pinciroli, V.; Ramella, G.; Candiani, I.; Bedeschi, A.; Tomasi, A.; Kline, B. J.; Martinez, C. A.; Yazbeck, D.; Kucera, D. J. Process Research and Development and Scale-up of a 4,4-Difluoro-3,3-Dimethylproline Derivative. *Org. Process Res. Dev.* **2008**, *12* (2), 322–338.
- [20] Kucera, D. J.; Saeed, N. L.; Scoot, W. R. Methods of Preparing Compounds Useful as Protease Inhibitors. WO 2005/054187 A1, 2005.
- [21] Tojo, G.; Fernández, M. *Oxidation of Primary Alcohols to Carboxylic Acids: A Guide to Current Common Practice*; Tojo, G., Ed.; Springer Science+Business Media, LLC, 2007.
- [22] Arends, I. W. C. E.; Sheldon, R. A. Modern Oxidation of Alcohols Using

- Environmentally Benign Oxidants. In *Modern Oxidation Methods*; Wiley Online Books; WILEY-VCH Verlag GmbH & Co. KGaA, Weinheim, 2010; pp 147–185.
- [23] Notari, B. Synthesis and Catalytic Properties of Titanium Containing Zeolites. *Innov. Zeolite Mater. Sci.* **1988**, *37*, 413–425.
- [24] Dijksman, A.; W. C. E. Arends, I.; A. Sheldon, R. Efficient Ruthenium–TEMPO-Catalysed Aerobic Oxidation of Aliphatic Alcohols into Aldehydes and Ketones. *Chem. Commun.* **1999**, No. 16, 1591–1592.
- [25] Corma, A.; Fornés, V.; Iborra, S.; Mifsud, M.; Renz, M. One-Pot Synthesis of Phenols from Aromatic Aldehydes by Baeyer–Villiger Oxidation with H<sub>2</sub>O<sub>2</sub> Using Water-Tolerant Lewis Acids in Molecular Sieves. *J. Catal.* **2004**, *221* (1), 67–76.
- [26] Wohlgemuth, R. Biocatalysis—Key to Sustainable Industrial Chemistry. *Curr. Opin. Biotechnol.* **2010**, *21* (6), 713–724.
- [27] Tao, J.; Xu, J.-H. Biocatalysis in Development of Green Pharmaceutical Processes. *Curr. Opin. Chem. Biol.* **2009**, *13* (1), 43–50.
- [28] Fagnoni, M.; Dondi, D.; Ravelli, D.; Albini, A. Photocatalysis for the Formation of the C-C Bond. *Chem. Rev.* **2007**, *107* (6), 2725–2756.
- [29] Albini, A. *Paradigms in Green Chemistry and Technology*; Springer, 2016.
- [30] Balzani, V.; Credi, A.; Venturi, M. Photochemical Conversion of Solar Energy. *ChemSusChem* **2008**, *1* (1–2), 26–58.
- [31] Protti, S.; Fagnoni, M. The Sunny Side of Chemistry: Green Synthesis by Solar Light. *Photochem. Photobiol. Sci.* **2009**, *8* (11), 1499–1516.
- [32] Ciamician, G. The Photochemistry of the Future. *Science* (80-. ). **1912**, *36* (926), 385–394.
- [33] Paternò, E.; Chieffi, G. Sintesi in Chimica Organica per Mezzo Della Luce. Nota II. Composti Degli Idrocarburi Non Saturi Con Aldeidi e Chetoni. *Gazz. Chim. Ital* **1909**, *39*, 341–361.
- [34] Schonberg, A.; Mustafa, A. Reactions of Non-Enolizable Ketones in Sunlight. *Chem. Rev.* **1947**, *40* (2), 181–200.

- [35] Wyman, G. M. The Cis-Trans Isomerization of Conjugated Compounds. *Chem. Rev.* **1955**, *55* (4), 625–657.
- [36] Yoon, T. P.; Ischay, M. A.; Du, J. Visible Light Photocatalysis as a Greener Approach to Photochemical Synthesis. *Nat. Chem.* **2010**, *2* (7), 527–532.
- [37] Dong, H.; Zeng, G.; Tang, L.; Fan, C.; Zhang, C.; He, X.; He, Y. An Overview on Limitations of TiO<sub>2</sub>-Based Particles for Photocatalytic Degradation of Organic Pollutants and the Corresponding Countermeasures. *Water Res.* **2015**, *79*, 128–146.
- [38] Fresno, F.; Portela, R.; Suárez, S.; Coronado, J. M. Photocatalytic Materials: Recent Achievements and near Future Trends. *J. Mater. Chem. A* **2014**, *2* (9), 2863–2884.
- [39] Halpern, A. Ascaridole in Chenopodium Oil. IV. The Synthesis of Ascaridole. *J. Am. Pharm. Assoc.* **1951**, *40* (2), 68–71.
- [40] Zhu, S.; Wang, D. Photocatalysis: Basic Principles, Diverse Forms of Implementations and Emerging Scientific Opportunities. *Adv. Energy Mater.* **2017**, *7* (23), 1–24.
- [41] Fujishima, A.; Honda, K. Electrochemical Photolysis of Water at a Semiconductor Electrode. *Nature* **1972**, *238* (5358), 37–38.
- [42] Gkika, E.; Troupis, A.; Hiskia, A.; Papaconstantinou, E. Photocatalytic Reduction of Chromium and Oxidation of Organics by Polyoxometalates. *Appl. Catal. B Environ.* **2006**, *62* (1), 28–34.
- [43] Limburg, B.; Bouwman, E.; Bonnet, S. Rate and Stability of Photocatalytic Water Oxidation Using [Ru(Bpy)<sub>3</sub>]<sup>2+</sup> as Photosensitizer. *ACS Catal.* **2016**, *6* (8), 5273–5284.
- [44] Schneider, T. W.; Ertem, M. Z.; Muckerman, J. T.; Angeles-Boza, A. M. Mechanism of Photocatalytic Reduction of CO<sub>2</sub> by Re(Bpy)(CO)<sub>3</sub>Cl from Differences in Carbon Isotope Discrimination. *ACS Catal.* **2016**, *6* (8), 5473–5481.
- [45] Sharma, S.; Sharma, A. Recent Advances in Photocatalytic Manipulations of Rose Bengal in Organic Synthesis. *Org. Biomol. Chem.* **2019**, *17* (18), 4384–4405.

- [46] Alonso-de Castro, S.; Ruggiero, E.; Ruiz-de-Angulo, A.; Rezabal, E.; Mareque-Rivas, J. C.; Lopez, X.; López-Gallego, F.; Salassa, L. Riboflavin as a Bioorthogonal Photocatalyst for the Activation of a Pt (IV) Prodrug. *Chem. Sci.* **2017**, *8* (6), 4619–4625.
- [47] Markushyna, Y.; Smith, C. A.; Savateev, A. Organic Photocatalysis: Carbon Nitride Semiconductors vs. Molecular Catalysts. *European J. Org. Chem.* **2020**, *2020* (10), 1294–1309.
- [48] Durgalakshmi, D.; Ajay Rakkesh, R.; Rajendran, S.; Naushad, M. Green Photocatalyst for Diverge Applications. In *Green Photocatalysts for Energy and Environmental Process*; Rajendran, S., Naushad, M., Ponce, L. C., Lichtfouse, E., Eds.; Springer International Publishing: Switzerland, 2019; pp 1–18.
- [49] Chen, X.; Shen, S.; Guo, L.; Mao, S. S. Semiconductor-Based Photocatalytic Hydrogen Generation. *Chem. Rev.* **2010**, *110* (11), 6503–6570.
- [50] Chan, S. H. S.; Yeong Wu, T.; Juan, J. C.; Teh, C. Y. Recent Developments of Metal Oxide Semiconductors as Photocatalysts in Advanced Oxidation Processes (AOPs) for Treatment of Dye Waste-Water. *J. Chem. Technol. Biotechnol.* **2011**, *86* (9), 1130–1158.
- [51] Friedmann, D.; Hakki, A.; Kim, H.; Choi, W.; Bahnemann, D. Heterogeneous Photocatalytic Organic Synthesis: State-of-the-Art and Future Perspectives. *Green Chem.* **2016**, *18* (20), 5391–5411.
- [52] Herrmann, J.-M. Fundamentals and Misconceptions in Photocatalysis. *J. Photochem. Photobiol. A Chem.* **2010**, *216* (2), 85–93.
- [53] Kisch, H. Visible Light Redox Activation of Small Molecules by Semiconductor Photocatalysis. *EPA Newsl.* **2016**, *89–90*, 170–182.
- [54] Kisch, H. Semiconductor Photocatalysis - Mechanistic and Synthetic Aspects. *Angew. Chemie - Int. Ed.* **2013**, *52* (3), 812–847.
- [55] Hennig, H. Semiconductor Photocatalysis. In *Semiconductor Photocatalysis: Principles and Applications*. By Horst Kisch; Wiley-VCH Verlag GmbH & Co. KGaA, 2015; p 85.

- [56] Mendive, C.; Bahnemann, D. Mechanisms in Heterogeneous Photocatalysis. In *Encyclopedia of Materials: Science and Technology*; Buschow, K. H. J., Ed.; Elsevier Ltd, 2011; pp 1–5.
- [57] Gerischer, H.; Heller, A. The Role of Oxygen in Photooxidation of Organic Molecules on Semiconductor Particles. *J. Phys. Chem.* **1991**, *95* (13), 5261–5267.
- [58] Emeline, A. V.; Kuznetsov, V. N.; Ryabchuk, V. K.; Serpone, N. Heterogeneous Photocatalysis: Basic Approaches and Terminology. In *New and Future Developments in Catalysis*; Suib, S. L. B. T., Ed.; Elsevier B. V.: Amsterdam, 2013; pp 1–47.
- [59] Zhang, F.; Wang, X.; Liu, H.; Liu, C.; Wan, Y.; Long, Y.; Cai, Z. Recent Advances and Applications of Semiconductor Photocatalytic Technology. *Appl. Sci.* **2019**, *9* (12).
- [60] Herrmann, J.-M. Heterogeneous Photocatalysis: Fundamentals and Applications to the Removal of Various Types of Aqueous Pollutants. *Catal. Today* **1999**, *53* (1), 115–129.
- [61] Nosaka, Y.; Nosaka, A. Understanding Hydroxyl Radical ( $\bullet\text{OH}$ ) Generation Processes in Photocatalysis. *ACS Energy Lett.* **2016**, *1* (2), 356–359.
- [62] Torres-Pinto, A.; Sampaio, M. J.; Silva, C. G.; Faria, J. L.; Silva, A. M. T. Metal-Free Carbon Nitride Photocatalysis with in Situ Hydrogen Peroxide Generation for the Degradation of Aromatic Compounds. *Appl. Catal. B Environ.* **2019**, *252*, 128–137.
- [63] Garg, A.; Singhania, T.; Singh, A.; Sharma, S.; Rani, S.; Neogy, A.; Yadav, S. R.; Sangal, V. K.; Garg, N. Photocatalytic Degradation of Bisphenol-A Using N, Co Codoped  $\text{TiO}_2$  Catalyst under Solar Light. *Sci. Rep.* **2019**, *9* (1), 765.
- [64] Song, F.; Li, W.; Sun, Y. Metal-Organic Frameworks and Their Derivatives for Photocatalytic water Splitting. *Inorganics* **2017**, *5* (3).
- [65] Malato, S.; Fernández-Ibáñez, P.; Maldonado, M. I.; Blanco, J.; Gernjak, W. Decontamination and Disinfection of Water by Solar Photocatalysis: Recent Overview and Trends. *Catal. Today* **2009**, *147* (1), 1–59.



- [66] Yang, Y.; Zeng, G.; Huang, D.; Zhang, C.; He, D.; Zhou, C.; Wang, W.; Xiong, W.; Li, X.; Li, B.; Dong, W.; Zhou, Y. Molecular Engineering of Polymeric Carbon Nitride for Highly Efficient Photocatalytic Oxytetracycline Degradation and H<sub>2</sub>O<sub>2</sub> Production. *Appl. Catal. B Environ.* **2020**, *272*, 118970.
- [67] Moreira, N. F. F.; Sampaio, M. J.; Ribeiro, A. R.; Silva, C. G.; Faria, J. L.; Silva, A. M. T. Metal-Free g-C<sub>3</sub>N<sub>4</sub> Photocatalysis of Organic Micropollutants in Urban Wastewater under Visible Light. *Appl. Catal. B Environ.* **2019**, *248*, 184–192.
- [68] Fernandes, R. A.; Sampaio, M. J.; Dražić, G.; Faria, J. L.; Silva, C. G. Efficient Removal of Parabens from Real Water Matrices by a Metal-Free Carbon Nitride Photocatalyst. *Sci. Total Environ.* **2019**, *716*, 135346.
- [69] Velegraki, T.; Hapeshi, E.; Fatta-Kassinos, D.; Poulios, I. Solar-Induced Heterogeneous Photocatalytic Degradation of Methyl-Paraben. *Appl. Catal. B Environ.* **2015**, *178*, 2–11.
- [70] Svoboda, L.; Praus, P.; Lima, M. J.; Sampaio, M. J.; Matýsek, D.; Ritz, M.; Dvorský, R.; Faria, J. L.; Silva, C. G. Graphitic Carbon Nitride Nanosheets as Highly Efficient Photocatalysts for Phenol Degradation under High-Power Visible LED Irradiation. *Mater. Res. Bull.* **2018**, *100*, 322–332.
- [71] Sampaio, M. J.; Bacsá, R. R.; Benyounes, A.; Axet, R.; Serp, P.; Silva, C. G.; Silva, A. M. T.; Faria, J. L. Synergistic Effect between Carbon Nanomaterials and ZnO for Photocatalytic Water Decontamination. *J. Catal.* **2015**, *331*, 172–180.
- [72] Sampaio, M. J.; Marques, R. R. N.; Tavares, P. B.; Faria, J. L.; Silva, A. M. T.; Silva, C. G. Tailoring the Properties of Immobilized Titanium Dioxide/Carbon Nanotube Composites for Photocatalytic Water Treatment. *J. Environ. Chem. Eng.* **2013**, *1* (4), 945–953.
- [73] Shen, X.; Shi, Y.; Shao, H.; Liu, Y.; Zhai, Y. Synthesis and Photocatalytic Degradation Ability Evaluation for Rhodamine B of ZnO@SiO<sub>2</sub> Composite with Flower-like Structure. *Water Sci. Technol.* **2020**, *80* (10), 1986–1995.
- [74] Ding, H.; Han, D.; Han, Y.; Liang, Y.; Liu, X.; Li, Z.; Zhu, S.; Wu, S. Visible Light Responsive CuS/ Protonated g-C<sub>3</sub>N<sub>4</sub> Heterostructure for Rapid

- Sterilization. *J. Hazard. Mater.* **2020**, 393, 122423.
- [75] Zhou, L.; Cai, M.; Zhang, X.; Cui, N.; Chen, G.; Zou, G. In Situ Nitrogen-Doped Black TiO<sub>2</sub> with Enhanced Visible-Light-Driven Photocatalytic Inactivation of *Microcystis Aeruginosa* Cells: Synthesis, Performance and Mechanism. *Appl. Catal. B Environ.* **2020**, 272, 119019.
- [76] Peeters, H.; Keulemans, M.; Nuyts, G.; Vanmeert, F.; Li, C.; Minjauw, M.; Detavernier, C.; Bals, S.; Lenaerts, S.; Verbruggen, S. W. Plasmonic Gold-Embedded TiO<sub>2</sub> Thin Films as Photocatalytic Self-Cleaning Coatings. *Appl. Catal. B Environ.* **2020**, 267, 118654.
- [77] Liu, Y.; Yu, Z.; Peng, Y.; Shao, L.; Li, X.; Zeng, H. A Novel Photocatalytic Self-Cleaning TiO<sub>2</sub> Nanorods Inserted Graphene Oxide-Based Nanofiltration Membrane. *Chem. Phys. Lett.* **2020**, 749, 137424.
- [78] Pedrosa, M.; Sampaio, M. J.; Horvat, T.; Nunes, O. C.; Dražić, G.; Rodrigues, A. E.; Figueiredo, J. L.; Silva, C. G.; Silva, A. M. T.; Faria, J. L. Visible-Light-Induced Self-Cleaning Functional Fabrics Using Graphene Oxide/Carbon Nitride Materials. *Appl. Surf. Sci.* **2019**, 497, 143757.
- [79] Wang, Z.; Li, C.; Domen, K. Recent Developments in Heterogeneous Photocatalysts for Solar-Driven Overall Water Splitting. *Chem. Soc. Rev.* **2019**, 48 (7), 2109–2125.
- [80] Acar, C.; Dincer, I.; Zamfirescu, C. A Review on Selected Heterogeneous Photocatalysts for Hydrogen Production. *Int. J. Energy Res.* **2014**, 38 (15), 1903–1920.
- [81] Naffati, N.; Sampaio, M. J.; Da Silva, E. S.; Nsib, M. F.; Arfaoui, Y.; Houas, A.; Faria, J. L.; Silva, C. G. Carbon-Nanotube/TiO<sub>2</sub> Materials Synthesized by a One-Pot Oxidation/Hydrothermal Route for the Photocatalytic Production of Hydrogen from Biomass Derivatives. *Mater. Sci. Semicond. Process.* **2020**, 115, 105098.
- [82] Silva, C. G.; Sampaio, M. J.; Marques, R. R. N.; Ferreira, L. A.; Tavares, P. B.; Silva, A. M. T.; Faria, J. L. Photocatalytic Production of Hydrogen from Methanol and Saccharides Using Carbon Nanotube-TiO<sub>2</sub> Catalysts. *Appl. Catal. B Environ.* **2015**, 178, 82–90.

- 
- [83] Sampaio, M. J.; Oliveira, J. W. L.; Sombrio, C. I. L.; Baptista, D. L.; Teixeira, S. R.; Carabineiro, S. A. C.; Silva, C. G.; Faria, J. L. Photocatalytic Performance of Au/ZnO Nanocatalysts for Hydrogen Production from Ethanol. *Appl. Catal. A Gen.* **2016**, *518*, 198–205.
- [84] Corma, A.; Garcia, H. Photocatalytic Reduction of CO<sub>2</sub> for Fuel Production: Possibilities and Challenges. *J. Catal.* **2013**, *308*, 168–175.
- [85] Hurtado, L.; Natividad, R.; García, H. Photocatalytic Activity of Cu<sub>2</sub>O Supported on Multi Layers Graphene for CO<sub>2</sub> Reduction by Water under Batch and Continuous Flow. *Catal. Commun.* **2016**, *84*, 30–35.
- [86] Han, C.; Wang, B.; Wu, N.; Shen, S.; Wang, Y. Deep and Selective Photoreduction of CO<sub>2</sub> to CH<sub>4</sub> over Ultrafine Pt Nanoparticles-Decorated SiC Nanosheets. *Appl. Surf. Sci.* **2020**, *515*, 145952.
- [87] Michelin, C.; Hoffmann, N. Photocatalysis Applied to Organic Synthesis – A Green Chemistry Approach. *Curr. Opin. Green Sustain. Chem.* **2018**, *10*, 40–45.
- [88] Pastrana-Martínez, L. M.; Silva, A. M. T.; Fonseca, N. N. C.; Vaz, J. R.; Figueiredo, J. L.; Faria, J. L. Photocatalytic Reduction of CO<sub>2</sub> with Water into Methanol and Ethanol Using Graphene Derivative–TiO<sub>2</sub> Composites: Effect of PH and Copper (I) Oxide. *Top. Catal.* **2016**, *59* (15), 1279–1291.
- [89] Yurdakal, S.; Tek, B. S.; Degirmenci, Ç.; Palmisano, G. Selective Photocatalytic Oxidation of Aromatic Alcohols in Solar-Irradiated Aqueous Suspensions of Pt, Au, Pd and Ag Loaded TiO<sub>2</sub> Catalysts. *Catal. Today* **2017**, *281, Part*, 53–59.
- [90] Gonzalez, M. A.; Howell, S. G.; Sikdar, S. K. Photocatalytic Selective Oxidation of Hydrocarbons in the Aqueous Phase. *J. Catal.* **1999**, *183* (1), 159–162.
- [91] Carneiro, J. T.; Moulijn, J. A.; Mul, G. Photocatalytic Oxidation of Cyclohexane by Titanium Dioxide: Catalyst Deactivation and Regeneration. *J. Catal.* **2010**, *273* (2), 199–210.
- [92] Lima, M. J.; Tavares, P. B.; Silva, A. M. T.; Silva, C. G.; Faria, J. L. Selective Photocatalytic Oxidation of Benzyl Alcohol to Benzaldehyde by
-

- Using Metal-Loaded g-C<sub>3</sub>N<sub>4</sub> Photocatalysts. *Catal. Today* **2017**, *287*, 70–77.
- [93] Fujihira, M.; Satoh, Y.; Osa, T. Heterogeneous Photocatalytic Oxidation of Aromatic Compounds on TiO<sub>2</sub>. *Nature* **1981**, *293* (5829), 206–208.
- [94] Gaya, U. I.; Abdullah, A. H. Heterogeneous Photocatalytic Degradation of Organic Contaminants over Titanium Dioxide: A Review of Fundamentals, Progress and Problems. *J. Photochem. Photobiol. C Photochem. Rev.* **2008**, *9* (1), 1–12.
- [95] Gołębiewska, A.; Kobylański, M. P.; Zaleska-Medynska, A. Fundamentals of Metal Oxide-Based Photocatalysis. In *Metal Oxide-Based Photocatalysis: Fundamentals and Prospects for Application*; Korotcenkov, G., Ed.; Elsevier Inc., 2018; pp 3–50.
- [96] Ohtani, B.; Prieto-Mahaney, O. O.; Li, D.; Abe, R. What Is Degussa (Evonik) P25? Crystalline Composition Analysis, Reconstruction from Isolated Pure Particles and Photocatalytic Activity Test. *J. Photochem. Photobiol. A Chem.* **2010**, *216* (2), 179–182.
- [97] Luttrell, T.; Halpegamage, S.; Tao, J.; Kramer, A.; Sutter, E.; Batzill, M. Why Is Anatase a Better Photocatalyst than Rutile? - Model Studies on Epitaxial TiO<sub>2</sub> Films. *Sci. Rep.* **2014**, *4* (1), 4043.
- [98] Hurum, D. C.; Agrios, A. G.; Gray, K. A.; Rajh, T.; Thurnauer, M. C. Explaining the Enhanced Photocatalytic Activity of Degussa P25 Mixed-Phase TiO<sub>2</sub> Using EPR. *J. Phys. Chem. B* **2003**, *107* (19), 4545–4549.
- [99] Grabowska, E.; Marchelek, M.; Paszkiewicz-Gawron, M.; Zaleska-Medynska, A. Metal Oxide Photocatalysts. In *Metal Oxide-Based Photocatalysis: Fundamentals and Prospects for Application*; Korotcenkov, G., Ed.; Elsevier Inc., 2018; pp 51–209.
- [100] Silva, C. G.; Sampaio, M. J.; Carabineiro, S. A. C.; Oliveira, J. W. L.; Baptista, D. L.; Bacsa, R.; Machado, B. F.; Serp, P.; Figueiredo, J. L.; Silva, A. M. T.; Faria, J. L. Developing Highly Active Photocatalysts: Gold-Loaded ZnO for Solar Phenol Oxidation. *J. Catal.* **2014**, *316*, 182–190.
- [101] Coleman, V. A.; Jagadish, C. Basic Properties and Applications of ZnO. In

- 
- Zinc Oxide Bulk, Thin Films and Nanostructures*; Jagadish, C., Pearton, S., Eds.; Elsevier Ltd, 2006.
- [102] Moezzi, A.; McDonagh, A. M.; Cortie, M. B. Zinc Oxide Particles: Synthesis, Properties and Applications. *Chem. Eng. J.* **2012**, *185*, 1–22.
- [103] Lu, C.; Wu, Y.; Mai, F.; Chung, W.; Wu, C.; Lin, W.; Chen, C. Degradation Efficiencies and Mechanisms of the ZnO-Mediated Photocatalytic Degradation of Basic Blue 11 under Visible Light Irradiation. *J. Mol. Catal. A Chem.* **2009**, *310* (1), 159–165.
- [104] Qi, K.; Cheng, B.; Yu, J.; Ho, W. Review on the Improvement of the Photocatalytic and Antibacterial Activities of ZnO. *J. Alloys Compd.* **2017**, *727*, 792–820.
- [105] Kumar, S.; Reddy, N. L.; Kumar, A.; Shankar, M. V.; Krishnan, V. Two Dimensional N-Doped ZnO-Graphitic Carbon Nitride Nanosheets Heterojunctions with Enhanced Photocatalytic Hydrogen Evolution. *Int. J. Hydrogen Energy* **2017**, *43* (8), 3988–4002.
- [106] Fernandes, R. A.; Sampaio, M. J.; Da Silva, E. S.; Serp, P.; Faria, J. L.; Silva, C. G. Synthesis of Selected Aromatic Aldehydes under UV-LED Irradiation over a Hybrid Photocatalyst of Carbon Nanofibers and Zinc Oxide. *Catal. Today* **2019**, *328*, 286–292.
- [107] Sampaio, M. J.; Benyounes, A.; Serp, P.; Faria, J. L.; Silva, C. G. Photocatalytic Synthesis of Vanillin Using N-Doped Carbon Nanotubes/ZnO Catalysts under UV-LED Irradiation. *Appl. Catal. A Gen.* **2018**, *551*, 71–78.
- [108] Di Mauro, A.; Fragalà, M. E.; Privitera, V.; Impellizzeri, G. ZnO for Application in Photocatalysis: From Thin Films to Nanostructures. *Mater. Sci. Semicond. Process.* **2017**, *69*, 44–51.
- [109] Ong, C. B.; Ng, L. Y.; Mohammad, A. W. A Review of ZnO Nanoparticles as Solar Photocatalysts: Synthesis, Mechanisms and Applications. *Renew. Sustain. Energy Rev.* **2018**, *81*, 536–551.
- [110] Thapa, D.; Huso, J.; Morrison, J. L.; Corolewski, C. D.; McCluskey, M. D.; Bergman, L. Achieving Highly-Enhanced UV Photoluminescence and Its
-

- Origin in ZnO Nanocrystalline Films. *Opt. Mater. (Amst)*. **2016**, *58*, 382–389.
- [111] Ola, O.; Maroto-Valer, M. M. Review of Material Design and Reactor Engineering on TiO<sub>2</sub> Photocatalysis for CO<sub>2</sub> Reduction. *J. Photochem. Photobiol. C Photochem. Rev.* **2015**, *24*, 16–42.
- [112] de Walle, A. J.; Van, C. G. Fundamentals of Zinc Oxide as a Semiconductor. *Reports Prog. Phys.* **2009**, *72* (12), 126501.
- [113] Wei, L.; Yu, C.; Zhang, Q.; Liu, H.; Wang, Y. TiO<sub>2</sub>-Based Heterojunction Photocatalysts for Photocatalytic Reduction of CO<sub>2</sub> into Solar Fuels. *J. Mater. Chem. A* **2018**, *6* (45), 22411–22436.
- [114] Ge, J.; Zhang, Y.; Park, S. J. Recent Advances in Carbonaceous Photocatalysts with Enhanced Photocatalytic Performances: A Mini Review. *Materials (Basel)*. **2019**, *12* (12).
- [115] Ong, W.-J.; Tan, L.-L.; Ng, Y. H.; Yong, S.-T.; Chai, S.-P. Graphitic Carbon Nitride (g-C<sub>3</sub>N<sub>4</sub>)-Based Photocatalysts for Artificial Photosynthesis and Environmental Remediation: Are We a Step Closer to Achieving Sustainability? *Chem. Rev.* **2016**, *116* (12), 7159–7329.
- [116] Wang, X.; Maeda, K.; Thomas, A.; Takanabe, K.; Xin, G.; Carlsson, J. M.; Domen, K.; Antonietti, M. A Metal-Free Polymeric Photocatalyst for Hydrogen Production from Water under Visible Light. *Nat. Mater.* **2009**, *8* (1), 76–80.
- [117] Lin, B.; Yang, G.; Yang, B.; Zhao, Y. Construction of Novel Three Dimensionally Ordered Macroporous Carbon Nitride for Highly Efficient Photocatalytic Activity. *Appl. Catal. B Environ.* **2016**, *198*, 276–285.
- [118] Luo, L.; Zhang, A.; Janik, M. J.; Song, C.; Guo, X. Facile Fabrication of Metal-Free Urchin-like g-C<sub>3</sub>N<sub>4</sub> with Superior Photocatalytic Activity. *RSC Adv.* **2016**, *6* (97), 94496–94501.
- [119] Gu, S.; Xie, J.; Li, C. M. Hierarchically Porous Graphitic Carbon Nitride: Large-Scale Facile Synthesis and Its Application toward Photocatalytic Dye Degradation. *RSC Adv.* **2014**, *4* (103), 59436–59439.
- [120] Lima, M. J.; Silva, A. M. T.; Silva, C. G.; Faria, J. L. Graphitic Carbon

- Nitride Modified by Thermal, Chemical and Mechanical Processes as Metal-Free Photocatalyst for the Selective Synthesis of Benzaldehyde from Benzyl Alcohol. *J. Catal.* **2017**, *353*, 44–53.
- [121] Bellardita, M.; García-López, E. I.; Marci, G.; Krivtsov, I.; García, J. R.; Palmisano, L. Selective Photocatalytic Oxidation of Aromatic Alcohols in Water by Using P-Doped g-C<sub>3</sub>N<sub>4</sub>. *Appl. Catal. B Environ.* **2018**, *220*, 222–233.
- [122] Liu, X.; Li, C.; Zhang, B.; Yuan, M.; Ma, Y.; Kong, F. A Facile Strategy for Photocatalytic Degradation of Seven Neonicotinoids over Sulfur and Oxygen Co-Doped Carbon Nitride. *Chemosphere* **2020**, *253*, 126672.
- [123] Wang, M.; Zhou, X.; Cai, X.; Wang, H.; Fang, Y.; Zhong, X. Hierarchically Porous, Ultrathin N-Doped Carbon Nanosheets Embedded with Highly Dispersed Cobalt Nanoparticles as Efficient Sulfur Host for Stable Lithium–Sulfur Batteries. *J. Energy Chem.* **2020**, *50*, 106–114.
- [124] Zhang, M.; Duan, Y.; Jia, H.; Wang, F.; Wang, L.; Su, Z.; Wang, C. Defective Graphitic Carbon Nitride Synthesized by Controllable Co-Polymerization with Enhanced Visible Light Photocatalytic Hydrogen Evolution. *Catal. Sci. Technol.* **2017**, *7* (2), 452–458.
- [125] Zhang, J.; Chen, X.; Takanebe, K.; Maeda, K.; Domen, K.; Epping, J. D.; Fu, X.; Antonietti, M.; Wang, X. Synthesis of a Carbon Nitride Structure for Visible-Light Catalysis by Copolymerization. *Angew. Chemie Int. Ed.* **2010**, *49* (2), 441–444.
- [126] Kim, H.; Gim, S.; Jeon, T. H.; Kim, H.; Choi, W. Distorted Carbon Nitride Structure with Substituted Benzene Moieties for Enhanced Visible Light Photocatalytic Activities. *ACS Appl. Mater. Interfaces* **2017**, *9* (46), 40360–40368.
- [127] Kong, L.; Yan, J.; Li, P.; Liu, S. F. Fe<sub>2</sub>O<sub>3</sub>/C-C<sub>3</sub>N<sub>4</sub>-Based Tight Heterojunction for Boosting Visible-Light-Driven Photocatalytic Water Oxidation. *ACS Sustain. Chem. Eng.* **2018**, *6* (8), 10436–10444.
- [128] Luo, B.; Song, R.; Geng, J.; Jing, D.; Huang, Z. Strengthened Spatial Charge Separation over Z-Scheme Heterojunction Photocatalyst for Efficient Photocatalytic H<sub>2</sub> Evolution. *Appl. Surf. Sci.* **2019**, *475*, 453–461.

- [129] Pichat, P.; Courbon, H.; Disdier, J.; Mozzanega, M.-N.; Herrmann, J.-M. Heterogeneous Photocatalysis: NO Decomposition and Oxidation of Butanols by No over TiO<sub>2</sub> at Room Temperature. *Stud. Surf. Sci. Catal.* **1981**, 7 (Part B), 1498–1499.
- [130] Cunningham, J.; Hodnett, B. K. Kinetic Studies of Secondary Alcohol Photo-Oxidation on ZnO and TiO<sub>2</sub> at 348 K Studied by Gas-Chromatographic Analysis. *J. Chem. Soc. Faraday Trans. 1 Phys. Chem. Condens. Phases* **1981**, 77 (11), 2777–2801.
- [131] Verma, R. S.; Padalia, R. C.; Singh, V. R.; Goswami, P.; Chauhan, A.; Bhukya, B. Natural Benzaldehyde from *Prunus Persica* (L.) Batsch. *Int. J. Food Prop.* **2017**, 20 (sup2), 1259–1263.
- [132] Brenna, E.; Fronza, G.; Fuganti, C.; Gatti, F. G.; Serra, S. Biotechnological Tools to Produce Natural Flavors and Methods to Authenticate Their Origin. In *Innovation in Food Engineering: New techniques and products*; Passos, M. L., Ribeiro, C. P., Eds.; Taylor & Francis Group, LLC, 2010; pp 81–106.
- [133] Marotta, R.; Di Somma, I.; Spasiano, D.; Andreozzi, R.; Caprio, V. Selective Oxidation of Benzyl Alcohol to Benzaldehyde in Water by TiO<sub>2</sub>/Cu(II)/UV Solar System. *Chem. Eng. J.* **2011**, 172 (1), 243–249.
- [134] Machado, G. D. C.; Gomes, M.; Antunes, O. A. C.; Oestreicher, E. G. Enzymatic Resolution of DL-Phenylglycine. *Process Biochem.* **2005**, 40 (10), 3186–3189.
- [135] Cox, M.; Klass, G.; Koo, C. W. M. Manufacturing By-Products from, and Stereochemical Outcomes of the Biotransformation of Benzaldehyde Used in the Synthesis of Methamphetamine. *Forensic Sci. Int.* **2009**, 189 (1), 60–67.
- [136] Shukla, V. B.; Kulkarni, P. R. L-Phenylacetylcarbinol (L-PAC): Biosynthesis and Industrial Applications. *World J. Microbiol. Biotechnol.* **2000**, 16 (6), 499–506.
- [137] Peng, H.-N.; Ye, L.-M.; Zhang, M.; Yang, Y.-C.; Zheng, J. Synthesis and Antimicrobial Activity of 3,4-Dihydropyrimidin-2(1H)-One Derivatives Containing a Hydrazone Moiety. *Heterocycl. Commun.* **2018**, 24 (2), 113–



- 117.
- [138] Bruhne, F.; Lipper, K. Process for the Preparation of Benzaldehyde. 4229379, 1980.
- [139] Kantam, M. L.; Choudary, B. M.; Sreekanth, P.; Rao, K. K.; Naik, K.; Kumar, T. P.; Khan, A. A. Process for the Production of Benzaldehyde by the Catalytic Liquid Phase Air Oxidation of Toluene. US6495726B1, 2002.
- [140] Aprahamian, N. S. Process for the Production of Benzaldehyde. US3931330A, 1976.
- [141] Du, M.; Zeng, G.; Ye, C.; Jin, H.; Huang, J.; Sun, D.; Li, Q.; Chen, B.; Li, X. Solvent-Free Photo-Thermocatalytic Oxidation of Benzyl Alcohol on Pd/TiO<sub>2</sub> (B) Nanowires. *Mol. Catal.* **2020**, *483*, 110771.
- [142] Farrag, M.; Yahya, R. Selective Solar Photocatalytic Oxidation of Benzyl Alcohol to Benzaldehyde over Monodispersed Cu Nanoclusters/TiO<sub>2</sub>/Activated Carbon Nanocomposite. *J. Photochem. Photobiol. A Chem.* **2020**, *396*, 112527.
- [143] Si, J.; Liu, Y.; Chang, S.; Wu, D.; Tian, B.; Zhang, J. AgBr@TiO<sub>2</sub>/GO Ternary Composites with Enhanced Photocatalytic Activity for Oxidation of Benzyl Alcohol to Benzaldehyde. *Res. Chem. Intermed.* **2017**, *43* (4), 2067–2080.
- [144] Hu, Y.; Zhao, G.; Pan, Q.; Wang, H.; Shen, Z.; Peng, B.; Busser, G. W.; Wang, X.; Muhler, M. Highly Selective Anaerobic Oxidation of Alcohols over Fe-Doped SrTiO<sub>3</sub> under Visible Light. *ChemCatChem* **2019**, *11* (20), 5139–5144.
- [145] Du, M.; Zeng, G.; Huang, J.; Sun, D.; Li, Q.; Wang, G.; Li, X. Green Photocatalytic Oxidation of Benzyl Alcohol over Noble-Metal-Modified H<sub>2</sub>Ti<sub>3</sub>O<sub>7</sub> Nanowires. *ACS Sustain. Chem. Eng.* **2019**, *7* (10), 9717–9726.
- [146] Zhang, J.; Meng, S.; Ye, X.; Ling, C.; Zhang, S.; Fu, X.; Chen, S. Synergistic Effect of Photocatalysis and Thermocatalysis for Selective Oxidation of Aromatic Alcohols to Aromatic Aldehydes Using Zn<sub>3</sub>In<sub>2</sub>S<sub>6</sub>@ZnO Composite. *Appl. Catal. B Environ.* **2017**, *218*, 420–429.
- [147] Zhang, L.; Jiang, D.; Irfan, R. M.; Tang, S.; Chen, X.; Du, P. Highly Efficient

- and Selective Photocatalytic Dehydrogenation of Benzyl Alcohol for Simultaneous Hydrogen and Benzaldehyde Production over Ni-Decorated  $Zn_{0.5}Cd_{0.5}S$  Solid Solution. *J. Energy Chem.* **2019**, *30*, 71–77.
- [148] Ghobadifard, M.; Mohebbi, S.; Radovanovic, P. V. Selective Oxidation of Alcohols by Using  $CoFe_2O_4/Ag_2MoO_4$  as a Visible-Light-Driven Heterogeneous Photocatalyst. *New J. Chem.* **2020**, *44* (7), 2858–2867.
- [149] Krivtsov, I.; Ilkaeva, M.; García-López, E. I.; Marcì, G.; Palmisano, L.; Bartashevich, E.; Grigoreva, E.; Matveeva, K.; Díaz, E.; Ordóñez, S. Effect of Substituents on Partial Photocatalytic Oxidation of Aromatic Alcohols Assisted by Polymeric  $C_3N_4$ . *ChemCatChem* **2019**, *11* (11), 2713–2724.
- [150] Lopes, J. C.; Sampaio, M. J.; Fernandes, R. A.; Lima, M. J.; Faria, J. L.; Silva, C. G. Outstanding Response of Carbon Nitride Photocatalysts for Selective Synthesis of Aldehydes under UV-LED Irradiation. *Catal. Today* **2020**, *357*, 32–38. <https://doi.org/10.1016/j.cattod.2019.03.050>.
- [151] Li, F.; Wang, Y.; Du, J.; Zhu, Y.; Xu, C.; Sun, L. Simultaneous Oxidation of Alcohols and Hydrogen Evolution in a Hybrid System under Visible Light Irradiation. *Appl. Catal. B Environ.* **2018**, *225*, 258–263.
- [152] Lima, M. J.; Sampaio, M. J.; Silva, C. G.; Silva, A. M. T.; Faria, J. L. Magnetically Recoverable  $Fe_3O_4/g-C_3N_4$  Composite for Photocatalytic Production of Benzaldehyde under UV-LED Radiation. *Catal. Today* **2019**, *328*, 293–299.
- [153] Ding, J.; Xu, W.; Wan, H.; Yuan, D.; Chen, C.; Wang, L.; Guan, G.; Dai, W.-L. Nitrogen Vacancy Engineered Graphitic  $C_3N_4$ -Based Polymers for Photocatalytic Oxidation of Aromatic Alcohols to Aldehydes. *Appl. Catal. B Environ.* **2018**, *221*, 626–634.
- [154] Zhou, M.; Yang, P.; Wang, S.; Luo, Z.; Huang, C.; Wang, X. Structure-Mediated Charge Separation in Boron Carbon Nitride for Enhanced Photocatalytic Oxidation of Alcohol. *ChemSusChem* **2018**, *11* (22), 3949–3955.
- [155] Navio, J. A.; Gómez, M. G.; Pradera Adrian, M. A.; Mota, J. F. Partial or Complete Heterogeneous Photocatalytic Oxidation of Neat Toluene and 4-Picoline in Liquid Organic Oxygenated Dispersions Containing Pure or

- Iron-Doped Titania Photocatalysts. *J. Mol. Catal. A Chem.* **1996**, *104* (3), 329–339.
- [156] Méndez-Román, R.; Cardona-Martínez, N. Relationship between the Formation of Surface Species and Catalyst Deactivation during the Gas-Phase Photocatalytic Oxidation of Toluene. *Catal. Today* **1998**, *40* (4), 353–365.
- [157] Gassim, F. A.-Z. G.; Alkhateeb, A. N.; Hussein, F. H. Photocatalytic Oxidation of Benzyl Alcohol Using Pure and Sensitized Anatase. *Desalination* **2007**, *209* (1), 342–349.
- [158] Fernandes, R. A.; Sampaio, M. J.; Faria, J. L.; Silva, C. G. Aqueous Solution Photocatalytic Synthesis of *p*-Anisaldehyde by Using Graphite-like Carbon Nitride Photocatalysts Obtained via the Hard-Templating Route. *RSC Adv.* **2020**, *10* (33), 19431–19442.
- [159] Eisenstadt, A. R.-H.; Keren, Y. K. M. Process for the Preparation of Octyl Methoxy Cinnamate. EP0509426B1, 1997.
- [160] Imashiro, R.; Kuroda, T. Highly Enantioselective Mukaiyama Aldol Reaction of  $\alpha,\alpha$ -Dichloro Ketene Silyl Acetal: An Efficient Synthesis of a Key Intermediate for Diltiazem. *J. Org. Chem.* **2003**, *68* (3), 974–979.
- [161] Matsumae, H.; Akatsuka, H.; Shibatani, T. Diltiazem Synthesis. In *Encyclopedia of Industrial Biotechnology: Bioprocess, Bioseparation and Cell Technology*; Flickinger, M. C., Ed.; John Wiley & Sons, Inc., 2010; pp 1–20.
- [162] Degner, D.; Barl, M.; Siegel, H. Electrochemical Production of 4-Position Substituted Benzaldehydialkylacetals. DE2848397A1, 1978.
- [163] Merk, C.; Huber, G. Process for Electrochemical Oxidation of Organic Compounds. US20010019020A1, 2001.
- [164] Palmisano, G.; Yurdakal, S.; Augugliaro, V.; Loddo, V.; Palmisano, L. Photocatalytic Selective Oxidation of 4-Methoxybenzyl Alcohol to Aldehyde in Aqueous Suspension of Home-Prepared Titanium Dioxide Catalyst. *Adv. Synth. Catal.* **2007**, *349* (6), 964–970.
- [165] Yurdakal, S.; Palmisano, G.; Loddo, V.; Augugliaro, V.; Palmisano, L.

- Nanostructured Rutile TiO<sub>2</sub> for Selective Photocatalytic Oxidation of Aromatic Alcohols to Aldehydes in Water. *J. Am. Chem. Soc.* **2008**, *130* (5), 1568–1569.
- [166] Augugliaro, V.; Loddo, V.; López-Muñoz, M. J.; Márquez-Álvarez, C.; Palmisano, G.; Palmisano, L.; Yurdakal, S. Home-Prepared Anatase, Rutile, and Brookite TiO<sub>2</sub> for Selective Photocatalytic Oxidation of 4-Methoxybenzyl Alcohol in Water: Reactivity and ATR-FTIR Study. *Photochem. Photobiol. Sci.* **2009**, *8* (5), 663–669.
- [167] Yurdakal, S.; Augugliaro, V. Partial Oxidation of Aromatic Alcohols via TiO<sub>2</sub> Photocatalysis: The Influence of Substituent Groups on the Activity and Selectivity. *RSC Adv.* **2012**, *2* (22), 8375–8380.
- [168] Bellardita, M.; Di Paola, A.; Megna, B.; Palmisano, L. Absolute Crystallinity and Photocatalytic Activity of Brookite TiO<sub>2</sub> Samples. *Appl. Catal. B Environ.* **2017**, *201*, 150–158.
- [169] Di Paola, A.; Bellardita, M.; Palmisano, L.; Barbieriková, Z.; Brezová, V. Influence of Crystallinity and OH Surface Density on the Photocatalytic Activity of TiO<sub>2</sub> Powders. *J. Photochem. Photobiol. A Chem.* **2014**, *273*, 59–67.
- [170] Zhai, W.; Xue, S.; Zhu, A.; Luo, Y.; Tian, Y. Plasmon-Driven Selective Oxidation of Aromatic Alcohols to Aldehydes in Water with Recyclable Pt/TiO<sub>2</sub> Nanocomposites. *ChemCatChem* **2010**, *3* (1), 127–130.
- [171] Bellardita, M.; Garlisi, C.; Venezia, A. M.; Palmisano, G.; Palmisano, L. Influence of Fluorine on the Synthesis of Anatase TiO<sub>2</sub> for Photocatalytic Partial Oxidation: Are Exposed Facets the Main Actors? *Catal. Sci. Technol.* **2018**, *8* (6), 1606–1620.
- [172] Yurdakal, S.; Augugliaro, V.; Loddo, V.; Palmisano, G.; Palmisano, L. Enhancing Selectivity in Photocatalytic Formation of *p*-Anisaldehyde in Aqueous Suspension under Solar Light Irradiation via TiO<sub>2</sub> N-Doping. *New J. Chem.* **2012**, *36* (9), 1762–1768.
- [173] Zhang, Y.; Tang, Z.-R.; Fu, X.; Xu, Y.-J. Engineering the Unique 2D Mat of Graphene to Achieve Graphene-TiO<sub>2</sub> Nanocomposite for Photocatalytic Selective Transformation: What Advantage Does Graphene Have over Its

- Forebear Carbon Nanotube? *ACS Nano* **2011**, *5* (9), 7426–7435.
- [174] Tsukamoto, D.; Ikeda, M.; Shiraishi, Y.; Hara, T.; Ichikuni, N.; Tanaka, S.; Hirai, T. Selective Photocatalytic Oxidation of Alcohols to Aldehydes in Water by TiO<sub>2</sub> Partially Coated with WO<sub>3</sub>. *Chem. – A Eur. J.* **2011**, *17* (35), 9816–9824.
- [175] Abd-Elaal, A.; Parrino, F.; Ciriminna, R.; Loddo, V.; Palmisano, L.; Pagliaro, M. Alcohol-Selective Oxidation in Water under Mild Conditions via a Novel Approach to Hybrid Composite Photocatalysts. *ChemistryOpen* **2015**, *4* (6), 779–785.
- [176] Qamar, M.; Elsayed, R. B.; Alhooshani, K. R.; Ahmed, M. I.; Bahnemann, D. W. Chemoselective and Highly Efficient Conversion of Aromatic Alcohols into Aldehydes Photo-Catalyzed by Ag<sub>3</sub>PO<sub>4</sub>. *Catal. Commun.* **2015**, *58*, 34–39.
- [177] Qamar, M.; Elsayed, R. B.; Alhooshani, K. R.; Ahmed, M. I.; Bahnemann, D. W. Highly Efficient and Selective Oxidation of Aromatic Alcohols Photocatalyzed by Nanoporous Hierarchical Pt/Bi<sub>2</sub>WO<sub>6</sub> in Organic Solvent-Free Environment. *ACS Appl. Mater. Interfaces* **2015**, *7* (2), 1257–1269.
- [178] Long, B.; Ding, Z.; Wang, X. Carbon Nitride for the Selective Oxidation of Aromatic Alcohols in Water under Visible Light. *ChemSusChem* **2013**, *6* (11), 2074–2078.
- [179] Augugliaro, V.; Camera-Roda, G.; Loddo, V.; Palmisano, G.; Palmisano, L.; Parrino, F.; Puma, M. A. Synthesis of Vanillin in Water by TiO<sub>2</sub> Photocatalysis. *Appl. Catal. B Environ.* **2012**, *111–112*, 555–561.
- [180] Jaffe, G. M.; Richard, W. R. Process for the Preparation of L-Dopa. US3714242A, 1973.
- [181] Wehrli, P. A. Process for the Preparation of 2,4,5-Trimethoxybenzaldehyde. US3855306A, 1974.
- [182] Fache, M.; Boutevin, B.; Caillol, S. Vanillin Production from Lignin and Its Use as a Renewable Chemical. *ACS Sustain. Chem. Eng.* **2016**, *4* (1), 35–46.

- [183] Ciriminna, R.; Fidalgo, A.; Meneguzzo, F.; Parrino, F.; Ilharco, L. M.; Pagliaro, M. Vanillin: The Case for Greener Production Driven by Sustainability Megatrend. *ChemistryOpen* **2019**, *8* (6), 660–667.
- [184] Mukhopadhyay, A. K. Derivatives of Para-Cresol. In *Industrial Chemical Cresols and Downstream Derivatives*; Dekker, M., Ed.; Chemical Industries; Taylor & Francis: New York, 2004; pp 63–96.
- [185] Araújo, J. D. P.; Grande, C. A.; Rodrigues, A. E. Vanillin Production from Lignin Oxidation in a Batch Reactor. *Chem. Eng. Res. Des.* **2010**, *88* (8), 1024–1032.
- [186] Di Paola, A.; Bellardita, M.; Megna, B.; Parrino, F.; Palmisano, L. Photocatalytic Oxidation of Trans-Ferulic Acid to Vanillin on TiO<sub>2</sub> and WO<sub>3</sub>-Loaded TiO<sub>2</sub> Catalysts. *Catal. Today* **2015**, *252*, 195–200.
- [187] Camera-Roda, G.; Augugliaro, V.; Cardillo, A.; Loddo, V.; Palmisano, G.; Palmisano, L. A Pervaporation Photocatalytic Reactor for the Green Synthesis of Vanillin. *Chem. Eng. J.* **2013**, *224*, 136–143.
- [188] Camera-Roda, G.; Cardillo, A.; Loddo, V.; Palmisano, L.; Parrino, F. Improvement of Membrane Performances to Enhance the Yield of Vanillin in a Pervaporation Reactor. *Membranes (Basel)*. **2014**, *4* (1), 96–112.
- [189] Wu, M.; Pang, J.-H.; Song, P.-P.; Peng, J.-J.; Xu, F.; Li, Q.; Zhang, X.-M. Visible Light-Driven Oxidation of Vanillyl Alcohol in Air with Au–Pd Bimetallic Nanoparticles on Phosphorylated Hydrotalcite. *New J. Chem.* **2019**, *43* (4), 1964–1971.
- [190] Bellardita, M.; Loddo, V.; Palmisano, G.; Pibiri, I.; Palmisano, L.; Augugliaro, V. Photocatalytic Green Synthesis of Piperonal in Aqueous TiO<sub>2</sub> Suspension. *Appl. Catal. B Environ.* **2014**, *144*, 607–613.
- [191] Li, X.; Choi, Y.; Yanakawa, Y.; Park, T. Piperonal Prevents High-Fat Diet-Induced Hepatic Steatosis and Insulin Resistance in Mice via Activation of Adiponectin/AMPK Pathway. *Int. J. Obes.* **2014**, *38* (1), 140–147.
- [192] Meriga, B.; Parim, B.; Chunduri, V. R.; Naik, R. R.; Nemani, H.; Suresh, P.; Ganapathy, S.; Uddand Rao, V. V. S. Antiobesity Potential of Piperonal: Promising Modulation of Body Composition, Lipid Profiles and Obesogenic

- 
- Marker Expression in HFD-Induced Obese Rats. *Nutr. Metab. (Lond)*. **2017**, *14* (1), 72.
- [193] Yamagishi, R.; Yokomaku, A.; Omoto, F.; Misao, K.; Takada, K.; Yoshimatsu, S.; Abe, A.; Hayashi, M. Sleep-Improving Effects of the Aromatic Compound Heliotropin. *Sleep Biol. Rhythms* **2010**, *8* (4), 254–260.
- [194] Stiehm, T.; Baur, M. Use of Piperonal as an Anti-Inflammatory Additive to Cosmetics and Medicaments. EP0997137A1, 2000.
- [195] Wen, P.; Wu, D.; Zheng, P.; Chen, P.; Liu, S.; Fu, Y. Highly Efficient Biosynthesis of Heliotropin by Engineered *Escherichia Coli* Coexpressing Trans-Anethole Oxygenase and Formate Dehydrogenase. *J. Agric. Food Chem.* **2019**, *67* (51), 14121–14128.
- [196] Harada, K.; Shirai, M.; Shiba, K.; Furuya, T. Process for Preparing Piperonal. US6686482B2, 2004.
- [197] Nakatani, K.; Inoue, T.; Nishizawa, T.; Numata, S.; Ishii, T. Process for Preparing Piperonal. US4157333A, 1977.
- [198] Borzatta, V.; Capparella, E.; Chiappino, R.; Impalà, D.; Poluzzi, E.; Vaccari, A. Oppenauer's Oxidation by Paraformaldehyde of Piperonyl Alcohol to Heliotropine. *Catal. Today* **2009**, *140* (1), 112–116.
- [199] Tkachenko, O.; Tarasov, A.; Kumar, N.; Simakova, O.; Campo, B.; Kustov, L.; Murzin, D. Comparative Study of Au Modified Beta, MCM-22, Mordenite, ZSM-5, MCM-41, Ce-MCM-41 Catalysts in Piperonyl Alcohol Oxidation. *Curr. Catal.* **2012**, *1*, 58–66.
- [200] Tkachenko, O. P.; Kustov, L. M.; Tarasov, A. L.; Klementiev, K. V; Kumar, N.; Murzin, D. Y. Pd/H-Beta Catalysts: Characterization and Reactivity in Piperonyl Alcohol Selective Oxidation. *Appl. Catal. A Gen.* **2009**, *359* (1), 144–150.
- [201] Chuck, R. Technology Development in Nicotinate Production. *Appl. Catal. A Gen.* **2005**, *280* (1), 75–82.
- [202] Badawy, A. A.-B. Pellagra and Alcoholism: A Biochemical Perspective. *Alcohol Alcohol.* **2014**, *49* (3), 238–250.
-

- [203] Stratigos, J. D.; Katsambas, A. Pellagra: A Still Existing Disease. *Br. J. Dermatol.* **1977**, *96* (1), 99–106.
- [204] Carlson, L. A. Nicotinic Acid: The Broad-Spectrum Lipid Drug. A 50<sup>th</sup> Anniversary Review. *J. Intern. Med.* **2005**, *258* (2), 94–114.
- [205] Sinthupoom, N.; Prachayasittikul, V.; Prachayasittikul, S.; Ruchirawat, S.; Prachayasittikul, V. Nicotinic Acid and Derivatives as Multifunctional Pharmacophores for Medical Applications. *Eur. Food Res. Technol.* **2015**, *240* (1), 1–17.
- [206] Kumar, S. Process Intensification of Nicotinic Acid Production via Enzymatic Conversion Using Reactive Extraction. *Chem. Biochem. Eng. Q.* **2009**, *23* (3), 367–376.
- [207] Cao, W.; Kattau, R. A.; Kreilis, G. Continuous Processes for the Hydrolysis of Cyanopyridines under Substantially Adiabatic Conditions. US5756750A, 1997.
- [208] Spasiano, D.; Raspolini, L.; Satyro, S.; Mancini, G.; Pirozzi, F.; Marotta, R. The Role of Superficial Radicals in the Kinetic Modeling of 3-Pyridinemethanol and 3-Pyridinecarboxyaldehyde Selective Oxidation to Vitamin B3 in Water by Means of a TiO<sub>2</sub>/Cu(II)/UV-Solar Photocatalytic System. *Chem. Eng. J.* **2016**, *283*, 1176–1186.
- [209] Spasiano, D.; Marotta, R.; Di Somma, I.; Mancini, G. Production of Pyridinecarboxy Aldehydes, Nicotinic and Isonicotinic and Picolinic Acids by TiO<sub>2</sub>-Sacrificial Photocatalysis at Ambient Conditions and in Aqueous Solution through Artificial Solar Radiation. *Appl. Catal. B Environ.* **2015**, *163*, 248–257.
- [210] Alfè, M.; Spasiano, D.; Gargiulo, V.; Vitiello, G.; Di Capua, R.; Marotta, R. TiO<sub>2</sub>/Graphene-like Photocatalysts for Selective Oxidation of 3-Pyridine-Methanol to Vitamin B3 under UV/Solar Simulated Radiation in Aqueous Solution at Room Conditions: The Effect of Morphology on Catalyst Performances. *Appl. Catal. A Gen.* **2014**, *487*, 91–99.
- [211] Yurdakal, S.; Çetinkaya, S.; Şarлак, M. B.; Özcan, L.; Loddo, V.; Palmisano, L. Photoelectrocatalytic Oxidation of 3-Pyridinemethanol to 3-Pyridinemethanal and Vitamin B3 by TiO<sub>2</sub> Nanotubes. *Catal. Sci. Technol.*



- 2020**, 10 (1), 124–137.
- [212] Yurdakal, S.; Yanar, Ş. Ö.; Çetinkaya, S.; Alagöz, O.; Yalçın, P.; Özcan, L. Green Photocatalytic Synthesis of Vitamin B3 by Pt Loaded TiO<sub>2</sub> Photocatalysts. *Appl. Catal. B Environ.* **2017**, 202, 500–508.
- [213] Sobahi, T. R.; Amin, M. S. Upgrading the Photocatalytic Achievement of G-C<sub>3</sub>N<sub>4</sub> Nanosheets along Decoration with Ag@TiO<sub>2</sub> Nanospheres for the Preparation of Vitamin B3. *Appl. Nanosci.* **2019**, 9 (8), 1621–1636.
- [214] Friedmann, D.; Hakki, A.; Kim, H.; Choi, W.; Bahnemann, D. Heterogeneous Photocatalytic Organic Synthesis: State-of-the-Art and Future Perspectives. *Green Chem.* **2016**, 18 (20), 5391–5411.
- [215] Faria, J. L.; Wang, W. Carbon Materials in Photocatalysis. In *Carbon Materials for Catalysis*; Serp, P., Figueiredo, J. L., Eds.; John Wiley & Sons, Inc., 2009; pp 481–506.
- [216] Wang, N.; Tan, F.; Wan, L.; Wu, M.; Zhang, X. Microfluidic Reactors for Visible-Light Photocatalytic Water Purification Assisted with Thermolysis. *Biomicrofluidics* **2014**, 8 (5), 54122.
- [217] Coley, C. W.; Abolhasani, M.; Lin, H.; Jensen, K. F. Material-Efficient Microfluidic Platform for Exploratory Studies of Visible-Light Photoredox Catalysis. *Angew. Chemie Int. Ed.* **2017**, 56 (33), 9847–9850.
- [218] Ibhaddon, O. A.; Fitzpatrick, P. Heterogeneous Photocatalysis: Recent Advances and Applications. *Catalysts* **2013**, 3 (1).
- [219] Mazierski, P.; Bajorowicz, B.; Grabowska, E.; Zaleska-Medynska, A. Photoreactor Design Aspects and Modeling of Light. In *Heterogeneous photocatalysis: From fundamentals to green applications*; Colmenares, J. C., Xu, Y.-J., Eds.; Springer-Verlag, 2016; pp 211–248.
- [220] Tian, C.; Zhang, Q.; Wu, A.; Jiang, M.; Liang, Z.; Jiang, B.; Fu, H. Cost-Effective Large-Scale Synthesis of ZnO Photocatalyst with Excellent Performance for Dye Photodegradation. *Chem. Commun.* **2012**, 48 (23), 2858–2860.
- [221] Serp, P. Carbon Nanotubes and Nanofibers in Catalysis. In *Carbon Materials for Catalysis*; Serp, P., Figueiredo, J. L., Eds.; John Wiley &

- Sons, Inc.: Hoboken, New Jersey, 2008; pp 309–372.
- [222] Bacsa, R.; Kihn, Y.; Verelst, M.; Dexpert, J.; Bacsa, W.; Serp, P. Large Scale Synthesis of Zinc Oxide Nanorods by Homogeneous Chemical Vapour Deposition and Their Characterisation. *Surf. Coatings Technol.* **2007**, *201* (22–23), 9200–9204.
- [223] Qureshi, M. I.; Patel, F.; Al-Baghli, N.; Abussaud, B.; Tawabini, B. S.; Laoui, T. A Comparative Study of Raw and Metal Oxide Impregnated Carbon Nanotubes for the Adsorption of Hexavalent Chromium from Aqueous Solution. *Bioinorg. Chem. Appl.* **2017**, *2017*.
- [224] Tian, L.; Ye, L.; Deng, K.; Zan, L. TiO<sub>2</sub>/Carbon Nanotube Hybrid Nanostructures: Solvothermal Synthesis and Their Visible Light Photocatalytic Activity. *J. Solid State Chem.* **2011**, *184* (6), 1465–1471.
- [225] Pastrana-Martínez, L. M.; Morales-Torres, S.; Likodimos, V.; Figueiredo, J. L.; Faria, J. L.; Falaras, P.; Silva, A. M. T. Advanced Nanostructured Photocatalysts Based on Reduced Graphene Oxide–TiO<sub>2</sub> Composites for Degradation of Diphenhydramine Pharmaceutical and Methyl Orange Dye. *Appl. Catal. B Environ.* **2012**, *123*, 241–256.
- [226] Thommes, M. Physical Adsorption Characterization of Nanoporous Materials. *Chem. Ing. Tech.* **2010**, *82* (7), 1059–1073.
- [227] Sing, K. S. W.; Everett, D. H.; Haul, R. A. W.; Moscou, L.; Pierotti, R. A.; Rouquerol, J.; Siemieniewska, T. Reporting Physisorption Data for Gas/Solid Systems with Special Reference to the Determination of Surface Area and Porosity. *Pure Appl. Chem.* **1985**, *57* (4), 603–619.
- [228] Baruwati, B.; Kumar, D. K.; Manorama, S. V. Hydrothermal Synthesis of Highly Crystalline ZnO Nanoparticles: A Competitive Sensor for LPG and EtOH. *Sensors Actuators B Chem.* **2006**, *119* (2), 676–682.
- [229] Kumar, S. S.; Venkateswarlu, P.; Rao, V. R.; Rao, G. N. Synthesis, Characterization and Optical Properties of Zinc Oxide Nanoparticles. *Int. Nano Lett.* **2013**, *3* (1), 30–36.
- [230] Mu, J.; Shao, C.; Guo, Z.; Zhang, Z.; Zhang, M.; Zhang, P.; Chen, B.; Liu, Y. High Photocatalytic Activity of ZnO–carbon Nanofiber

- Heteroarchitectures. *ACS Appl. Mater. Interfaces* **2011**, 3 (2), 590–596.
- [231] Lee, K. M.; Lai, C. W.; Ngai, K. S.; Juan, J. C. Recent Developments of Zinc Oxide Based Photocatalyst in Water Treatment Technology: A Review. *Water Res.* **2016**, 88, 428–448.
- [232] Qi, K.; Qi, H.; Xie, Y.; Wang, Y. Enhanced Photocatalytic Performance of ZnO through Coupling with Carbon Materials. *Gen. Chem.* **2017**, 3 (1), 113–117.
- [233] Kondrakov, A. O.; Ignatev, A. N.; Lunin, V. V.; Frimmel, F. H.; Bräse, S.; Horn, H. Roles of Water and Dissolved Oxygen in Photocatalytic Generation of Free OH Radicals in Aqueous TiO<sub>2</sub> Suspensions: An Isotope Labeling Study. *Appl. Catal. B Environ.* **2016**, 182, 424–430.
- [234] Zhang, M.; Wang, Q.; Chen, C.; Zang, L.; Ma, W.; Zhao, J. Oxygen Atom Transfer in the Photocatalytic Oxidation of Alcohols by TiO<sub>2</sub>: Oxygen Isotope Studies. *Angew. Chem. Int. Ed.* **2009**, 48 (33), 6081–6084.
- [235] Wang, Q.; Zhang, M.; Chen, C.; Ma, W.; Zhao, J. Photocatalytic Aerobic Oxidation of Alcohols on TiO<sub>2</sub>: The Acceleration Effect of a Brønsted Acid. *Angew. Chemie - Int. Ed.* **2010**, 49 (43), 7976–7979.
- [236] Ling, C.; Ye, X.; Zhang, J. J.; Zhang, J. J.; Zhang, S.; Meng, S.; Fu, X.; Chen, S. Solvothermal Synthesis of CdIn<sub>2</sub>S<sub>4</sub> Photocatalyst for Selective Photosynthesis of Organic Aromatic Compounds under Visible Light. *Sci. Rep.* **2017**, 7 (1), 27–43.
- [237] Yurdakal, S.; Palmisano, G.; Loddo, V.; Alagoz, O.; Augugliaro, V.; Palmisano, L. Selective Photocatalytic Oxidation of 4-Substituted Aromatic Alcohols in Water with Rutile TiO<sub>2</sub> Prepared at Room Temperature. *Green Chem.* **2009**, 11 (4), 510–516.
- [238] Hammett, L. P. The Effect of Structure upon the Reactions of Organic Compounds. Benzene Derivatives. *J. Am. Chem. Soc.* **1937**, 59 (1), 96–103.
- [239] Silva, C. G.; Faria, J. L. Photocatalytic Oxidation of Phenolic Compounds by Using a Carbon Nanotube-Titanium Dioxide Composite Catalyst. *ChemSusChem* **2010**, 3 (5), 609–618.

- [240] Marci, G.; García-López, E. I.; Palmisano, L. Polymeric Carbon Nitride (C<sub>3</sub>N<sub>4</sub>) as Heterogeneous Photocatalyst for Selective Oxidation of Alcohols to Aldehydes. *Catal. Today* **2018**, *315*, 126–137.
- [241] Nakata, K.; Fujishima, A. TiO<sub>2</sub> Photocatalysis: Design and Applications. *J. Photochem. Photobiol. C Photochem. Rev.* **2012**, *13* (3), 169–189.
- [242] Wen, J.; Xie, J.; Chen, X.; Li, X. A Review on G-C<sub>3</sub>N<sub>4</sub>-Based Photocatalysts. *Appl. Surf. Sci.* **2017**, *391*, 72–123.
- [243] Kou, J.; Lu, C.; Wang, J.; Chen, Y.; Xu, Z.; Varma, R. S. Selectivity Enhancement in Heterogeneous Photocatalytic Transformations. *Chem. Rev.* **2017**, *117* (3), 1445–1514.
- [244] Xu, Y.; Gong, Y.; Ren, H.; Liu, W.; Niu, L.; Li, C.; Liu, X. In Situ Structural Modification of Graphitic Carbon Nitride by Alkali Halides and Influence on Photocatalytic Activity. *RSC Adv.* **2017**, *7* (52), 32592–32600.
- [245] Li, Y.; Sun, Y.; Ho, W.; Zhang, Y.; Huang, H.; Cai, Q.; Dong, F. Highly Enhanced Visible-Light Photocatalytic NO<sub>x</sub> Purification and Conversion Pathway on Self-Structurally Modified g-C<sub>3</sub>N<sub>4</sub> Nanosheets. *Sci. Bull.* **2018**, *63* (10), 609–620.
- [246] Barman, S.; Sadhukhan, M. Facile Bulk Production of Highly Blue Fluorescent Graphitic Carbon Nitride Quantum Dots and Their Application as Highly Selective and Sensitive Sensors for the Detection of Mercuric and Iodide Ions in Aqueous Media. *J. Mater. Chem.* **2012**, *22* (41), 21832–21837.
- [247] Malik, R.; Tomer, V. K.; Kienle, L.; Chaudhary, V.; Nehra, S.; Duhan, S. Ordered Mesoporous Ag–ZnO@g-CN Nanohybrid as Highly Efficient Bifunctional Sensing Material. *Adv. Mater. Interfaces* **2018**, *5* (8), 1701357.
- [248] Le, S.; Jiang, T.; Li, Y.; Zhao, Q.; Li, Y.; Fang, W.; Gong, M. Highly Efficient Visible-Light-Driven Mesoporous Graphitic Carbon Nitride/ZnO Nanocomposite Photocatalysts. *Appl. Catal. B Environ.* **2017**, *200*, 601–610.
- [249] Da Silva, E. S.; Moura, N. M. M.; Coutinho, A.; Dražić, G.; Teixeira, B. M. S.; Sobolev, N. A.; Silva, C. G.; Neves, M. G. P. M. S.; Prieto, M.; Faria, J.

- L.  $\beta$ -Cyclodextrin as a Precursor to Holey C-Doped g-C<sub>3</sub>N<sub>4</sub> Nanosheets for Photocatalytic Hydrogen Generation. *ChemSusChem* **2018**, *11* (16), 2681–2694.
- [250] Da Silva, E. S.; Moura, N. M. M.; Neves, M. G. P. M. S.; Coutinho, A.; Prieto, M.; Silva, C. G.; Faria, J. L. Novel Hybrids of Graphitic Carbon Nitride Sensitized with Free-Base Meso-Tetrakis(Carboxyphenyl) Porphyrins for Efficient Visible Light Photocatalytic Hydrogen Production. *Appl. Catal. B Environ.* **2018**, *221*, 56–69.
- [251] Zhou, Y.; Zhang, L.; Huang, W.; Kong, Q.; Fan, X.; Wang, M.; Shi, J. N-Doped Graphitic Carbon-Incorporated g-C<sub>3</sub>N<sub>4</sub> for Remarkably Enhanced Photocatalytic H<sub>2</sub> Evolution under Visible Light. *Carbon N. Y.* **2016**, *99*, 111–117.
- [252] Gu, S.; Hsieh, C.-T.; Ashraf Gandomi, Y.; Chang, J.-K.; Li, J. J.; Li, J. J.; Zhang, H.; Guo, Q.; Lau, K. C.; Pandey, R. Microwave Growth and Tunable Photoluminescence of Nitrogen-Doped Graphene and Carbon Nitride Quantum Dots. *J. Mater. Chem. C* **2019**, *7* (18), 5468–5476.
- [253] Tan, J.; Chen, H.; Gao, Y.; Li, H. Nitrogen-Doped Porous Carbon Derived from Citric Acid and Urea with Outstanding Supercapacitance Performance. *Electrochim. Acta* **2015**, *178*, 144–152.
- [254] Liu, W.; Xu, S.; Guan, S.; Liang, R.; Wei, M.; Evans, D. G.; Duan, X. Confined Synthesis of Carbon Nitride in a Layered Host Matrix with Unprecedented Solid-State Quantum Yield and Stability. *Adv. Mater.* **2018**, *30* (2), 1704376.
- [255] Cao, X.; Ma, J.; Lin, Y.; Yao, B.; Li, F.; Weng, W.; Lin, X. A Facile Microwave-Assisted Fabrication of Fluorescent Carbon Nitride Quantum Dots and Their Application in the Detection of Mercury Ions. *Spectrochim. Acta Part A Mol. Biomol. Spectrosc.* **2015**, *151*, 875–880.
- [256] Luo, L.; Zhang, M.; Wang, P.; Wang, Y.; Wang, F. Nitrogen Rich Carbon Nitride Synthesized by Copolymerization with Enhanced Visible Light Photocatalytic Hydrogen Evolution. *New J. Chem.* **2018**, *42* (2), 1087–1091.
- [257] Li, M.; Zhang, S.; Liu, X.; Han, J.; Zhu, X.; Ge, Q.; Wang, H. Polydopamine

- and Barbituric Acid Co-Modified Carbon Nitride Nanospheres for Highly Active and Selective Photocatalytic CO<sub>2</sub> Reduction. *Eur. J. Inorg. Chem.* **2019**, 2019 (15), 2058–2064.
- [258] Chen, Y.; Zhang, J.; Zhang, M.; Wang, X. Molecular and Textural Engineering of Conjugated Carbon Nitride Catalysts for Selective Oxidation of Alcohols with Visible Light. *Chem. Sci.* **2013**, 4 (8), 3244–3248.
- [259] Li, Y.; Wang, M.-Q.; Bao, S.-J.; Lu, S.; Xu, M.; Long, D.; Pu, S. Tuning and Thermal Exfoliation Graphene-like Carbon Nitride Nanosheets for Superior Photocatalytic Activity. *Ceram. Int.* **2016**, 42 (16), 18521–18528.
- [260] Niu, P.; Zhang, L.; Liu, G.; Cheng, H.-M. Graphene-like Carbon Nitride Nanosheets for Improved Photocatalytic Activities. *Adv. Funct. Mater.* **2012**, 22 (22), 4763–4770.
- [261] Song, X.; Zhang, X.; Li, X.; Che, H.; Huo, P.; Ma, C.; Yan, Y.; Yang, G. Enhanced Light Utilization Efficiency and Fast Charge Transfer for Excellent CO<sub>2</sub> Photoreduction Activity by Constructing Defect Structures in Carbon Nitride. *J. Colloid Interface Sci.* **2020**, 578, 574–583.
- [262] Lei, G.; Cao, Y.; Zhao, W.; Dai, Z.; Shen, L.; Xiao, Y.; Jiang, L. Exfoliation of Graphitic Carbon Nitride for Enhanced Oxidative Desulfurization: A Facile and General Strategy. *ACS Sustain. Chem. Eng.* **2019**, 7(5), 4941–4950.
- [263] Dong, G.; Wen, Y.; Fan, H.; Wang, C.; Cheng, Z.; Zhang, M.; Ma, J.; Zhang, S. Graphitic Carbon Nitride with Thermally-Induced Nitrogen Defects: An Efficient Process to Enhance Photocatalytic H<sub>2</sub> Production Performance. *RSC Adv.* **2020**, 10 (32), 18632–18638.
- [264] Zhang, A.; Gu, L.; Hou, K.; Dai, C.; Song, C.; Guo, X. Mesoporous Structure-Tunable and Size-Controllable Hierarchical Porous Silica Nanospheres Synthesized by Aldehyde-Modified Stober Method. *RSC Adv.* **2015**, 5(72), 58355–58362.
- [265] Zhang, J.; Zhang, G.; Chen, X.; Lin, S.; Möhlmann, L.; Dołęga, G.; Lipner, G.; Antonietti, M.; Blechert, S.; Wang, X. Co-Monomer Control of Carbon Nitride Semiconductors to Optimize Hydrogen Evolution with Visible Light.

- 
- Angew. Chemie Int. Ed.* **2012**, *51* (13), 3183–3187.
- [266] Li, X.; Sun, Q.; Li, M.; Yang, J.; Chen, X.; Yang, Y.; Li, X.; Hu, T.; Sui, Y.; Wu, X. Photocatalytic Properties of Nano-Structured Carbon Nitride: A Comparison with Bulk Graphitic Carbon Nitride. *Int. J. Mater. Res.* **2017**, *109* (2), 129–135.
- [267] Cui, Y.; Huang, J.; Fu, X.; Wang, X. Metal-Free Photocatalytic Degradation of 4-Chlorophenol in Water by Mesoporous Carbon Nitride Semiconductors. *Catal. Sci. Technol.* **2012**, *2* (7), 1396–1402.
- [268] Cao, J.; Qin, C.; Wang, Y.; Zhang, H.; Sun, G.; Zhang, Z. Solid-State Method Synthesis of SnO<sub>2</sub>-Decorated g-C<sub>3</sub>N<sub>4</sub> Nanocomposites with Enhanced Gas-Sensing Property to Ethanol. *Materials (Basel)*. **2017**, *10* (6), 604.
- [269] Sim, L. C.; Wong, J. L.; Hak, C. H.; Tai, J. Y.; Leong, K. H.; Saravanan, P. Sugarcane Juice Derived Carbon Dot–Graphitic Carbon Nitride Composites for Bisphenol A Degradation under Sunlight Irradiation. *Beilstein J. Nanotechnol.* **2018**, *9*, 353–363.
- [270] Bao, Y.; Chen, K. AgCl/Ag/g-C<sub>3</sub>N<sub>4</sub> Hybrid Composites: Preparation, Visible Light-Driven Photocatalytic Activity and Mechanism. *Nano-Micro Lett.* **2016**, *8* (2), 182–192.
- [271] Gao, D.; Liu, Y.; Liu, P.; Si, M.; Xue, D. Atomically Thin B Doped G-C<sub>3</sub>N<sub>4</sub> Nanosheets: High-Temperature Ferromagnetism and Calculated Half-Metallicity. *Sci. Rep.* **2016**, *6*, 1–8.
- [272] Wu, S.-Z.; Yu, Y.-X.; Zhang, W.-D. Processing Graphitic Carbon Nitride for Improved Photocatalytic Activity. *Mater. Sci. Semicond. Process.* **2014**, *24*, 15–20.
- [273] Wang, H.; Zhang, X.; Xie, J.; Zhang, J.; Ma, P.; Pan, B.; Xie, Y. Structural Distortion in Graphitic-C<sub>3</sub>N<sub>4</sub> Realizing an Efficient Photoreactivity. *Nanoscale* **2015**, *7* (12), 5152–5156.
- [274] Choudhury, B.; Paul, K. K.; Sanyal, D.; Hazarika, A.; Giri, P. K. Evolution of Nitrogen-Related Defects in Graphitic Carbon Nitride Nanosheets Probed by Positron Annihilation and Photoluminescence Spectroscopy. *J.*
-

- Phys. Chem. C* **2018**, 122 (16), 9209–9219.
- [275] Zhu, J.; Xiao, P.; Li, H.; Carabineiro, S. A. C. Graphitic Carbon Nitride: Synthesis, Properties, and Applications in Catalysis. *ACS Appl. Mater. Interfaces* **2014**, 6 (19), 16449–16465.
- [276] Bai, Z.; Bai, Z.; Gao, T.; Bai, Z.; Zhu, Y. Preparation Effects on the Morphology and Photocatalytic Properties of Carbon Nitride Nanotubes. *Results Phys.* **2019**, 13, 102254.
- [277] Ovcharov, M.; Shcherban, N.; Filonenko, S.; Mishura, A.; Skoryk, M.; Shvalagin, V.; Granchak, V. Hard Template Synthesis of Porous Carbon Nitride Materials with Improved Efficiency for Photocatalytic CO<sub>2</sub> Utilization. *Mater. Sci. Eng. B* **2015**, 202, 1–7.
- [278] Katsumata, H.; Sakai, T.; Suzuki, T.; Kaneco, S. Highly Efficient Photocatalytic Activity of G-C<sub>3</sub>N<sub>4</sub>/Ag<sub>3</sub>PO<sub>4</sub> Hybrid Photocatalysts through Z-Scheme Photocatalytic Mechanism under Visible Light. *Ind. Eng. Chem. Res.* **2014**, 53 (19), 8018–8025.
- [279] Wang, Z.; Guan, W.; Sun, Y.; Dong, F.; Zhou, Y.; Ho, W.-K. Water-Assisted Production of Honeycomb-like g-C<sub>3</sub>N<sub>4</sub> with Ultralong Carrier Lifetime and Outstanding Photocatalytic Activity. *Nanoscale* **2015**, 7 (6), 2471–2479.
- [280] Zhang, H.; Guo, L.-H.; Zhao, L.; Wan, B.; Yang, Y. Switching Oxygen Reduction Pathway by Exfoliating Graphitic Carbon Nitride for Enhanced Photocatalytic Phenol Degradation. *J. Phys. Chem. Lett.* **2015**, 6 (6), 958–963.
- [281] Wang, Y.; Zhao, S.; Zhang, Y.; Chen, W.; Yuan, S.; Zhou, Y.; Huang, Z. Synthesis of Graphitic Carbon Nitride with Large Specific Surface Area via Copolymerizing with Nucleobases for Photocatalytic Hydrogen Generation. *Appl. Surf. Sci.* **2019**, 463, 1–8.
- [282] Wei, Y.; Jiao, J.; Zhao, Z.; Zhong, W.; Li, J.; Liu, J.; Jiang, G.; Duan, A. 3D Ordered Macroporous TiO<sub>2</sub>-Supported Pt@CdS Core–Shell Nanoparticles: Design, Synthesis and Efficient Photocatalytic Conversion of CO<sub>2</sub> with Water to Methane. *J. Mater. Chem. A* **2015**, 3 (20), 11074–11085.



- [283] Wang, T.; Yan, X.; Zhao, S.; Lin, B.; Xue, C.; Yang, G.; Ding, S.; Yang, B.; Ma, C.; Yang, G.; Yang, G. A Facile One-Step Synthesis of Three-Dimensionally Ordered Macroporous N-Doped TiO<sub>2</sub> with Ethanediamine as the Nitrogen Source. *J. Mater. Chem. A* **2014**, *2* (37), 15611–15619.
- [284] Zhou, Z.; Li, K.; Deng, W.; Li, J.; Yan, Y.; Li, Y.; Quan, X.; Wang, T. Nitrogen Vacancy Mediated Exciton Dissociation in Carbon Nitride Nanosheets: Enhanced Hydroxyl Radicals Generation for Efficient Photocatalytic Degradation of Organic Pollutants. *J. Hazard. Mater.* **2020**, *387*, 122023.
- [285] Krivtsov, I.; Garcia Lopez, E.; Marci, G.; Palmisano, L.; Amghouz, Z.; R. García, J.; Ordóñez, S.; Díaz, E. Selective Photocatalytic Oxidation of 5-Hydroxymethyl-2-Furfural to 2,5-Furandicarboxyaldehyde in Aqueous Suspension of g-C<sub>3</sub>N<sub>4</sub>. *Appl. Catal. B Environ.* **2017**, *204*, 430–439.
- [286] Kobielski, M.; Mikrut, P.; Macyk, W. Photocatalytic Synthesis of Chemicals. In *Advances in Inorganic Chemistry*; van Eldik, R., Macyk, W. B. T.-A. in I. C., Eds.; Academic Press, 2018; Vol. 72, pp 93–144.
- [287] Lee, H. L.; Sofer, Z.; Mazánek, V.; Luxa, J.; Chua, C. K.; Pumera, M. Graphitic Carbon Nitride: Effects of Various Precursors on the Structural, Morphological and Electrochemical Sensing Properties. *Appl. Mater. Today* **2017**, *8*, 150–162.
- [288] Liu, L.; Deng, Q.-F.; Ma, T.-Y.; Lin, X.-Z.; Hou, X.-X.; Liu, Y.-P.; Yuan, Z.-Y. Ordered Mesoporous Carbons: Citric Acid-Catalyzed Synthesis, Nitrogen Doping and CO<sub>2</sub> Capture. *J. Mater. Chem.* **2011**, *21* (40), 16001–16009.
- [289] Wyrzykowski, D.; Hebanowska, E.; Nowak-Wiczak, G.; Makowski, M.; Chmurzyński, L. Thermal Behaviour of Citric Acid and Isomeric Aconitic Acids. *J. Therm. Anal. Calorim.* **2011**, *104* (2), 731–735.
- [290] Wu, J.; Li, N.; Fang, H.-B.; Li, X.; Zheng, Y.-Z.; Tao, X. Nitrogen Vacancies Modified Graphitic Carbon Nitride: Scalable and One-Step Fabrication with Efficient Visible-Light-Driven Hydrogen Evolution. *Chem. Eng. J.* **2019**, *358*, 20–29.
- [291] Ran, J.; Ma, T. Y.; Gao, G.; Du, X.-W.; Qiao, S. Z. Porous P-Doped

- Graphitic Carbon Nitride Nanosheets for Synergistically Enhanced Visible-Light Photocatalytic H<sub>2</sub> Production. *Energy Environ. Sci.* **2015**, 8 (12), 3708–3717.
- [292] Jourshabani, M.; Shariatnia, Z.; Badiei, A. Sulfur-Doped Mesoporous Carbon Nitride Decorated with Cu Particles for Efficient Photocatalytic Degradation under Visible-Light Irradiation. *J. Phys. Chem. C* **2017**, 121 (35), 19239–19253.
- [293] Tang, J.-Y.; Kong, X. Y.; Ng, B.-J.; Chew, Y.-H.; Mohamed, A. R.; Chai, S.-P. Midgap-State-Mediated Two-Step Photoexcitation in Nitrogen Defect-Modified g-C<sub>3</sub>N<sub>4</sub> Atomic Layers for Superior Photocatalytic CO<sub>2</sub> Reduction. *Catal. Sci. Technol.* **2019**, 9 (9), 2335–2343.
- [294] Chen, Z.; Sun, P.; Fan, B.; Liu, Q.; Zhang, Z.; Fang, X. Textural and Electronic Structure Engineering of Carbon Nitride via Doping with  $\pi$ -Deficient Aromatic Pyridine Ring for Improving Photocatalytic Activity. *Appl. Catal. B Environ.* **2015**, 170–171, 10–16.
- [295] Yaghoubi, H.; Li, Z.; Chen, Y.; Ngo, H. T.; Bhethanabotla, V. R.; Joseph, B.; Ma, S.; Schlaf, R.; Takshi, A. Toward a Visible Light-Driven Photocatalyst: The Effect of Midgap-States-Induced Energy Gap of Undoped TiO<sub>2</sub> Nanoparticles. *ACS Catal.* **2015**, 5 (1), 327–335.
- [296] Chen, Y.; Wang, B.; Lin, S.; Zhang, Y.; Wang, X. Activation of  $n \rightarrow \pi^*$  Transitions in Two-Dimensional Conjugated Polymers for Visible Light Photocatalysis. *J. Phys. Chem. C* **2014**, 118 (51), 29981–29989.
- [297] Mao, J.; Peng, T.; Zhang, X.; Li, K.; Ye, L.; Zan, L. Effect of Graphitic Carbon Nitride Microstructures on the Activity and Selectivity of Photocatalytic CO<sub>2</sub> Reduction under Visible Light. *Catal. Sci. Technol.* **2013**, 3 (5), 1253–1260.
- [298] Manke, A.-M.; Geisel, K.; Fetzer, A.; Kurz, P. A Water-Soluble Tin(IV) Porphyrin as a Bioinspired Photosensitiser for Light-Driven Proton-Reduction. *Phys. Chem. Chem. Phys.* **2014**, 16 (24), 12029–12042.
- [299] Madhumitha, A.; Preethi, V.; Kanmani, S. Photocatalytic Hydrogen Production Using TiO<sub>2</sub> Coated Iron-Oxide Core Shell Particles. *Int. J. Hydrogen Energy* **2018**, 43 (8), 3946–3956.

- [300] Kang, Y.; Yang, Y.; Yin, L.-C.; Kang, X.; Liu, G.; Cheng, H.-M. An Amorphous Carbon Nitride Photocatalyst with Greatly Extended Visible-Light-Responsive Range for Photocatalytic Hydrogen Generation. *Adv. Mater.* **2015**, *27* (31), 4572–4577.
- [301] Miller, T. S.; Jorge, A. B.; Suter, T. M.; Sella, A.; Corà, F.; McMillan, P. F. Carbon Nitrides: Synthesis and Characterization of a New Class of Functional Materials. *Phys. Chem. Chem. Phys.* **2017**, *19* (24), 15613–15638.
- [302] Xu, X.; Lai, L.; Zeng, T.; Yu, Y.; He, Z.; Chen, J.; Song, S. In Situ Formation of Pyridine-Type Carbonitrides-Modified Disorder-Engineered C-TiO<sub>2</sub> Used for Enhanced visible-Light-Driven Photocatalytic Hydrogen Evolution. *J. Phys. Chem. C* **2018**, *122* (33), 18870–18879.
- [303] Mohamed, M. A.; M. Zain, M. F.; Minggu, L. J.; Kassim, M. B.; Jaafar, J.; Saidina Amin, N. A.; Mohd Hir, Z. A.; Rosmi, M. S. Enhancement of Visible Light Photocatalytic Hydrogen Evolution by Bio-Mimetic C-Doped Graphitic Carbon Nitride. *Int. J. Hydrogen Energy* **2019**, *44* (26), 13098–13105.
- [304] Fang, J.; Fan, H.; Li, M.; Long, C. Nitrogen Self-Doped Graphitic Carbon Nitride as Efficient Visible Light Photocatalyst for Hydrogen Evolution. *J. Mater. Chem. A* **2015**, *3* (26), 13819–13826.
- [305] Zhang, M.; Wang, X. Two Dimensional Conjugated Polymers with Enhanced Optical Absorption and Charge Separation for Photocatalytic Hydrogen Evolution. *Energy Environ. Sci.* **2014**, *7* (6), 1902–1906.
- [306] Zhang, J.; Zhang, M.; Lin, S.; Fu, X.; Wang, X. Molecular Doping of Carbon Nitride Photocatalysts with Tunable Bandgap and Enhanced Activity. *J. Catal.* **2014**, *310*, 24–30.
- [307] Xia, P.; Zhu, B.; Yu, J.; Cao, S.; Jaroniec, M. Ultra-Thin Nanosheet Assemblies of Graphitic Carbon Nitride for Enhanced Photocatalytic CO<sub>2</sub> Reduction. *J. Mater. Chem. A* **2017**, *5* (7), 3230–3238.
- [308] Zhao, Q.; Yang, C.; Liu, R. Ultrathin Graphitic Carbon Nitride Nanosheets as Efficient Catalysts for Degradation of Pollutants under Visible Light. *ChemistrySelect* **2019**, *4* (40), 11815–11821.

- [309] Serpone, N. Heterogeneous Photocatalysis and Prospects of TiO<sub>2</sub>-Based Photocatalytic DeNO<sub>x</sub>ing the Atmospheric Environment. *Catalysts* **2018**, *8* (11).
- [310] Augugliaro, V.; Bellardita, M.; Loddo, V.; Palmisano, G.; Palmisano, L.; Yurdakal, S. Overview on Oxidation Mechanisms of Organic Compounds by TiO<sub>2</sub> in Heterogeneous Photocatalysis. *J. Photochem. Photobiol. C Photochem. Rev.* **2012**, *13* (3), 224–245.
- [311] Niu, P.; Liu, G.; Cheng, H. M. Nitrogen Vacancy-Promoted Photocatalytic Activity of Graphitic Carbon Nitride. *J. Phys. Chem. C* **2012**, *116* (20), 11013–11018.
- [312] Tu, W.; Xu, Y.; Wang, J.; Zhang, B.; Zhou, T.; Yin, S.; Wu, S.; Li, C.; Huang, Y.; Zhou, Y.; Zou, Z.; Robertson, J.; Kraft, M.; Xu, R. Investigating the Role of Tunable Nitrogen Vacancies in Graphitic Carbon Nitride Nanosheets for Efficient Visible-Light-Driven H<sub>2</sub> Evolution and CO<sub>2</sub> Reduction. *ACS Sustain. Chem. Eng.* **2017**, *5* (8), 7260–7268.
- [313] Zhang, Y.; Gao, J.; Chen, Z. A Solid-State Chemical Reduction Approach to Synthesize Graphitic Carbon Nitride with Tunable Nitrogen Defects for Efficient Visible-Light Photocatalytic Hydrogen Evolution. *J. Colloid Interface Sci.* **2019**, *535*, 331–340.
- [314] Dias, E. M.; Christoforidis, K. C.; Francàs, L.; Petit, C. Tuning Thermally Treated Graphitic Carbon Nitride for H<sub>2</sub> Evolution and CO<sub>2</sub> Photoreduction: The Effects of Material Properties and Mid-Gap States. *ACS Appl. Energy Mater.* **2018**, *1* (11), 6524–6534.
- [315] Niu, P.; Qiao, M.; Li, Y.; Huang, L.; Zhai, T. Distinctive Defects Engineering in Graphitic Carbon Nitride for Greatly Extended Visible Light Photocatalytic Hydrogen Evolution. *Nano Energy* **2018**, *44*, 73–81.
- [316] Yang, P.; Zhao, J.; Qiao, W.; Li, L.; Zhu, Z. Ammonia-Induced Robust Photocatalytic Hydrogen Evolution of Graphitic Carbon Nitride. *Nanoscale* **2015**, *7* (45), 18887–18890.
- [317] Niu, P.; Yin, L.-C.; Yang, Y.-Q.; Liu, G.; Cheng, H.-M. Increasing the Visible Light Absorption of Graphitic Carbon Nitride (Melon) Photocatalysts by Homogeneous Self-Modification with Nitrogen Vacancies. *Adv. Mater.*

- 2014**, 26 (47), 8046–8052.
- [318] Kang, Y.; Yang, Y.; Yin, L.-C.; Kang, X.; Wang, L.; Liu, G.; Cheng, H.-M. Selective Breaking of Hydrogen Bonds of Layered Carbon Nitride for Visible Light Photocatalysis. *Adv. Mater.* **2016**, 28 (30), 6471–6477.
- [319] Sun, B.; Yu, H.; Yang, Y.; Li, H.; Zhai, C.; Qian, D.-J.; Chen, M. New Complete Assignment of X-Ray Powder Diffraction Patterns in Graphitic Carbon Nitride Using Discrete Fourier Transform and Direct Experimental Evidence. *Phys. Chem. Chem. Phys.* **2017**, 19 (38), 26072–26084.
- [320] Fina, F.; Callear, S. K.; Carins, G. M.; Irvine, J. T. S. Structural Investigation of Graphitic Carbon Nitride via XRD and Neutron Diffraction. *Chem. Mater.* **2015**, 27 (7), 2612–2618.
- [321] Langford, J. I.; Wilson, A. J. C. Scherrer after Sixty Years: A Survey and Some New Results in the Determination of Crystallite Size. *J. Appl. Crystallogr.* **1978**, 11 (2), 102–113.
- [322] Ibad, M. F.; Kosslick, H.; Tomm, J. W.; Frank, M.; Schulz, A. Impact of the Crystallinity of Mesoporous Polymeric Graphitic Carbon Nitride on the Photocatalytic Performance under UV and Visible Light. *Microporous Mesoporous Mater.* **2017**, 254, 136–145.
- [323] Lin, L.; Yu, Z.; Wang, X. Crystalline Carbon Nitride Semiconductors for Photocatalytic Water Splitting. *Angew. Chemie Int. Ed.* **2019**, 58 (19), 6164–6175.
- [324] Son, E. J.; Lee, Y. W.; Ko, J. W.; Park, C. B. Amorphous Carbon Nitride as a Robust Photocatalyst for Biocatalytic Solar-to-Chemical Conversion. *ACS Sustain. Chem. Eng.* **2019**, 7 (2), 2545–2552.
- [325] Würtele, M. A.; Kolbe, T.; Lipsz, M.; Külberg, A.; Weyers, M.; Kneissl, M.; Jekel, M. Application of GaN-Based Ultraviolet-C Light Emitting Diodes – UV LEDs – for Water Disinfection. *Water Res.* **2011**, 45 (3), 1481–1489.
- [326] Song, K.; Mohseni, M.; Taghipour, F. Application of Ultraviolet Light-Emitting Diodes (UV-LEDs) for Water Disinfection: A Review. *Water Res.* **2016**, 94, 341–349.
- [327] Ibrahim, M. A. S.; MacAdam, J.; Autin, O.; Jefferson, B. Evaluating the

- Impact of LED Bulb Development on the Economic Viability of Ultraviolet Technology for Disinfection. *Environ. Technol.* **2014**, 35 (4), 400–406.
- [328] Miller, T. S.; Jorge, A. B.; Suter, T. M.; Sella, A.; Corà, F.; McMillan, P. F. Carbon Nitrides: Synthesis and Characterization of a New Class of Functional Materials. *Phys. Chem. Chem. Phys.* **2017**, 19 (24), 15613–15638.
- [329] He, P.; Tang, X.; Chen, L.; Xie, P.; He, L.; Zhou, H.; Zhang, D.; Fan, T. Patterned Carbon Nitride–Based Hybrid Aerogel Membranes via 3D Printing for Broadband Solar Wastewater Remediation. *Adv. Funct. Mater.* **2018**, 28 (29), 1801121.
- [330] Wu, P.; Wang, J.; Zhao, J.; Guo, L.; Osterloh, F. E. Structure Defects in G-C<sub>3</sub>N<sub>4</sub> Limit Visible Light Driven Hydrogen Evolution and Photovoltage. *J. Mater. Chem. A* **2014**, 2 (47), 20338–20344.
- [331] Yuan, Y.; Zhang, L.; Xing, J.; Utama, M. I. B.; Lu, X.; Du, K.; Li, Y.; Hu, X.; Wang, S.; Genç, A.; Dunin-Borkowski, R.; Arbiol, J.; Xiong, Q. High-Yield Synthesis and Optical Properties of g-C<sub>3</sub>N<sub>4</sub>. *Nanoscale* **2015**, 7 (29), 12343–12350.
- [332] Dijkstra, M. F. J.; Michorius, A.; Buwalda, H.; Panneman, H. J.; Winkelman, J. G. M.; Beenackers, A. A. C. . Comparison of the Efficiency of Immobilized and Suspended Systems in Photocatalytic Degradation. *Catal. Today* **2001**, 66 (2), 487–494.

